Investigation of metal-rich half-Heusler Thermoelectrics: Synthesis, Structure and Properties

Sonia Agata Barczak

Submitted for the degree of Doctor of Philosophy

Heriot-Watt University

Institute of Chemical Sciences

May 2018

ABSTRACT

Thermoelectric materials that can directly convert heat into electricity offer a possible avenue to address the world's increasing demand for energy. Metal-rich half-Heusler compounds are of interest due to their favourable electronic transport properties. Unfortunately, widespread application is limited by comparatively high thermal conductivity.

The effect of processing and excess metal (Ni and Cu) on thermoelectric properties of MNiSn, $M_{0.5}M'_{0.5}NiSn$ (M = Ti, Zr, Hf) and $Ti_{0.5}Zr_{0.25}Hf_{0.25}NiSn$ materials was investigated and is discussed in Chapters 3 and 4. This work revealed that Cu is effective n-type dopant, which improves electronic properties of half-Heusler materials. Detailed structure analysis, which included high-resolution synchrotron X-ray diffraction, neutron powder diffraction and electron microscopy revealed that most of the excess metals are randomly distributed on the interstitial sites, producing significant point defect scattering of phonons. In addition, Cu segregation leads to grain-by-grain compositional variations, with grains tending towards either half-Heusler or full-Heusler composition.

In addition to the microstructural and properties studies, an in-situ neutron powder diffraction experiment was used to understand the formation of Ni-rich $TiNi_{1+y}Sn$ (y = 0, 0.075 and 0.25) and multiphase $M_{0.5}M'_{0.5}NiSn$ compositions during solid-state reaction. As described in Chapter 5, the half-Heusler formation occurs through a complex, multistep reaction, which involves many intermediates. ZrNiSn and $Ti_{0.5}Zr_{0.25}Hf_{0.25}NiSn$ underwent spontaneous self-propagating combustions, which is a new route to prepare impurity-free half-Heusler alloys.

The last results Chapter describes the analysis of neutron total scattering data using Reverse Monte Carlo modelling. This study was performed to gain insight into spatial distribution of excess Ni within the half-Heusler structure. It confirmed random distribution of excess metal on the interstitial sites.

ACKNOWLEDGMENTS

I would like to take some time to thank all the people who supported and assisted me during this project. First, I wish to thank my supervisor Dr Jan-Willem Bos for supervising this PhD. I appreciate his support since the day I began working on my undergraduate Master's research project. Thanks to his encouragement, guidance and invaluable suggestions this PhD has been completed.

I would also like to acknowledge Dr Mathew Tucker at Oak Ridge National Laboratory complex. I have been extremely lucky to have a host who cared so much about my work, whose rich knowledge, insightful suggestions and conversations enabled me to complete one of my research projects. Thank you for the warm welcome and for making my time in Tennessee so invaluable and interesting.

I must also thank the technical and support staff at Heriot-Watt University – Alan Barton and Mary Pratt, for conversations, urgent orders and repairs. Thanks are due to the ICS staff who contributed to my learning and development throughout my undergraduate degree and PhD. I also thank Dr Ron Smith and Dr Ivan da Silva – our local contacts at ISIS, Prof. Chiu Tang – local contact at Diamond; Dr Jim Buckman, Dr Donald MacLaren and Dr John Halpin, who carried out the electron microscopy studies; Dr Michael Pollet and Dr Rodolphe Decourt, who carried out thermal properties measurements.

Throughout my study, I have made many amazing friends and memories. The members of the Bos group have contributed to my personal and professional time at Heriot-Watt University. I would like to thank Daniella Ferluccio. You have always been there for me and for a good moan! Over the years have become a friend and I truly hope that we will be given a chance to work together in the future. My special thanks are extended to Dr Srinivas Popuri. I regard you as my "second supervisor". Thank you for your witty support to push myself. I would also like to thank other past group members that I had the pleasure to work with – Dr Ruth Downie and Dr Maryana Asaad.

My special words of thanks go to my family and friends. I am grateful to my parents, who always believed in me and encouraged me to reach the tops. The last words of acknowledgments I have saved for my fiancé Michał Bryś. You have been with me all these years making them best years of my life. Your support, encouragement and patience, especially during the last few months, helped me to complete this PhD.

I would like to dedicate this thesis to my family.

DECLARATION STATEMENT

TABLE OF CONTENTS

LIST OF PUBLICATIONS BY THE CANDIDATE ix
LIST OF ABREVIATIONS x
Chapter 1 - Introduction 1
1.1. Thermoelectric Effects 2
1.1.1. The Seebeck Effect 2
1.1.2. The Peltier Effect 3
1.1.3. The Thomson Effect 5
1.2. Thermoelectric Devices 5
1.3. The Figure-of-Merit ZT and Thermoelectric Efficiency 6
1.4. Electronic Properties of Solids 8
1.4.1. Molecular Orbital Theory 8
1.4.2. Free Electron Theory 9
1.4.3. Band Structure of Metals, Insulators and Semiconductors 11
1.5. Thermoelectric Properties 12
1.5.1. Seebeck Coefficient (S) 12
1.5.2. Electrical Conductivity (σ) 14
1.5.3. Lattice Vibrations 15
1.5.4. Thermal Conductivity (κ) 16
1.6. State of Art Thermoelectric Materials 17
1.6.1. SnSe 18
1.6.2. PbTe-based alloys 20
1.6.3. Caged Compounds – Skutterudites and Clathrates 21
1.7. Half-Heuslers 22
1.7.1. Crystal Structure 22
1.7.2. Electronic Structure 23
1.7.3. Vibrational Properties 25
1.7.4. Full-Heusler 27
1.7.5. Thermoelectric Properties of Half-Heusler Alloys 27
1.7.5.1. Isovalent Substitution in MNiSn (M = Ti, Zr, Hf) 28
1.7.5.2. Aliovalent Substitution in MNiSn (M = Ti, Zr, Hf) 30
1.7.5.3. Excess Metal in MNiSn Composites 31
1.7.5.3.1. Full-Heusler Micro-Inclusions 33
1.7.5.3.1. Full-Heusler Nano-Inclusions 35
1.7.5.3.1. Random Distribution of Excess Metal 41

1.7.5.4. Synthesis Technique *42*
1.8. Aims and Objectives **43**
Chapter 2 - Experimental Method, Characterisations and Theory 45
2.1. Introduction **45**
2.2. Synthesis Methods **45**
2.2.1. Solid-State Reactions ***45***
2.2.2. Densification – Hot Pressing ***45***
2.3. Structure Determination **46**
2.3.1. X-Ray Diffraction ***47***
2.3.1.1. Background and Theory *47*
2.3.1.2. Powder Diffraction *52*
2.3.1.3. Bruker D8 Advance Diffractometer *52*
2.3.2. High Resolution Synchrotron X-ray Diffraction ***53***
2.3.2.1. Background and Theory *53*
2.3.2.2. I11 Beamline *54*
2.3.3. Neutron Powder Diffraction ***55***
2.3.3.1. Background and Theory *55*
2.3.3.2. POLARIS *57*
2.3.3.3. GEM *58*
2.3.4. Rietveld Refinement ***59***
2.3.4.1. Observed Intensities *59*
2.3.4.2. Calculated Intensities *59*
2.3.4.3. The Reflection-Profile Function, ϕ *60*
2.3.4.4. Preferred Orientation Function, P_{hkl} *60*
2.3.4.5. Absorption Factor, A *61*
2.3.4.6. Background Intensity, y_i(back) *61*
2.3.4.7. Quality of Rietveld Refinement *61*
2.3.5. Total Scattering and Pair Distribution Function (PDF) ***62***
2.3.6. Crystallography Software ***64***
2.3.6.1. GSAS Software *64*
2.3.6.2. TOPAS Academic Software (Version 6) *64*
2.3.6.3. RMCProfile *64*
2.3.7. Electron Microscopy ***65***
2.3.7.1. Background and Theory *65*
2.3.7.2. Transmission Electron Microscopy and Scanning Transmission Electron Microscopy *65*

2.3.7.3. Scanning Electron Microscopy 67
2.3.7.4. Energy Dispersive X-ray 68
2.3.7.5. Experimental Set-Up 68
2.4. Physical Properties **69**
2.4.1. Electrical Resistivity ***69***
2.4.2. Seebeck Coefficient ***70***
2.4.2.1. Measurement 70
2.4.2.2. Single Parabolic Band (SPB) Model 71
2.4.3. Thermal Conductivity ***72***
2.4.3.1. Measurement 72
2.4.3.2. Debye-Callaway approximation 74
2.4.4. Hall Coefficient and Carrier Concentration ***76***
Chapter 3 - Beneficial Contribution of Interstitial Metals on the Thermoelectric Properties of TiNiSn **78**
3.1. Introduction **78**
3.2. Synthesis and Characterisation **79**
3.3. $TiNiCu_ySn$ ($0 \leq y \leq 0.25$) **80**
3.3.1. X-ray Powder Diffraction ***80***
3.3.2. Neutron Powder Diffraction ***85***
3.3.3. Scanning Electron Microscopy ***86***
3.3.4. Transmission Electron Microscopy ***86***
3.3.5. Thermoelectric Properties ***90***
3.3.6. Discussion ***96***
3.4. Off-stoichiometric $Ti_{1+x}Ni_{1+y}Sn$ **98**
3.4.1. X-ray Powder Diffraction ***98***
3.4.2. Neutron Powder Diffraction ***98***
3.4.3. High-Resolution Synchrotron X-ray Diffraction Study ***101***
3.4.4. Scanning Electron Microscopy ***103***
3.4.5. Thermoelectric Properties ***104***
3.4.6. Discussion ***108***
3.5. Conclusions **109**
Chapter 4 - Impact of excess Cu on the thermoelectric properties of $MNiCu_{0.075}Sn$, $M_{0.5}M'_{0.5}NiCu_{0.075}Sn$ (M = Ti, Zr, Hf) and $Ti_{0.5}Zr_{0.25}Hf_{0.25}NiCu_ySn$ ($0 \leq y \leq 0.075$) **110**
4.1. Introduction **110**
4.2. Synthesis and Characterisation **110**

4.3. $MNiCu_{0.075}Sn$ and $M_{0.5}M'_{0.5}NiCu_{0.075}Sn$ (M = Ti, Zr, Hf,) 111
4.3.1. Neutron Powder Diffraction 111
4.3.1.1. $MNiCu_{0.075}Sn$ (M = Ti, Zr, Hf) 111
4.3.1.2. $M_{0.5}M'_{0.5}NiCu_{0.075}Sn$ (M = Ti, Zr, Hf) 113
4.3.2. High-resolution Synchrotron X-ray Diffraction Study 113
4.3.3. Scanning Electron Microscopy 117
4.3.4. Thermoelectric Properties 117
4.4. $Ti_{0.5}Zr_{0.25}Hf_{0.25}NiCu_ySn$ ($0 \leq y \leq 0.075$) 121
4.4.1. X-ray Powder Diffraction 121
4.4.2. Neutron Powder Diffraction 122
4.4.3. High-Resolution Synchrotron X-ray Diffraction Study 124
4.4.4. Scanning Electron Microscopy 125
4.4.5. Thermoelectric Properties 126
4.5. Discussion and Conclusions 131
Chapter 5 - In-situ Neutron Powder Diffraction Monitoring of Half-Heusler Formation 134
5.1. Introduction 134
5.2. Experimental Procedure and Characterisation 135
5.3. $TiNi_{1+y}Sn$ (y = 0, 0.075, 0.25) series 135
5.4. ZrNiSn and $Ti_{0.5}Zr_{0.25}Hf_{0.25}NiSn$ 143
5.4.1. In-situ Neutron Powder Diffraction Monitoring 143
5.4.2. Thermoelectric Properties 145
5.5. $Ti_{0.5}Zr_{0.5}NiSn$, $Ti_{0.5}Hf_{0.5}NiSn$ and $Zr_{0.5}Hf_{0.5}NiSn$ 147
5.6. Discussion 153
Chapter 6 - Distribution of Excess Ni within the Half-Heusler Matrix Investigated Using Pair Distribution Function Analysis 156
6.1. Introduction 156
6.2. Experimental Procedure 156
6.3. X-ray and Neutron Powder Diffraction 157
6.4. Theoretical PDF Functions 159
6.5. Reverse Monte Carlo Modelling 160
6.5.1. Stoichiometric TiNiSn Model 161
6.5.2. TiNiSn with Excess Ni 163
6.5.3. TiNiSn with Excess Ni – Atom Swap Modelling 164
6.5.4. TiNiSn with Excess Ni – Grey Atom Model 166
6.6. Discussion 168

Chapter 7 - Conclusions 170

7.1. Chapter 3 – $TiNiCu_ySn$ ($0 \leq y \leq 0.25$) and off-stoichiometric $Ti_{1+x}Ni_{1+y}Sn$ 170

7.2. Chapter 4 – Multiphase Cu-doped half-Heusler compounds 171

7.3. Chapter 5 – In-situ Neutron Powder Diffraction Experiment 172

7.4. Chapter 6 – Application of Pair Distribution Function 172

7.5. Summary and Further Work 172

References 176

Appendix A i

Appendix B ii

Appendix C iv

Appendix D ix

LIST OF PUBLICATIONS BY THE CANDIDATE

1. “Impact of interstitial Ni on the thermoelectric properties of the half-Heusler TiNiSn” – S. A. Barczak, J. Buckman, R. I. Smith, A. R. Baker, E. Don, I. Forbes and J. W. G. Bos, *Materials*, 2018, **11**, 356.

2. “Grain by grain compositional variations and interstitial metals – a new route towards achieving high performance in half-Heusler thermoelectrics” – S. A. Barczak. J. Halpin, J. Buckman, R. Decourt, M. Pollet, R. I. Smith, D. MacLaren and J. W. G. Bos, *ACS Applied Materials and Interfaces*, 2018, **10**, 4786-4793.

3. “Compositions and thermoelectric properties of XNiSn (X = Ti, Zr, Hf) half-Heusler alloys” – R. A. Downie, S. A. Barczak, R. I. Smith and J. W. G. Bos, *Journal of Materials Chemistry C*, 2015, **3**, 10534-10542.

4. “Thermoelectric properties of Fe and Al double substituted $MnSi_{\gamma}$ ($\gamma \sim 1.73$)” – S. A. Barczak, R. A. Downie, S. R. Popuri, R. Decourt, M. Pollet and J. W. G. Bos, *Journal of Solid State Chemistry*, 2015, **227**, 55-59.

LIST OF ABREVIATIONS

1D	one-dimensional
2D	two-dimensional
3D	three-dimensional
AO	atomic orbital
CB	conduction band
DFT	density functional theory
DOS	density of states
EDX	energy dispersive X-ray
FIB	focused ion beam
FH	full-Heusler
FWHM	full width at half maximum
HH	half-Heusler
MFP	mean free path
MO	molecular orbital
NPD	neutron powder diffraction
PDF	pair distribution function
PDOS	partial density of states
RMC	reverse Monte-Carlo
SEM	scanning electron microscopy
SPS	self-propagating synthesis
SPB	single parabolic band
SS	solid-state
SSR	solid-state reaction
STEM	scanning transmission electron microscopy
SXRD	synchrotron X-ray powder diffraction
TEM	transmission electron microscopy
VB	valence band
XRD	X-ray powder diffraction
ZT	thermoelectric figure-of-merit

Chapter 1 - Introduction

The rapid economic growth and human development all over the world leads to increasing demand for energy. In today's world, most of the energy is produced by burning fossil fuels (natural gas, coal, oil), which are becoming increasingly depleted and scarce. In addition, fossil fuels cause the emission of greenhouse gases, which result in noticeable and irreversible climate change. In the last few decades, alternative energy technologies such as solar photovoltaic,[1, 2] wind turbine[3] and bio-fuel[4] have attracted significant interest due to their environmental friendliness and renewable nature. An alternative approach to enhance energy efficiency is waste heat recovery.

It has been estimated that only 30% of worldwide energy produced from fossil fuels is used effectively, with the remainder wasted as heat released into the atmosphere.[5, 6] Thermoelectric materials can directly generate electricity from heat sources and vice versa, by using the Seebeck and the Peltier effects, respectively. The recovery of waste heat, even a small amount, would increase the overall process efficiency and reduce economic loss. Solid-state thermoelectric generators do not contain any moving parts and operate without mechanical movement; therefore, they are reliable and silent. These devices are easily scalable and have a long life-span. They are classified as a green technology, as no heat, gaseous or chemical waste are emitted during electricity production.[7-9] Thermoelectric devices can be applied in many areas e.g. space, automobile and buildings.

For numerous space exploration missions, radioisotope thermoelectric generators have been used to convert the thermal power from radioisotope heat sources. These devices operate continuously without the sun, which suits well with long missions.[7] More recently, thermoelectric generators were installed in car exhaust systems. Energy captured using a thermoelectric generator may be used by electrical components of the vehicle without additional engine load.[10] Beside waste heat recovery, thermoelectric generators were investigated for their use in solar energy conversion. Here, sunlight would be converted by solar connector into heat and then transformed by a thermoelectric device into valuable electricity.[11]

In addition to power generation, thermoelectric devices can be used for refrigeration i.e. thermal energy (in the form of cooling or heating) is produced when electricity is applied. The main advantage of thermoelectric cooling (also known as Peltier cooling) is a lack of

moving parts, which makes the system quiet. Moreover, it does not contain ozone-depleting chlorofluorocarbons or other materials, which may require periodical service or replenishment.[12] Thus, thermoelectric coolers are more reliable and often a greener option, compared with conventional systems. Current applications include portable refrigerators, cooling of lasers diodes and integrated circuit chips, cooling of electronic devices and industrial temperature control.[7, 12]

Unfortunately, thermoelectric devices are not used for large scale commercial application, mainly due to their low energy-conversion efficiency (10-15%) and high cost. The top performing materials, bismuth telluride and lead chalcogenides have attracted significant interest, however their application is limited because of scarce tellurium and lead toxicity. As a result, researchers all over the world are trying to design novel materials composed of cheap and abundant elements with significantly improved properties.

This thesis presents work on several half-Heuslers, which show good thermoelectric properties and are promising candidates for waste heat recovery. The main reason for the exploration of TiNiSn-based half-Heuslers is their environmental friendliness, high abundance of constituent elements, high thermal stability and resistance to oxidation at high temperature.[13, 14] The structure and properties of TiNiSn-based and multiphase half-Heusler alloys was extensively investigated using laboratory X-ray, high resolution synchrotron X-ray and neutron powder diffraction as well as electron microscopy. In-situ neutron powder diffraction was performed to monitor the formation of these materials. In addition, physical properties such as electrical resistivity, Seebeck coefficient and thermal conductivity have been measured and analysed using various models.

1.1. Thermoelectric Effects

1.1.1. The Seebeck Effect

In 1821, Thomas Johann Seebeck described the first of the thermoelectric effects that later was named after him. He constructed a closed loop using wires of two dissimilar materials (metals A and B) and held the junctions between the metals at different temperatures (see Figure 1.1). The induced current was visualised with magnetic needle, which deflected to the created magnetic field. It was recognised later that the magnetic field was generated due to an electrical current flowing in the loop. The applied temperature gradient within a material creates differing chemical potential for the charge carriers at both ends. To compensate for this differing potential, the charge carriers flow

through the material (from the hot to the cold end). They accumulate at one end resulting in electrostatic repulsions, which forces some carriers to diffuse back to the hot side. When the differing chemical and electrostatic repulsion potentials are balanced, the maximum charge build up is achieved. A build-up of charge means that a voltage is generated between the junctions. The magnitude of the induced voltage (ΔV) (also called the Seebeck voltage) is proportional to the temperature gradient (ΔT), defining the Seebeck coefficient (S). This is presented in Equation 1.1:[15]

$$S = \frac{\Delta V}{\Delta T} \qquad \text{Equation (1.1)}$$

The Seebeck coefficient is discussed in more detail in Section 1.5.1, while the method used to measure Seebeck coefficient and Single Parabolic Band model that was applied to analyse its temperature dependence are described in Section 2.4.2.

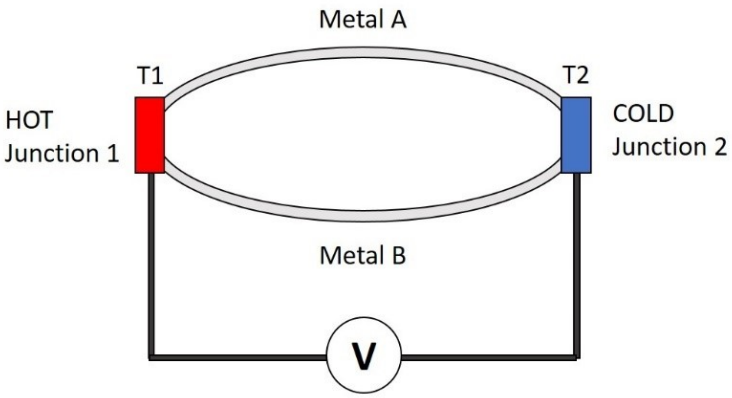

Figure 1.1. Schematic representation of the Seebeck effect, where two metals A and B form a closed loop, with different temperatures ($T1 > T2$) at the junctions.

1.1.2. The Peltier Effect

In 1834, Jean Peltier discovered the second of the thermoelectric effects (Peltier effect), which is the reverse of the Seebeck effect. Peltier found that by applying an electric current through the closed circuit containing two materials, small heating or cooling effect occurs, depending on the current's direction. In the Peltier effect, a temperature gradient is created: one junction becomes cooler while the other becomes hotter. As shown in Figure 1.2a, when the current flows from metal A to metal B, heat is absorbed at junction 1 (cooling) and is rejected at junction 2 (heating). When the direction of the current is reversed (see Figure 1.2b), junction 1 is heated and junction 2 is cooled.[16]

The ratio of heat that was absorbed or evolved at a junction of two materials (Q) to the amount of current flowing through the circuit (I) defines the Peltier coefficients (Π) of these two materials and is given by Equation (1.2):

$$Q = (\Pi_A - \Pi_B)I \qquad \text{Equation (1.2)}$$

Interestingly, the amount of heat absorbed at the cooled junction is reduced compared to the ideal value. This is caused by heat conduction and Joule heating, which always accompany the Peltier effect. In heat conduction, the temperature difference naturally drives the movement of the charge carriers from the hot to the cold end, causing heat to flow. Joule heating is the process where flow of the electrical current through a material produces a heat. It is proportional to the square of the current (I^2) and resistance (R), as described in Equation 1.3:

$$Q = RI^2 \qquad \text{Equation (1.3)}$$

Both, heat conduction and Joule heating increase with increasing current. When the current is small (and resulting temperature gradient is not too large), the cooling power is positive. Although, as the current is increased further, the Joule heating becomes dominant factor (as it is proportional to I^2) and a point is reached at which the cooling power reaches its maximum value.[16, 17]

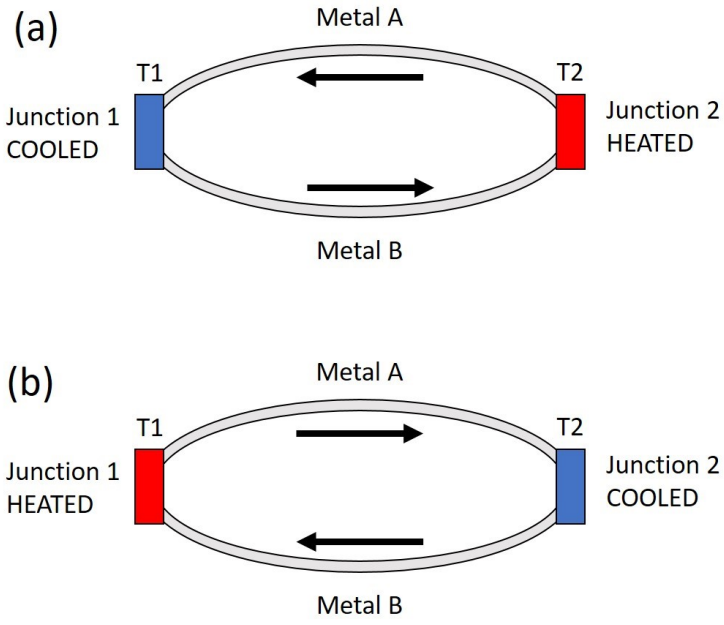

Figure 1.2. Schematic representation of the reversible Peltier effect.

As shown in Equation 1.4, the Peltier coefficient (Π) can be presented in terms of the Seebeck coefficient (S):

$$\Pi = ST \qquad \text{Equation (1.4)}$$

Where T is the absolute temperature.[17]

1.1.3. The Thomson Effect

In 1855, William Thomson (Lord Kelvin) established the relationship between Seebeck and Peltier effects. This third thermoelectric effect is known as the Thomson effect. It states that for a single homogeneous material in a temperature gradient, heat is absorbed or generated as an electrical current is applied. This can be expressed by the formula:

$$\tau = \frac{Q}{I\Delta T} \qquad \text{Equation (1.5)}$$

where τ is the Thomson coefficient, Q is the heat, I is the current and ΔT is the temperature difference in the homogeneous conductor.

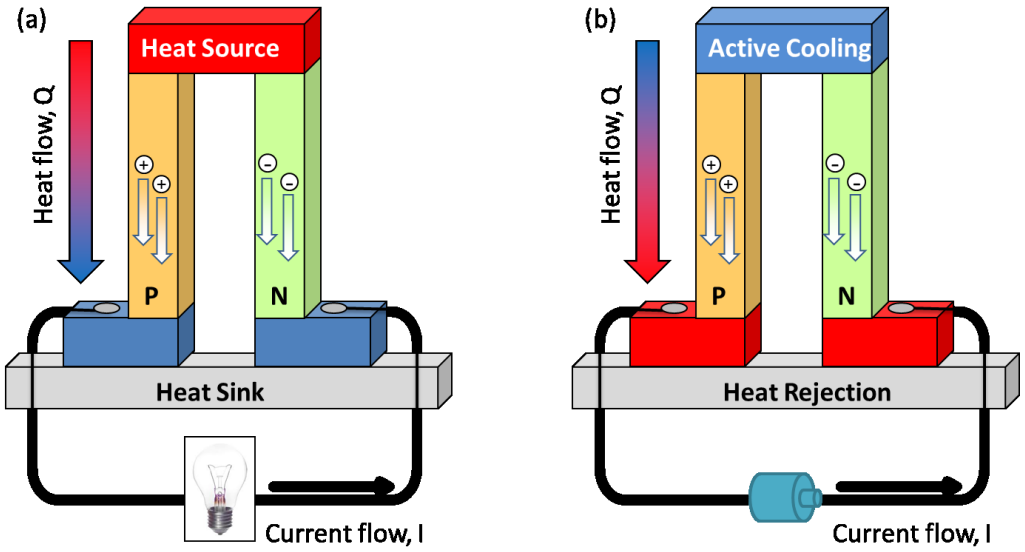

Figure 1.3. Schematic representation of thermoelectric modules in **(a)** heat-to-electricity conversion mode and **(b)** heat pumping (cooling) mode.

1.2. Thermoelectric Devices

Thermoelectric modules consist of n-type and p-type semiconductors, which are electrically connected in series and thermally connected in parallel. The dominant charge

carriers in the n-type materials are electrons, while p-type semiconductors contain free electron holes.

In power generation mode, illustrated in Figure 1.3a, a temperature gradient is exploited. The charge carriers at the hot end diffuse towards the cold end, producing an electrostatic potential (ΔV). Therefore, the Seebeck effect is the basis of thermoelectric power generation. If the circuit is completed, a current will flow through the external circuit.[8, 18] In cooling mode, a current is applied and heat is pumped from one junction to the other.[19] This process is represented schematically in Figure 1.3b. To increase the operating voltage and spread of heat flow, a thermoelectric device is composed of multiple couples.

1.3. The Figure-of-Merit *ZT* and Thermoelectric Efficiency

The thermoelectric efficiency (known as Z or the thermoelectric figure of merit) was defined by Altenkirch in 1911.[5] The Z can be multiplied by the absolute temperature (T), which yields the most widely known form of thermoelectric efficiency - the dimensionless figure of merit (ZT). The ZT is given by Equation 1.6:

$$ZT = \frac{S^2 \sigma T}{\kappa} \qquad \text{Equation (1.6)}$$

where S is the Seebeck coefficient, σ is electrical conductivity and κ is the thermal conductivity. There are three factors that contribute to thermal conductivity: an electronic part (κ_{el}), which is the heat carried by the charge carriers, a lattice contribution ($\kappa_{lattice}$), which is heat conducted by phonons and a bipolar contribution (κ_b), which is observed when both types of carrier are present. The S and σ are combined to make up the power factor ($S^2\sigma$) of the material.

To attain a high ZT value, a material should possess high S and σ, while κ should be low. However, ZT maximisation is not straightforward as these three transport parameters are interrelated through the material's band structure. Figure 1.4 illustrates the conflict and suggests how each of the parameters can be optimised using carrier concentration.[20] The maximum ZT is reported in the carrier concentration range 10^{19} - 10^{20} cm^{-3} (region characteristic for semiconductors). Lower carrier concentration region is characteristic for insulators, where high S and low κ are limited by low σ. A high carrier concentration (as found in metals) promotes high σ. Unfortunately, the ZT is significantly reduced due to low S and high κ.[20] The above analysis confirms that heavily doped semiconductors

are the most suitable materials for thermoelectric applications. Therefore, most of the research focusses in this area.

The major aim of thermoelectric research is to design materials, which will enhance the efficiency of solid-state thermoelectric generators. The power generation efficiency (η) is evaluated with the following formula:

$$\eta = \frac{T_{hot} - T_{cold}}{T_{hot}} \frac{\sqrt{1 + ZT_{device}} - 1}{\sqrt{1 + ZT_{device}} + \frac{T_{cold}}{T_{hot}}} \qquad \text{Equation (1.7)}$$

where T_{hot} and T_{cold} are the temperatures of the hot and cold sides, while ZT_{device} is the average of ZT over the exploited temperature gradient. To reach a high efficiency, which will allow widespread application, both the ZT and temperature difference must be high enough. Commercially available solar thermoelectric generators are based on nanostructured Bi_2Te_3 alloys, and achieve efficiency of ~5% for a temperature difference of 100 ºC.[21] Several automobile companies have been developing waste heat recovery systems, which would help to improve the fuel economy.[18]

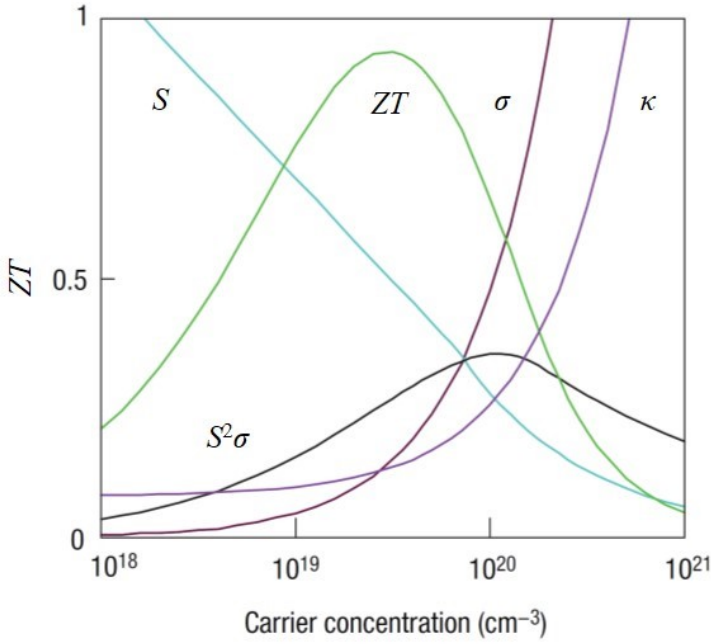

Figure 1.4. Representation of ZT optimisation through the carrier concentration,[20]

1.4. Electronic Properties of Solids

1.4.1. Molecular Orbital Theory

Molecular orbital (MO) theory is the approach used to describe the bonding in simple and complex polyatomic molecules. This model assumes that electrons are not localised on one atom or between two atoms, but instead occupy molecular orbitals (MO) that can cover entire molecule. MOs are formed by the overlap (interaction) of atomic orbitals (AO) on all of the individual atoms in the molecule. The number of formed MOs will always equal the number of AOs of the constituent atoms. Each AO can have either positive or negative phase, therefore these AOs can overlap in two possible ways: in-phase and out-phase. A bonding MO (lower energy) is the result of constructive interference of neighbouring AO, while antibonding MO (higher energy) arises from destructive interference (see Figure 1.5).[22, 23] The relative energies of AOs and the MOs they form can be presented using molecular orbital diagrams, illustrated by the Figure 1.6.

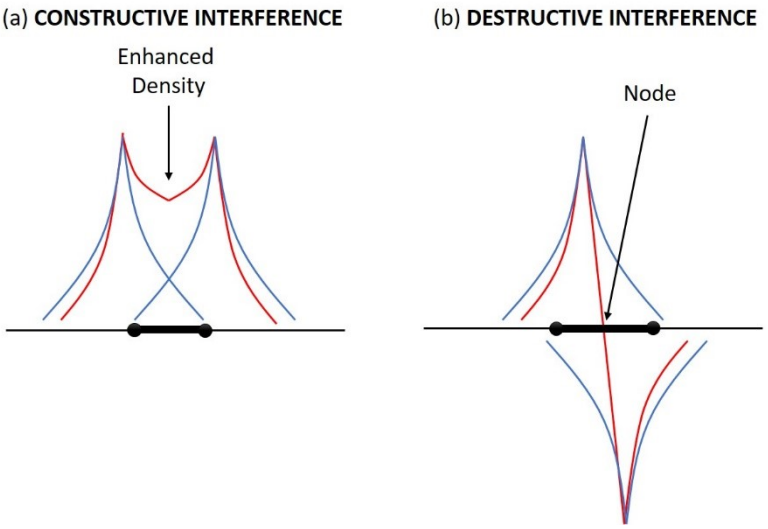

Figure 1.5. (a) Overlap of atomic orbitals that have the same sign (in-phase overlap) leads to the constructive interference and enhancement of electron density. **(b)** Overlap of atomic orbitals with opposite sign (out-phase) results in destructive interference. This interference leads to a nodal surface in an antibonding molecular orbital. Reproduced from reference 22.

As the number of atoms increases, more MOs that are closer in energy to one another are formed (Figure 1.6b). Eventually there are so many atoms that a continuous level, called

a band is generated (Figure 1.6c). These bands extend over the whole solid. The core electrons of each atom stay localised but the valence electrons occupy the lower band (called valence band - VB), while at 0 K the upper band (conduction band – CB) remains vacant. The region between the VB and CB is called band gap (E_g). The width of the energy gap defines whether a material is a metal, an insulator or a semiconductor.

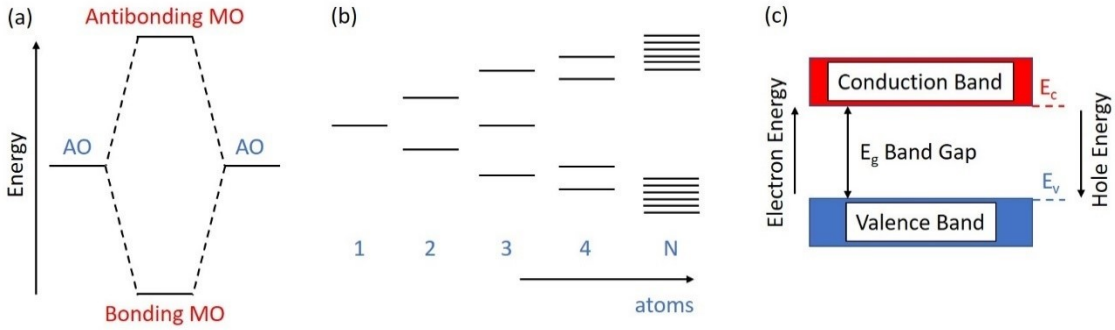

Figure 1.6. (a) Molecular orbital (MO) energy level diagram for two interacting atomic orbitals (AO). **(b)** Formation of energy bands with increasing number of atoms. **(c)** A simplified energy diagram of solids. Reproduced from references 5, 22.

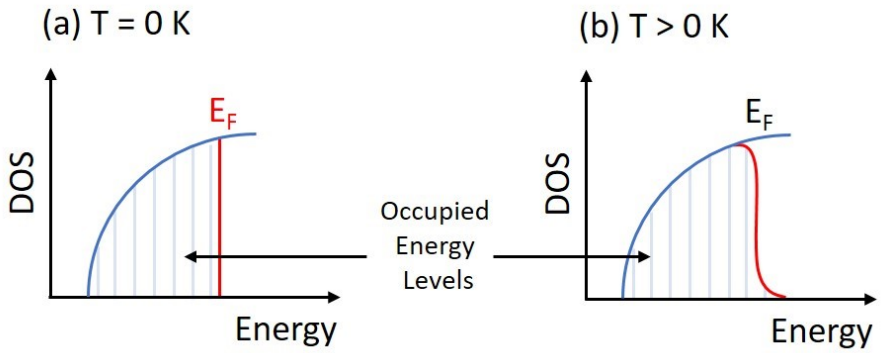

Figure 1.7. Density of states (DOS) for a band formed using the free electron model for **(a)** $T = 0$ K and **(b)** $T > 0$ K. The occupied energy levels are shaded. Reproduced from reference 24.

1.4.2. Free Electron Theory

In free electron theory, a solid (crystal) is regarded as a potential well (region that surrounds a local minimum of potential energy), inside which the loosely held valence electrons are free to move, unaffected by the atomic nuclei or by each other. The energy

levels occupied by the electrons are quantised and the levels are filled with two electrons per level starting from the bottom, until all electrons are used up. The highest occupied level is defined as the Fermi level and the corresponding energy is the Fermi energy (E_F). The number of energy levels that are available for electrons to occupy at a given energy is called the density of states (DOS). A plot of the DOS is illustrated in Figure 1.7. At absolute zero, the E_F is sharp (Figure 1.7a). Above 0 K, some electrons near E_F possess enough thermal energy and are promoted to empty levels above E_F (Figure 1.7). Therefore, some states above E_F are occupied, while others below E_F are vacant.[24]

Free electron theory is slightly oversimplified, as in reality, the potential well is periodic, rather than as a continuum. Here, the positively charged nuclei are arranged in a regular repeating manner. The potential energy of electrons is the lowest when it passes close to the nuclei, while it increases as it passes through maximum between adjacent nuclei, as shown in Figure 1.8.

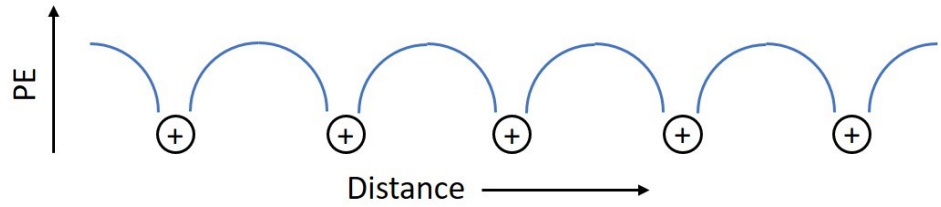

Figure 1.8. Potential energy (PE) of electrons in a regular lattice of solid. Reproduced from reference 24.

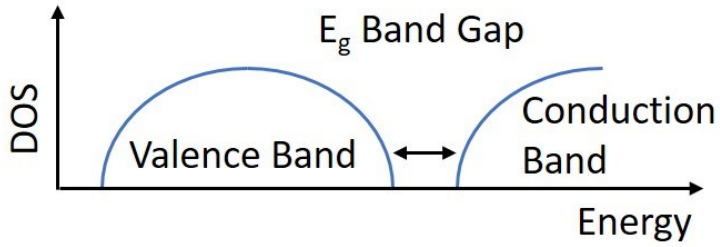

Figure 1.9. The density of states (DOS) diagram determined by solving the Schrödinger equation for a periodic potential function. Reproduced from reference 24.

By solving the Schrödinger equation for a periodic lattice, it was found that only certain bands are permitted for electrons. This results in discontinuities in the DOS diagram and band gap, as illustrated in Figure 1.9.

Above discussions shows that both MO theory and free electron approximation lead to similar conclusions about the existence of energy bands in solids.

1.4.3. Band Structure of Metals, Insulators and Semiconductors

A solid has metallic properties when the filled VB overlaps with an empty CB (there is no energy gap). Since there is little space between VB and CB, electrons can move freely between the bands.

Insulators and semiconductors have similar band structures, with full (rather than partially filled) VB and completely empty CB. The E_F lies in the middle of the band gap E_g, as shown in Figure 1.10a. The main difference is the size of the E_g. The number of electrons (n) in the CB depends on the magnitude of the E_g and temperature (T) and can be calculated with Equation 1.8:

$$n = n_0 \exp\left(-\frac{E_g}{k_B T}\right) \qquad \text{Equation (1.8)}$$

where k_B is the Boltzmann constant and n_0 is the total number of carriers. The conductivity in insulator is negligibly small. These materials are characterised by large E_g (> 3eV), therefore very few electrons in VB have sufficient thermal energy to migrate into the empty band above. Diamond with a E_g ~6eV is an example of insulator. E_g of a semiconductor is significantly smaller than for an insulator (usually in the range 0.5 – 3.0 eV), therefore even at low temperatures electrons can be moved into the CB.[5] As the temperature increases more electrons are thermally excited to enter the CB, leading to increased conductivity.

The electrons promoted to the CB are regarded as negative charge carriers. When an electron moves to the CB it leaves behind a vacancy (hole) in the VB, which is regarded as a positive charge carrier. Holes move when an electron enters them, leaving its own position vacant as a new hole. In intrinsic semiconductors, the VB is fully filled at 0 K, while at $T > 0$ K, the only charge carriers present (electrons in the CB and holes in the VB) are the result of thermal excitation of electrons into CB. They are called intrinsic charge carriers. In intrinsic semiconductors, the E_F lies in the middle of the band gap (see Figure 1.10a). Pure silicon that has 4 valence electrons per atom is an example of intrinsic semiconductor.

Addition of a small number of atoms with 5 valence electrons (e.g. phosphorus) into pure silicon, causes an introduction of additional electrons into the material. These valence

electrons are weakly bound to their parent atoms and occupy an energy level (donor level) located just below the CB. As presented in Figure 1.10b, the electrons can be easily promoted from the donor level into the CB. Semiconductors doped in this manner are called n-type semiconductors.

On the other hand, pure silicon can be substituted with small number of atoms that have 3 valence electrons (eg. aluminium), creating a deficit in the number of valence electrons in the material. The electron-accepting level is created just above the VB, as illustrated in Figure 1.10c. The electrons from the VB can be easily promoted into an acceptor level, leaving behind holes in the VB. These positively charged holes are responsible for the p-type conduction.[24]

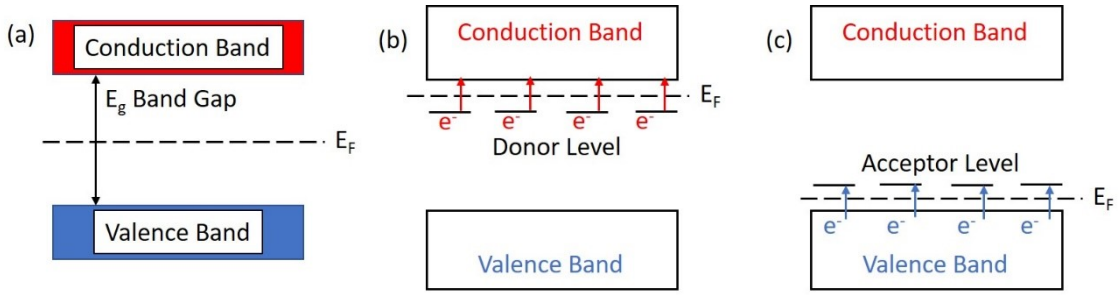

Figure 1.10. Band structure of **(a)** intrinsic semiconductor, **(b)** n-type semiconductor and **(c)** p-type semiconductor. Reproduced from reference 24.

1.5. Thermoelectric Properties

1.5.1. Seebeck Coefficient (S)

As defined in Equation 1.1, the Seebeck coefficient (*S*) is a measure of the voltage that is induced when the material is exposed to a temperature gradient. Negative sign of *S* indicates n-type conduction and electrons as the main charge carriers, while positive values are observed for p-type materials with electron holes as major charge carriers. Presence of both charge carriers results in low *S*-values. As the temperature difference is applied, both carriers will move to the cold end of the couple and cancel out induced voltage. This can be deduced from the Equation 1.9, for semiconductor containing both charge carriers:

$$S = \frac{S_n\sigma_n + S_p\sigma_p}{\sigma_n + \sigma_p} \qquad \text{Equation (1.9)}$$

where S_n and S_p are the partial Seebeck coefficient for electrons and holes, respectively and σ_n and σ_p are corresponding electrical conductivities. S_n and S_p have opposite sign, so they cancel out leading to small magnitude of S.[17] This also explains the S decrease at high temperatures, where minority charge carriers have sufficient thermal energy to be excited from the VB to the CB.

The S can be also expressed using the Mott equation:

$$S = \frac{\pi^2}{3}\frac{k_B^2 T}{e}\frac{d\ln\sigma(E)}{dE}\bigg|_{E=E_F} \qquad \text{Equation (1.10)}$$

which relates S to the electronic structure. Here, k_B denotes Boltzmann constant, e is the charge of the carrier, $\sigma(E)$ is the energy dependent electrical conductivity, E_F is the Fermi energy and T is absolute temperature. This approximation is only valid if the electronic scattering is independent of energy. Then $\sigma(E)$ is proportional to the DOS at energy, E. Based on the Equation 1.10, rapid change in DOS near E_F leads to large S values.[25] Therefore, materials with complex structure as well as narrow and sharps bands near E_F are required to enhance the S value, which is desirable for high performance thermoelectric. Figure 1.11 shows hypothetical electronic band structures for two semiconductors, one with a simple structure (panel a – one band extremum in the CB and VB) and one with a complex electronic structure (panel b – multiple extrema in the CB and VB). When the systems are n-doped (see E_F'), more extrema are populated in the complex system (b) than in the simple system (a). Because $S^2\sigma$ depends on the number of populated extrema, system (b) will have higher $S^2\sigma$.[25]

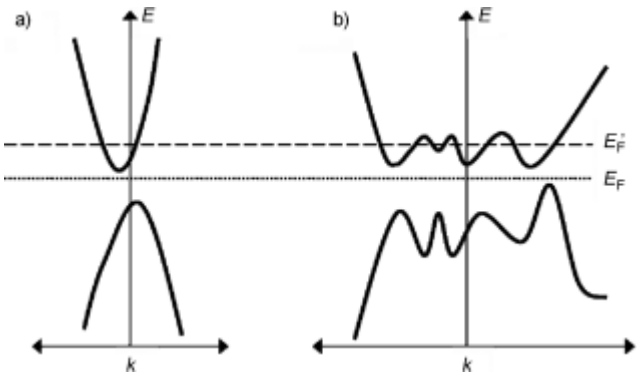

Figure 1.11. Hypothetical electronic band structure for **(a)** simple system with one extremum and **(b)** complex system with multiple extrema in the valence and conduction bands. E_F denotes Fermi energy, while E_F' corresponds to Fermi energy upon n-type doping.[25]

For heavily doped materials (degenerate semiconductors) with parabolic band dispersion, Equation (1.10) can be simplified assuming free electron dispersion and energy-independent scattering approximation.[20] Here S is formulated as:

$$S = \frac{8\pi^2 k_B^2}{3eh^2} m^* T \left(\frac{\pi}{3n}\right)^{2/3} \qquad \text{Equation (1.11)}$$

where h is the Planck constant, n is the carrier concentration and m^* is the density of states effective mass of carriers, which is related to the band effective mass (m_b^*), through the number of equivalent degenerated valleys of the band structure (N_V):[6]

$$m^* = (N_V)^{2/3} m_b^* \qquad \text{Equation (1.12)}$$

It is evident from Equation 1.11 that high S values are observed in materials with low n and large m^*. This provides a conflict with the requirements of σ. As discussed in the next section, high σ requires high carrier concentration and low m^* (Equation 1.14 and 1.15). Therefore, a compromise between S and σ has to be found in order to enhance the figure of merit ZT, as illustrated in Figure 1.4.

The measurement of S over a wide temperature range can be used to estimate the thermal band gap (E_g) of a semiconducting material. In a typical degenerate semiconductor, the magnitude of the Seebeck coefficient $|S|$ increases with temperature and reaches the maximum $|S|_{max}$ followed by a decrease. The maximum S is attributed to the bipolar conduction. Here, an electron-hole pair is thermally excited across the band gap and $|S|$ decreases due to the cancelling effect of the two types of carriers.[26] The Goldsmid-Sharp formula:[27]

$$E_g = 2e|S|_{max} T_{max} \qquad \text{Equation (1.13)}$$

is widely used to estimate the E_g value, where T_{max} is the temperature at which $|S|_{max}$ occurs.

1.5.2. Electrical Conductivity (σ)

The electrical conductivity (σ) quantifies the ability of a material to conduct an electric current. It is the reciprocal of the electrical resistivity (ρ) that quantifies how strongly a material opposes the flow of electric current. As shown in Equation 1.14, σ (and ρ) are related to carrier concentration (n) and the mobility of the charge carrier (μ)[20]:

$$\sigma = \frac{1}{\rho} = ne\mu \qquad \text{Equation (1.14)}$$

The carrier mobility is given by following equation[28]:

$$\mu = e(\frac{\tau}{m^*}) \qquad \text{Equation (1.15)}$$

where e is the charge of the carrier, τ is the relaxation time between scattering events and m^* is the effective mass. High σ can be attained through the enhancement of carrier mobility as well as carrier concentration. Heavy carriers (with large m^*) will move slower, therefore small m^* is desired for high mobility. As mentioned in Section 1.5.1, this is conflicting situation with S, which requires large m^*, as defined in Equation 1.11. Therefore, increasing τ is the only possibility to improve σ, without S reduction.

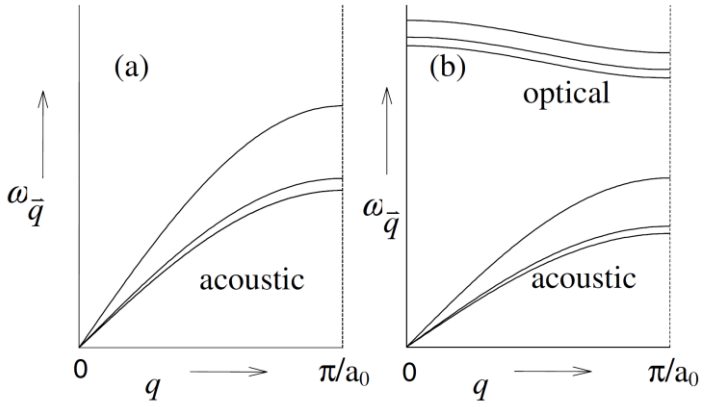

Figure 1.12. Schematic phonon dispersion curves for a given direction of wave vector $\vec{q}$ of **(a)** monoatomic lattice and **(b)** diatomic lattice. a_0 denotes the lattice parameter.[29]

1.5.3. Lattice Vibrations

In any solid, each atom is bonded to its neighbour, therefore, displacement of any atom will disturb the rest of the specimen. The atoms are in continual vibration about their equilibrium positions (crystal lattice), which strongly depends on neighbouring atoms. These crystal lattice vibrations can be represented by waves. The quantised lattice vibrations are referred to as phonons. The total number of vibrational modes is equal to $3N$, where N is the number of atoms. The phonon dispersion curve for a solid consists of acoustic and optical branches (see Figure 1.12). If there are N atoms per unit cell, there will be 3 acoustic branches (one longitudinal and two transverse) and $3N - 3$ optic branches. The acoustic branches are low-frequency and correspond to atoms in the unit cell that move in same phase. The optical branches are high-frequency and represent atoms in the unit cell, which move in opposite phases. Due to small group velocity, which

is determined from the slope of the dispersion curve, optical phonons are usually not effective in transporting heat energy. However, their interaction with acoustic phonons (that are main heat conductors) may affect the heat conduction.[17, 29]

1.5.4. Thermal Conductivity (κ)

Thermal conductivity (κ) measures the ability of a material to conduct heat. It consists of three contributions: electronic thermal conductivity (κ_{el}), lattice thermal conductivity ($\kappa_{lattice}$) and bipolar contribution (κ_b). The κ_{el} relates to the charge carriers (free electrons or electron holes) that move and transfer electric current as well as heat. The $\kappa_{lattice}$ describes the movement of phonons through the lattice, while κ_b is due to the presence of both charge carriers – electrons and electron holes.

The κ_{el} is related to the σ and can be estimated using the Wiedemann-Franz relationship:

$$\kappa_{el} = L\sigma T = ne\mu LT \qquad \text{Equation (1.16)}$$

where L is the Lorenz number. L can be approximated (L = 2.45 x 10^{-8} WΩK^{-2} for degenerate and L = 1.48 x 10^{-8} W Ω K^{-2} for non-degenerate semiconductors)[5, 20] or calculated using the single parabolic band approximation (see Section 2.4.2.2).[30] It is evident from Equation 1.16 that σ enhancement has a negative effect on κ, as large σ results in high value of κ_{el}.

As discussed in Section 1.5.1, presence of both types of carriers (n- and p-type) affects the thermoelectric performance. The σ is the sum of the conductivities of the separate carriers ($\sigma = \sigma_n + \sigma_p$). However, the κ_{el} is not simply the sum of the thermal conductivities of separate carriers:

$$\kappa_{el} = \kappa_{el,n} + \kappa_{el,p} + \frac{\sigma_n \sigma_p}{\sigma_n + \sigma_p}(S_n - S_p)^2 T \qquad \text{Equation (1.17)}$$

There is an additional term associated with the bipolar flow, which can be much larger than either $\kappa_{el,n}$ or $\kappa_{el,p}$.

An effective method to enhance the figure of merit ZT, is to reduce $\kappa_{lattice}$, which is the only component not related to the material's electronic structure. As discussed above, all other parameters (σ, S, κ_{el}) are correlated and cannot be optimised independently. In a simple crystalline solid material, the lattice component of the thermal conductivity ($\kappa_{lattice}$) is determined using the specific heat (C_v), the phonon velocity (v) and mean free path of phonon between collisions (l) according to the following equation:

$$\kappa_{lattice} = \frac{1}{3} C_v v l \qquad \text{Equation (1.18)}$$

As the mean free path is related through the phonon velocity to the phonon relaxation time (τ) ($l = v\tau$), the above equation can be written as:

$$\kappa_{lattice} = \frac{1}{3} C_v v^2 \tau \qquad \text{Equation (1.19)}$$

However, all the terms in Equation 1.18 are frequency-dependent (ω) and vary across the phonon spectrum. Use of the Callaway approximation gives Equation 1.20:

$$\kappa_{lattice} = \frac{1}{3} \int_0^{\omega_D} C(\omega) v_g(\omega)^2 \tau(\omega) d\omega \qquad \text{Equation (1.20)}$$

The Debye model assumes that an average group phonon velocity (v_g) is equal to the velocity of sound (v_s) in solids and is constant for all the phonon branches. If we define the Debye temperature $\theta_D = \hbar\omega_D/k_B$ and $x = \hbar\omega/k_B$, within the Debye approximation, the $\kappa_{lattice}$ is expressed as:

$$\kappa_{lattice} = \frac{k_B}{2\pi^2 v_s} \left(\frac{k_B}{\hbar}\right)^3 T^3 \int_0^{\theta_D/T} \tau(x) \frac{x^4 e^x}{(e^x - 1)^2} dx \qquad \text{Equation (1.21)}$$

Equation 1.21 is usually called Debye-Callaway approximation for the lattice thermal conductivity,[29, 31] which is discussed in section 2.4.3.2.

1.6. State of Art Thermoelectric Materials

In this section, an overview of progress in thermoelectric materials development is given. Figure 1.13 summarises the maximum reported *ZT* values of current thermoelectric compositions as a function of publication year.[32] Bi_2Te_3, PbTe and Si-Ge alloys were discovered during the 1950s and 1960s, commencing the growth of the thermoelectric community. However, the development of these materials was rather slow until the 1990s. Over 20 years ago, Hicks and Dresselhaus proposed that low dimensionality can be used to modify and improve the thermoelectric properties.[33, 34] These dimensionally reduced quantum well structures can be incorporated into the bulk materials, resulting in scattering of the heat-carrying phonons and significant reduction of the $\kappa_{lattice}$.[35] The 'Phonon Glass Electron Crystal' (PGEC), proposed by Slack[36], was another important idea. PGEC materials have an electronic structure characteristic of crystalline solids but show a low $\kappa_{lattice}$ similar to amorphous materials. Such unusual properties can be found in materials with complex structure, which may contain voids or tunnels that are large enough to accommodate atoms or group of atoms of small size. The phonons are scattered by the

atoms leading to reduced thermal conductivity. This approach was successfully applied in clathrates[37] and skutterudite[38] based compounds. Thanks to these two concepts, thermoelectric materials development received another major impulse, which continues till today.

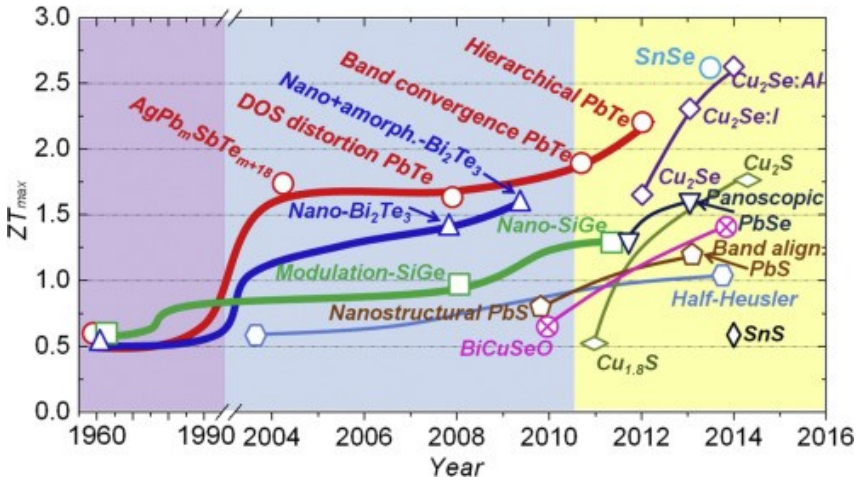

Figure 1.13. The maximum *ZT* value of state of art, bulk thermoelectric materials against the publication year.[32]

In the following sections, an overview of some of the key thermoelectric materials is given, followed by in-depth discussion of half-Heusler compounds that are the topic of this PhD thesis.

1.6.1. SnSe

A record high $ZT = 2.6$ was very recently reported in a single crystal of SnSe.[39] At room temperature, SnSe adopts an unusual layered orthorhombic structure (space group: *Pnma*), a heavily-distorted NaCl derivative, which results in ultralow κ. A room temperature view of the SnSe crystal structure is shown in Figure 1.14. In the *b*-*c* plane, there are two-atom-thick Sn-Se slabs with strong Sn-Se bonding, which are linked with weaker Sn-Se bonding along the *a* direction. The structure contains highly distorted $SnSe_7$ coordination polyhedral, consisting of three short (solid grey line) and four long (dashed blue line) Sn-Se bonds, and a lone pair of the Sn^{2+}, sterically accommodated between the four long Sn-Se bonds. The two-atom-thick Sn-Se slabs are corrugated, creating zig-zag accordion-like projection along the *b* axis. At ~750 – 800 K, SnSe undergoes a displacive

phase transition from lower symmetry *Pnma* to higher symmetry *Cmcm* phase. The temperature dependence of *ZT* along different axial orientations is shown in Figure 1.14e. High *ZT* values along the *b* and *c* axis were observed near and above the transition temperature. The *ZT* ~ 2.6 at 923 K along the *b* axis, can be explained by high carrier mobility, which is 3 times higher than that along the *c* axis and 10 times higher than that along the *a* axis. SnSe single crystal also shows low κ of ~0.46, 0.70 and 0.68 W m^{-1} K^{-1} along the *a*, *b* and *c* axis direction, respectively. These low values decrease further with increasing temperature.[39]

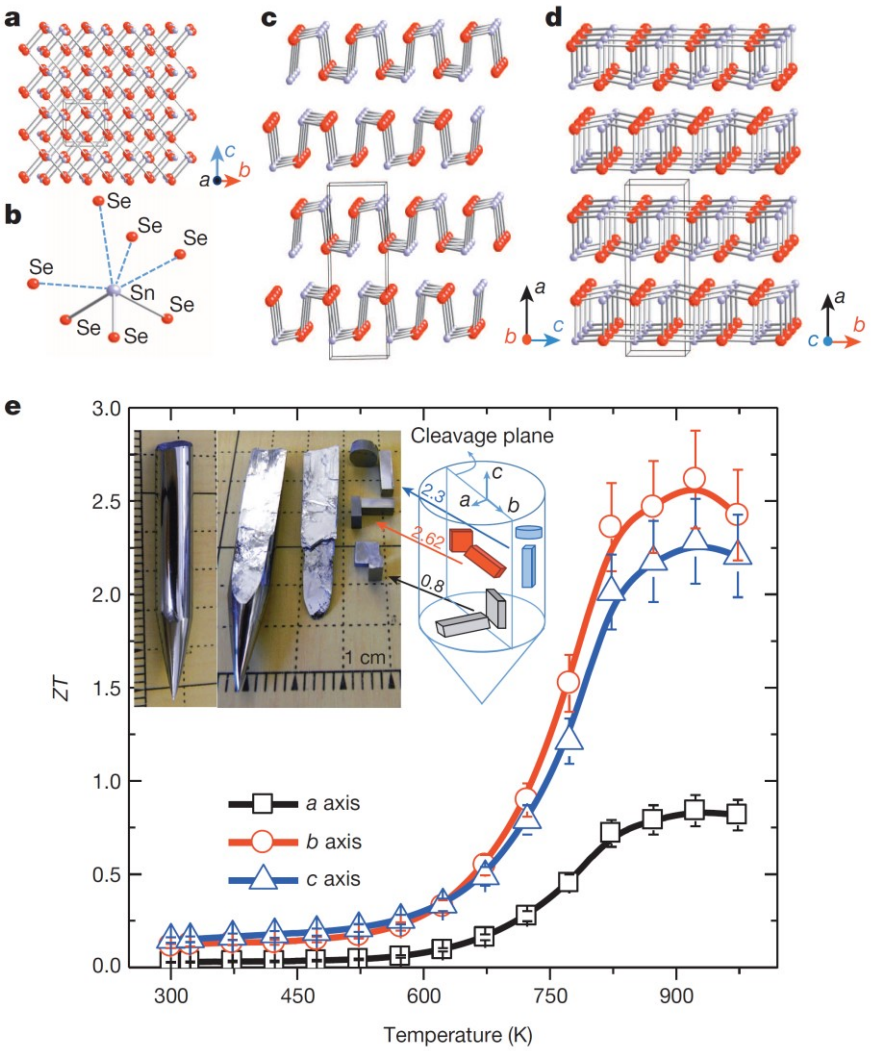

Figure 1.14. *Pnma* crystal structure of SnSe: **(a)** structure along the *a* axis, **(b)** highly distorted $SnSe_7$ polyhedron, **(c)** structure along *b* axis, **(d)** structure along the *c* axis. **(e)** Temperature dependence of *ZT* along different axial orientations.[39]

Since the initial report, many research groups have focused on polycrystalline SnSe.[40-42] Unfortunately, the high *ZT* values observed in SnSe single crystals have not been reproduced in polycrystalline samples. This is due to significantly lower carrier mobility of polycrystalline SnSe and therefore reduced $S^2\sigma$ values. The other reason is the big difference in κ. Three different crystallographic orientations observed in SnSe single crystal are averaged in polycrystalline samples and therefore are much more difficult to control due to the varying degree of preferential orientation.[6]

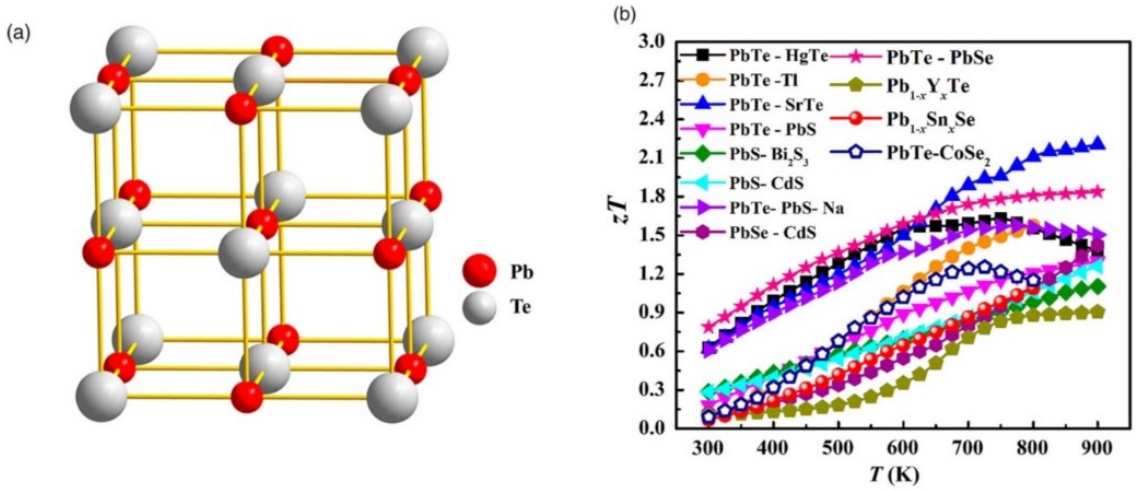

Figure 1.15. (a) Crystal structure of PbX (X = Te, Se and S). **(b)** Overview of the temperature dependence of *ZT* for leading PbTe-based materials.[37]

1.6.2. PbTe-based alloys

Lead chalcogenides (PbX; X = S, Se or Te) are materials containing Pb^{2+} cations and X^{2-} anions. They crystallise in the NaCl crystal structure consisting of two interpenetrating face-centred cubic sublattices; one each for cations and anions (see Figure 1.15a). Due to the accommodating nature of the NaCl structure, lead chalcogenides can be easily alloyed with many other compounds that show similar crystal structure.[37] Such approach results in reduction of $\kappa_{lattice}$ and improved thermoelectric properties. In 2004, Hsu *et al.*[43] prepared a family of so-called LAST phases (lead-antimony-silver-telluride) and reported a $ZT \sim 1.7$ at 800 K for $AgPb_{18}SbTe_{20}$ ($AgSbTe_2$ + 18 PbTe). Replacement of Pb^{2+} with Ag^+ and Sb^{3+} resulted in formation of fine nanoinclusions that effectively scatter phonons, while having a minor effect on the carrier mobility. The temperature dependence of *ZT* for other PbTe-based materials (Figure 1.15b) suggests they can be used for heat recovery

in a wide temperature range. However, their application is limited by the toxicity of Pb and scarcity of Te.

1.6.3. Caged Compounds – Skutterudites and Clathrates

The 'Phonon Glass Electron Crystal' (PGEC) materials (proposed by Slack) must have a large unit cell containing heavy atoms, small electronegativity difference between constituent elements and a high charge mobility. Slack suggested that PGEC-behaviour may be observed in cage-like compounds that contain voids or tunnels. The guest atom or group of atoms of small size fills the voids within the structure and acts as independent oscillator (rattle effect). It interacts with the phonon modes and reduces the transport of phonons, leading to lower κ. PGEC-like behaviour was experimentally observed in filled skutterudites and intermetallic clathrates.[44]

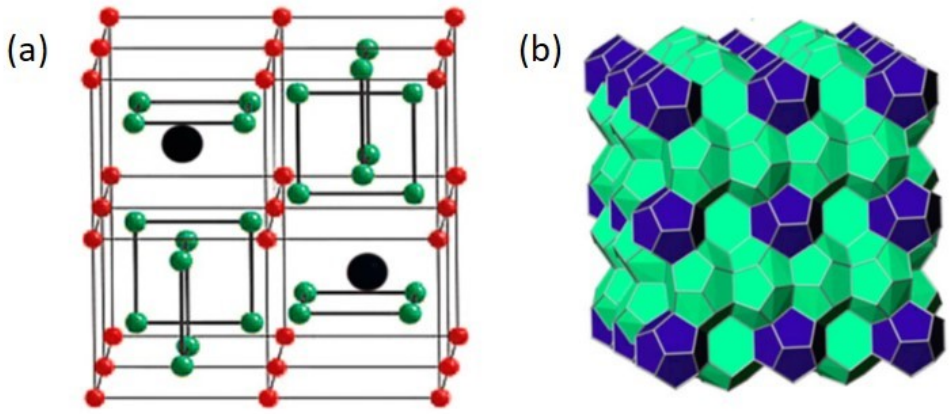

Figure 1.16. (a) Schematic representation of the crystal structure of skutterudites, where red spheres denote transition metal M, green spheres represent elements of group 15 and black spheres correspond to voids that can be filled by a guest atom.[37] **(b)** Crystal structure of a Type-I clathrate. Green denotes E_{24} cage, while blue corresponds to E_{20} cage.[37]

The skutterudites have the general formula MX_3 (M = Co, Rh or Ir; X = P, As or Sb). As shown in Figure 1.16a, the unit cell can be considered to consist of eight cubes of the transition metal M, with six of these cubes filled with square planar rectangles of the group 15 element (X). The two remaining voids can be filled by the guest atoms with ionic radii smaller than the cage.[45] The most studied skutterudites for thermoelectric applications are based on $CoSb_3$, due to their environmentally benign composition, high

carrier mobility, low ρ and good S. The $\kappa_{lattice}$ can be effectively reduced by filling the structural site with rare-earth, alkaline-earth, alkali metals and other metals.[37]

Similar to skutterudites, clathrates have an open framework that enables filling of the structural voids by a guest atom. Clathrates are composed of tetrahedrally coordinated Al, Si, Ga, Ge, Sn, etc. atoms with polyhedral cages of different size. The shape and number of cages is used to classify the clathrate type. Figure 1.16 illustrates a Type-I clathrate with the general formula $A_2B_6E_{46}$. Here, E is the tetrahedrally coordinated framework, while A and B are fillers that are encapsulated in cage E_{20} and E_{24}, respectively. The subscript corresponds to the number of atoms that form the respective cage. The filler atoms act as rattlers that scatter phonons, leading to low $\kappa_{lattice}$.[37]

Figure 1.17. Schematic representation of the half-Heusler crystal structure.

1.7. Half-Heuslers

1.7.1. Crystal Structure

Half-Heuslers are ternary intermetallics with the general formula MYZ, where M is an early transition metal, Y is a late transition metal and Z is a main group element (typically Sn or Sb). The compounds of this family crystallise in the cubic MgCuSb-type structure with space group $F\bar{4}3m$. As shown in Figure 1.17, the structure consists of three interpenetrating face-centred cubic sublattices, each occupied by one of the constituent elements and a fourth sublattice that remains vacant. M occupies Wyckoff position *4a* (0, 0, 0), Y is located on *4c* (¼, ¼, ¼) and Z occupies *4c* (½, ½, ½).[46] The *4d* site (¾, ¾, ¾) remains unoccupied. As discussed later, this site can be filled by a small amount of excess transition metal. As M, Y and Z can be selected from many different elements, the half-Heuslers can show various properties. For example, PtMnSb and NiMnSb[47] have a valence electron count (VEC) of 22 and are half-metallic ferromagnets. On the other hand,

compositions with VEC = 18, such as ZrNiSn[48] or NbFeSb[49, 50] are semiconductors that have great potential for thermoelectric applications.

Half-Heuslers with VEC = 18 have a closed shell electronic configuration and are highly stable. These materials generally display excellent semiconducting electrical properties due to the presence of a narrow bandgap. The work presented in this thesis is focused on VEC = 18 compositions based on MNiSn (M = Ti, Zr, Hf). To advance the properties of half-Heusler compounds it is necessary to understand the distribution of atoms. Within the structure, elements on the Wyckoff positions *4b* and *4c* form a zinc blende sublattice with a strong covalent bonding interaction. The atoms on positions *4a* and *4b* built a rock-salt sublattice, which has strong ionic character. Figure 1.18 summarises the relationship between these different crystal lattices.[46, 51]

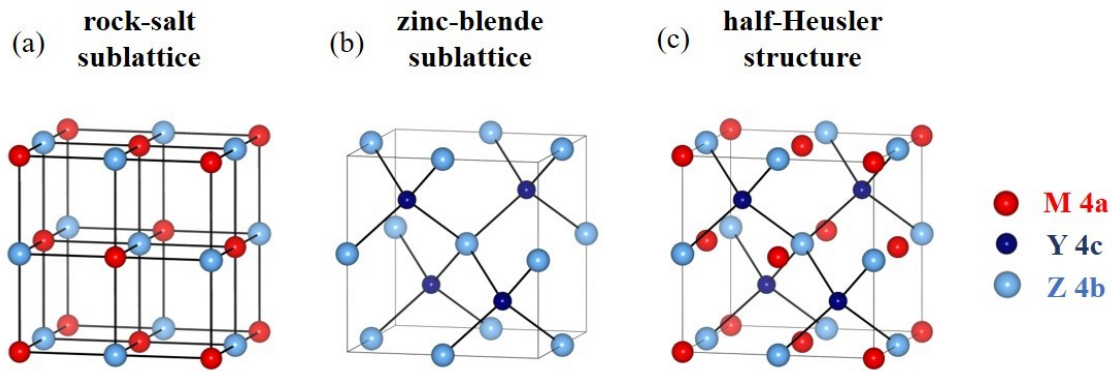

Figure 1.18. Structure of **(a)** rock-salt sublattice and **(b)** zinc blende sublattice that combined form half-Heusler material **(c)**.

1.7.2. Electronic Structure

As indicated above, the VEC determines the properties of half-Heusler intermetallics with general formula MYZ. Taking ZrNiSn as an example, the chemical bonding based on the molecular orbital theory approach is illustrated in Figure 1.19.[52] The orbitals were colour coded to show different elemental contributions. In the zinc blende $[NiSn]^{4-}$ sublattice (Figure 1.19c), the 5*s* and 5*p* states of Sn (Figure 1.19b) are fully occupied and hybridise with empty 4*s* and 4*p* orbitals of Ni (figure 1.19a). Low energy, bonding orbitals (a_1 and t_2), as well as high energy anti-bonding orbitals (a_1* and t_2*) are formed. The occupied 3*d* orbitals of Ni do not interact with Sn. The interaction between $[NiSn]^{4-}$ and Zr^{4+} (Figure 1.19e) is shown in Figure 1.19d.

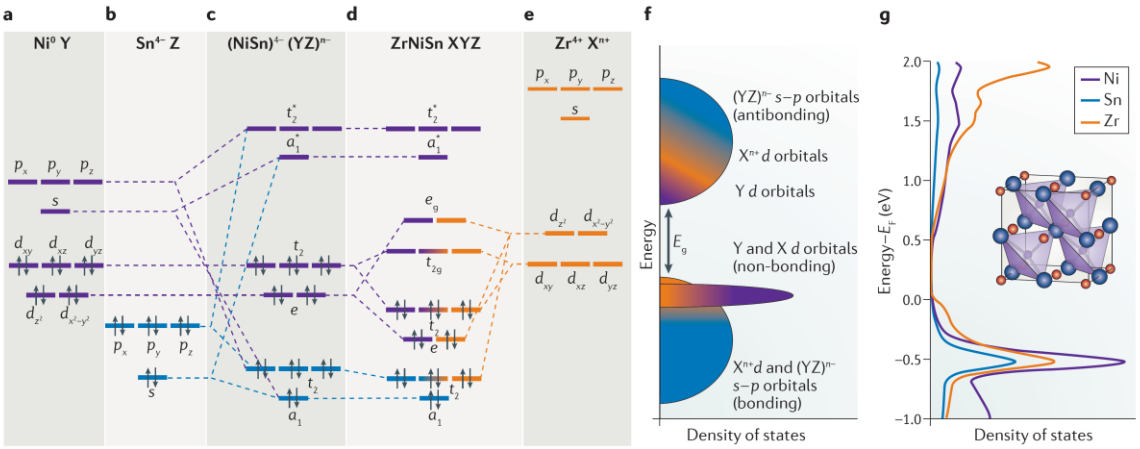

Figure 1.19. (a-g) Colour-coded evolution of molecular orbitals of ZrNiSn. **(b)** Schematic formation of the density of states in $X^{n+}(YZ)^{n-}$ (X denotes M). **(b)** The calculated partial density of states of ZrNiSn indicating elemental contributions, showing different elemental contributions. E_f denotes Fermi energy.[52]

The 3*d* orbitals of Ni (t_2 and *e*) interact with the empty Zr 3*d* states and form two sets of orbitals (double degenerate *e* orbitals and triple degenerate *t* orbitals) – one with bonding and one with anti-bonding character. This creates weak covalent interaction. Created hybrid orbitals are separated by an energy gap. The highest occupied molecular orbitals (HOMO) have mainly Ni character, while lowest unoccupied molecular orbitals (LUMO) have a strong Zr contribution. In other words, the valence band has a strong Ni contribution and the conduction band has predominantly Zr character.

As discussed in Section 1.4.1, the molecular orbital theory approach can be used to attain simplified representation of the DOS of ZrNiSn (Figure 1.19f). Due to the higher electropositive character of Zr^{4+}, the atomic orbitals are higher in energy and therefore the orbital contributions to the conduction band are from the interaction between Zr^{4+} and Ni *d* orbitals. The filled *d* orbitals will have mostly Ni-like character. However, there is mixing of Zr^{4+} and Ni d orbitals, which can be seen in the calculated partial DOSs (Figure 1.19g). It is evident that there is some Zr^{4+} contribution to the flat *d* band, but this contribution is smaller than Ni. The flat Ni *d* orbitals are not observed at the VB edge because of larger overlap of *s* and *p* bonding orbitals. As a result, wider band dispersion and the interaction between Ni *d* and Sn *s-p* orbitals are reported. [52]

The energetic configuration is influenced by the composition of investigated material. The energy separation of the bonding and antibonding orbitals will increase with a

stronger *Y* and *Z* bonding interaction. This will lead to *s* and *p* valence orbitals at lower energy and *Y d* orbitals at the valence band edge, as shown in Figure 1.19f. Another example is substitution of M (here denoted as X) with an element of higher electronegativity (eg. Zr with Ti). This will increase influence of X on the heavy Y *d* orbitals, changing the electronic transport.[52]

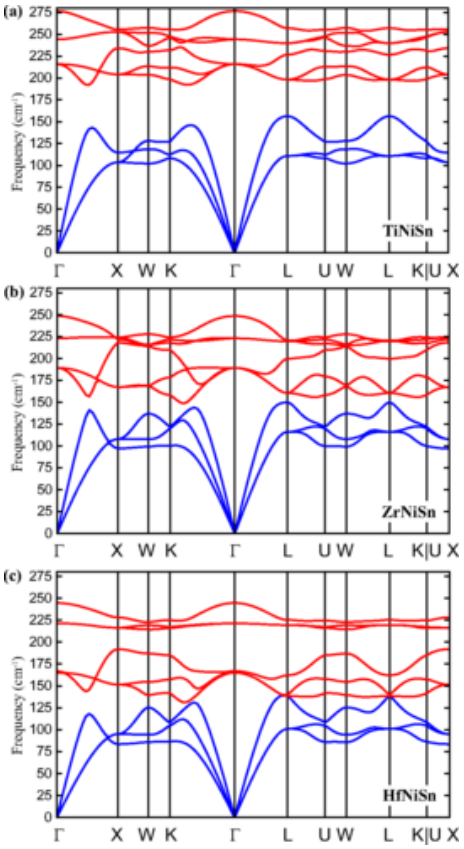

Figure 1.20. Phonon dispersion curves of **(a)** TiNiSn, **(b)** ZrNiSn and **(c)** HfNiSn. Optical bands are shown in red and acoustic in blue.[53]

1.7.3. Vibrational Properties

Phonon dispersion curves for half-Heusler MNiSn (*M* = Ti, Zr, Hf) are shown in Figure 1.20.[53] The frequency of optical bands changes with the *M* element. The most noticeable acoustic-optical band gap is reported for TiNiSn. In ZrNiSn, the lower optical modes drop in frequency causing the closure of band gap. In HfNiSn, the optical and acoustic bands drop even lower in frequency causing optical-acoustic band mixing. Also, new gap centred at 200 cm^{-1} is observed, suggesting that the location of the lower optical bands can be altered by the substitution on the M site.[53]

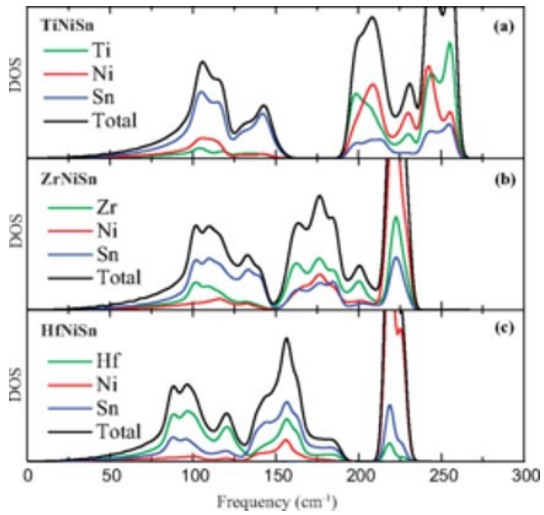

Figure 1.21. Total density of states (black line) and colour-coded partial density of states for **(a)** TiNiSn, **(b)** ZrNiSn and **(c)** HfNiSn.[53]

The total phonon density of states (DOS) and partial phonon density of states (PDOS) are shown in Figure 1.21.[53] Similarly, to phonon dispersion curves, the total DOS peaks shift towards lower frequency as the mass of the M element increases. The acoustic modes are dominated by the heaviest element: Sn in TiNiSn and ZrNiSn; Hf in HfNiSn. As discussed in Section 1.5.3, the acoustic modes are main heat conductors. Therefore, the change in dominance from Sn to Hf in PDOS suggests that alloying on the M-site would have a greater effect on $\kappa_{lattice}$ of HfNiSn than TiNiSn. In TiNiSn and ZrNiSn, the optical modes are largely composed of M and Ni, while Ni and Sn dominate in HfNiSn structure.[53]

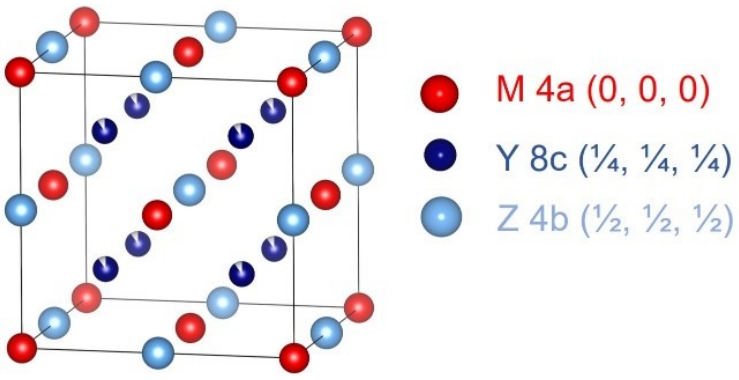

Figure 1.22. Schematic representation of the full-Heusler structure.

1.7.4. Full-Heusler

As shown in Figure 1.22, the full-Heusler compounds with the general formula MY_2Z are closely related to the half-Heusler materials. Here, M is Ti, Zr, or Hf, Y corresponds to Ni or Co and *Z* denotes to Sn and Sb. Similarly to the half-Heusler materials, they consist four interpenetrating face-centred cubic sublattices. The main difference is that the normally vacant site in half-Heusler is fully occupied with the transition metal Y, resulting in increase of space group symmetry (from $F\bar{4}3m$ to $Fm\bar{3}m$).

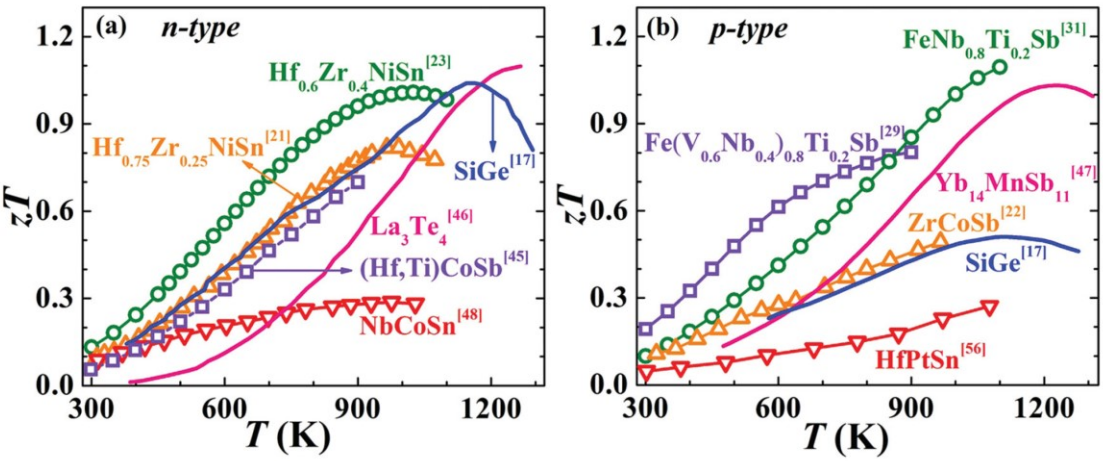

Figure 1.23. Comparison of thermoelectric performance on **(a)** n-type and **(b)** p-type half-Heusler compounds.[54]

1.7.5. Thermoelectric Properties of Half-Heusler Alloys

The half-Heusler materials with VEC = 18 per unit cell are characterised by a small band gap (0 – 1.1 eV), which is suitable for moderate temperature (700 – 900 K) applications.[13] Because of the mechanical strength, long-term stability, resistance to oxidation at high temperatures, cheap and environmentally friendly elements, the half-Heusler compounds can be used in large-scale production.[55] The most promising n-type materials are based on MNiSn,[48, 56-60] while good p-type performance can be extracted from compositions based on MCoSb and M'FeSb (with M = Ti, Zr, Hf and M' = V, Nb).[50, 61-64] As shown in Figure 1.23,[54] high $ZT \sim 1.0$ was achieved for both n- and p-type half-Heusler alloys. The wide-spread application is limited by large κ. The main strategy to improve thermoelectric efficiency involves the reduction of $\kappa_{lattice}$ through enhancement of phonon scattering. This approach was applied during this research, with various methods discussed in relevant result chapters.

1.7.5.1. Isovalent Substitution in MNiSn (M = Ti, Zr, Hf)

In isovalent substitution, ions are replaced by other ions with the same charge, therefore no additional changes are required to maintain charge balance.[24] During early studies, the thermal conductivity of half-Heuslers (MNiSn and MCoSb) alloys was successfully reduced by substitution on the M site. In 1997, Hohl *et al*.[65] investigated the $Ti_xZr_{1-x}NiSn$, $Ti_xHf_{1-x}NiSn$ and $Zr_xHf_{1-x}NiSn$ systems and found that alloying significantly reduces the $\kappa_{lattice}$. By varying the ratio of Ti, Zr and Hf, strain and mass fluctuations are expected, which scatter the phonons responsible for thermal transport.[69] It has been shown that a lower κ in p-type $Hf_{1-x}Ti_xCoSb_{0.8}Sn_{0.2}$ and n-type $Hf_{0.75x}Ti_xZr_{0.25}NiSn_{0.99}Sb_{0.01}$ systems can be achieved due to larger differences in the atomic mass and size between Ti and Hf, compared with Zr and Hf.[66, 67] Recently, Eliassen *et al*.[68] calculated the $\kappa_{lattice}$ of the binary half-Heusler mixtures, $Ti_xHf_{1-x}NiSn$ and $Zr_xHf_{1-x}NiSn$. The values rapidly decrease for x in the range 0 – 0.1, with significantly slower reduction for x = 0.1 – 0.9. This suggests that even low substitution is an effective procedure to scatter phonons. The $Ti_xHf_{1-x}NiSn$ compositions exhibit the lowest values with a shallow minimum observed around $Ti_{0.5}Hf_{0.5}NiSn$, due to the largest mass-disorder scattering parameter Γ_M (Equation 2.41) and strain fluctuation parameter Γ_S (Equation 2.42).[68]

Common observation for substituted compositions is phase separation that introduces additional boundary scattering.[69, 70] The phase separation, which occurs on the micrometre-scale is responsible for enhanced scattering of long-wavelength phonons and the reduction of the $\kappa_{lattice}$.[63, 70-74] Samples without substitution at the M position are single phase with homogeneous distribution of all elements. The alloying of Zr and Hf does not result in phase separation because the chemical behaviour of both atoms is very similar. Due to lanthanide contraction, they have nearly the same atomic radii.[70, 75-78] In other words, the ZrNiSn and HfNiSn are fully miscible and form a solid solution. In contrast, the mixing of Ti with Zr and/or Hf results in Ti-rich regions and Ti-poor (Zr/Hf-rich) areas.[79] The miscibility gap between (Zr/Hf)NiSn and TiNiSn results in the formation of multi-phase regions that can be used to improve *ZT* values. A reduction of approximately 50% in κ was recently achieved for phase-separated $Ti_{0.5}Hf_{0.5}CoSb_{0.85}Sn_{0.15}$ compound compared to single phase $TiCoSb_{0.85}Sn_{0.15}$.[80] The structural investigation carried out by Schwall *et al*.[71] using synchrotron X-ray diffraction and scanning electron microscopy revealed that the microstructure of $Ti_{0.5}Zr_{0.25}Hf_{0.25}NiSn$ consists of three temperature stable half-Heusler phases (see Figure 1.24a). The exceptional *ZT* = 1.2 at 830 K (due to

low κ) was explained by the intrinsic phase separation and formation of Ti-rich and (Zr/Hf)-rich half-Heusler phases (see Figure 1.24b).

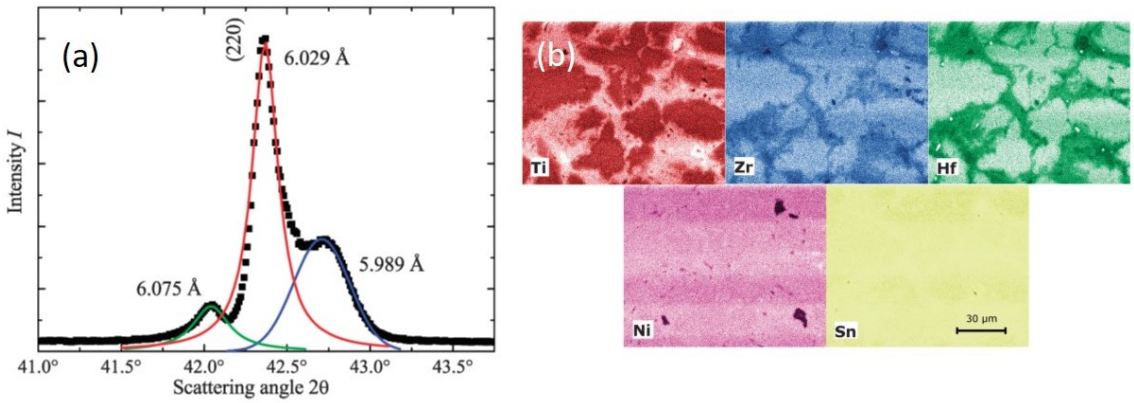

Figure 1.24. (a) Close up of (220) half-Heusler reflection of $Ti_{0.5}Zr_{0.25}Hf_{0.25}NiSn$ measured by X-ray synchrotron radiation. **(b)** EDX elemental maps of constituent elements showing phase separated $Ti_{0.5}Zr_{0.25}Hf_{0.25}NiSn$ alloy.[71]

Density functional theory (DFT) was used to predict the phase stability and solubility limits of half-Heusler phases defined by $(Ti_xZr_yHf_{1-x-y})NiSn$.[81] It was found that the DFT formation energies are positive for all intermediate $Ti_{1-x}Zr_xNiSn$ and $Ti_{1-x}Hf_xNiSn$ compositions, implying only the parent, pure MNiSn (M = Ti, Zr, Hf) are stable at zero temperature. All three MNiSn compounds have similar band structures,[82-84] however TiNiSn has significantly lower lattice parameter (a = 5.9297(1) Å) compared with HfNiSn (a = 6.0795(1) Å) and ZrNiSn (a = 6.1089(1) Å).[85] This suggest that mixing TiNiSn with Zr/HfNiSn comes with an elastic energy strain penalty, leading to positive formation energies. In contrast, the lattice mismatch between ZrNiSn and HfNiSn is significantly smaller leading to several intermediate compositions of $Zr_{1-x}Hf_xNiSn$ with small negative formation energy. This indicates that a solid solution of $Zr_{1-x}Hf_xNiSn$ should be thermodynamically stable even at low temperatures.[81]

Another approach to improve thermoelectric properties of half-Heusler alloys is partial replacing of Ni with Pd[86, 87] or Pt.[88] Yang *et al.*[86] found that Pd alloying on the Ni sublattice of $Zr_{0.5}Hf_{0.5}NiSn_{0.99}Sb_{0.01}$ leads to significant reduction of $\kappa_{lattice}$. Because Pd is significantly larger and heavier than Ni, the strain field fluctuation Γ_S (Equation 2.42) is dominant parameter. Xie *et al.*[88] substituted Pt at Ni site of the optimised

$Hf_{0.65}Zr_{0.35}NiSn_{0.98}Sb_{0.02}$ composition which introduced additional disorder. The $\kappa_{lattice}$ over the whole measured temperature range decreases with increasing Pt content, with 40% reduction at 870 K observed for $Hf_{0.65}Zr_{0.35}Ni_{0.85}Pt_{0.15}Sn_{0.98}Sb_{0.02}$. The Callaway model (see Section 2.4.3.2 for details) revealed strong point defect scattering in phonon transport, which was consistent with $\kappa_{lattice} \sim T^{-0.5}$ relationship.[89]

1.7.5.2. Aliovalent Substitution in MNiSn (M = Ti, Zr, Hf)

In aliovalent solid solutions, ions are substituted with ions that have different charge. This can lead to electronic doping or formation of vacancies and interstitials.[24] Such substitutions can be done on each of the three occupied half-Heusler sublattices. As discussed in Section 1.7.2, the molecular orbital diagram reveals $(NiSn)^{-4}$ bonding orbitals, which are filled with the valence electrons of the M^{4+} cations to make a valence band.[52] Taking ZrNiSn as an example, substitution of Zr^{4+} with an atom of a different valence (e.g. Sc^{3+}) leads to p-type material.[48, 90]

The most common dopant for n-type MNiSn materials is Sb, which has one more *p*-electron than Sn and acts as an effective electron-dopant. Sb-doping has a pronounced effect on the resistivity, with a metallic temperature dependence observed, even for very small amounts (< 0.5%) of Sb. Sb dramatically affects the charge carrier concentration and therefore the electrical transport, leading to great enhancement of $S^2\sigma$.[91-93] For example, the carrier concentration increases from 1×10^{20} cm^{-3} of $Ti_{0.5}Hf_{0.5}NiSn$ to 8×10^{20} cm^{-3} of $Ti_{0.5}Hf_{0.5}NiSn_{0.98}Sb_{0.02}$.[92] A similar trend was observed for Bi-doped $Zr_{0.5}Hf_{0.5}NiSn_{1-x}Bi_x$ ($0 \leq x \leq 0$) samples, confirming that substitution of Sn with small amounts of group 15 element has great effect on transport properties.[94]

As discussed in the previous section, various (Ti/Zr/Hf)NiSn half-Heusler alloys exhibit enhanced *ZT* values, due to the strain and mass difference as well as intrinsic phase separation. The thermoelectric performance can be optimised further with Sb-doping. An excellent example is the n-type $Zr_{1-x}Hf_{1-x}NiSn_{1-y}Sb_y$ system, with *ZT* values as high as ~1.0 at ~1000 K.[77, 95] The *ZT* enhancement is due to the maximised point defect scattering caused by alloying on the M site and simultaneous tuning of the charge carrier concentration with Sb on the Sn-site. [67, 77, 95] A similar approach was applied in $Ti_{1-x}Hf_xNiSn_{1-y}Sb_y$, with *ZT* ~1.09 ± 0.11 at 800 K reported in $Ti_{0.5}Hf_{0.5}NiSn_{0.98}Sb_{0.02}$.[92]

Another approach to improve thermoelectric efficiency is substitution on the M site. In Nb-doped $Ti_{0.3-x}Nb_xZr_{0.35}Hf_{0.35}NiSn$, the σ increased with only a slight reduction of the *S*

leading to enhanced $S^2\sigma$ and ZT.[96] Additionally, change to metallic temperature dependence is observed upon Nb introduction.[96, 97] More recently, Rogl *et al*.[98] reported Nb- and V-doping in the (Ti/Zr)$NiSn_{0.98}Sb_{0.02}$, while Lkhagvasuren *et al*.[99] investigated substitution and addition of Mn in TiNiSn.

1.7.5.3. Excess Metal in MNiSn Composites

The half-Heusler crystal structure has a vacant *4d* tetrahedral interstitial site, which is fully filled in the full-Heusler structure. In recent years, the MNiSn-MNi_2Sn system has been investigated by increasing amount of Ni added to the half-Heusler matrix.[60, 100-102] Addition of a small amount of Ni offers a simple approach to achieve improved ZT.[14] No additional elements are required, as for doping or alloying. Although the conversion of half-Heusler to full-Heusler results in only a marginal increase in the unit cell parameter (~3%), the crystal structure drastically changes from the noncentrosymmetric to centrosymmetric. Moreover, both compounds exhibit drastically different physical properties. The half-Heusler compounds are semiconducting with small band gap, while full-Heuslers are metallic. The ability to interchange between half-Heusler and full-Heusler structure with addition or removal of Ni enables the manipulation of the thermoelectric properties.[100] Therefore, many research groups have investigated the effect of adding excess metal into MNiSn, however conflicting results on the thermoelectric properties and morphology have been observed.

To answer the question: '*how excess metal is incorporated into the crystal structure?*', the solubility between the half-Heusler MNiSn and full-Heusler MNi_2Sn phases should be recognised. Recently Romaka *et al*.[103] carried out electronic structure calculations to establish effect of Ni addition on the electronic structure and chemical bonding as one goes from TiNiSn to $TiNi_2Sn$. Filling the vacant *4d* site with Ni in half-Heusler gradually delocalized the *s* and *p* orbitals of Sn in the VB resulting in weaker Ni and Sn covalent bonding, destabilising the structure. Moreover, the hybridisation between Ni and Sn changes significantly. In TiNiSn, *p* orbitals of Sn overlap with d_{z2} and d_{x2-y2} orbitals of Ni, whereas in $TiNi_2Sn$ *S* and *p* orbitals of Sn interact with all *d* orbitals of Ni. Authors concluded that such different chemical bonding explains lack of solubility of the half-Heusler and full-Heusler phases.[103] In a follow-up paper,[104] ZrNiSn-$ZrNi_2Sn$ and HfNiSn-$HfNi_2Sn$ composition range were investigated using X-ray diffraction and electron probe microanalysis (EPM). EPM revealed that for $ZrNi_{1+x}Sn$, up to x = 0.30 can be introduced before $ZrNi_2Sn$ is formed (see Figure 1.25a). All samples with x in range 0.30-0.65

consist of half-Heusler and full-Heusler phases, while single phase $ZrNi_2Sn$ is observed for $x \geq 0.65$ compositions. Similar results were attained for samples with $HfNi_{1+x}Sn$ compositions, with single half-Heusler phase observed for $x \leq 0.30$, single full-Heusler reported for $x \geq 0.70$ and the mixture of HfNiSn and $HfNi_2Sn$ in-between (Figure 1.25b).[104]

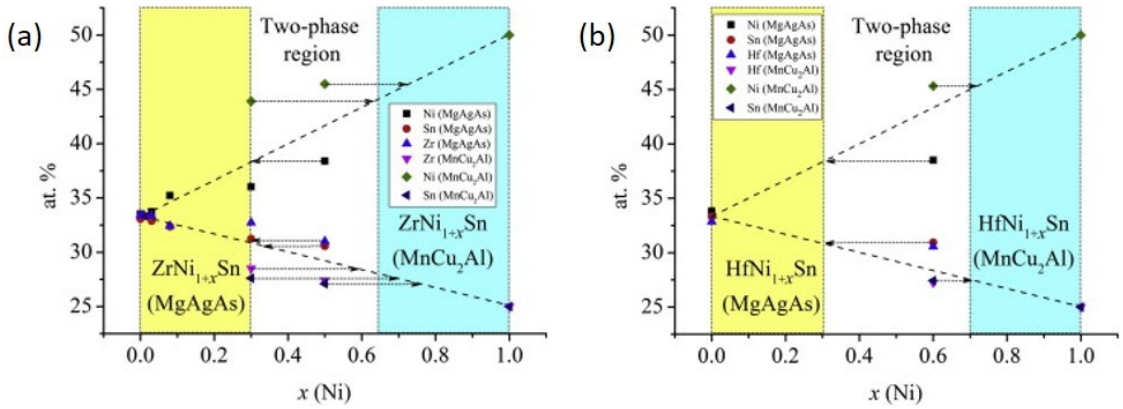

Figure 1.25. Phase composition of **(a)** $ZrNiSn$-$ZrNi_2Sn$ and **(b)** $HfNiSn$-$HfNi_2Sn$ alloys from EPM data collected at room temperature.[104]

A more recent paper,[53] confirmed the above observation with very low Ni solubility limit in TiNiSn, ZrNiSn and HfNiSn alloys, even at high temperatures. Any excess Ni introduced above the solution limit will result in the formation of two-phase mixture of half-Heusler and full-Heusler. In $TiNi_{1+x}Sn$ (Figure 1.26a), a large miscibility gap is observed over the entire temperature. A negligible Ni solubility is observed at 300K, which increases to 1% at 1450 K. In contrast, the Ni solubility in $ZrNi_{1+x}Sn$ is also negligible at 300 K, however it steadily increases to 5.8% at 1450 K, with maximum (11.0%) observed at 1700 K (Figure 1.26b). For $HfNi_{1+x}Sn$, the solubility limit is also negligible at 300 K, but it increases to 1.0% at 1450 K and 2.3% at 1700 K (Figure 1.26c). The study suggests that a secondary full-Heusler phase will precipitate within a half-Heusler matrix, when excess Ni concentration is greater than values stated above.

These and other theoretical studies[105, 106] have shown that the segregation of excess Ni into distinct full-Heusler is more favourable than its random distribution on the vacant *4d* site in half-Heusler structure. Electron microscopy has revealed a variety of full-Heusler phases, with size varying from nanoinclusions to microscopically segregated phases. In the following part of thesis, the impact of micro- full-Heusler inclusions, nano- full-

Heusler inclusions and randomly distributed on the *4d* site excess metal (Co, Ni, Cu) will be discussed.

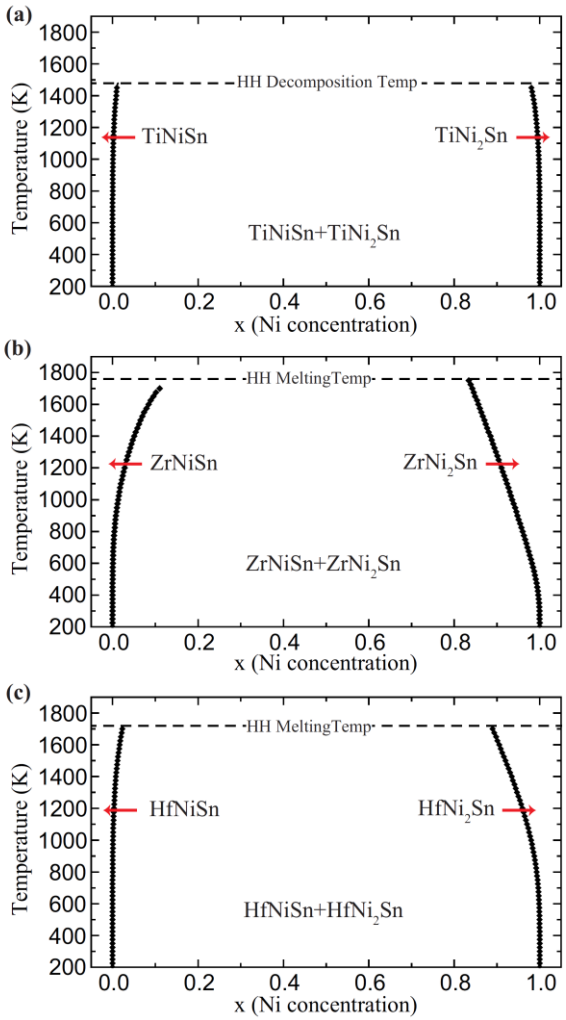

Figure 1.26. Thermodynamic phase diagram as a function of temperature and Ni content in **(a)** $TiNi_{1+x}NiSn$, **(b)** $ZrNi_{1+x}Sn$ and **(c)** $HfNi_{1+x}Sn$.[53]

1.7.5.3.1. Full-Heusler Micro-Inclusions

An early transmission electron microscopy (TEM) study of $TiNi_{1.5}Sn$ revealed the presence of micron-size full-Heusler regions within the half-Heusler matrix. Interestingly, smaller half-Heusler regions were identified within the full-Heusler domains.[107] A similar morphology was observed by Douglas *et al.*[108] who prepared $TiNi_{1+y}Sn$ samples with significantly smaller Ni content (y = 0 and 0.15). Scanning electron microscopy (SEM) suggests the presence of a two-phase material with non-uniform morphology of micron sized segregated full-Heusler inclusions. Energy dispersive X-ray analysis (EDX) revealed dispersion of small TiNiSn particles (1 μm in

diameter) within the full-Heusler. In a follow-up paper,[109] the authors confirmed that the size of the full-Heusler inclusions increases with the Ni content, leading to interconnected $TiNi_2Sn$ phases (see Figure 1.27). 10 – 30% reduction in κ and 50% increase in the σ was observed for $TiNi_{1.15}Sn$, compared to parent TiNiSn. The reduction of κ as the Ni content increases is explained by the presence of micron-sized Heusler inclusions, which effectively scatter heat-carrying phonons. Similar behaviour was also observed in samples prepared using microwave synthesis, ball milling and spark plasma sintering consolidation.[101] Birkel *et al.*[101] conclude that there is a direct correlation between the reduction of the κ and amount of full-Heusler inclusions. The $TiNi_{1.10}Sn$ and $TiNi_{1.15}Sn$ compounds exhibit the lowest κ_{RT} = 3.6 – 3.7 W m^{-1} K, while the highest ZT = 0.6 at 750 K was reported for a sample with 5% excess Ni. These studies suggest that the phase segregation has a beneficial effect on the thermoelectric properties.

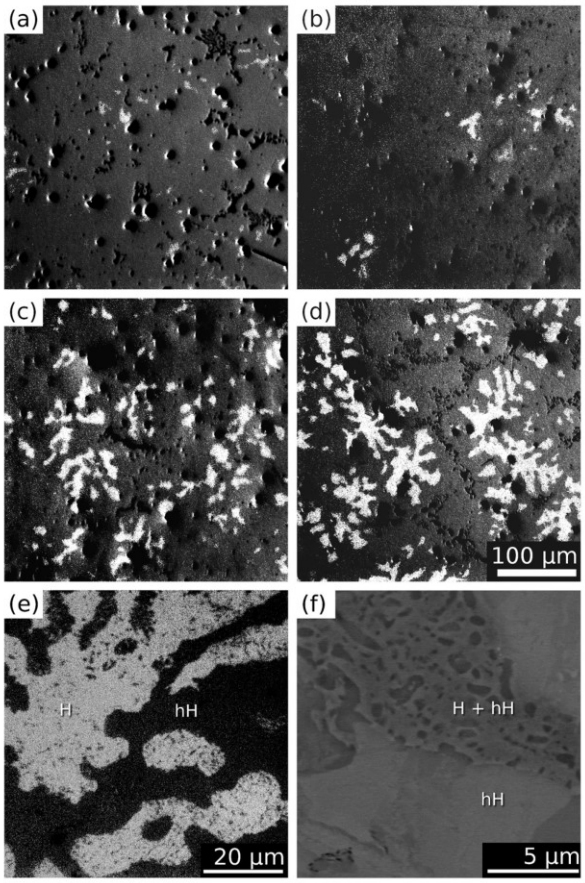

Figure 1.27. Optical microscopy images of $TiNi_{1+y}Sn$: **(a)** y = 0.00, **(b)** y = 0.05, **(c)** y = 0.15 and **(d-e)** y = 0.20. **(f)** Backscattered scanning electron microscopy image of y = 0.15. The hH and H denote half-Heusler and full-Heusler, respectively. Light regions are H, while charcoal is hH.[109]

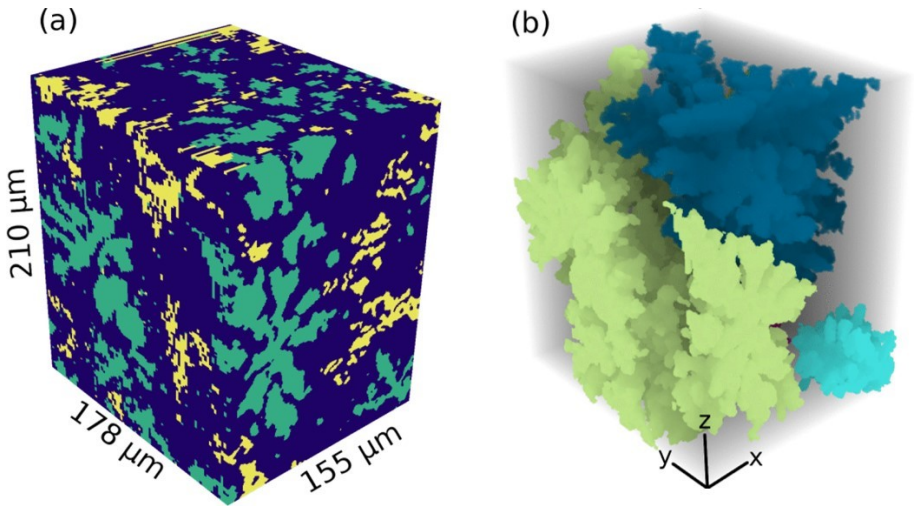

Figure 1.28. 3D visualisation of $TiNi_{1.20}Sn$. **(a)** Surfaces of the volume coloured by phase: TiNiSn (blue), $TiNi_2Sn$ (green), Ti-Sn binary (yellow). **(b)** Reconstruction of the three largest full-Heusler phase regions. Each shown with different colour.[110]

A challenging aspect of electron microscopy is that it allows 2D visualisation of phases and grains that are generally 3D in nature. To address this issue, Douglas *et al.* investigated the 3D microstructure of melt-prepared $TiNi_{1.20}Sn$ using a TriBeam tomography system.[110] EDX spectroscopy was used to define 3 phases: half-Heusler TiNiSn, full-Heusler $TiNi_2Sn$ and a Ti-Sn binary phase ($Ti_5Ni_{1-y}Sn_3$). The reconstructed volume (coloured by phase) is shown in Figure 1.28a. 20% of the volume corresponds to the full-Heusler phase, which is consistent with the nominal excess Ni content. The largest contiguous full-Heusler features were isolated from this dataset (see Figure 1.28b). The two largest features (blue and green) encompass 90% of total full-Heusler volume. The large regions (hundreds of microns) suggest that the full-Heusler phase reached a percolation threshold in this sample. This explains higher κ compared with less Ni-doped samples.[109]

1.7.5.3.1. Full-Heusler Nano-Inclusions

There are a significant number of reports that observe the formation of full-Heusler nano-inclusions in the half-Heusler structure. In 2012, Chai *et al.* investigated the microstructure of TiNiSn alloy, which was prepared using a solid-liquid reaction-sintering process.[111, 112] The EPM analysis revealed that the final composition was slightly off-stoichiometric with a small amount of excess Ni ($TiNi_{1.1}Sn$). Detailed TEM study

revealed a high density of coherent nano-sized full-Heusler precipitates within the half-Heusler matrix. The ellipsoid nanoparticles (with average 5 nm diameter) and nano-sized discs (~50 nm long and up to 10 nm thick) were mostly observed. The formation of the full-Heusler nanoparticles was explained via a phase separation process. At high temperatures, a single phase solid solution between half-Heusler and full-Heusler is observed. In this phase, a mixture of Ni atoms and vacancies is found on the *4d* sublattice. Upon cooling, phase separation occurs – this *4d* sublattice decomposes into a vacant sublattice (as in TiNiSn) and a Ni-occupied sublattice (as in $TiNi_2Sn$). This two-phase mixture of half-Heusler and full-Heusler regions is stable at low temperatures.

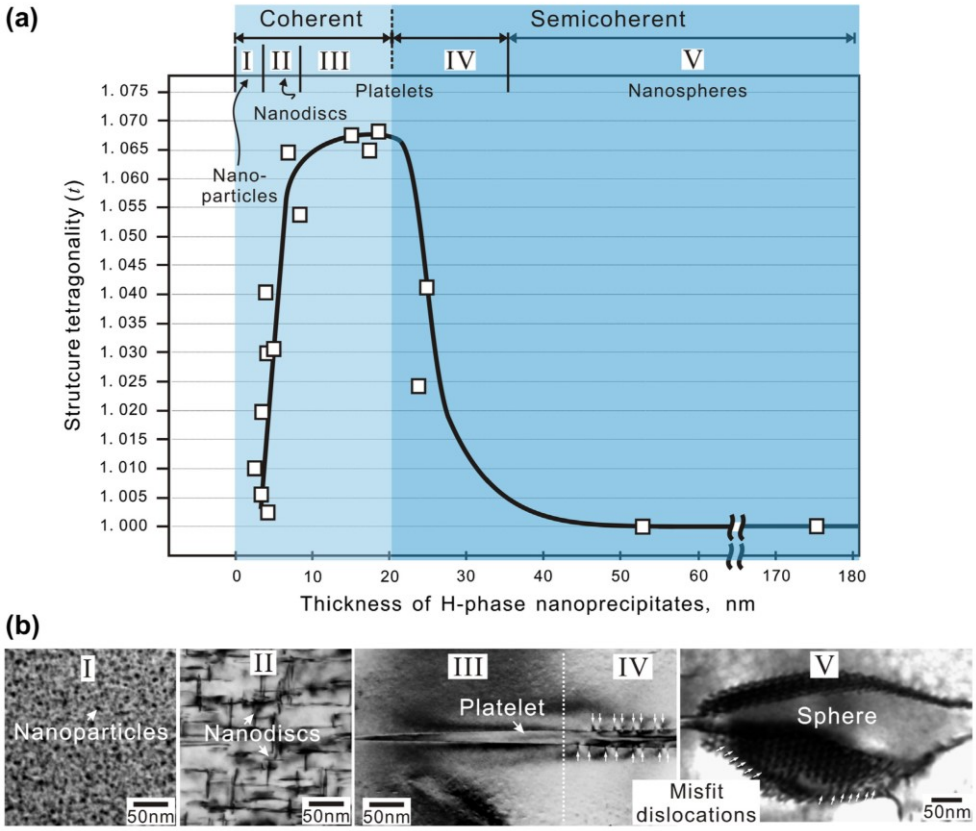

Figure 1.29. (a) Evolution of full-Heusler inclusions as a function of thickness size. **(b)** TEM images of the nanoprecipitates.[113]

In their later report, Chai *et al.*[113] explained in more detail the formation of a wide range of inclusions, which are reproduced in Figure 1.29. Such a wide range of sizes suggests a gradual coarsening of statistically distributed Ni atoms into segregated inclusions. The authors proposed a possible coarsening mechanism, where excess Ni occupy structural

vacancies, which cluster together and form Ni-rich clusters. These clusters serve as coarsening sites for Heusler phase nanoprecipitates. They coarse further, forming nanoparticles, nanodiscs, platelets and spheres.[113] Similar inclusions were observed by the authors in their follow-up works related to $Ti_{0.2}Zr_{0.8}Ni_{1.1}Sn$[114] and $ZrNi_{1.1}Sn$.[102] Do *et al.*[115] carried out computational study of $ZrNi_{1+y}Sn$ to investigate the distribution of excess Ni in the structure and found that gradually added Ni atoms prefer to stay close to each other and form nanoclusters, supporting the experimental results.

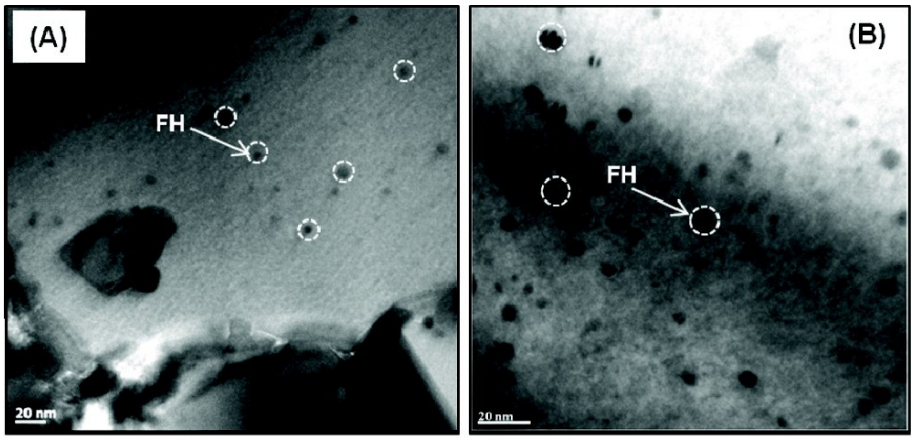

Figure 1.30. TEM images of $Zr_{0.25}Hf_{0.75}Ni_{1+y}Sn$: **(a)** y = 0.02 and **(b)** y = 0.05.[116]

There is some discrepancy over the effect of full-Heusler nano-inclusions on the electronic and thermoelectric properties of the half-Heuslers. Some groups report that the presence of a secondary full-Heusler phase induces the reduction of the κ. Phonons are efficiently scattered by micron- or nano-sized full-Heusler inclusions, without significantly influencing the electron transport within the system.[113] For example, Liu *et al.*[100] observed a reduction in $\kappa_{lattice}$ at room temperature from 13 to 9 W m^{-1} K^{-1} for $Ti_{0.1}Zr_{0.9}NiSn$, upon addition of 10% excess Ni. Addition of excess Ni has a beneficial effect on the electronic properties of half-Heusler compounds. Large enhancement in the *S* with minor decrease in the σ was reported.[100, 116-119] In 2011, Makongo *et al.*[116] investigated the $Zr_{0.25}Hf_{0.75}Ni_{1+y}Sn$ (y = 0, 0.02, 0.05) and $Zr_{0.25}Hf_{0.75}Ni_{1+y}Sn_{0.975}Bi_{0.025}$ (y = 0, 0.02, 0.03, 0.04, 0.06 and 0.10) systems. A TEM study of $Zr_{0.25}Hf_{0.75}Ni_{1+y}Sn$ revealed well dispersed, spherically shaped nanometer-scale full-Heusler precipitates in the bulk half-Heusler matrix (Figure 1.30). For the sample with y = 0.02, the inclusions are on the order of <1 to 3 nm. Increasing the Ni content to y = 0.05, resulted in a higher

density and larger (~1 to 20 nm) full-Heusler precipitates. In addition, lamellar features (2-8 nm thick and up to 30 nm long) were observed for $Zr_{0.25}Hf_{0.75}Ni_{1.05}Sn$.

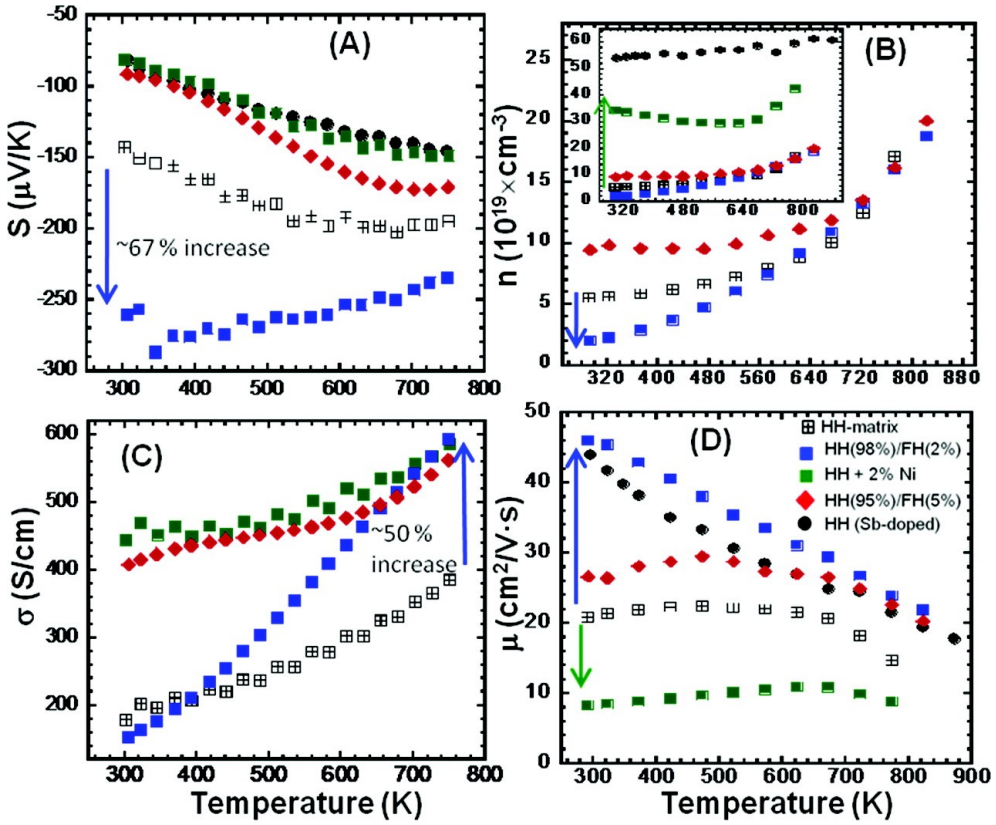

Figure 1.31. Temperature dependence of **(a)** Seebeck coefficient (S), **(b)** charge carrier concentration (n), **(c)** electrical conductivity (σ) and **(d)** carrier mobility (μ) for $Zr_{0.25}Hf_{0.75}Ni_{1+y}Sn$.[116]

The thermoelectric properties of the $Zr_{0.25}Hf_{0.75}Ni_{1+y}Sn$ series are shown in Figure 1.31.[116] At 300 K, the addition of 2% full-Heusler precipitates results in a significant enhancement of the S without the usual reduction in σ, due to an increased carrier mobility. The authors explained the decrease in the carrier density (Figure 1.31b) using the carrier filtering mechanism, which was first proposed by Faleev and Leonard.[120] This model considers scattering of electron on the band bending at the interfaces between bulk semiconductor and metallic inclusions. In $Zr_{0.25}Hf_{0.75}Ni_{1+y}Sn$ nanocomposites, the addition of Ni results in formation of incoherent or coherent grain boundaries at the interface of half-Heusler matrix and full-Heusler inclusions (see Figure 1.32 a-b).[116] At the interface, the energy difference of CB minima between the matrix and inclusion creates energy barrier (ΔE). The ΔE heights decreases as a function of the full-Heusler size. The reduction in carrier

concentration near room temperature was explained by the filtering (trapping) of low energy carrier (electrons) by energy barrier, while enabling transmission of high-energy carriers (see Figure 1.32c). As the temperature increases, the carrier density increases (Figure 1.31b). "Low energy" carriers of half-Heusler matrix are thermally excited and access energy channels across the energy barrier ΔE, contributing to the electronic transport.[116] Interestingly, as the Ni content is increased to y = 0.05, the carrier concentration increases, *S* is reduced and *σ* increases (figure 1.31). This suggests lack of the carrier filtering due to the large average size of the inclusions in this sample.

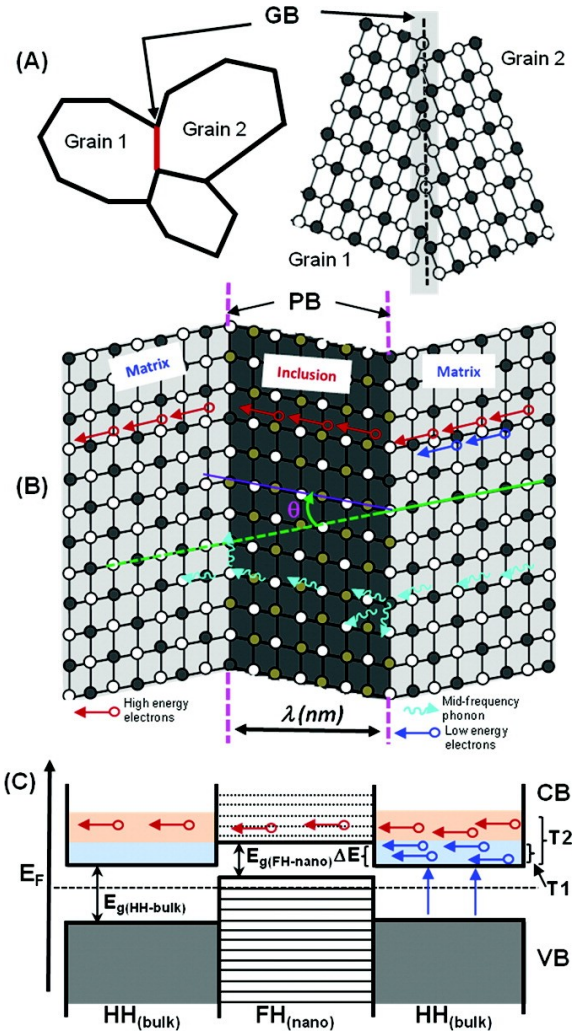

Figure 1.32. Schematic representation of **(a)** incoherent interface at grain boundaries (GB), **(b)** coherent grain boundaries (PB) and **(c)** nanometer scale hetero-junction between bulk half-Heusler matrix and nanometer scale full-Heusler inclusion, highlighting the filtering of low energy carriers.[116]

In a follow-up paper, the $Ti_{0.1}Zr_{0.9}Ni_{1+y}Sn$ ($y \leq 0.1$) system was investigated.[100] High-resolution transmission electron microscopy (HRTEM) was used to resolve the morphology, average size and size distribution of secondary full-Heusler phase. It revealed nearly spherical inclusions, suggesting co-nucleation followed by the isotropic growth. The carrier density of $Ti_{0.1}Zr_{0.9}Ni_{1+y}Sn$ compositions decreases upon addition of Ni, which is due to the formation of full-Heusler precipitates and filtering of low energy carriers. In addition, the magnitude of Seebeck coefficient increases with Ni content with 200% improvement at 300 K observed for $y = 0.10$. This is due to larger effective carrier mass ($m^* = 0.60$ for $y = 0$ and $m^* = 0.80$ for $y = 0.10$; evaluated using a Pisarenko plot), suggesting that in addition to reducing carrier concentration, the full-Heusler inclusion also influences carrier mobility.

The carrier filtering concept was successfully extended to the p-type $Ti_{0.5}Hf_{0.5}Co_{1+y}Sb_{0.9}Sn_{0.1}$.[118] Addition of excess Co results in coherently embedded full-Heusler structures within the half-Heusler crystal lattice, which influence the electronic transport. For example, S_{300K} increases from 100 to 240 $\mu V\ K^{-1}$ upon addition of 5% Co, which corresponds to a ~140% increase, while only a ~50% decrease from $\sigma_{RT} = 135$ S cm^{-1} ($y = 0$) to $\sigma_{RT} = 62$ S cm^{-1} ($y = 0.05$) is observed. This is consistent with the carrier density reduction. Large improvement in S and moderate reduction in σ result in large enhancement in the $S^2\sigma$. For example, ~225% improvement at 300 K and ~44% increase at 775 K are observed for $Ti_{0.5}Hf_{0.5}Co_{1.05}Sb_{0.9}Sn_{0.1}$ compared with the parent half-Heusler.

Large reduction in κ can be achieved using "a panoscopic approach", which includes all-scale hierarchical architectures. The phonons are effectively scattered across multiple length scales – from atomic-scale lattice disorder, nanoscale endotaxial precipitates and scattering from mesoscale grain boundaries.[121, 122] Such an approach was applied in $Zr_{0.7}Hf_{0.3}Ni_{1+y}Sn$ to prepare a half-Heusler matrix containing full-Heusler inclusions with various length scales.[123] The TEM for optimised $y = 0.03$ composition is shown in Figure 1.33. It revealed uniform distribution of various length scale full-Heusler inclusions within the half-Heusler matrix. HRTEM revealed coherent interfaces between the half-Heusler matrix and full-Heusler inclusion. A good $ZT = 0.96$ at 773 K was attained for the $y = 0.03$ composition, which is ~250% higher compared to that for $y = 0$. The ZT enhancement was due to a significant κ decrease (~34%) and a simultaneous improvement in the $S^2\sigma$ (~165%). Introduction of excess Ni leads to a wide range of the full-Heusler phases, which are responsible for scattering of phonons on all length scale. The S enhancement (~51%) can be explained by the filtering of low energy carriers.

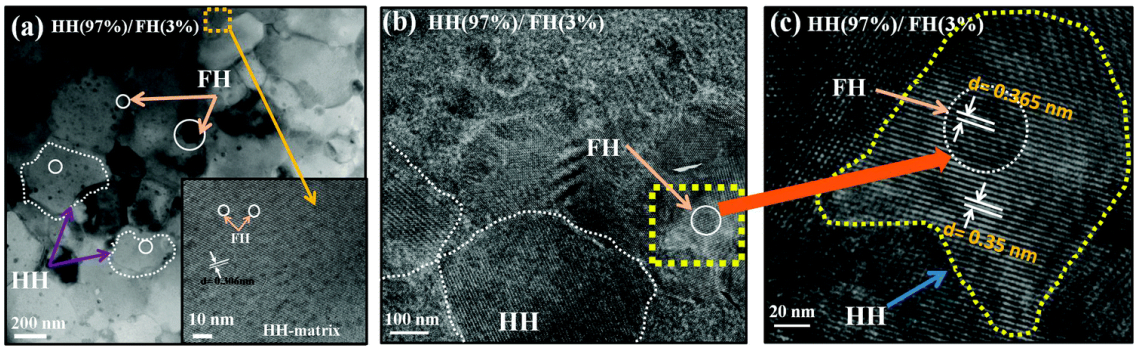

Figure 1.33. (a) Low-magnification TEM image of $Zr_{0.7}Hf_{0.3}Ni_{1.03}Sn$ showing the contrast between half-Heusler (HH – dark grey) and full-Heusler (FH – black). The inset presents high-resolution image of FH precipitate. **(b)** Image showing the various lengths of the FH inclusions. **(c)** HRTEM image showing coherent interface between the HH matrix and the FH inclusion.[123]

1.7.5.3.1. Random Distribution of Excess Metal

Despite multiple studies that indicate clustering of excess Ni and formation of full-Heusler inclusions as a favourable mechanism, statistical distribution of Ni on the interstitial sites has been suggested by several groups. In 2006, Muta *et al.*[124] prepared ZrNiSn-based alloys and found that addition of 5% Ni did not cause the formation of impurity phases, suggesting incorporation of excess metal into the half-Heusler bulk. Hazama *et al.*[125-127] reported a linear increase in the lattice parameter of main half-Heusler phase, following Vegard's law. It suggests systematic change and some solubility limit of Ni within TiNiSn. Similar unit cell expansion was observed by Douglas.[101, 109] Neutron powder diffraction studies carried by Downie suggested that up to 6 – 7% of Ni can be statistically distributed on the *4d* site.[128, 129] Unfortunately, this technique does not provide information about spatial distribution as data can be equally well fitted using the $TiNi_{1+y}Sn$ model or a mixture of (1 – y) TiNiSn and (y) $TiNi_2Sn$ with the same lattice parameter.[14] The authors investigated also the effect of other transition metals (Cu and Co) on thermoelectric properties of TiNiSn.[60] It was found that Ni- and Cu-doped materials form TiNiSn matrix with nanosegregated $TiNi_2Sn$ and $TiNi_{1+d}Cu_{1-d}Sn$, respectively. Interestingly, the $TiNiCo_ySn$ materials are composed of the $TiNi_{1-y}Co_ySn$ half-Heusler matrix with $TiNi_{2-y}Co_ySn$ full-Heuslers. The investigation of thermoelectric properties revealed systematic changes upon excess metal introduction, attributed to the formation of in-gap states.

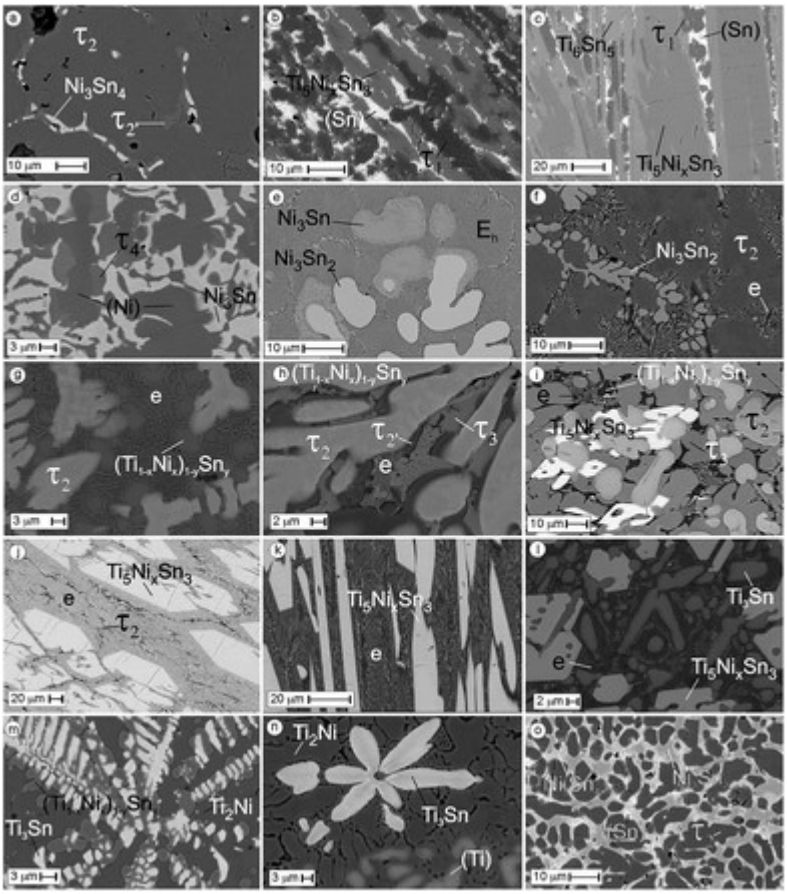

Figure 1.34. Microstructure of selected as-cast samples. τ_1 – half-Heusler phase, τ_2 – full-Heusler, τ_3 – Ti_2Ni_2Sn, τ_4 – $Ti_{1-x}Sn_xNi_3$.[130]

1.7.5.4. Synthesis Technique

The extensively investigated TiNiSn-based systems have been prepared using a variety of fabrication protocols, which include arc-melting of constituent elements,[103, 128] induction levitation melting,[109] microwave preparation,[131] powder metallurgy[113] and solid-state reactions[119, 129] followed by consolidation.[132] However due to the large differences in melting point and presence of competing binary phases that are present in the Ti-Ni-Sn phase diagram it is difficult to prepare impurity-free, stoichiometric TiNiSn compound.[103, 109] Some of these intermediates have melting point significantly higher compared to TiNiSn (T_m = 1182 ºC) and as a result are much more stable. Long annealing is essential step to improve the homogeneity of half-Heusler alloys as well as to reduce the amount of impurity phases. Only recently, the projection of liquidus- and solidus surfaces of the Ti-Ni-Sn phase diagram and precise information on the solidification path became available.[130] Investigation of the alloys in as-cast state (Figure 1.34) revealed that the full-Heusler phase (τ_2 – $TiNi_2Sn$) has crystallised first. It melts at 1447 °C and exhibits

a wide homogeneity range at sub-solidus temperatures. In contrast, the half-Heusler phase (τ_1) has much lower thermodynamic stability, which leads to smaller primary crystallisation field. The above observations were confirmed by Verma *et. al*[133], who examined the alloy with nominal stoichiometry $TiNi_{1.2}Sn$. Here, full-Heusler dendrites are the first phase forming from the melt. As the full-Heusler phases crystallizes further, Ni is depleted and the solidification path moves from $TiNi_2Sn$ towards TiNiSn.

Interestingly, the microstructure formation and solubility limit of (Ti/Zr/Hf)NiSn compositions depends on the synthesis protocol. Populoh *et al*.[73] prepared $Ti_{0.37}Zr_{0.37}Hf_{0.26}NiSn$ using arc melting followed by annealing and observed (Zr/Hf)-rich phase that due to the higher melting point solidify first in form of dendrites. The Ti-rich regions solidify later and fill in the interdendritic regions. Similar observation was made through detailed electron microscopy and EDX study of $Ti_{0.33}Zr_{0.33}Hf_{0.33}NiSn$, which confirmed that Zr/Hf-rich grains are surrounded by a Ti-rich region with some evidence of $TiNi_2Sn$ segregation within Ti-rich domains.[72] The solid-state method does not proceed through the melt, therefore completely different microstructure is obtained. Recently, Downie *et al*.[85, 134] prepared $M_{0.5}M'_{0.5}NiSn$ compositions using solid-state synthesis protocol and did not observe the dendritic features, characteristic for arc-melted compositions.

1.8. Aims and Objectives

The aim of this thesis is the investigation and development of MNiSn and $M_{0.5}M'_{0.5}NiSn$ (M = Ti, Zr, Hf) based half-Heusler alloys. The synthesis methods and an overview of the characterisation techniques used in the work throughout this thesis are presented in Chapter 2. Chapter 3 reports the effect of excess metal (Ni, Cu) and synthesis protocol on the crystal structure and thermoelectric properties of TiNiSn. The work presented in Chapter 4 was motivated by the promising properties of the $TiNiCu_ySn$ series. Diffraction techniques and electron microscopy were used to investigate the microstructure of $MNiCu_{0.075}Sn$, $M_{0.5}M'_{0.5}NiCu_{0.075}Sn$ (M = Ti, Zr, Hf) and $Ti_{0.5}Zr_{0.25}Hf_{0.25}NiCu_ySn$ ($0 \leq y \leq 0.075$) compositions and to establish structure-properties relationships. As there is little known about the process that governs the formation of half-Heusler through solid-state reaction, in-situ neutron powder monitoring was applied to examine the process. Additionally, pair distribution analysis was performed to gain insight into the spatial distribution of excess Ni within half-Heusler matrix. The results of these experiments are

presented in Chapter 5 and 6, respectively. Finally, Chapter 7 provides the summary of main findings and possible further work in this area.

Chapter 2 - Experimental Method, Characterisations and Theory

2.1. Introduction

This Chapter provides information on how the half-Heusler materials discussed in this thesis were synthesised via solid-state reactions, consolidated using hot-pressing and prepared for structural characterisation and physical property measurements. Additionally, it introduces X-ray, high-resolution synchrotron X-ray and neutron powder diffraction and electron microscopy, which were the main techniques used to attain insight into a material's microstructure. Evaluation of thermoelectric properties included measuring the Seebeck coefficient, electrical resistivity, thermal conductivity and Hall coefficient.

2.2. Synthesis Methods

Solid-state reactions followed by hot pressing have been used to synthesise the half-Heusler materials within in this thesis. All compositions were prepared from a stoichiometric mixture of high purity (≥ 99.8%) elemental precursors that were obtained from either Alfa Aesar or Sigma-Aldrich.

2.2.1. Solid-State Reactions

Powders of elemental precursors were homogenised using an agate mortar and pestle and cold-pressed into 13 mm diameter pellets using a 10-ton press. The disks were wrapped in tantalum foil, sealed under vacuum in a quartz tube and annealed at high temperature (850 – 900 °C) for 24 hours, after which homogenisation was conducted and second annealing was carried out at 850 – 900 °C for 2 weeks. Prolonged annealing at elevated temperature enables diffusion of atoms, formation of target product and reaction completion. Specific details for each series are given in the relevant results chapters.

2.2.2. Densification – Hot Pressing

Sample porosity and low density can significantly affect the measured electrical and thermal conductivity. Particularly thermal conductivity can be dominated by porosity, which makes determination of the intrinsic materials property difficult. Hot pressing, where temperature and pressure are applied simultaneously, was used to improve the

density of the prepared materials. The hot-press used here was built in-house and is used to consolidate thermoelectric materials over the 500 ºC – 1100 ºC temperature range under an argon atmosphere. The schematic representation for the experimental setup is shown in Figure 2.1. The powdered sample was loaded into a graphite die and placed inside the induction coil (located in the main hot press chamber). The temperature was raised to 850 – 950 ºC, with the sample held at the target temperature for 20 minutes under 80 MPa of applied pressure. The samples consolidated under these conditions show 90 – 100% of the theoretical density (see Appendix A for details).

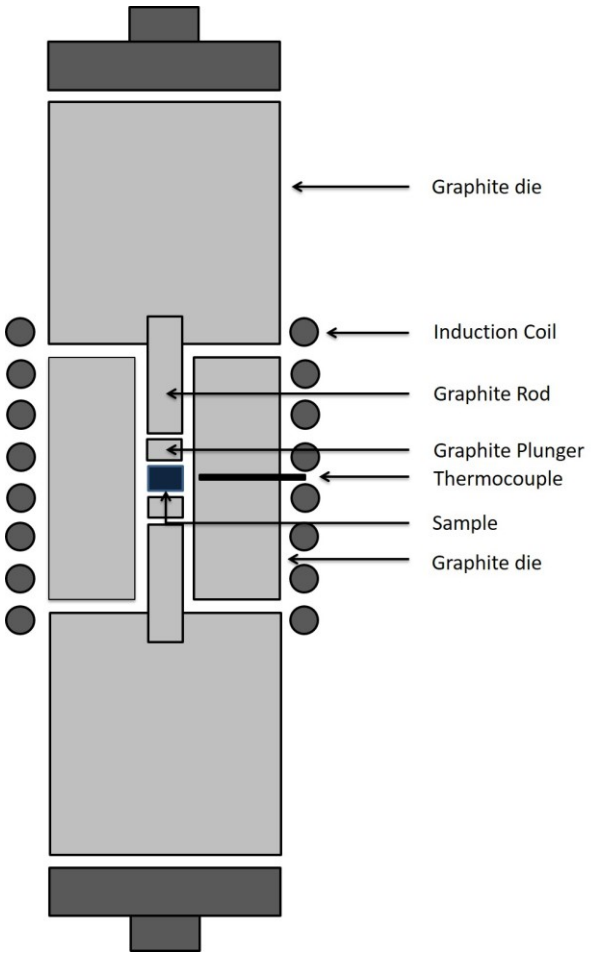

Figure 2.1. Schematic representation of the uniaxial hot press system used in this work.

2.3. Structure Determination

Knowledge of the material's structure on the atomic level is essential for understanding and predicting the physical properties of materials. Dislocations, inclusions and other imperfections can have a significant effect on the microstructure and can be responsible for property variations. Compositions investigated in this thesis were characterised using a combination of laboratory X-ray, high-resolution synchrotron X-ray and neutron

powder diffraction techniques. They provide information at the unit cell level and can help in determination of the microstructural properties. To characterise the microstructure further, selected half-Heusler samples were analysed using scanning and transmission electron microscopy. In this thesis section, each technique is considered with a summary of how it operates and what kind of information can be attained using it.

2.3.1. X-Ray Diffraction

2.3.1.1. Background and Theory

X-ray crystallography is the technique used since the early part of 20th century to determine the three-dimensional (3D) crystalline structure at the atomic level. In 1912, Max von Laue showed that atoms in a single crystal can be precisely observed, due to the periodicity of crystal lattice.[135] X-rays are electromagnetic radiation with wavelength of ~1 Å, which is located between γ-rays and the ultraviolet region. Monochromated X-rays that are used in the laboratory-based diffractometers are generated by accelerating a beam of electrons through a voltage of ~30 kV and striking it into a water-cooled metal target (e.g. copper). The incident electrons hit the metal surface and ionise some of the Cu, by expelling 1*s* (*K* shell) electrons. An electron in an outer orbital (2*p* – *L* shell or 3*p* – *M* shell) moves down to fill up the vacant 1*s* orbital, emitting X-ray radiation of a specific wavelength (2*p* → 1*s* transition: K_α = 1.5418 Å; 3*p* → 1*p* transition: K_β = 1.3922 Å). The desired wavelength (here K_α radiation) is selected using a sheet of Ni foil, which is effective in absorbing the Cu K_β radiation.

Any crystal structure is built of layers or planes of atoms that are stacked to form 3D array of atoms. The Bragg equation describes the diffraction in terms of X-rays that are scattered by sets of lattice planes. Each crystallographic plane acts as a semi-transparent mirror that reflects the incident radiation. It is characterised by the Miller indices (the index triplet *hkl*). Planes that are parallel have the same indices and are equally separated by the distance d_{hkl}. X-rays are reflected by lattice planes as illustrated in Figure 2.2. The reflected X-ray beams interfere with each other leading to constructive or destructive interference. A reflection is observable if constructive interference occurs, which is achieved when the path length difference (xyz) between the beams is an integer number of wavelengths (xyz = $n\lambda$). This is summarised by Equation (2.1), where θ is the Bragg incident angle, n is an integer and λ is the wavelength of the incident radiation.[24, 136, 137]

$$2d_{hkl} \sin\theta = n\lambda \qquad \text{Equation (2.1)}$$

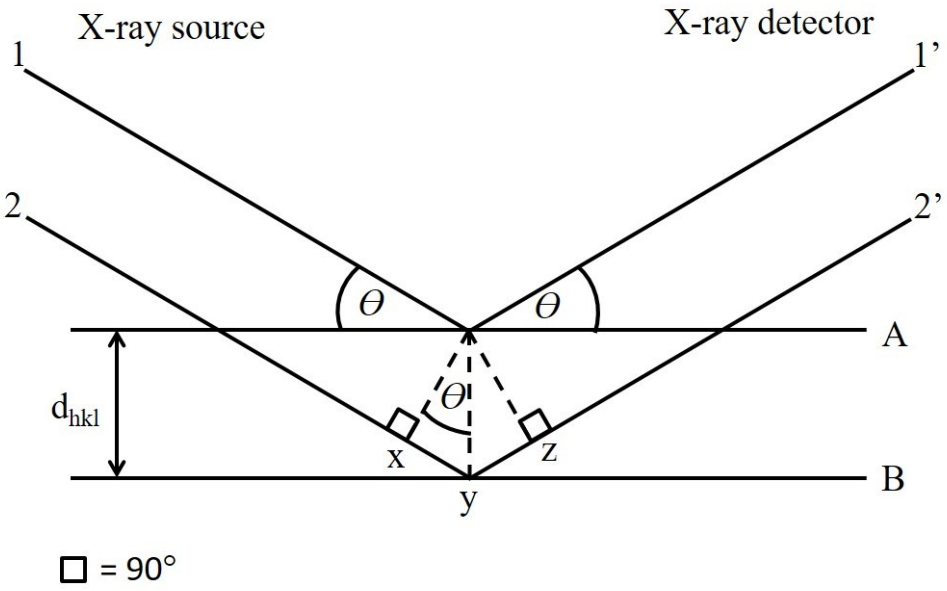

Figure 2.2. Geometrical illustration of the Bragg's law.

Each set of lattice planes within a crystalline structure produces a reflection at a given Bragg angle θ. Because θ and λ are known, the d-spacing for each (hkl) reflection can be determined through Bragg's law and used to calculate the unit cell parameters. As shown by Equation 2.2, the unit cell parameters for orthogonal crystals (i.e. $\alpha = \beta = \gamma = 90^{o}$) can be found:

$$\frac{1}{d_{hkl}^2} = \frac{h^2}{a^2} + \frac{k^2}{b^2} + \frac{l^2}{c^2} \qquad \text{Equation (2.2)}$$

In this relationship, the h, k and l are attained from an indexed diffraction pattern. Summarising, the positions of multiple Bragg reflections are used to evaluate the unit cell parameters.

Analysis of the diffracted peak intensity could provide valuable information about structural features such as atomic positions, bond lengths and angles. The electrons in atoms are almost exclusively responsible for the scattering of X-rays. To quantify the scattering intensity, the scattered amplitude of all the electrons in all the atoms in the crystal has to be added. The result is expressed as the atomic scattering factor (f), which is the ratio of the scattering amplitude by an atom divided by the amplitude scattered by a single electron. As the atomic scattering factor depends on the number of electrons, it is a unique quantity for each element. It increases with number of electrons in the atom (hence with the atomic number, Z). The scattering power of an atom (f_n), derived from

quantum mechanical calculations of electron density around an atom is approximated by the following relationship:

$$f_n = \sum_{n=1}^{4} a_n \exp\left[-b_n \left(\frac{\sin\theta}{\lambda}\right)^2\right] + c_n \qquad \text{Equation (2.3)}$$

where a_n, b_n and c_n are the Cromer-Mann coefficients, which vary for each atom or ion.[138] It is also found that due to the scattering of X-rays from different parts of the electron cloud, the path difference between scattered X-rays occurs and f_n varies as a function of $\sin\theta/\lambda$ (θ is the scattering angle). At zero scattering angle, all scattered rays are in phase (constructive interference) and f would be equal to Z. As the scattering angle increases, destructive interference increases and f falls below Z. This explains why the reflection intensities become increasingly weak at high angle.[138, 139]

To attain the total intensity of radiation that is scattered by a unit cell, a summation of the scattering from all atoms in the unit cell must be performed. Adding together the waves that were scattered from each set of (*hkl*) planes independently results in a quantity called the structure factor $F(hkl)$. The $F(hkl)$ accounts for the amplitude of radiation scattering from an atom in a reflective plane (*hkl*) and the phase difference of the scattered waves. The phase angle (ϕ) (measured in radians) describes the amount by which two scattered waves are out of step. The relative positions of two atoms in the unit cell and the directions along which the waves are superimposed impact the phase difference component. The directions are specified by the Bragg equation and are denoted by the *hkl* indices of planes involved in the scattering. Therefore, the phase angle of the wave scattered from an atom is expressed as:

$$\phi_n = 2\pi(hx_n + ky_n + lz_n) \qquad \text{Equation (2.4)}$$

where x_n, y_n and z_n are fractional coordinates of atom.[138, 139] The summation of the scattering from each atom in the unit cell that contains N atoms gives the final $F(hkl)$:

$$F(hkl) = \sum_{n=1}^{N} f_n \exp[2\pi i(hx_n + k_y n + lz_n)] \qquad \text{Equation (2.5)}$$

This equation can be re-written as:

$$F(hkl) = \sum_{n=1}^{N} f_n \cos 2\pi(hx_n + ky_n + lz_n) + i \sum_{n+1}^{N} f_n \sin 2\pi(hx_n + ky_n + lz_n) \qquad \text{Equation (2.6)}$$

where i is the square root of -1. The intensity of a given (hkl) reflection is equal to the modulus of $F(hkl)$ squared, as defined in Equation (2.7).[138]

$$I(hkl) = |F(hkl)|^2 \qquad \text{Equation (2.7)}$$

$$I(hkl) = \left\{\sum_{n=1}^{N} f_n \cos 2\pi(hx_n + ky_n + lz_n)\right\}^2 + \left\{i\sum_{n+1}^{N} f_n \sin 2\pi(hx_n + ky_n + lz_n)\right\}^2$$

The temperature factor is an important correction applied to intensity calculations. The atoms in crystalline solids are not stationary and vibrate, to an extent that depends on the temperature. Therefore, even at room temperature, atoms in any given (hkl) plane will vibrate, which may have a considerable effect upon the intensity of a diffracted beam. This will result in the smearing of the electron density and reduction of the atomic scattering factor (f_n). This leads to significantly reduced intensities. To account for this effect, the f_n factor is multiplied by a term containing an isotropic displacement parameter (U_{ISO}):

$$f_n' = f_n \exp\left[-8\pi^2 U_{ISO}\left(\frac{\sin\theta}{\lambda}\right)^2\right] \qquad \text{Equation (2.8)}$$

assuming an atom vibrates equally in all directions. The U_{ISO} measures the displacement of an atom about its average position and is equal to the square of the mean atomic displacement.[138, 140] Therefore, Equation 2.5 can be re-written as:

$$F(hkl) = \sum_{n=1}^{N} f_n \exp[-8\pi^2 U_{ISO}\left(\frac{\sin\theta}{\lambda}\right)^2] \times \exp[2\pi i(hx_n + k_y n + lz_n)] \qquad \text{Equation (2.9)}$$

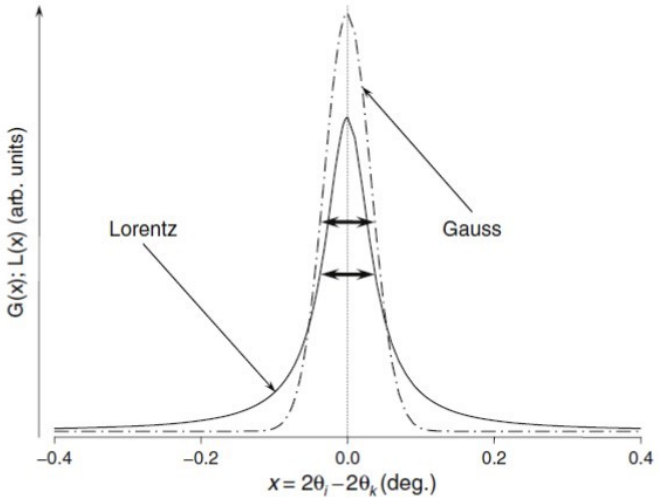

Figure 2.3. The representation of Gaussian (dash-dotted line) and Lorentzian (solid line) peak shape function. Thick horizontal arrows present full widths at half maximum.[141]

The shape of the Bragg reflections can provide valuable information about the disorder and defects within crystal structure. The four most common empirical peak-shape functions are: Gaussian, Lorentzian, Pseudo-Voigt and the Pearson-VII functions. The first two functions describe Gaussian and Lorentzian distributions of the peak's intensity. It is evident from Figure 2.3 that the Gaussian function has a rounded maximum and no tail at the base, while the Lorentzian function is characterised by a long tail on each side of the peak's base and sharp maximum. The shapes of collected Bragg peaks are usually best described using a mixture of these two functions. The Pseudo-Voigt function is a linear combination of a Gaussian and Lorentzian.[141]

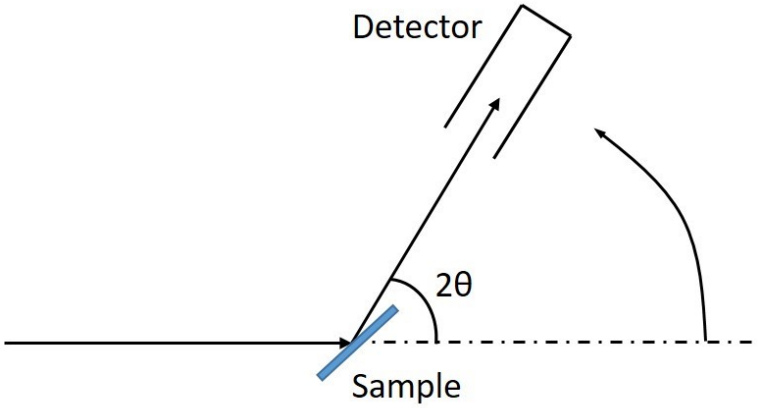

Figure 2.4. Principle of the X-ray powder diffraction experiment.

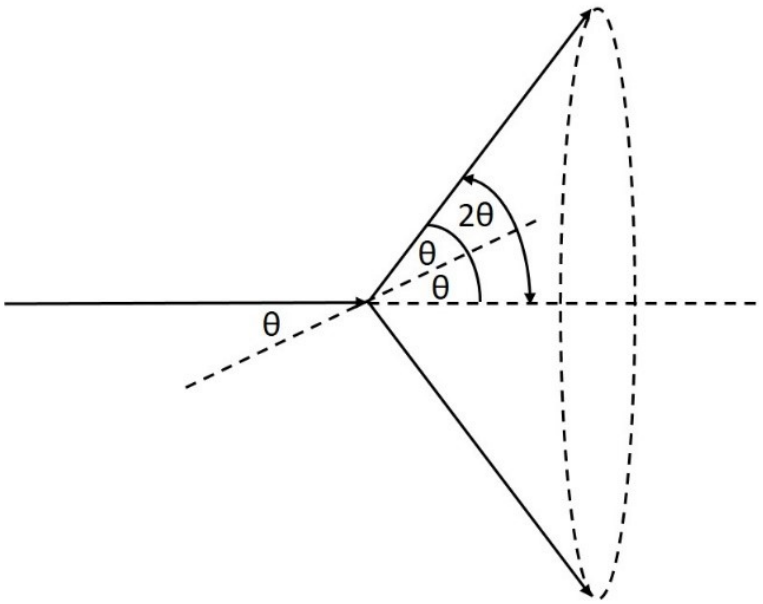

Figure 2.5. Cones of X-rays diffracted from a powdered sample.

2.3.1.2. Powder Diffraction

The synthesis of single crystals, which are sufficiently large to be studied using a conventional single-crystal experiment can be a difficult and challenging task. In X-ray powder diffraction, a large number of randomly orientated crystallites are exposed to the beam. Due to the random crystallites orientation, all *hkl* reflections are observable by scanning through 2θ. The powder diffraction experiment set up is shown in Figure 2.4. The monochromatic X-ray beam hits the powdered sample that is placed on a sample holder. The diffracted X-rays from the *hkl* planes are detected by a moveable detector. For every set of lattice planes, the diffracted radiation forms a cone with angle 2θ, producing a circle on the detectors (Figure 2.5). These are Debye-Scherrer cones. Each cone consists of a large number of closely spaced diffracted beams and corresponds to a set of *hkl* diffraction planes. The only requirement is that the planes are located at the Bragg angle θ to the incident beam.[24]

The intensities of the powder diffraction pattern are recorded as a function of angle (θ). The Bragg angle and corresponding intensity are attained for each reflection. The disadvantage of polycrystalline diffraction is that the full 3D diffraction pattern is compressed into a one-dimensional (1D) pattern (with θ as the only variable), resulting in the overlap of reflections. The determination of exact peak positions and relative intensity contributions can be difficult.

Powder diffractions is often used as a 'fingerprint' techniques to qualitatively identify crystalline phases or compounds. Each crystalline phase that is present in bulk samples will give characteristic set of reflections in a diffraction pattern. For fast investigation, identified peaks can be compared to a database of known patterns.

2.3.1.3. Bruker D8 Advance Diffractometer

Laboratory X-ray powder diffraction data were collected using a Bruker D8 Advance diffractometer. This instrument is fitted with a Bruker Lynx Eye linear detector and uses a monochromated Cu $K_{\alpha 1}$ radiation (λ = 1.54056 Å). A small amount of finely grounded powder was sprinkled onto a glass slide, adhered using propanol and placed into the polymethacrylate sample holder. 8 hour scans were collected over the range $10^{o} \leq 2\theta \leq 120^{o}$ (stepsize = 0.009215°/counting time = 2.8 s/step). To check for phase formation and sample purity, the collected data was compared to the diffraction patterns in the International Centre for Diffraction Data (ICDD) and The Inorganic Crystal Structure

Database (ICSD)[142] databases, using the EVA software package. The collected scans were used for Rietveld refinements as discussed in section 2.3.4.1.

2.3.2. High Resolution Synchrotron X-ray Diffraction

2.3.2.1. Background and Theory

Synchrotron X-ray sources are large-scale national and international facilities such as the Diamond Light Source at the Harwell Science and Innovation Campus in Oxfordshire, UK. Synchrotron radiation is produced through the acceleration of electrons or positrons to a speed close to that of light. The fast-moving particles are constrained by bending magnets to move in a circle in ultra-high vacuum tubes or storage rings. The radiation is formed tangentially to the electron path every time the particle beam is forced to change direction on passing through magnetic field. The schematic representation of a storage ring, which is typically hundreds of meters in diameter is shown in Figure 2.6.[24, 143]

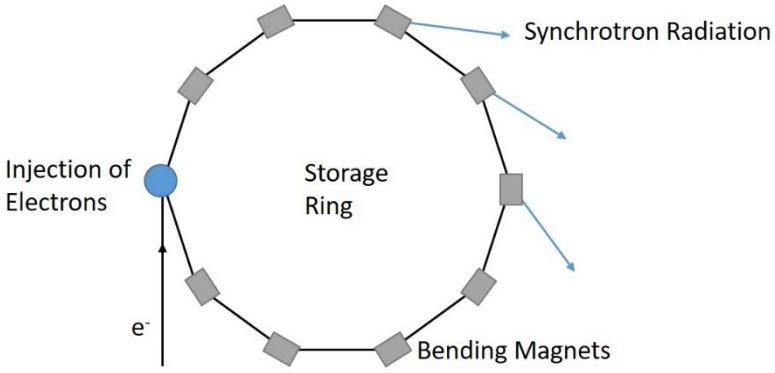

Figure 2.6. Schematic diagram presenting the operation of a synchrotron storage ring.

Highly collimated radiation is directed off to various diffraction and spectroscopic instruments. This high intensity beam can be tuned to specific energy (from infrared to hard X-rays). For crystallography experiments, a monochromator is used to select the desired wavelength. Synchrotron X-ray radiation has several advantages compared to a conventional, laboratory-based source. Its high intensity allows for quick collection of high quality diffraction patterns, even from very small crystals or samples that normally give relatively weak diffraction. Rapid collection time enables the study of sensitive and chemically unstable compounds. It is also very useful during time-resolved studies such as phase transitions and the monitoring of solid-state reactions.[24, 143]

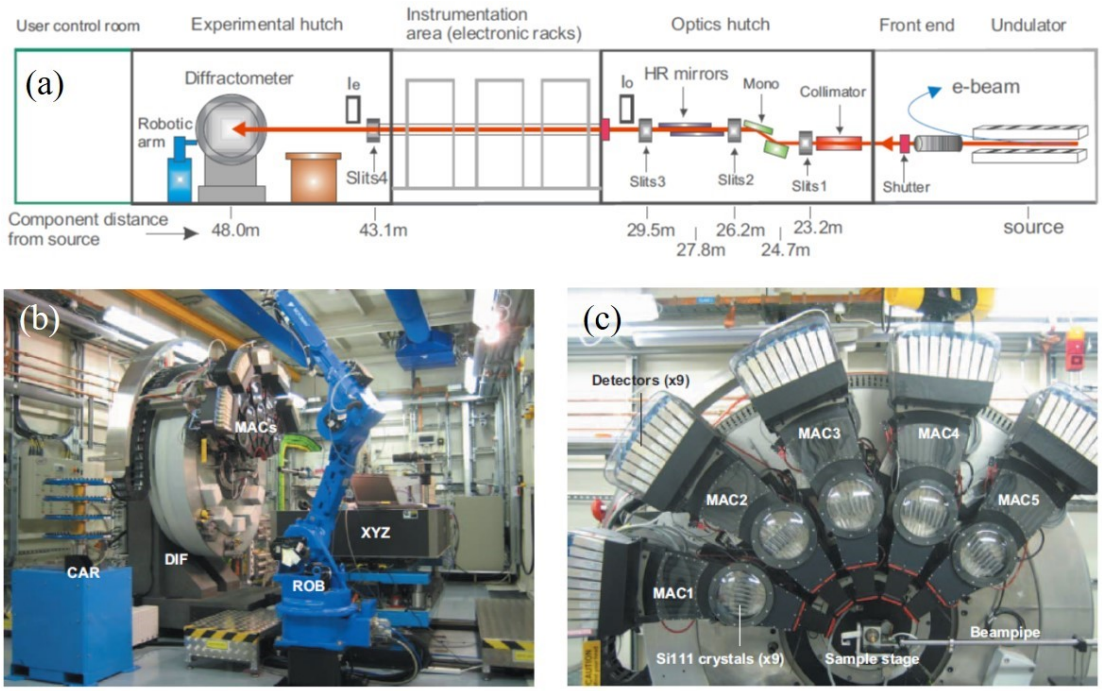

Figure 2.7. (a) Schematic representation of Beamline I11 highlighting the main components. **(b)** I11 experimental hutch presenting the heavy-duty diffractometer (DIF), MAC-detectors (MACs), robotic arm (ROB), carousel that can hold 200 specimens (CAR), heavy duty table (XYZ). **(c)** 5 arms of MAC detectors; each with 9 Si (111) analysing crystals and 9 detectors.[144]

2.3.2.2. I11 Beamline

Analysis of the half-Heusler compounds prepared for this thesis was done using the synchrotron X-ray powder diffraction beamline (I11) at the Diamond Light Source. The schematic layout and various components of the I11 beamline with approximate distances from the X-ray source are shown in Figure 2.7a. The instrument is designed to produce X-rays ranging from 5 to 30 keV (0.4 – 2.1 Å). For ambient measurements, a capillary is picked from the carousel and placed by the industrial robotic arm at the centre of a diffractometer (Figure 2.7b). The I11 multi-MAC arrangement is illustrated in Figure 2.7c. Five identical MAC-arms contains nine Si (111) analysing crystals, with each having its own detector. The crystal analyser eliminates shifts in the Bragg peak positions and improves pattern resolution. The MAC-arms (mounted at 30º intervals) move over the instrument's 2θ-circle. For fast collection time, each analyser-detector stage scans through a small area of the total diffraction pattern. Nine individual patterns are collected by each MAC-arm. These are corrected for the crystal offset and summed to give a single

pattern for each stage. The final pattern is constructed by combining scans collected by each of the five MAC-arms.[144, 145]

A small amount of finely ground sample was mounted on the outside of glass capillary using a thin layer of lubricant. The prepared capillaries were loaded into robotic carousel. High-resolution diffraction patterns (λ = 0.825921 Å, step size 0.002) were collected for samples prior to hot-pressing (collection time = 1800 s) and after hot-pressing (collection time = 3600 s). Details of the investigated samples are given in the relevant results chapters.

2.3.3. Neutron Powder Diffraction

Neutron powder diffraction is another technique that can provide information on the crystal structure of material. One of the differences between X-ray and neutron diffraction is the scattering mechanism. With neutrons, the rays are scattered from the atomic nuclei rather than the electron cloud, which offers several advantages. Like with X-ray diffraction patterns, peak positions and intensities are used to extract information on the lattice parameters and site occupancies, respectively.

2.3.3.1. Background and Theory

Nuclear reactors and spallation sources are the two main types of neutron sources. The Institute Laue-Langevin (ILL) in Grenoble is an example of a high flux reactor, which utilizes a self-sustaining chain reaction. Here, thermal neutrons cause the fission of ^{235}U nuclei, which is accompanied by the release of high-energy (MeV) neutrons. These neutrons are deaccelerated to the appropriate thermal wavelength range by collisions in a moderator. The thermal neutrons cause further fission, allowing continuous supply.[146] Nuclear reactors usually offer a constant wavelength source. By scanning through the Bragg angle θ (defined in Bragg's law – Equation 2.1), the d-spacing is calculated. This technique will not be discussed any further as it was not used for experiments detailed in this thesis.

ISIS at the Rutherford Appleton Laboratory in the UK (adjacent to Diamond) is an example of a spallation neutron source. Here, H^+ ions are accelerated by proton synchrotron to create a proton beam of high energy (typically 500 – 800 MeV), which is bombarded on to a heavy metal target (tungsten). Upon impact, neutrons are ejected from

the nuclei of tungsten in a process called spallation. The protons are grouped into pulses allowing pulses of neutrons to be delivered. Similar to the nuclear reactor source, the resulting neutrons have to be moderated to the required wavelength before travelling to various instruments. Thermal neutrons are selected as they have wavelength similar to the inter-atomic spacing in crystals. The neutron's wavelength can be determined by the measurement of the time ('time-of-flight' – TOF) that is required by neutrons to travel between the source and detector, as short wavelength neutrons travel faster compared to those with longer wavelength.[143, 146]

Neutrons scattered by the sample are recorded as a function of the TOF. The wavelength (λ) is related to TOF (t) by Equation (2.10):

$$\lambda = \frac{ht}{mL} \qquad \text{Equation (2.10)}$$

where h is Planck's constant, m is the mass of neutron and L (in metres) is the neutron flight path. The d-spacing (d_{hkl}) for a given set of diffracting planes (hkl) can be calculated by substituting Equation (2.10) into Bragg's equation (Equation 2.1) and rearranging:

$$d_{hkl} = \frac{ht}{2mL \sin\theta} \qquad \text{Equation (2.11)}$$

The diffraction of neutrons can be described in a similar way to the X-ray diffraction. The main difference is that X-rays are scattered by the electron cloud, resulting in scattering that is linearly proportional to the atomic number of element. Therefore, heavy atoms (with many electrons) can be easily localised, while light elements are difficult to see (due to their low electron density). In contrast, neutrons are scattered by atomic nuclei and the scattering power (also called scattering length) varies randomly by element and isotope. It is independent of the atomic number, therefore even light atoms (e.g. hydrogen) and isotopes of the same element (e.g. hydrogen and deuterium) can be identified. The neutron scattering length of atoms used in this thesis are shown in Table 2.1.[147] Another advantage of neutrons is that the scattering power is independent of $\sin\theta/\lambda$ (unlike for X-ray scattering), therefore the intensity of diffraction peaks does not decrease with the increasing Bragg angle. The final advantage of neutrons, is that they possess spin of ½ and interact with unpaired electrons of an element. As a result, the magnetic scattering is recorded enabling investigation of material magnetic structure. The intensity of magnetic peaks decreases with increasing Bragg angle because, similarly to X-rays the interaction is with the electrons in the atom. The disadvantage of neutrons is weak intensity of beam compared with rather strong X-ray source. This can be overcome by measurement of

larger crystals or greater quantities of finely ground sample. On the other hand, neutrons are more penetrating than X-rays, offering experiments in which the analysed composition is placed in container which is not penetrable by X-rays.[143, 146]

Table 2.1. Coherent scattering length of elements that were used in this thesis.[147]

Element	Coherent Scattering Length (fm)
Ti	-3.4
Zr	7.2
Hf	7.7
Ni	10.3
Cu	7.7
Sn	6.2

2.3.3.2. POLARIS

The POLARIS instrument at ISIS is a medium resolution powder diffractometer. This instrument was used to analyse the crystal structure of the half-Heusler alloys prepared for this thesis. As shown in Figure 2.8, the diffracted neutrons are recorded by 6 banks of sensitive detectors (total of 40 detector modules) that are arranged around the sample, offering wide detector coverage. Each bank has a different purpose – e.g. the backscattering bank (bank 5) offers the best resolution and is frequently used to solve complex or multiphase samples that have overlapping peaks, while detectors set at 2θ = 90º are extremely useful for samples within complex sample environments.

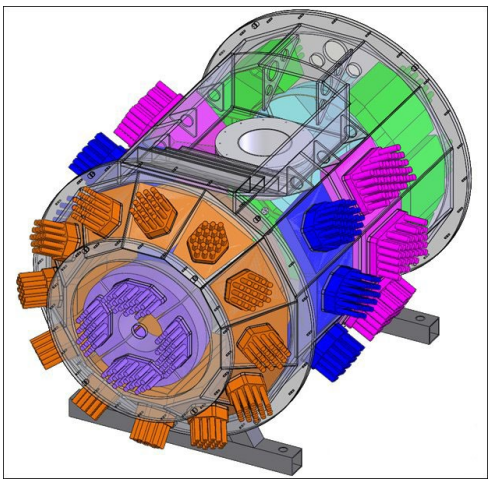

Figure 2.8. Schematic representation of POLARIS powder diffractometer at ISIS with the 5 banks presented in different colours.[148]

1-2 g of finely ground samples were loaded into small (8 mm in diameter) Vanadium cans. Vanadium is used during neutron diffraction experiments as it has low coherent neutron scattering length[147] leading to negligible Bragg reflections from the sample container. As the measurements were carried out at ambient conditions, samples were loaded into the sample changer. The collection current was 200 – 400 μA, which can be achieved in 2-3 hours. The Mantid software[149] was used for data reduction and background/instrumental subtractions.

2.3.3.3. GEM

The in-situ neutron powder diffraction experiment used to investigate the formation of selected half-Heusler samples was carried out using the GEM diffractometer at the ISIS facility. The GEneral Materials diffractometer (GEM) offers excellent detector array, which covers a wide range in scattering angles (2θ = 1.1º-169.3º). As it focuses on the intensity and resolution of collected data, a wide variety of studies of ordered and disordered materials can be performed. As shown in Figure 2.9, the sample is situated within an evacuated sample tank, with 8 detector banks located around the sample tank.[150]

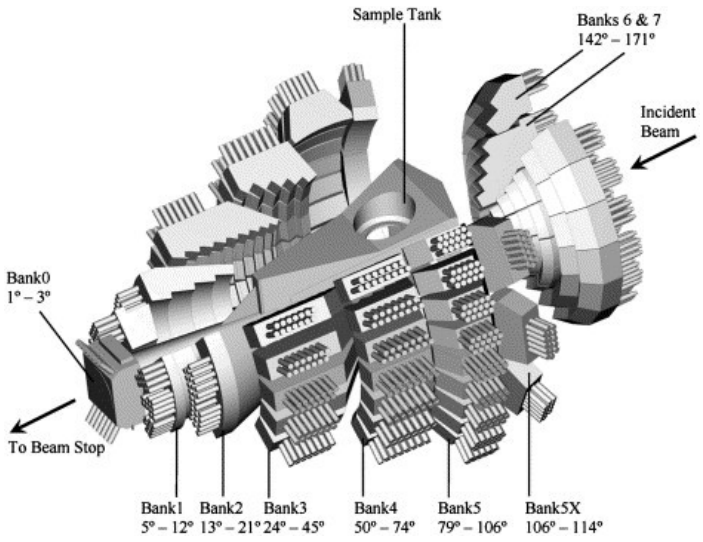

Figure 2.9. Schematic representation of GEM diffractometer at ISIS.[150]

4.5 g of elemental precursors were thoroughly mixed using an agate mortar and pestle and cold-pressed using a 10-ton press into 13 mm diameter pellets, that were then cut into smaller pieces and stacked on top of each other. To avoid oxidation and reagent

evaporation, each sample was tightly wrapped in vanadium foil and placed in the ~10 mm diameter vanadium can. The samples were heated in a high-vacuum furnace up to 900 ºC with a ramp rate of 3 ºC/min. Data were continuously collected in 10 minutes intervals. At 900 ºC each sample was held for a few hours. Data continued to be collected during both, annealing and cooling down, using the same collection procedure. The Mantid software[149] was used for data reduction and background/instrumental subtractions.

2.3.4. Rietveld Refinement

The Rietveld refinement method is a valuable technique used to refine the crystal structure of powdered materials.[151-153] It is a least squares refinement method where a collected diffraction pattern is compared with a profile that is calculated. The calculated profile can be adjusted through the refinement of structural parameters such as dimensions of unit cell, atomic coordinates and displacement parameters. The aim of the Rietveld refinement is to minimise the residual, S_y, as defined in Equation 2.12:

$$S_y = \sum_i w_i \big(y_i(obs) - y_i(calc)\big)^2$$

$$w_i = \frac{1}{y_i(obs)} \qquad \text{Equation (2.12)}$$

where y_i(obs) is the intensity observed at a given 2θ angle and y_i(calc) refers to calculated intensity at the ith step of the pattern. The sum i is over all data points. In other words, the difference between the observed and calculated intensities should be minimised.[154, 155]

2.3.4.1. Observed Intensities

A powder diffraction pattern is a collection of individual reflection profiles. Each reflection profile has a peak height, width and position. The integrated area is proportional to Bragg intensity (I_{hkl}), which is proportional to the square of absolute value of the structure factor, $|F(hkl)|^2$. The structure factor was discussed in section 2.3.1.1.

2.3.4.2. Calculated Intensities

The calculated intensities are evaluated by summing the contributions from the background and neighbouring Bragg reflections. This is represented by Equation 2.13:

$$y_i(calc) = s\sum_{hkl} L_{hkl}|F(hkl)|^2\phi(2\theta_i - 2\theta_{hkl})P_{hkl}A + y_i(back) \quad \text{Equation (2.13)}$$

where S is the scale factor, L_{hkl} contains Lorentz factor, polarization and multiplicity factors, $F(hkl)$ is the structure factor defined by Equation 2.4, $\phi(2\theta_i - 2\theta_{hkl})$ is the reflection profile function, P_{hkl} is the preferred orientation function, A is an absorption factor and y_i(back) is the background. To minimise S_y (Equation 2.12), all factors defined in the equation above can be adjusted and refined. However, the relationship between the intensities and the adjustable parameters is non-linear. Therefore, a good starting model is essential. A least-squares procedure which uses a poor model will either diverge or lead to a false global minimum.

2.3.4.3. The Reflection-Profile Function, ϕ

The width of the diffraction peak, known as "full width at half-maximum" (FWHM) is 2θ dependent. The shape of low-resolution, constant wavelength peaks at a neutron diffractometer can be usually described using a Gaussian function. Equation 2.14 describes the typical parameterisation of the angular dependence of the FWHM for a Gaussian function:

$$(\text{FWHM})^2 = \text{U}\tan^2\theta + \text{V}\tan\theta + \text{W} \quad \text{Equation (2.14)}$$

where θ is the Bragg angle, U, V and W are the refinable parameters. As discussed in section 2.3.1.1, the Pseudo-Voigt function may be more suitable for higher resolution measurements. The variation of the Lorentzian width with Bragg angle is typically expressed as in Equation 2.15:

$$FWHM = \frac{X}{\cos\theta} + Y\tan\theta \quad \text{Equation (2.15)}$$

Here, X (particle size broadening) and Y (micro-strain broadening) can be refined.

2.3.4.4. Preferred Orientation Function, P_{hkl}

The theory of powder diffraction assumes that an infinite amount of randomly orientated crystallites is present in the sample. Preferred orientation occurs when crystallites in a powder are orientated along certain axis, or set of axes. This can lead to increased intensity of all specific (*hkl*) reflections (eg. *0k0*). To address the particle's non-randomness, the preferred orientation factor (P_{hkl}) can be introduced. This may be difficult or even impossible to correct when preferred orientation is severe. This can be

avoided through the careful preparation of powdered specimen to physically increase particle's random distribution.

2.3.4.5. Absorption Factor, A

Absorption is observed when the incident radiation is absorbed by the specimen instead of being scattered. The absorption effect depends on the instrument geometry, focusing method, elements present and sample thickness. The absorption factor (A) can be used to model this effect. It is usually a constant value for a given geometry.

2.3.4.6. Background Intensity, $y_i(back)$

Each diffraction pattern has a different level of background that must be considered. For a glass sample holder, an amorphous hump may be observed in the background (especially at small angle) if the sample is too small or too thin. The background can be evaluated using three methods. The first one is to apply a linear interpolation between peaks. The second is to use supplied tables with background intensities. The final method is to apply a specific background function. The third approach was used during the investigation of samples presented in this thesis. A linear interpolation function was applied during the refinement to laboratory X-ray and neutron powder diffraction patterns, while the Chebyshev polynomial was used during the investigation of high-resolution synchrotron X-ray diffraction data.

2.3.4.7. Quality of Rietveld Refinement

The quality of the Rietveld refinement can be monitored using the profile residual or reliability factor (R_p), the weighted profile residual (R_{wp}), the expected profile residual (R_{exp}) and the goodness of fit (χ^2); described by Equations 2.16 – 2.19.

$$R_p = \frac{\sum_{i=1}^{n} |y_i(obs) - y_i(calc)|}{\sum_{i=1}^{n} y_i(obs)} \times 100\% \qquad \text{Equation (2.16)}$$

$$R_{wp} = \left[\frac{\sum_{i=1}^{n} w_i(y_i(obs) - y_i(calc))^2}{\sum_{i=1}^{n} w_i(y_i(obs))^2}\right]^{1/2} \times 100\% \qquad \text{Equation (2.17)}$$

$$R_{exp} = \left[\frac{n-p}{\sum_{i=1}^{n} w_i(y_i(obs))^2}\right]^{1/2} \times 100\% \qquad \text{Equation (2.18)}$$

$$\chi^2 = \frac{\sum_{i=1}^{n} w_i(y_i(obs) - y_i(calc))^2}{n-p} = \left[\frac{R_{wp}}{R_{exp}}\right]^2 \qquad \text{Equation (2.19)}$$

where n is the total number of points measured in the powder diffraction pattern, y_i(obs) is the intensity observed at ith data point, y_i(calc) is the calculated intensity of ith point, w_i is the weight of ith data point, p is the number of free least square parameters. A simple analysis indicates that better fit leads to lower values of all residuals. Visual inspection of the observed and calculated powder patterns is a complementary technique used to ensure the quality of Rietveld refinement. It also includes representation of tick marks, which indicate the calculated positions of Bragg reflections.[141]

2.3.5. Total Scattering and Pair Distribution Function (PDF)

Total scattering is a technique used to study disordered crystalline, amorphous and nanocrystalline materials. The traditional crystallographic structure determination using e.g. Rietveld method, is based on the analysis of Bragg reflections leading to the average structure of materials. However, for many materials, the interesting properties are due to defects and deviations from the average structure. The study of diffuse scattering intensities can provide valuable information about atomic structure and local deviations. The diffuse scattering component appears in-between the Bragg reflections, with intensity often hard to see and measure. It slowly varies with Q (magnitude of the scattering vector) and forms part of the continuous background. As discussed in section 2.3.4.6, background is usually discarded during conventional analysis. The total-scattering technique treats both the Bragg and the diffuse component simultaneously.[156]

The PDF data should be collected over as wide Q-range (30 – 50 Å^{-1}) as possible with good instrumental resolution. Q is the momentum transfer and can be expressed as $Q = 4\pi\sin(\theta)/\lambda$. The scattering from crystals does not become flat until very high Q values are reached, as local structures may be extremely well defined. Measurements performed over a small Q-range result in low real-space resolution, that often may be sufficient in studies of glasses and liquids. Instruments at spallation neutron sources (eg. GEM, POLARIS, NIMROD at ISIS) and X-ray synchrotron sources provide high quality total-scattering data to large Q values. The main advantage of neutrons is no decreasing atomic form factor that reduces the intensity of coherent scattering at high-Q.[156, 157]

The collected data are corrected for secondary effects such as absorption, background scattering, multiple scattering within the sample or incoherent scattering. For neutron

diffraction, scattering from the vanadium can is also removed. Carefully normalised data gives the experimental total scattering structure factor $F(Q)$ and the total radial distribution function $G(r)$,[158] which are related by the following Fourier transforms:

$$F(Q) = \rho_0 \int_0^\infty 4\pi r^2 G(r) \frac{\sin Qr}{Qr} dr \qquad \text{Equation (2.20)}$$

$$G(r) = \frac{1}{(2\pi)^3 \rho_0} \int_0^\infty 4\pi Q^2 F(Q) \frac{\sin Qr}{Qr} dQ \qquad \text{Equation (2.21)}$$

where $\rho_0 = N/V$ is the average number density (in atoms Å^{-3}). The function $G(r)$ is also called the pair distribution function (PDF) and these terms are used interchangeably. The PDF analysis, gives the probability of finding an atom at a given distance from another atom.[159] The $G(r)$ is a sum of the partial radial distribution functions $g_{ij}(r)$:

$$G(r) = \sum_{i,j=1}^{n} c_i c_j \bar{b_i} \bar{b_j} [g_{ij}(r) - 1] \qquad \text{Equation (2.22)}$$

$$g_{ij}(r) = \frac{n_{ij}(r)}{4\pi r^2 dr \rho_j} \qquad \text{Equation (2.23)}$$

where i and j represent atoms, n is the total number of distinct chemical species, c_i and c_j are concentrations of species, $\bar{b_i}$ and $\bar{b_j}$ are the neutron coherent scattering length. The $\rho_j = c_j\rho_0$ and $n_{ij}(r)$ is the number of atoms type j within a distance $r + dr$ of an atom type i. The $G(r)$ is then related to the differential correlation function $D(r)$ by:

$$D(r) = 4\pi r \rho_0 G(r) \qquad \text{Equation (2.24)}$$

$D(r)$ provides a more balanced presentation of the information in the sharp peaks at low-r region and the broader features over the intermediate r-range.[160]

The reverse Monte Carlo (RMC) method is a procedure used to analyse PDF data. In this big-box method, a large number of atoms are placed in a box and moved randomly, one at a time. After each move, calculated structural functions are compared with the experimental Bragg pattern, $G(r)$ and $F(Q)$. If improvement is observed, the move is accepted. If the fit is worse, the move is accepted but with a reduced probability. Atoms move around the box until good agreement between calculated and experimental data is achieved.[161] The investigated box must be sufficiently large, so it reflects well the local structural correlations (evident in the PDF), while fitting the average structure information contained in the Bragg component.[162]

2.3.6. Crystallography Software

2.3.6.1. GSAS Software

The Rietveld refinements of the laboratory X-ray and neutron powder diffraction data were performed using GSAS software with its user interface, EXPGUI.[163, 164] GSAS (the General Structure Analysis System) was designed by Allen C. Larson and Robert B. Von Dreele to process and analyse both single crystal and powder diffraction data. It can handle multiple sets of data. Moreover, powder diffraction data containing mixture of phases can be analysed, resulting in refined structural parameters for each phase.

2.3.6.2. TOPAS Academic Software (Version 6)

TOPAS is the analysis program written by Alan Coelho for the analysis of powder diffraction data.[165] It allows for analysis of constant wavelength and time-of-flight X-ray and neutron data using Rietveld or Pawley fitting. The academic version of TOPAS runs by editing text in input file, which can be done using jEdit. This program was used during Rietveld refinements of the synchrotron X-ray diffraction data.

2.3.6.3. RMCProfile

The RMC is implemented in the RMCProfile software.[161, 166] It is used to determine the local structure of crystalline materials as well as to analyse the disordered systems. It allows simultaneous fit to many data types (e.g. neutron and X-ray total scattering, Bragg profiles, single crystal diffuse scattering). A variety of constraints is used to ensure atomic models, which are consistent with all available data. The quality of the refinement is defined by the χ^2 value:

$$\chi^2 = \sum_j (y_j^{exp} - y_j^{calc})/\sigma_j^2 \qquad \text{Equation (2.25)}$$

where j indicates a data point, y_j^{exp} and y_j^{calc} are the experimental value and the value calculated from the refined box, respectively, σ_j is the weighting factor for an individual data set. The χ^2_{RMC} parameter consists of χ^2 values from different data sets – F(Q), G(r), Bragg and the penalties. Random translations and swaps are accepted when lower χ^2_{RMC} are observed. The process is repeated until no further change in the fit's quality is observed and the final 3D configuration fits all experimental datasets. Fitting to the Bragg profile provides information on long-range average structure, while medium- and short-range ordering is attained by modelling of PDF.[159]

2.3.7. Electron Microscopy

2.3.7.1. Background and Theory

Electron microscopy provides several tools that can be used for the characterisation of materials. In this technique, a specimen's surface is bombarded with focused, high energy electrons. Similar to X-ray and neutron diffraction, the electron beam interacts with atoms in the sample, resulting in a wide range of signals, which are collected and analysed to attain structural and chemical information. The results include electron diffraction, backscattered electron diffraction, electron energy loss spectroscopy, energy dispersive X-ray spectroscopy. A schematic is shown in Figure 2.10. These methods can be employed to gain information on the grain orientation, local variation in the atomic structure such as defects or vacancies, local displacements and chemical compositions from micro- to atomic scale level.[167]

In electron microscopy, a beam of electrons is typically produced from a tungsten filament and accelerated by applying a potential difference (V). As shown in Equation 2.26, the electron wavelength is related to the applied voltage.

$$\lambda = \frac{h}{\sqrt{2meV}} \qquad \text{Equation (2.26)}$$

where h is the Planck's constant, m and e are mass and charge of the electron, V is the applied voltage. The wavelength of the electrons is smaller than typical X-ray wavelengths (e.g. $\lambda \approx 0.09$ Å at $V = 20$ kV), resulting in smaller Bragg angles and narrow diffraction cones. To use electrons for image formation, the electron beam must be focused, which is achieved by applying electrostatic or magnetic field. The images can be recorded in either bright or dark field. In dark field imaging, the diffracted beams form the image, which appears bright on a dark background. In bright field imaging, the transmitted electrons form the image, which appears dark on a bright background.[24]

2.3.7.2. Transmission Electron Microscopy and Scanning Transmission Electron Microscopy

In transmission electron microscopy (TEM), electrons penetrate a thin sample (thinner than ~0.2 μm) with transmitted electrons being detected. In this high-resolution technique, ultrafine details of material microstructure (smaller than 0.1 μm) can be distinguished. Sample preparation is an important step in TEM analysis. The sample must be very thin to avoid the absorption of incident electron beam. Electrolytic thinning, and

ion milling are examples of thinning procedures. To attain high-quality TEM images, there must be enough brightness a difference between adjacent areas. The TEM contrast is generated by the difference in the number of electrons being scattered away from the transmitted beam. Mass-density contrast (from amorphous specimens) and diffraction contrast (from crystalline specimens) are two mechanisms by which electron scattering created images.[168, 169]

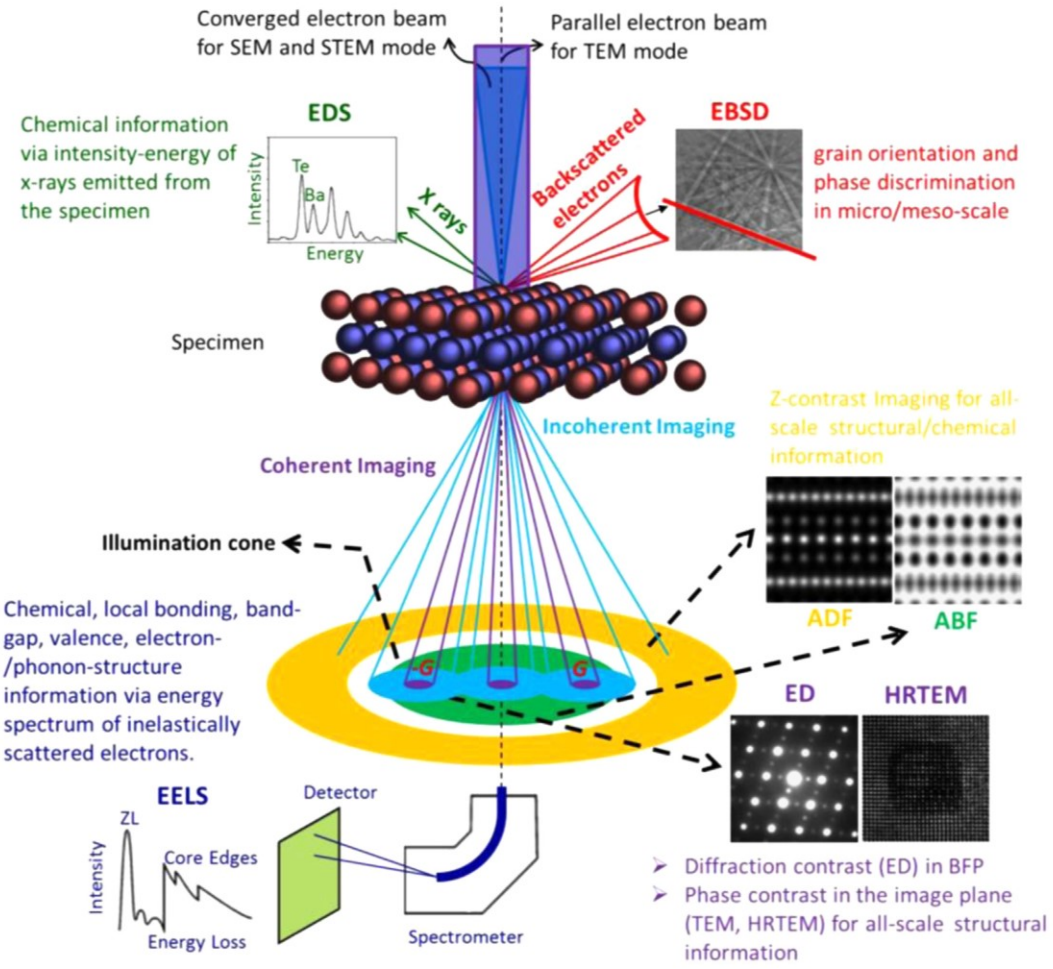

Figure 2.10. Interaction of electrons with specimen and scanning transmission electron microscopy. EDS – energy dispersive X-ray spectroscopy, EELS – electron energy loss spectroscopy, ED – electron diffraction, EBSD – electron back-scattered diffraction, HRTEM – high-resolution transmission electron microscopy, ABF – angular bright field, ADF – annular dark field.[167]

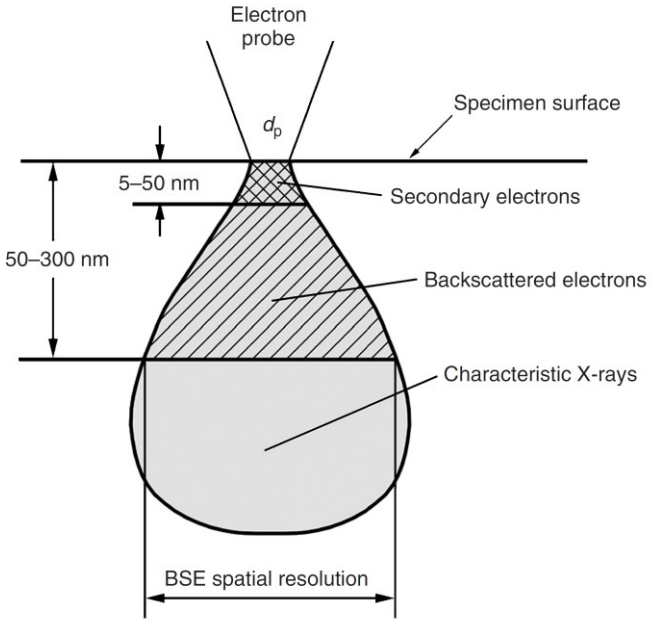

Figure 2.11. The interaction zone of backscattered electrons and secondary electrons, below a samples surface.[169]

2.3.7.3. Scanning Electron Microscopy

In scanning electron microscopy (SEM), a focused electron beam scans over the surface of material with high resolution and high depth of field. Due to its large depth of field, the 3D image is attained. The SEM technique is easier to operate, compared to TEM. Sample preparation involves surface polishing and, if necessary, thin metallic coating that prevents the charge build-up.[24] There are two electron signals collected by a detector: backscattered electrons (BSE) and secondary electrons (SE). The BSEs are incident electrons scattered by atomic nuclei in the material. The BSEs yield compositional contrast images. The SEs are ejected from atoms in the specimen. They are used for surface topographic images.[169]

As shown in Figure 2.11, the BSEs and SEs escape from different parts of interaction zones in the specimen. The SEs have low energy (several eV), therefore they escape from a depth of 5 – 50 nm (near the specimen surface). In contrast, the energy of BSEs is much higher (close to that of incident electrons), enabling their escape from a significantly deeper region of interaction zone (50 – 300 nm). The SE image has a better spatial resolution and is a topographic image of the material, while the BSE image provides very useful compositional contrast. The size of the interaction zone or interaction volume (usually described as pear-shaped) increases with the energy of electron beam (E_0).

Electrons with low incident energy require less inelastic collisions to bring them to rest. The interaction zone depends also on the atomic number *Z*. Its volume decreases with increasing *Z*, as the density of solid materials tends to increase with the atomic number. Summarising, the interaction zone gets small at low incident energy and for materials with higher atomic number (see Figure 2.12).[168, 169]

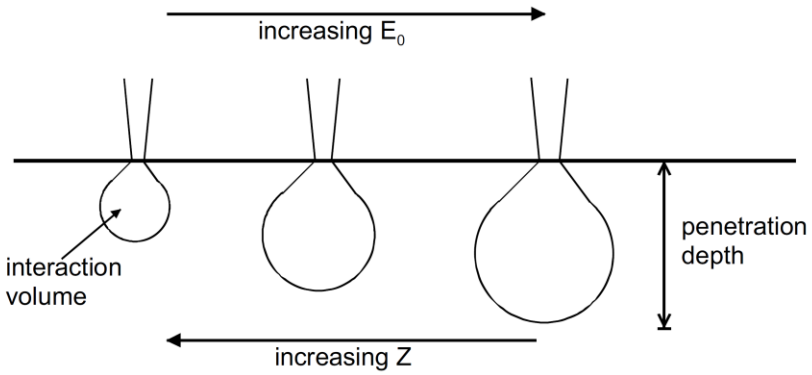

Figure 2.12. Dependence of the interaction zone and penetration depth with incident energy E_0 and atomic number *Z* of the incident electrons.[168]

2.3.7.4. Energy Dispersive X-ray

In energy dispersive X-ray (EDX) spectroscopy, the energy of X-rays that are emitted from the interaction zone (see Figure 2.10) is measured and used to determine the chemical elements present. SEM and TEM are equipped with EDX that uses the incident electron beam to promote the emission of characteristic X-rays. As discussed in Section 2.3.1.1, X-rays are produced when a core electron is emitted from its original position in an atom and the vacancy is refilled by an outer shell electron. The energy of this X-ray beam depends on the energy difference between the core and valence shells and is element specific. Therefore we can identify a chemical element from the characteristic X-rays that it emits.[169] The EDX in SEM and TEM is used to generate maps of elemental distribution in a sample.

2.3.7.5. Experimental Set-Up

TEM: TEM and EDX analysis of selected $TiNiCu_ySn$ (y = 0.10 and 0.20; before and after hot-pressing) half-Heusler samples was performed at the University of Glasgow by Dr Donald A. MacLaren and Dr John D. Halpin, on a JOEL JEM-ARM200cF equipped with

a cold field-emission gun operating at 200 kV. Cross-section samples for TEM were milled directly from hot-pressed pellets using an FEI Nova Nanolab Focused Ion Beam system, yielding lamella that were typically 50 – 100 nm thick. These were mounted onto Cu support grids that produced a weak Cu signal in EDX spectra due to secondary scattering. In contrast, samples before hot pressing were mounted on an Al grid to avoid this problem and so the Cu content could be determined more accurately. STEM-EDX analysis was performed using a Bruker X-Flash detector. Background subtracted K_α peaks were used for compositional analysis. The microscope is also equipped with a 965 Quantum ER spectrometer for Electron Energy Loss Spectroscopy (EELS). EELS elemental analysis was performed using the $L_{2,3}$ edges of Ti, Ni and Cu and the $M_{4,5}$ edge of Sn. Spectra were deconvolved to remove multiple scattering effect, background subtracted and analysed using the cross-section data with Digital Micrograph. The accuracy of absolute quantification of compositions using EELS is estimated to be of order 5%.

SEM: The homogeneity and microstructure of various half-Heusler alloys were confirmed using a Quanta 650 FEG SEM operated at 20 kV in high-vacuum and equipped with an Oxford Instruments X-max 150^N detector for EDX mapping. The EDX mapping was performed without further calibration. Prior to analysis the surface of each sample was polished with fine Al_2O_3 sand paper down to 0.3 μm roughness. Measurements were carried out by Dr Jim Buckmann at Heriot-Watt University.

2.4. Physical Properties

Measurement of the thermoelectric figure of merit *ZT* is necessary for the characterisation of a bulk thermoelectric material as well as for a further design and improvement. The Seebeck coefficient, electrical resistivity and thermal conductivity (from the thermal diffusivity and heat capacity) are key thermoelectric properties. Their measurements were carried out where possible for all samples presented in this thesis. In addition, the Hall measurements were done to evaluate the charge carrier concentration and mobility.

2.4.1. Electrical Resistivity

Electrical resistivity (ρ) measurements were performed using the 4-point method using a Linseis LSR-3 instrument. As shown in Figure 2.13, a bar-shaped sample is placed between two Platinum electrodes and then located in the primary furnace. The sample bar

is heated up to the specific temperature by the furnace. When the required temperature is reached, a temperature gradient is created by the secondary heater located in the lower electrode block. The resistance (R) is measured by applying a constant current (I) from one end of the sample to the other, while the voltage change (dV) is measured by thermocouple at two intermediate points. To ensure a uniform distribution of current in the sample, the thermocouples were placed sufficiently far from the ends of bar. The ρ of materials is then calculated from the measured R ($R = V/I$) using the following equation:

$$\rho = \frac{RA}{L} \qquad \text{Equation (2.27)}$$

where A is the cross-sectional area of the sample and L is the separation of the inner probe contacts.

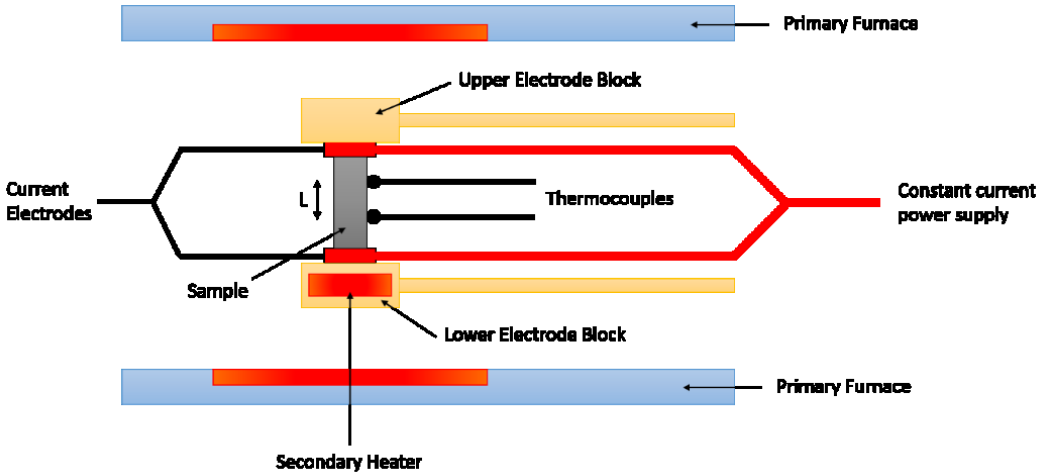

Figure 2.13. Sample and contact arrangement for resistivity and Seebeck coefficient measurements in the Linseis LSR-3 device.

2.4.2. Seebeck Coefficient

2.4.2.1. Measurement

High temperature measurements (30 – 500 ºC) of Seebeck coefficient (S) were carried at the same time as the resistance measurements using a Linseis LSR-3 instrument. Therefore, the instrument set up is the same as discussed in the resistivity section. The temperature gradient (ΔT = 30 ºC) between primary furnace and lower electrode is created, while the magnitude of induced voltage is measured by the thermocouples.

2.4.2.2. Single Parabolic Band (SPB) Model

The single parabolic band (SPB) model[170] can be used to model the electrical transport properties of material that contains a single type of charge carriers. This is the simplest model that can help in the optimisation or enhancement of thermoelectric efficiency. The analysis using SPB approximation may also suggest more complex behaviour that affects the material's properties. Multiband effects[171] or nonparablicity[172] are examples when SPB model does not describe the transport well. SPB model can be applied to one sample, however modelling of a series of samples can test the accuracy and provide new ways to improve thermoelectric properties. The key aspect of a SPB approximation is its development in a region where minority charge carriers are negligible and can be omitted. In heavily doped (degenerate) semiconductors at moderate temperatures, the Seebeck S and ρ increase with temperature until thermal excitation of electron-holes pairs occurs at high temperatures. The low temperature, degenerate region can be successfully analysed using SPB model.

SPB can be also successfully applied to samples with alloy scattering.[173] In SPB model all transport coefficients can be obtained by solving the Boltzmann transport equations. By using Fermi integral (Equation 2.28), S can be calculated using the following expressions:

$$F_j(\eta) = \int_0^\infty \frac{\varepsilon^j d\varepsilon}{1 + Exp[\varepsilon - \eta]} \qquad \text{Equation (2.28)}$$

$$S = \frac{k_B}{e}\left(\frac{2F_1}{F_0} - \eta\right) \qquad \text{Equation (2.29)}$$

Using m^* and η, the charge carrier concentration can be evaluated:

$$n = 4\pi\left(\frac{2m^* k_B T}{h^2}\right)^{3/2} F_{1/2} \qquad \text{Equation (2.30)}$$

In Equations 2.28-2.30, k_B is Boltzmann's constant, e is the electron charge, h is the Planck's constant, m^* is the effective carrier mass, η is the reduced Fermi level defined as ($\eta_F = (E_F - E_c)/k_B T$) where E_F is the chemical potential and E_c is the energy conduction band bottom, $F_j(\eta)$ is the Fermi integral and ε is the reduced energy. The effective mass m^* can be derived using experimental S and charge carrier concentration (n). However, in this thesis the literature value of m^* was used. The $m^* = 2.8\ m_e$ was chosen, as this value is characteristic for n-type half-Heusler materials.[172]

The Hall carrier concentration ($n_H = 1/R_H e$) is related to the experimental carrier concentration (n) via $n_H = n/r_H$, where the Hall factor (r_H) is expressed by:

$$r_H = \frac{3}{2}\frac{F_{\frac{1}{2}}(\eta)F_{-\frac{1}{2}}(\eta)}{2F_0^2(\eta)} \qquad \text{Equation (2.31)}$$

The SPB model can be also used to calculate the Lorenz number (L) as a function of temperature using the following equation:

$$L = \frac{k_B}{e^2}\frac{3F_0F_2 - 4{F_1}^2}{{F_0}^2} \qquad \text{Equation (2.32)}$$

It is used to evaluate the electronic contribution (κ_{el}) to the total thermal conductivity (κ). The electronic component was calculated via the Wiedemann-Franz relationship, $\kappa_{el} = LT/\rho$, it is then subtracted from κ to obtain an estimate for the lattice thermal contribution ($\kappa_{lattice} = \kappa - \kappa_{el} = \kappa - LT/\rho$). Frequently, the evaluated L value is lower than the metallic or degenerate semiconductor limit $L = 2.45 \times 10^{-8}$ WΩK^{-2}. Therefore, using L that was estimated over the whole temperature range gives much more satisfactory values for κ_{el}.

Recently, Kim *et. al*.[30] proposed a simplified equation that can be used to calculate L:

$$L = 1.5 + \exp\left[-\frac{|S|}{116}\right] \qquad \text{Equation (2.33)}$$

where L is in 10^{-8} WΩK^{-2} and S is in μVK^{-1}. This equation is independent of temperature or doping. It is accurate within 5% for SPB approximation and within 20% for materials where more complexity (eg. non-parabolicity, Kane bands, multiple bands) is introduced.

2.4.3. Thermal Conductivity

2.4.3.1. Measurement

Thermal diffusivity (α) was measured with the thermal flash method using a Linseis LFA-1000 instrument. Noncontact measurement, fast measurement time and high accuracy make the flash method the most widely used technique of diffusivity determination.[174] Cylindrical pellets (approximately 13 mm diameter and 1.0 – 1.5 mm thickness) were sprayed with a thin layer of carbon paint. This is essential to maximise energy absorption by the samples as well as to prevent emissivity. The prepared sample was loaded on a sample robot, which is located in a furnace (see Figure 2.14). The furnace was then evacuated to ~3.0×10^{-2} mbar and heated up to desired temperature. At the required temperature, one side of the pellet is irradiated with an extremely short but very intense, programmed laser pulse. The energy absorbed by the face of pellet causes homogeneous

temperature increase at the exposed surface and stimulates the temperature rise on the rear of disk. The temperature rise at the opposite surface is continuously monitored using sensitive, high speed detector.

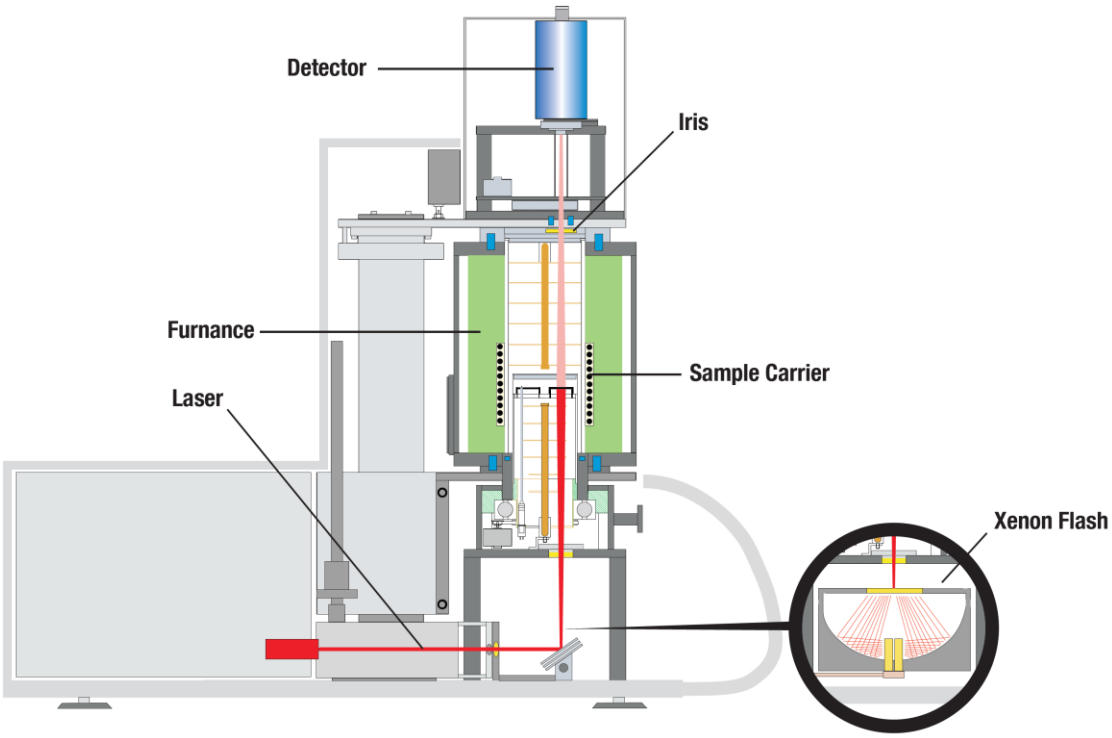

Figure 2.14. Schematic representation of Linseis LFA-1000 instrument.

The specific heat capacity (C_p) was measured using a Perkin Elmer DSC 8500 device that operates in the heat flow mode. The Differential Scanning Calorimetry (DSC) measures the change in sample's heat capacity with temperature variation. A few milligrams of finely ground sample were heated, while the variation in its heat capacity was recorded as changes in the heat flow.

The α and C_p values were combined with experimental density (d) of the disk to evaluate the total thermal conductivity (κ) using the following formula:

$$\kappa = \alpha d C_p \qquad \text{Equation (2.34)}$$

where κ is measured in W m^{-1} K^{-1}.

A porosity correction[132]:

$$\frac{\kappa_p}{\kappa} = 1 - \frac{4}{3}\phi; \text{where } \phi = \frac{100 - \%density}{100} \qquad \text{Equation (2.35)}$$

was applied to compositions with %density below 95%. Here %density is the ratio of experimental (d) to crystallographic ($d_{crystal}$) density. The experimental density, crystallographic density, the experimental total thermal conductivity (κ_p) and the porosity corrected thermal conductivity (κ) for all samples discussed in this thesis are summarised in Appendix A.

2.4.3.2. Debye-Callaway approximation

The Debye-Callaway model is an approximation for analysis of phonons that travel through the lattice of thermoelectric material.[31] The κ_{lattice} can be fitted using the modified Callaway model[175]:

$$\kappa_{lat} = \frac{k_B}{2\pi^2 v_s}\left(\frac{k_B T}{\hbar}\right)^3 \int_0^{\frac{\theta_D}{T}} \frac{x^4 e^x}{\tau_{ph}^{-1}(e^x-1)^2} dx \qquad \text{Equation (2.36)}$$

where $x = \frac{\hbar\omega}{k_B T}$ is the reduced energy (ω denotes the phonon frequency). Other terms include Boltzmann constant (k_B), reduced Planck's constant ($\hbar$), velocity of sound (v_S), Debye temperature (θ_D). The Phonon relaxation rate (τ_{ph}) can be evaluated by adding the rates of individual scattering mechanisms:

$$\tau_{ph}^{-1} = \tau_B^{-1} + \tau_{PD}^{-1} + \tau_U^{-1} \qquad \text{Equation (2.37)}$$

where τ_B is the grain boundary scattering, τ_{PD} is the point defect scattering and τ_U is the phonon-phonon Umklapp interaction.[176] Therefore, the combined relaxation time for half-Heusler alloys can be expressed as:

$$\tau_{ph}^{-1} = \frac{v_s}{L} + A_{PD}\omega^4 + B_U T\omega^2 \qquad \text{Equation (2.38)}$$

The following literature constant values were used in our fittings: θ_D (TiNiSn)[85] = 367 K and v_S (TiNiSn)[106] = 3630 ms^{-1}. The coefficients L, A_{PD} and B_U are fitting parameters, which are discussed in more details in the following section.

1. Grain boundary scattering: Grain boundaries are efficient scatters of long-wavelength phonons. Boundary scattering can be estimated using following equation:

$$\tau_B^{-1} = \frac{v_s}{L} \qquad \text{Equation (2.39)}$$

where L is the grain size.

2. Point defect scattering: Point defect scattering can scatter mid- to high- frequency phonons, due to their ω^4 frequency dependence. The relaxation time of point defect scattering can be expressed as[177]:

$$\tau_{PD}^{-1} = A\omega^4 = \frac{V_0}{4\pi v_s^3}\Gamma\omega^4 \qquad \text{Equation (2.40)}$$

where V_0 is the volume per atom and Γ is the disorder scattering parameter. The V_0 value is the volume of unit cell of analysed material (from Rietveld refinement of X-ray powder diffraction data) divided by the total number of atoms in this unit cell. The Γ term is the sum of mass (Γ_M) and strain (Γ_S) fluctuation scattering parameters ($\Gamma = \Gamma_M + \Gamma_S$), which could be expressed using the following equations[86]:

$$\Gamma_M = \frac{\sum_{i=1}^{n} c_i \left(\frac{\overline{M_i}}{\overline{\overline{M}}}\right)^2 f_i^1 f_i^2 (\frac{M_i^1 - M_i^2}{M_i})^2}{\sum_{i=1}^{n} c_i} \qquad \text{Equation (2.41)}$$

$$\Gamma_S = \frac{\sum c_i \left(\frac{\overline{M_i}}{\overline{\overline{M}}}\right)^2 f_i^1 f_i^2 \varepsilon_i (\frac{r_i^1 - r_i^2}{r_i})^2}{\sum_{i=1}^{n} c_i} \qquad \text{Equation (2.42)}$$

Here c_i is the relative degeneracy of the site. For example, TiNiSn has 3 sites (n = 3, A_1 = Ti, A_2 = Ni and A_3 = Sn) and $c_1 = c_2 = c_3 = 1$. The fractional occupation is denoted as f_i; $\overline{M}_i$ and $\bar{r}_i$ are the average mass and radii for respective atoms and $\overline{\overline{M}}$ is the average mass of the compound. The Γ_S and Γ_M terms describe the changes to the phonon relaxation time caused by the point defects. They also take into account changes in the atomic size and interatomic coupling forces between the host and impurity atoms.[177]

The disorder scattering parameter (Γ) can be also calculated using Equation 2.43[86]:

$$\frac{\kappa_L}{\kappa_L^P} = \frac{\tan^{-1}(u)}{u}$$
$$u^2 = \frac{\pi^2 \theta_D V_0}{h v_s^2} \kappa_L^P \Gamma_{expt} \qquad \text{Equation (2.43)}$$

where u is the disorder scaling parameter, while h is the Planck constant. The κ and κ_L^P terms denote thermal conductivity of sample with and without disorder, respectively.

3. Umklapp scattering: Umklapp phonon-phonon interaction is important at temperatures above the Debye temperature (θ_D). It is described by the following equation:

$$\tau_U^{-1} = \frac{2}{(6\pi^2)^{1/3}} \frac{k_B V_0^{1/3} \gamma^2 \omega^2 T}{\bar{M} v_s^3} = B\omega^2 T \qquad \text{Equation (2.44)}$$

Here, $\bar{M}$ is the average mass and γ is the Gruneisen parameter that describes the anharmonicity of the bonding.

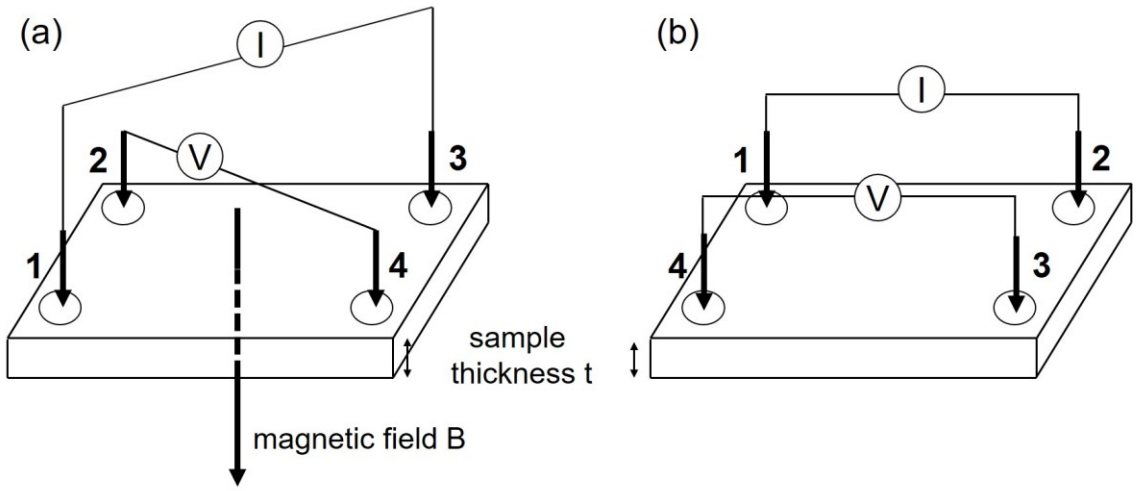

Figure 2.15. (a) Hall coefficient and **(b)** electrical resistivity measurements in van der Pauw geometry. *I* denotes the current, while *V* corresponds to the voltage.

2.4.4. Hall Coefficient and Carrier Concentration

The Hall effect is a measure of voltage that is induced when the current carrying conductor is exposed to both the current (*I*) and magnetic field (*B*). The Hall voltage is expressed as:

$$V_H = \frac{IB}{nqt} \qquad \text{Equation (2.45)}$$

where n is the carrier density, q is the charge (q = -e for electrons and q = +e for holes) and t is sample thickness. The quantity $1/nq$ is called the Hall coefficient (R_H). The carrier mobility (μ) can be evaluated from the ρ and Hall coefficient measurement by using the following equation:

$$\mu = \left|\frac{1}{nq\rho}\right| = \left|\frac{R_H}{\rho}\right| \qquad \text{Equation (2.46)}$$

In the late 1950s, van der Pauw developed a technique, which is used to measure the resistivity and the Hall coefficient. During the Hall measurement, a positive magnetic field (*P*) is applied perpendicularly to the sample surface (see Figure 2.15a). The current is applied on point 1 and taken out of lead 3 (I_{13}), while the Hall voltage is measured between points 2 and 4. Same measurement is carried for V_{42P}, V_{13P} and V_{31P} with I_{31}, I_{42}

and I_{24}, respectively. Once the measurement is completed, a positive magnetic field is replaced with the negative one (N) and the above procedure is repeated to obtain the voltage measurement V_{13N}, V_{31N}, V_{24N} and V_{42N}. To calculate the carrier density and Hall mobility, the voltage difference for positive and negative field is worked out for four pairs (e.g. $V_{13} = V_{13P} - V_{13N}$).

The overall Hall voltage is then calculated as:

$$V_H = (V_{13} + V_{31} + V_{24} + V_{42})/8 \qquad \text{Equation (2.47)}$$

The positive sing of V_H indicates p-type material, while negative sign is observed for the n-type material. The carrier concentration (n) is calculated using the V_H and rearranged Equation 2.45, while the Hall mobility is calculated by inserting the evaluated carrier density and ρ (from the resistance measurement) into Equation 2.46.

For resistance measurement the magnetic field is set to zero ($B = 0$), the current I_{12} is applied and the voltage difference ($V_{43} = V_4 - V_3$) is measured (see Figure 2.15b). The polarity of the current is reversed (I_{21}) so V_{34} is measured. Same procedure is repeated for the remaining values (V_{41}, V_{14}, V_{12}, V_{21}, V_{23}, V_{32}). The resistance ($R = V/I$) was calculated for eight current-voltage pairs. The materials resistance (R_S) is determined using two characteristic resistances:

$$\begin{aligned} R_A &= (R_{21,34} + R_{12,43} + R_{43,12} + R_{34,21})/4 \\ R_B &= (R_{32,41} + R_{23,14} + R_{14,23} + R_{41,32})/4 \end{aligned} \qquad \text{Equation (2.48)}$$

and the van der Pauw equation:

$$\exp\left(-\frac{\pi R_A}{R_S}\right) + \exp\left(-\frac{\pi R_B}{R_S}\right) = 1 \qquad \text{Equation (2.49)}$$

The resistivity of bulk material (as these presented in this thesis) is calculated from R_s using the following expression:

$$\rho = R_s t \qquad \text{Equation (2.50)}$$

Chapter 3 - Beneficial Contribution of Interstitial Metals on the Thermoelectric Properties of TiNiSn

3.1. Introduction

As discussed in Chapter 1, the introduction of excess metal is an excellent approach to reduce the thermal conductivity of half-Heusler alloys. Most of the reported work has focussed on the $MNi_{1+y}Sn$ system (M = Ti, Zr, Hf), where Ni segregates into Ni-rich domains or causes the formation of MNi_2Sn (full-Heusler) micro- or nano-inclusions within the half-Heusler matrix.[100, 101, 111, 113, 178] Recently Downie *et al*.[60] reported the microstructure and properties of $TiNiM_ySn$ compositions (M = Co, Ni and Cu) that were prepared using solid-state reaction protocol. The authors showed that excess transition metals can be used to control the electronic properties of the half-Heusler alloys. The investigated materials were not hot-pressed, therefore full thermoelectric characterisation was not performed.

In the first part of this chapter, the phase segregation in hot-pressed Cu-rich $TiNiCu_ySn$ half-Heusler alloys is investigated. The diffraction and electron microscopy studies have shown that the behaviour of the excess metal is complex. Uniform half-Heusler structures on the nanoscale level are produced. Here, most of the excess metals randomly occupy interstitial sites creating significant point scattering of phonons. The segregation is observed as grain-by-grain compositional variations, leading to the formation of a low fraction of grains with full-Heusler composition. In addition, extrusion of excess Cu from the half-Heusler matrix is observed upon hot-pressing. This produces Cu-rich interfacial wetting layers between grains that appear to facilitate the formation of coherent grain boundaries. Only small amounts of excess Cu ($y < 0.1$) are needed to achieve the optimal performance with $S^2/\rho = 2 – 4$ mW m^{-1} K^{-2} and low $\kappa_{lattice} = 4 – 5$ W m^{-1} K^{-1}. The best samples have a temperature-averaged $ZT_{device} = 0.3 – 0.4$ and estimated leg power outputs of 6 – 7 W cm^{-2} from a 323 – 773 K temperature gradient. The latter are comparable to the leading HfNiSn-based compositions.[56-58] These results are intriguing because they do not follow the prevailing trend to optimise half-Heusler systems towards boundary scattering from inclusions, but suggest the alternative strategy of employing interstitial point defect scattering is viable. Coupled with the use of inexpensive elements, this development could lead to commercially-viable thermoelectric generator manufacture.

The study shown in the second part of this chapter was motivated by a desire to get a better understanding of the impact of the small amounts of excess Ni that are found in TiNiSn, and if possible to prepare stoichiometric TiNiSn. To achieve this, a range of non-stoichiometric $Ti_{1+x}Ni_{1+y}Sn$ samples were synthesised by solid-state reactions and their structures and compositions were analysed by neutron and synchrotron X-ray powder diffraction and scanning electron microscopy. The prepared compositions form with varying amounts of excess Ni, while the Ti and Sn content shows little variation, demonstrating that the observed changes in properties are linked to the excess Ni. The excess Ni effectively disrupts the thermal transport and leads to n-type carrier doping, yielding a promising $ZT = 0.40$ at a relatively low temperature of 600 – 700 K.

3.2. Synthesis and Characterisation

The $TiNiCu_ySn$ series ($0 \leq y \leq 0.25$) and non-stoichiometric $Ti_{1+x}Ni_{1+y}Sn$ half-Heusler alloys (TiNiSn, $Ti_{1.02}NiSn$, $Ti_{1.02}Ni_{1.02}Sn$, $Ti_{1.05}Ni_{1.05}Sn$, $TiNi_{1.02}Sn$ and $TiNi_{1.075}Sn$) were synthesised via solid-state reactions. The starting reagents were thoroughly mixed and cold pressed using a 10-ton press into 13 mm diameter pellets. Samples were wrapped in tantalum foil and initially annealed in the vacuum-sealed quartz tube at 850 °C for 24 hours using 10°C/min heating and 20°C/min cooling stages. The samples were then re-homogenised and annealed in an evacuated quartz tube at 850 °C for additional 2 weeks. For this second step, the quartz tubes were inserted directly into the furnace at 850 °C and at the end of the two-week heating period they were air quenched from 850 °C. The resulting products were ground using a mortar and pestle and hot pressed at 875 °C for $TiNiCu_ySn$ samples and 950 °C for $Ti_{1+x}Ni_{1+y}Sn$ samples at 80 MPa for 20 minutes, using the home-built system that was discussed in Section 2.2.2. One disk was used for the electrical properties measurement, while the second one for diffusivity measurement, which were carried out according to the procedure described in Section 2.4. The remaining pieces were used for the X-ray, high resolution synchrotron X-ray and neutron powder diffraction experiments and electron microscopy analysis. The Hall coefficient and charge carrier concentration were measured for selected $TiNiCu_ySn$ ($y = 0$ and 0.075) and $Ti_{1+x}Ni_{1+y}Sn$ samples according to the procedure described in Section 2.4.4.

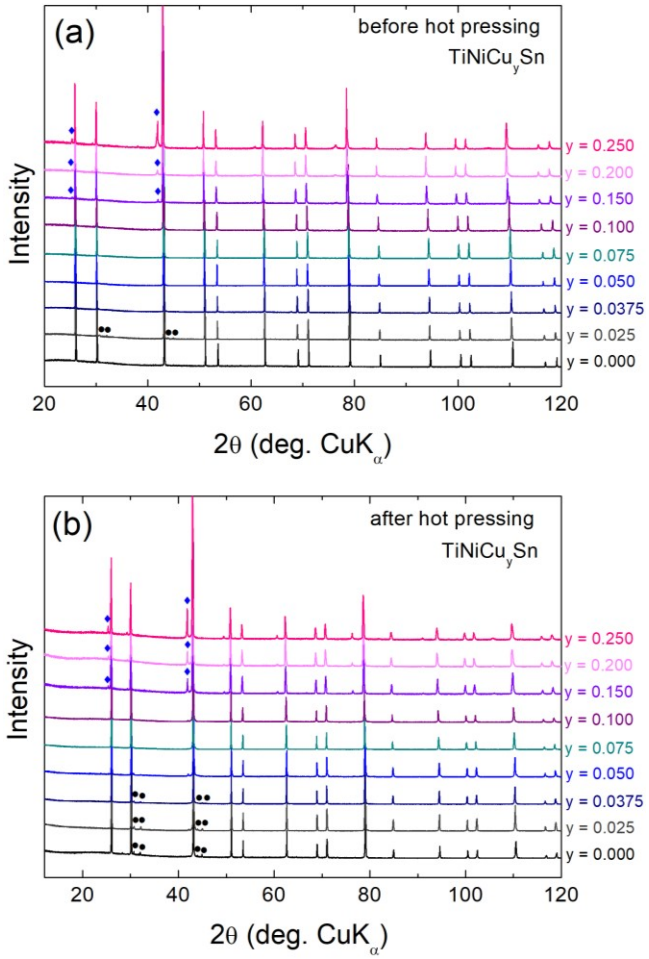

Figure 3.1. X-ray diffraction patterns for $TiNiCu_ySn$ before and after hot pressing. All main peaks can be indexed on the half-Heusler structure. Blue rhombus are for $TiNi_2Sn$ (full-Heusler), while the black circles denote elemental Sn.

3.3. $TiNiCu_ySn$ ($0 \leq y \leq 0.25$)

3.3.1. X-ray Powder Diffraction

To verify the phase composition of the $TiNiCu_ySn$ samples, XRD patterns were collected before and after hot pressing. The full datasets are shown in Figure 3.1 and a close-up of the main half-Heusler and full-Heusler reflections is shown in Figure 3.2. Visual inspection confirmed that the main Bragg peaks can be indexed on half-Heusler and full-Heusler phases, while small amount of elemental Sn was observed for $y < 0.0375$. For $y \leq 0.10$ only half-Heusler reflections were present, while for $y \geq 0.15$ distinct full-Heusler peaks are also evident. These observations suggest that for $y \leq 0.1$ the excess Cu is accommodated and dispersed within the TiNiSn matrix, while for larger y-values some of the excess Cu has segregated into distinct full-Heusler domains with a size large enough to lead to coherent diffraction. The amount of full-Heusler phase for $y \geq 0.15$

increases upon hot-pressing (Figure 3.2a), while the lattice parameter of the half-Heusler phase is reduced (Figure 3.2b) and the half-Heusler peaks are broadened (Figure 3.2 c and d). The decrease of the half-Heusler lattice parameter is particularly evident for samples with a large Cu content ($y \geq 0.15$), however small reductions are also observed for $y = 0.075$ and 0.1.

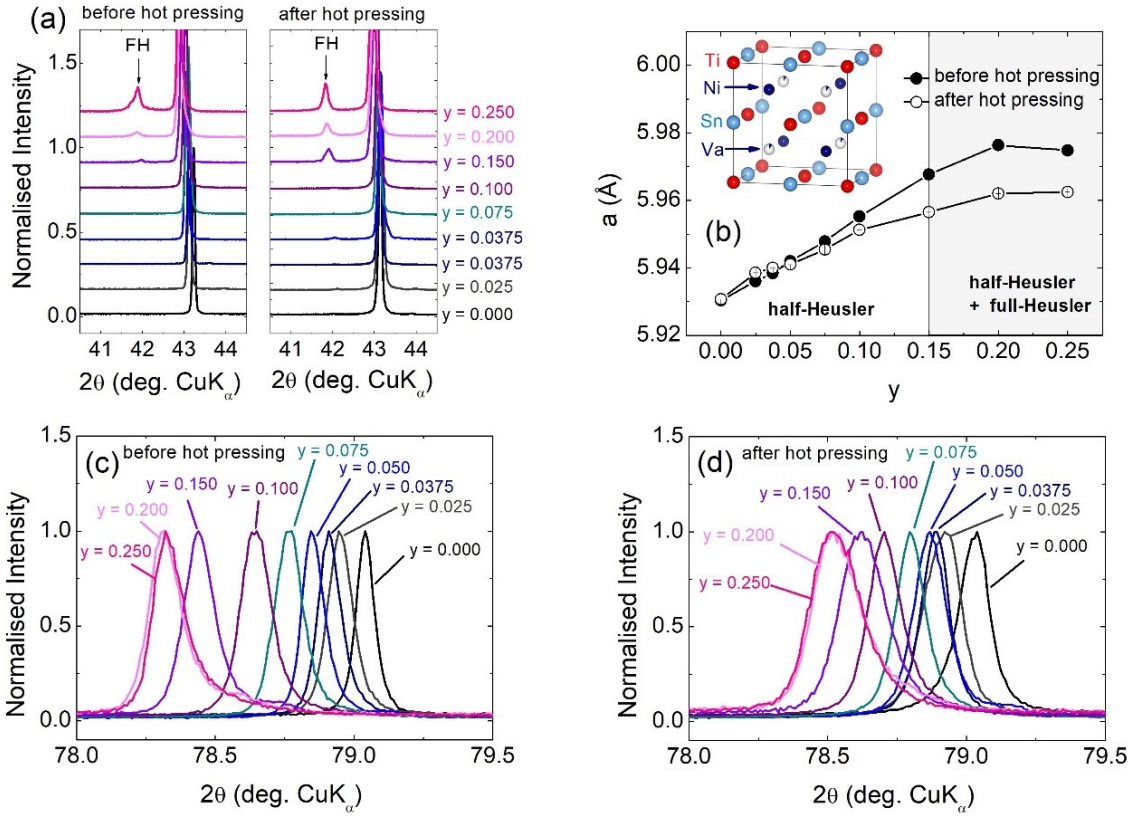

Figure 3.2. (a) Close-up of the main half-Heusler and full-Heusler reflection in X-ray powder diffraction, **(b)** lattice parameters before and after hot pressing, (**c, d**) close-up of the high-resolution (422) half-Heusler reflection before and after hot-pressing, respectively. The inset to panel (b) illustrates the half-Heusler structure, including the "vacant" tetrahedral site that is partially occupied in the $TiNiCu_ySn$ samples.

Peak broadening is often attributed to a reduction in grain size, which was not observed by microscopy in this study (see Section 3.3.3 and 3.3.4). Instead, peak broadening and reduction of half-Heusler lattice parameter upon hot-pressing are attributed to the Cu segregation, which causes grain-by-grain compositional variations. Individual grains tend to separate towards either half-Heusler or full-Heusler compositions. The sharp half-Heusler reflections shown in Figure 3.2c arise from a homogeneous distribution of Cu throughout a strained half-Heusler lattice, while the peak shift and broadening observed

Table 3.1. Lattice Parameters (*a*), weight percentages (*wt%*), fractional site occupancies (*occ*), thermal displacement parameters (U_{iso}/Å^2) and refined compositions for the half-Heusler and distinct full-Heusler phases that were used to fit the Polaris neutron powder diffraction data collected on the $TiNiCu_ySn$ ($y \leq 0.25$) series, before hot pressing.

y		**0**	**0.05**	**0.10**	**0.25**		
Half-Heusler		**Half-Heusler**	**Half-Heusler**	**Half-Heusler**	**Half-Heusler**	**Full-Heusler**	
Before hot pressing							
a (Å)		5.93208(4)	5.9395(1)	5.95367(4)	5.97092(6)	**a (Å)**	6.1135(2)
wt%		100	100	100	81.7(1)	**wt%**	18.3(1)
Ti (4a)	**U_{iso}**	0.00453(8)	0.00465(8)	0.00525(8)	0.0063(1)	**Ti (4a) U_{iso}**	0.0050(5)
Ni (4c)	**U_{iso}**	0.00425(4)	0.00492(5)	0.00550(6)	0.00603(7)	**Sn (4b) U_{iso}**	0.0039(4)
Ni / Cu	**Occ**	0.031(1)	0.02 / 0.054(1)	0.03 / 0.089(1)	0.03 / 0.147(2)	**Ni / Cu Occ**	0.714 / 0.180
(4d)	**U_{iso}**	0.00425(4)	0.00492(5)	0.00550(6)	0.00603(7)	**(8c) U_{iso}**	0.0131(3)
Sn (4b)	**U_{iso}**	0.00372(6)	0.00406(6)	0.00476(6)	0.00567(9)	**Refined composition**	$TiNi_{1.428}Cu_{0.360)}Sn$
Refined composition		$TiNi_{1.031(1)}Sn$	$TiNi_{1.03}Cu_{0.054(1)}Sn$	$TiNi_{1.03}Cu_{0.089(1)}Sn$	$TiNi_{1.03}Cu_{0.147(2)}Sn$	**Average composition**	$TiNi_{1.094}Cu_{0.181}Sn$
χ^2 (Rietveld) / χ^2 (Le Bail)		1.02	0.99	0.98	0.85		
wR_p (%)	**bank 3**	2.70	2.32	2.99	3.35		
	bank 4	2.50	1.92	2.47	2.68		
	bank 5	3.08	2.66	2.59	2.96		
R_p (%)	**bank 3**	2.84	2.76	2.96	3.44		
	bank 4	4.11	3.55	3.65	4.20		
	bank 5	4.27	3.61	3.81	4.41		

Half-Heusler space group = $F\bar{4}3m$ – Ti: 4a (0,0,0), occ. 1.00; Ni(1) 4c (¼, ¼, ¼), occ. 1.00; Ni(2) / Cu: 4d (¾, ¾, ¾). Occ. 0.03 / refined; Sn: 4b (½, ½, ½), occ. 1.00. **Full-Heusler** space group = $Fm\bar{3}m$ – Ti: 4a (0,0,0), occ. 1.00; Ni / Cu: 8c (¼, ¼, ¼), occ. fixed to EDX composition; Sn: 4b ((½, ½, ½), occ. 1.00

Table 3.2. Lattice Parameters (*a*), weight percentages (*wt%*), fractional site occupancies (*occ*), thermal displacement parameters (U_{iso}/Å^2) and refined compositions for the half-Heusler and distinct full-Heusler phases that were used to fit the Polaris neutron powder diffraction data collected on the $TiNiCu_ySn$ ($y \leq 0.25$) series, after hot pressing.

		0	0.05	0.10	0.25		
		Half-Heusler	**Half-Heusler**	**Half-Heusler**	**Half-Heusler**	**Full-Heusler**	
After hot pressing							
a (Å)		5.93099(4)	5.93800(4)	5.94939(4)	5.95732(5)	**a (Å)**	6.1168(1)
wt%		100	100	100	88.7(1)	**wt%**	11.3(1)
Ti (4a)	U_{iso}	0.00432(8)	0.00476(7)	0.00497(8)	0.00534(9)	**Ti (4a)** U_{iso}	0.0131(9)
Ni (4c)	U_{iso}	0.00413(5)	0.00483(5)	0.00529(6)	0.00569(6)	**Sn (4b)** U_{iso}	0.0089(5)
Ni / Cu	**Occ**	0.030(1)	0.03 / 0.033(1)	0.03 / 0.073(1)	0.03 / 0.103(1)	**Ni / Cu Occ**	0.714 / 0.180
(4d)	U_{iso}	0.00413(5)	0.00483(5)	0.00529(6)	0.00569(6)	**(8c)** U_{iso}	0.0141(3)
Sn (4b)	U_{iso}	0.00364(6)	0.00426(6)	0.00467(7)	0.00499(7)	**Refined composition**	$TiNi_{1.428}Cu_{0.360)}Sn$
Refined composition		$TiNi_{1.030(1)}Sn$	$TiNi_{1.03}Cu_{0.033(1)}Sn$	$TiNi_{1.03}Cu_{0.073(1)}Sn$	$TiNi_{1.03}Cu_{0.103(1)}Sn$	**Average composition**	$TiNi_{1.069}Cu_{0.128}Sn$
χ^2 **(Rietveld) /** χ^2 **(Le Bail)**		0.97	0.95	0.96	1.04		
wR$_p$ (%)	**bank 3**	2.45	3.08	3.00	3.41		
	bank 4	1.94	2.28	2.16	2.55		
	bank 5	1.79	2.11	2.12	2.37		
R$_p$ (%)	**bank 3**	2.73	3.12	3.09	3.09		
	bank 4	3.41	3.54	3.34	3.56		
	bank 5	2.70	3.15	3.02	3.59		

Half-Heusler space group = $F\bar{4}3m$ – Ti: 4a (0,0,0), occ. 1.00; Ni(1) 4c (¼, ¼, ¼), occ. 1.00; Ni(2) / Cu: 4d (¾, ¾, ¾). Occ. 0.03 / refined; Sn: 4b (½, ½, ½), occ. 1.00.
Full-Heusler space group = $Fm\bar{3}m$ – Ti: 4a (0,0,0), occ. 1.00; Ni / Cu: 8c (¼, ¼, ¼), occ. fixed to EDX composition; Sn: 4b ((½, ½, ½), occ. 1.00

in Figure 3.2d indicates that the samples become less uniform. Varying amount of excess Cu is trapped in half-Heusler grains leading to a distribution of lattice parameters. Observed broader diffraction peaks arise from an incoherent summation over all diffracting grains. In contrast, full-Heusler peaks become sharper with increased intensity (Figure 3.2a), suggesting that the full-Heusler grains are more homogeneous and abundant upon hot-pressing. This assessment is confirmed by Rietveld analysis of NPD data.

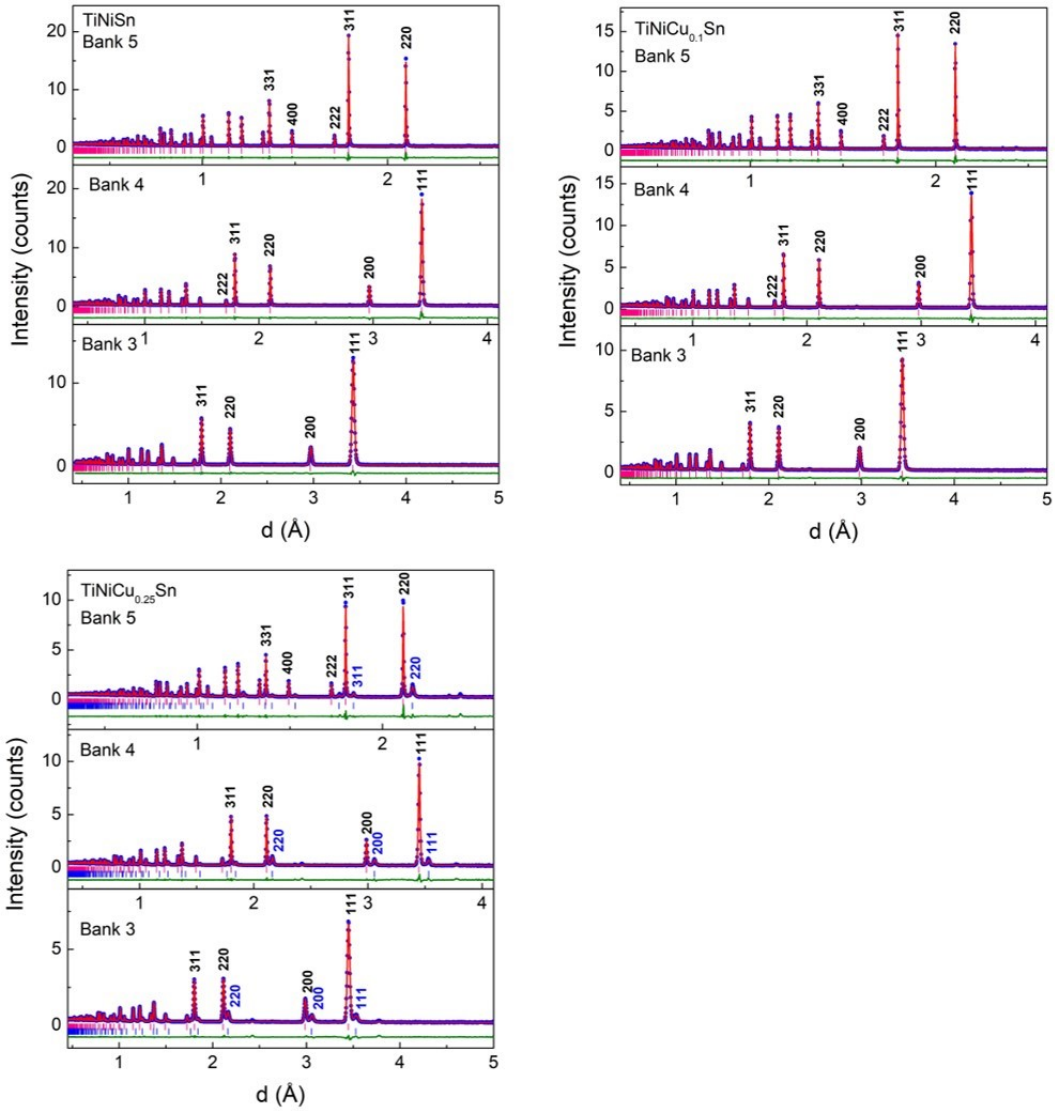

Figure 3.3. Observed (blue circles), calculated (red, solid line) and difference (solid, green line) neutron powder diffraction Rietveld profiles for the y = 0, 0.1 and 0.25 $TiNiCu_ySn$ samples before hot pressing. Only metal-rich half-Heusler phases were observed for $y \leq 0.1$, while both half-Heusler (magenta markers) and distinct full-Heusler phases (blue markers) were needed to fully fit the y = 0.25 sample.

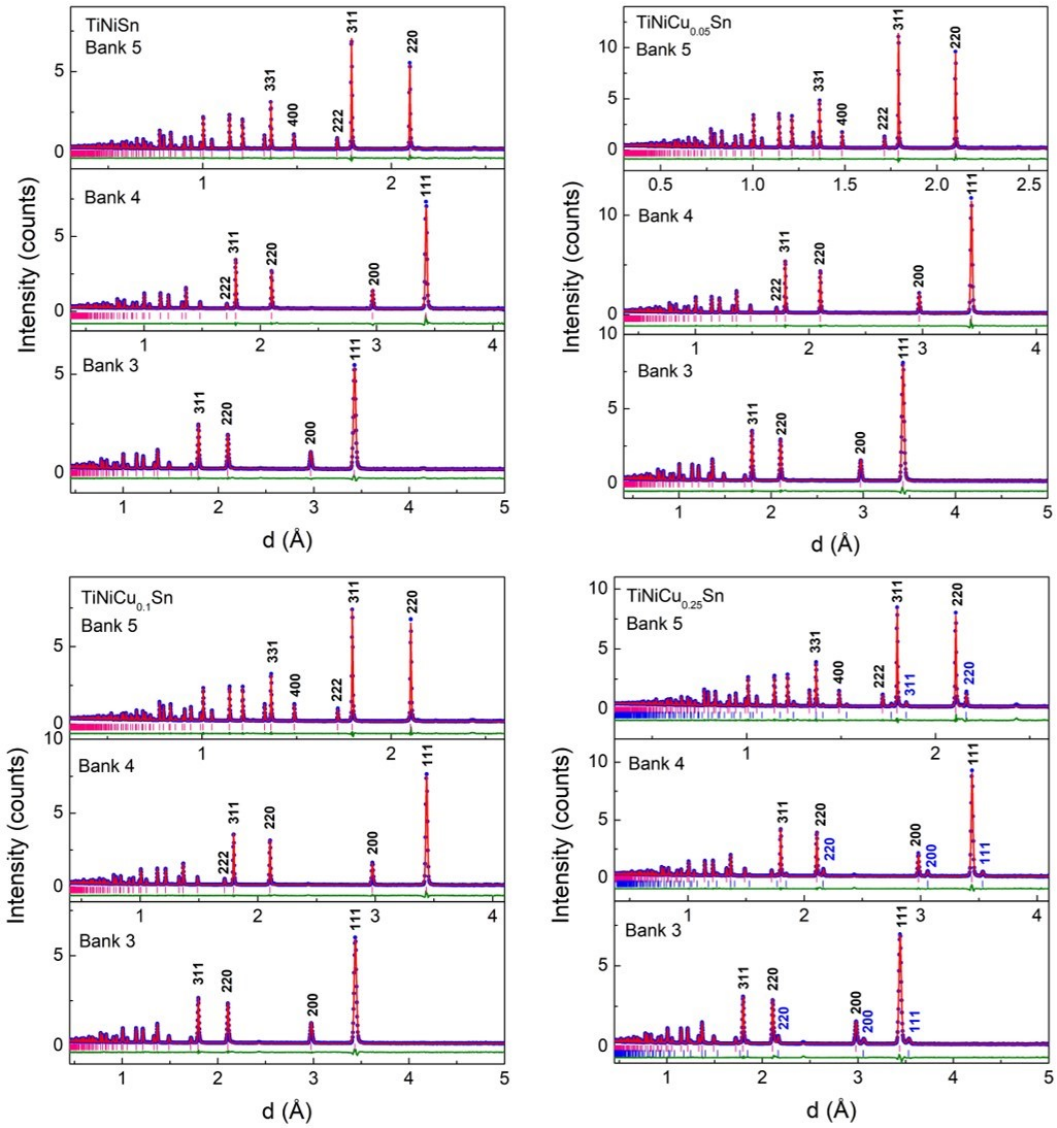

Figure 3.4. Observed (blue circles), calculated (red, solid line) and difference (solid, green line) neutron powder diffraction Rietveld profiles for the y = 0, 0.05, 0.1 and 0.25 $TiNiCu_ySn$ samples after hot pressing. Only metal-rich half-Heusler phases were observed for y ≤ 0.1, while both half-Heusler (magenta) and distinct full-Heusler phases (blue markers) were needed to fully fit the y = 0.25 sample.

3.3.2. Neutron Powder Diffraction

NPD data for y = 0, 0.05, 0.1 and 0.25 were collected using the POLARIS instrument. The final Rietveld fits are shown in Figures 3.3 and 3.4 for samples before and after hot pressing, while the refined structural parameters, compositions and fit statistics are given in Table 3.1 and 3.2. NPD was used to obtain information on the average composition of the half-Heusler phases as well as to determine the amount of excess Cu/Ni that was successfully introduced on the interstitial site of half-Heusler matrix. This technique is

suited to this because of the good scattering contrast between Ti, Ni, Cu and Sn. It was confirmed that $y \leq 0.10$ samples (before and after hot pressing) contain only half-Heusler phase with no evidence for distinct full-Heusler reflection. Therefore, the half-Heusler phase was modelled using a metal-rich half-Heusler structure with Ni fully occupying the *4c* (¼, ¼, ¼) site and excess Cu placed on the normally vacant *4d* (¾, ¾, ¾) sublattice. Free refinement of *4d* site occupancy resulted in higher than nominal Cu content, (e.g. the refined composition for y = 0.05 was $Ti[Ni][Cu_{0.073(1)}]Sn$), suggesting that this position is occupied by another, more strongly scattering element. The addition of 3% Ni onto *4d* site brings the Cu amount closer to the nominal value. This level of Ni was selected as Rietveld analysis of y = 0 reveals the spontaneous presence of 3% excess Ni in a parent material, which is unaffected by hot pressing. The presence of a small amounts of excess Ni in nominally stoichiometric TiNiSn is in agreement with previous work.[60, 128] The final fitted half-Heusler compositions for the y = 0.05, y = 0.1 and y = 0.25 samples are $TiNi[Ni_{0.03}Cu_{0.054(1)}]Sn$, $TiNi[Ni_{0.03}Cu_{0.089(1)}]Sn$ and $TiNi[Ni_{0.03}Cu_{0.147(1)}]Sn$ before hot pressing. In all cases, the application of pressure and temperature during hot pressing leads to migration of Cu out of the TiNiSn with final compositions: $TiNi[Ni_{0.03}]Sn$ for y = 0, $TiNi[Ni_{0.03}Cu_{0.033(1)}]Sn$ for y = 0.05, $TiNi[Ni_{0.03}Cu_{0.073(1)}]Sn$ for y = 0.10 and $TiNi[Ni_{0.03}Cu_{0.103(1)}]Sn$ for y = 0.25.

3.3.3. Scanning Electron Microscopy

The morphology and composition of the hot-pressed $TiNiCu_{0.10}Sn$ and $TiNiCu_{0.25}Sn$ samples was investigated by SEM. BSE and EDX elemental maps are shown in Figure 3.5. Elemental analysis for the y = 0.1 sample confirms the presence of a metal-rich half-Heusler phase with estimated composition $Ti_{1.00}Ni_{1.004(9)}Cu_{0.093(9)}Sn_{1.045(9)}$. In addition to the main phase, small amounts of a Cu-rich alloy phase were observed, which may be linked to the extrusion of Cu during hot pressing. The y = 0.25 sample showed evidence for large scale segregation into metal-rich half-Heusler and distinct full-Heusler grains with EDX-based compositions of $Ti_{1.00}Ni_{1.002(8)}Cu_{0.095(5)}Sn_{1.031(9)}$ and $Ti_{1.00}Ni_{1.428(8)}Cu_{0.360(6)}Sn_{1.031(9)}$. The obtained EDX compositions are in good agreement with those from NPD.

3.3.4. Transmission Electron Microscopy

The TEM data are consistent with powder diffraction and SEM. The $TiNiCu_{0.25}Sn$ sample was selected for investigation because higher Cu content is easier to map. Similar

structural features are observed for $TiNiCu_{0.10}Sn$. A scanning transmission electron microscopy (STEM) image of a thin lamella selected from the centre of the y = 0.25 hot-pressed sample is shown in Figure 3.6. It reveals boundaries between grains that are several microns in diameter. There is no evidence of voids or holes between grains, consistent with full densification. A small number of white streaks and spots are observed, some of which are analysed further by electron energy loss spectroscopy (EELS); see Figure 3.7. The EELS revealed that both the grain boundary and the occasional brighter spots on either side are Cu-rich. The relative intensities of Ti, Ni and Sn on either side of the grain boundary are similar and we conclude that the grains are both of half-Heusler composition, with Cu content around ~2%, the estimated EELS detectability limit in this case.

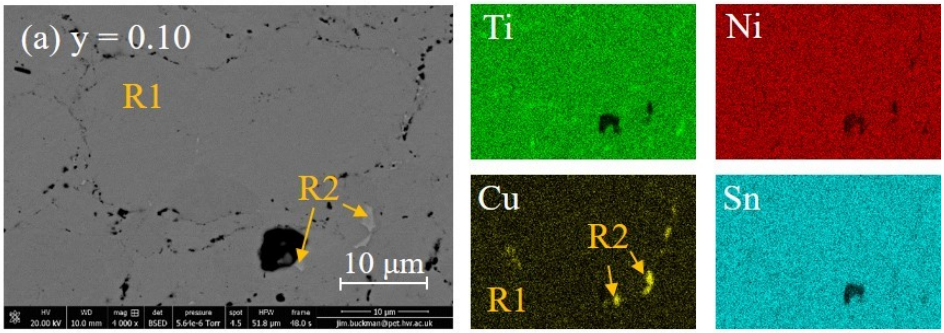

R1 (main grey region – half-Heusler matrix): $Ti_{1.00}Ni_{1.004(9)}Cu_{0.093(9)}Sn_{1.045(9)}$
R2 (bright Cu-rich regions – metal alloy inclusions): $Ti_{0.20(7)}Ni_{0.25(8)}Cu_{1.00}Sn_{0.57(8)}$

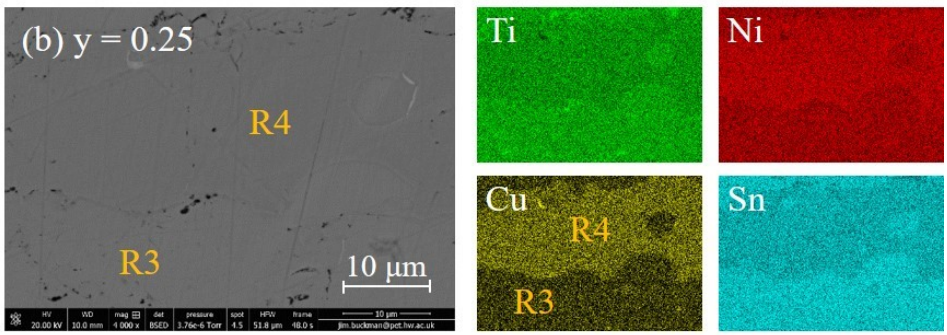

R3 (main grey region – half-Heusler matrix): $Ti_{1.00}Ni_{1.002(8)}Cu_{0.095(5)}Sn_{1.020(8)}$
R4 (bright Cu-rich regions – full-Heusler phase): $Ti_{1.00}Ni_{1.428(8)}Cu_{0.360(6)}Sn_{1.031(9)}$

Figure 3.5. Backscattered scanning electron microscopy images and element-specific EDX maps for **(a)** the y = 0.1 and **(b)** y = 0.25 $TiNiCu_ySn$ samples.

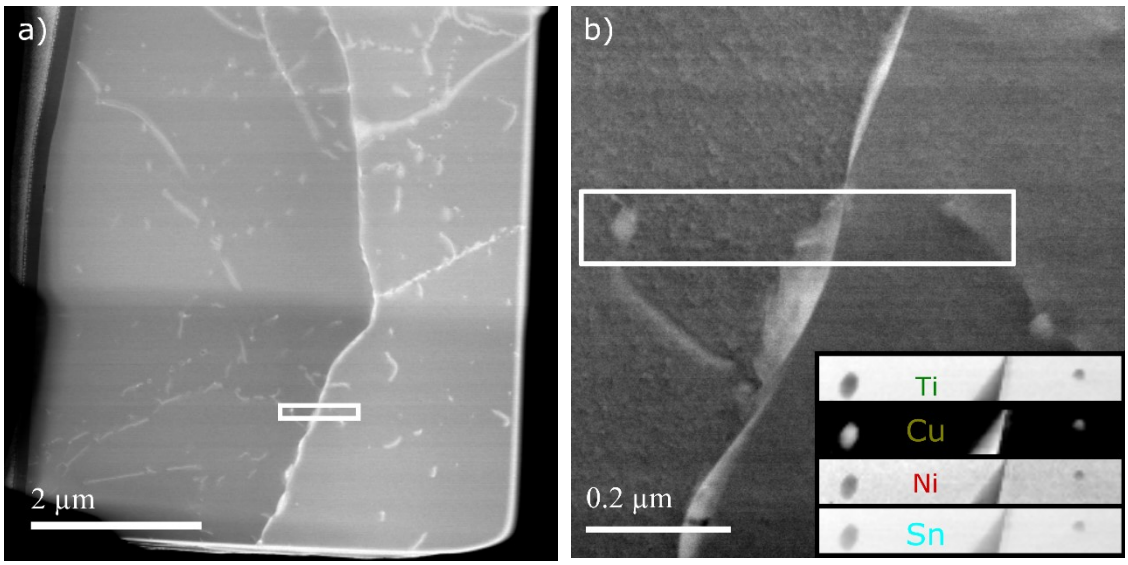

Figure 3.6. STEM analysis of consolidated $TiNiCu_{0.25}Sn$. **(a)** In dark field STEM, grain boundaries and strain-induced defects appear bright. The lamella has been selected from the centre of the as-prepared sample and thinned using FIB techniques (the material to the lower half of the image has been thinned further than that above). **(b)** Elemental analysis, across a typical grain boundary and spot-features with (inset) maps of the distribution Ti, Cu, Ni and Sn within the indicated region. Both the boundary and the spots are copper-rich. The approximate location of image (b) is indicated in image (a).

An important conclusion from the TEM analysis is that there is no evidence for nanoscale full-Heusler inclusions, apart from these infrequent Cu-rich spots. There is no obvious splitting of diffraction spots from individual grains, or contrast variations in TEM or STEM, that would suggest nanoscale half-Heusler-full-Heusler segregation. Instead, elemental mapping indicates that individual micron-sized grains have a relatively uniform composition but can differ from their neighbours, producing what we term here as grain-by-grain compositional variations and the formation of Cu-rich grain boundaries (see Figure 3.7a). The sample is oriented to view the grain in the left half of the image along a (111) direction, consistent with the indexed spots in the selected area electron diffraction pattern (inset). The material in the right half of the image is aligned along a (1n0)-type direction, contributing the circled spots to the diffraction pattern. The grain boundary itself appears (in projection) to be of order 2 nm wide but is coherent, with the lattice lines in the two grains meeting at 135° and without obvious dislocations within the field of view. EELS elemental analysis of a much wider region across the same boundary is presented in Figure 3.7b-c and suggest compositions of $Ti_{1.0}Ni_{1.04}Sn_{1.09}$ in the right grain and $Ti_{1.0}Ni_{1.22}Cu_{0.33}Sn_{1.02}$ in the left grain (again noting the estimated 2% detectability

limit for EELS). There is no obvious texture in the elemental maps on either side of the grain boundary, suggesting a very uniform composition within each grain. As observed in Figure 3.6, the grain boundary is Cu-rich, indicating the formation of a Cu 'wetting layer' that high resolution imaging suggests is coherent with the surrounding lattices.

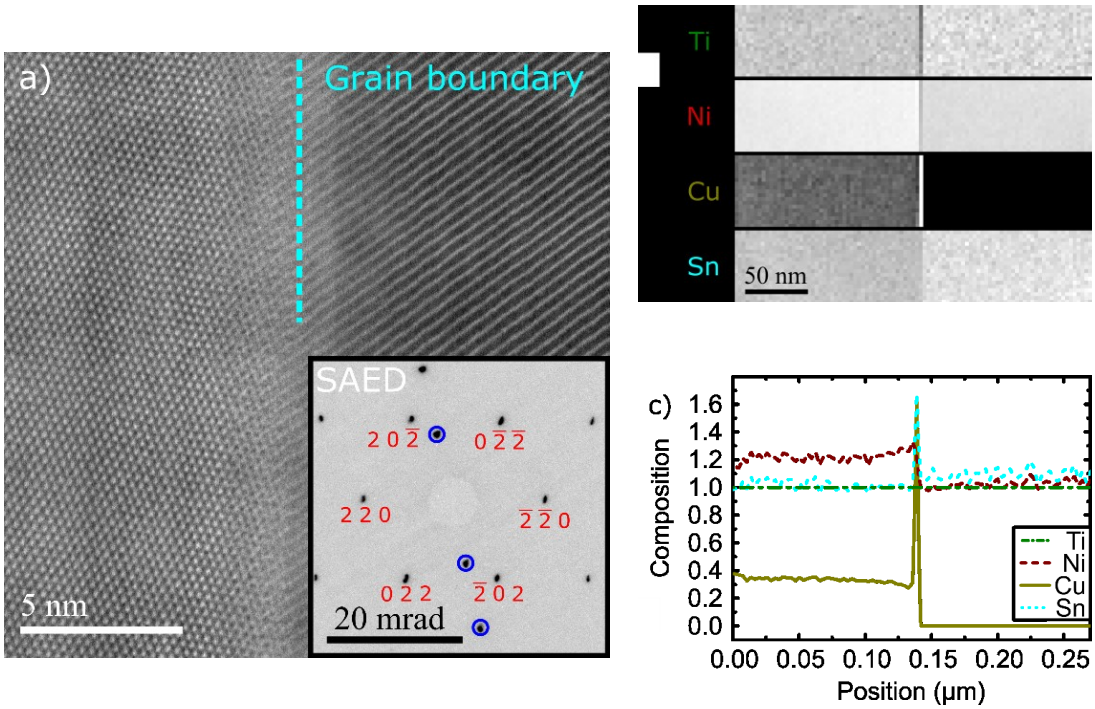

Figure 3.7. **(a)** High resolution STEM image with (inset) selected area diffraction of a boundary between a Cu-rich (left) and a Cu- deficient grain (right). Diffraction spots from the lower grain are circled. The two lattices appear to meet coherently. **(b)** EELS analysis across the boundary indicates uniform composition within each of the grains and a clear Cu enrichment at the boundary. **(c)** The approximate composition of the two regions is $Ti_{1.0}Ni_{1.04}Sn_{1.09}$ in the right region and $Ti_{1.0}Ni_{1.22}Cu_{0.33}Sn_{1.02}$ in the left region.

The main conclusion from the TEM is therefore that the composition of individual grains differs with segregation of excess metals (Ni and Cu) towards a small number of full-Heusler grains. There is no evidence of nanoscale-texturing of the Cu content to form an appreciable number of nanoscale Cu inclusions that would affect the bulk thermal transport.

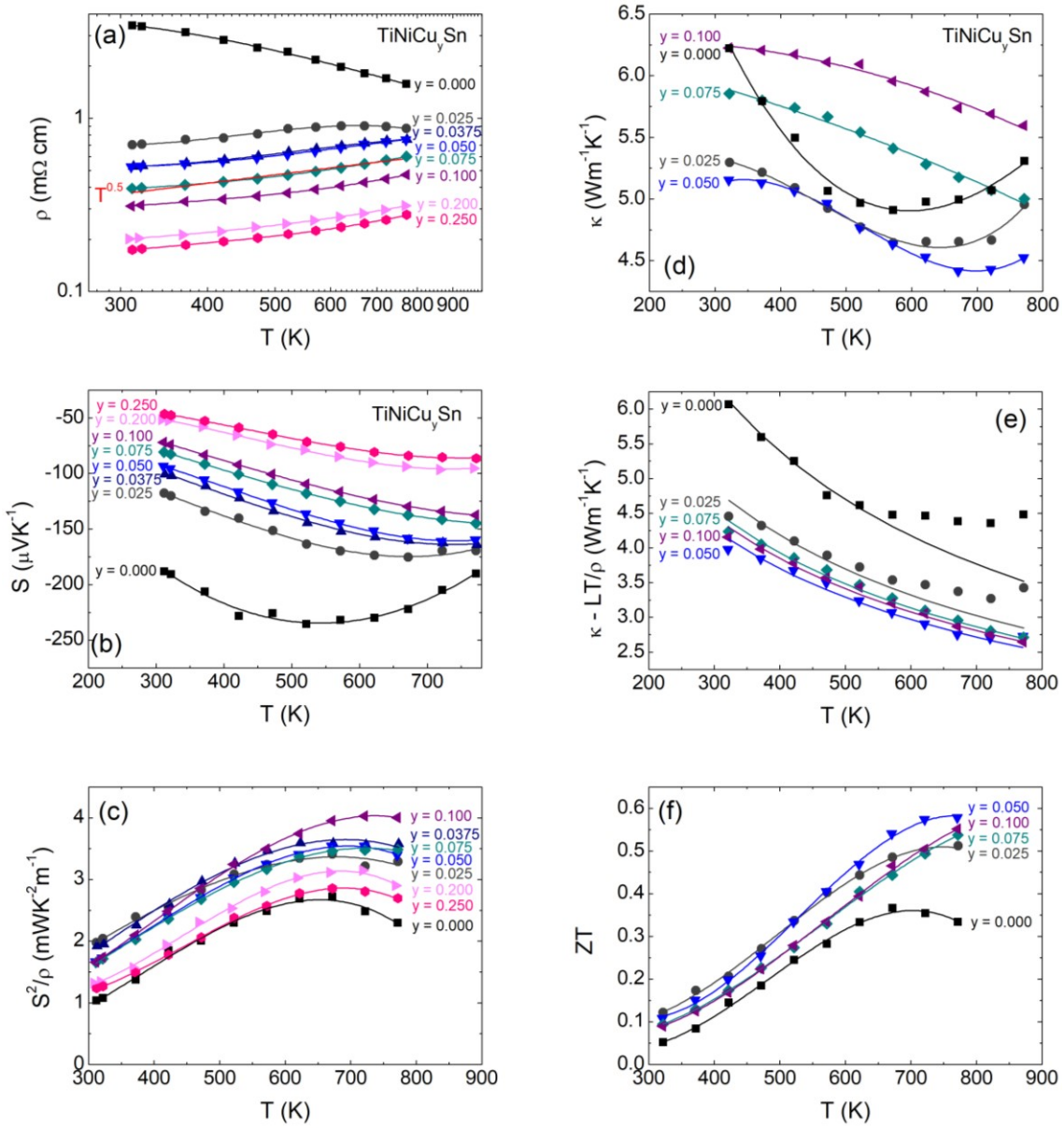

Figure 3.8. Temperature dependence of **(a)** the electrical resistivity (ρ) **(b)** the Seebeck coefficient (S) **(c)** the thermoelectric power factor (S^2/ρ) **(d)** the total thermal conductivity (κ) **(e)** the lattice thermal conductivity ($\kappa - LT/\rho$) and **(f)** the figure of merit ZT for the TiNiCu$_y$Sn samples. The solid lines in panel (e) are Debye-Callaway fits.

3.3.5. Thermoelectric Properties

The $\rho(T)$, $S(T)$ and $S^2/\rho(T)$ for the TiNiCu$_y$Sn ($0 \leq y \leq 0.25$) samples are shown in Figure 3.8. The magnitudes of $S(T)$ and $\rho(T)$ both decrease with increasing Cu content (Figure 3.8 a-b). The TiNiSn is a non-degenerate semiconductor with decreasing $\rho(T)$. The $\rho(T)$ changes to a metallic temperature dependence upon introduction of excess Cu, which is indicative of high-levels of doping and degenerate semiconducting behaviour. All

samples show n-type semiconducting behaviour, as indicated by the negative values of $S(T)$. The $S(T)$ for TiNiSn has a maximum near 550 K, which indicates presence of minority charge carriers (p-type) at high temperatures. This peak move to 675 K for y = 0.025 and was not observed for higher Cu content.

Efficient n-type doping was confirmed by Hall measurements. The carrier concentration increases by an order of magnitude as Cu content increases from y = 0 to y = 0.075 (from $n = 1.03 \times 10^{20}$ cm^{-3} to $n = 1.46 \times 10^{21}$ cm^{-3}, respectively). Interestingly, the carrier mobility for these two samples is nearly identical: $\mu = 12.3$ cm^2 V^{-1} s^{-1} (y = 0) and $\mu = 12.9$ cm^2 V^{-1} s^{-1} (y = 0.075), suggesting that the presence of excess Cu does not lead to increased carrier scattering. As a result, ρ_{300K} decreases by a factor of eight, from 3.4 mΩ cm (for y = 0) to 0.4 mΩ cm (for y = 0.075). The $\rho(T)$ and its relationship $\rho \sim T^z$ can be used to determine the dominant charge carrier scattering mechanism. In the degenerate limit, carriers are usually scattered by acoustic phonons for which $z = 3/2$.[172] By the evaluation of the slope (z) of log[ρ] against log[T], a relationship $\rho \sim T^{0.5}$ was observed for y ≥ 0.025 samples (Figure 3.8a) indicating that the disorder or alloy scattering is the main mechanism. This is in keeping with the presence of excess Ni and Cu on the interstitial site of the half-Heusler structure.

The Goldsmid-Sharp formula[27] (Equation 1.13) was used to estimate the thermal band gap (E_g) for y = 0 and 0.025. The resulting $E_g = 0.25$ eV is substantially reduced compared to the DFT values of $E_g = 0.5$ eV for TiNiSn, suggesting the presence of in-gap states.[179] The resulting S^2/ρ is greatly increased and attains maximum values of ~2 mW m^{-1} K^{-2} at 323 K and ~4 mW m^{-1} K^{-2} at 700 K for 0.05 ≤ y ≤ 0.1 (Figure 3.8c). The 323 K and peak values are ~100% and ~60% improved compared to TiNiSn. Increasing y above 0.1 results in a reduction of the measured S^2/ρ, which correlates with the observation of significant amounts of distinct, metallic full-Heusler phases in diffraction.

To examine the transport properties of TiNiCu$_y$Sn (y = 0.025, 0.05, 0.075 and 0.10) samples, we assumed the CB falls within the framework of the SPB model. This model assumes that carrier concentration and carrier effective mass (m^*) do not change with increasing temperature. A $m^* = 2.8m_e$ was chosen, as this value is characteristic for n-type MNiSn half-Heuslers.[172] The temperature dependence of S was modelled using SPB and is shown in Figure 3.9a. The results agree well with the experimental data up to 500-550 K. At higher temperatures, deviations from the experimental curve is observed. This suggests either that multiple bands contribute to the electronic transport or that the bands

are non-parabolic, such as for example the Kane model applied to ZrNiSn-based half-Heusler.[172] To obtain a reliable estimate of the Lorentz number (L), Equation 2.33 was used. This formula is estimated to be within 20% accurate for thermoelectric materials with non-SPB carrier transport.[30] As shown in Figure 3.9b, L decreases with increasing temperature. For all samples, L is much lower than the L value for degenerate semiconductor (2.45×10^{-8} $W\Omega K^{-2}$),[20] resulting in lower values for the electronic component of thermal conductivity, $\kappa_{el} = LT/\rho$ (Figure 3.9c).

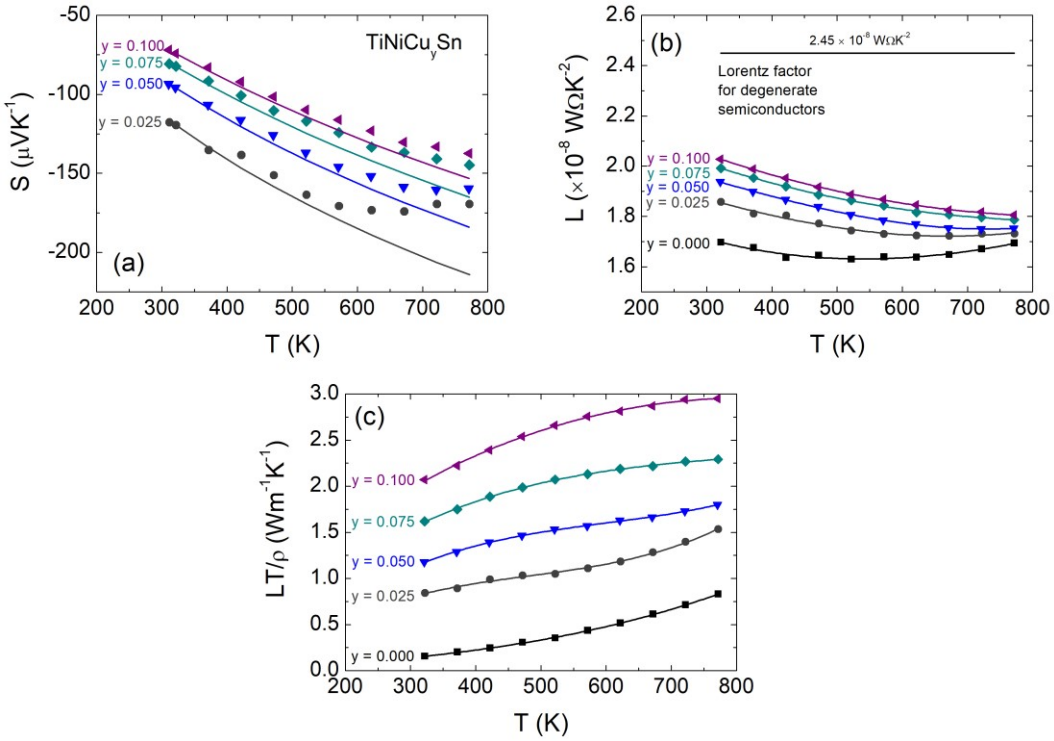

Figure 3.9. Temperature dependence of **(a)** the Seebeck coefficient and the single parabolic band (SPB) prediction (solid lines), **(b)** the Lorentz number (L) obtained using the approximation outlined in Ref. 30 and **(c)** the electronic thermal conductivity (κ_{el} = LT/ρ) for the TiNiCu$_y$Sn samples.

The temperature dependence of heat capacity (C_p) and thermal diffusivity (α) for the $0 \leq y \leq 0.1$ compositions are presented in Figure B1 (Appendix B). The evaluated κ is presented in Figure 3.8d. TiNiSn shows a clear increase in κ(T) above 550 K due to the onset of minority conduction but the trend is gradually suppressed as y increases and is not evident for the y = 0.075 and y = 0.1 samples. At 323 K, κ = 6.2 W m^{-1} K^{-1} for y = 0 decreases to κ = 5.2 W m^{-1} K^{-1} for y = 0.05 and then increases to a similar κ = 6.2 W m^{-1}

K^{-1} for y = 0.1. The increase for y > 0.05 is caused by the metallic nature of the samples and the rapid increase in LT/ρ (see Figure 3.9c). The extracted lattice thermal conductivity ($\kappa_{lattice} = \kappa - LT/\rho$) is shown in Figure 3.8e. Substantial reduction from 6.0 W m^{-1} K^{-1} for y = 0 to 4.5 W m^{-1} K^{-1} for y = 0.025 at 323 K was observed, while similar values are observed for larger y values. Similarly to the $S(T)$, TiNiSn has a minimum near 550 K, that shifts towards ~700 K for y = 0.05 and was not observed for y ≥ 0.075, indicating the bipolar thermal transport due to the presence of p-type charge carriers. The observed $\kappa_{lat,323\ K}$ = 6 W m^{-1} K^{-1} for TiNiSn is much smaller than $\kappa_{lat,323\ K}$ ~ 15 W m^{-1} K^{-1} from computational work[68, 180] and comparable to the values reported for ZrNiSn (κ_{lat} = 17.2 W m^{-1} K^{-1}) and HfNiSn (κ_{lat} = 14.5 W m^{-1} K^{-1}).[181]

Table 3.3. 323 – 550 K Callaway fit parameters for the $TiNiCu_ySn$ samples. The *4d* site occupancy was taken from Rietveld fits to the neutron powder diffraction data. Γ and Γ_{exp} are calculated (Equation 3.1) and fitted point-defect scattering parameters, respectively.

Composition	*4d*-site occupancy	κ_{323K}-LT/ρ (W m^{-1} K^{-1})	Γ	Γ_{exp}
TiNiSn	$Ni_{0.030}$	6.0	0.07	0.06
$TiNiCu_{0.025}Sn$	$Ni_{0.03}Cu_{0.018(1)}$ [a)]	4.5	0.11	0.12
$TiNiCu_{0.05}Sn$	$Ni_{0.03}Cu_{0.033(1)}$	4.0	0.14	0.16
$TiNiCu_{0.075}Sn$	$Ni_{0.03}Cu_{0.053(1)}$ [a)]	4.2	0.17	0.14
$TiNiCu_{0.1}Sn$	$Ni_{0.03}Cu_{0.073(1)}$	4.2	0.21	0.14

For all fits: B = 5 μm and $B_U = 2.1 \times 10^{-18}$ S K^{-1}, [a)] interpolated value

As discussed above, the microstructure of these materials is complex and changes upon hot pressing. No evidence for nanoscale full-Heusler inclusions is observed; the only full-Heusler phases observed in microscopy are macroscopically segregated full-Heusler grains, which give rise to distinct diffraction peaks in XRD and NPD. Calculations of the phonon mean free path (MFP) for half-Heuslers suggest that 90% of the thermal transport occurs by phonons with a MFP < 1 μm.[182] TEM reveals the presence of large relatively uniform grains of 2-5 μm dimensions, therefore the main reduction in $\kappa_{lattice}$ must be caused by the interstitial metals within the half-Heusler grains.

To investigate the effect of excess Cu on the thermal transport, the $\kappa_{lattice}$ was modelled using the Debye-Callaway model (see Section 2.4.3.2), with the final fits shown in Figure 3.8e and results given in Table 3.3. An initial fit for TiNiSn using the boundary scattering parameter L = 5 μm yielded the disorder parameter Γ_{exp} = 0.06 and Umklapp phonon-

phonon scattering $B_U = 2.1 \times 10^{-18}$ S K^{-1}. For the y > 0 samples, L and B_U were kept fixed, leaving point defect scattering as the only refineable parameter. The Γ value can be also calculated using Equations 2.41-2.42. Interstitials would be expected to have the same ω^4 dependence as point-defects and may be expected to have a strong impact on the local structure due to the formation of additional chemical bonds, leading to large disorder parameters. This is similar to the analogous and better studied situation of introducing vacancies. Equation 2.41 was adapted to account for the interstitials:

$$\Gamma = 0.25x(1-x)\left(\left(\frac{M_i}{\bar{\bar{M}}}\right) - 2\right)^2 \qquad \text{Equation (3.1)}$$

where x is the fraction of interstitials, M_i is the mass of the interstitial and $\bar{\bar{M}}$ is the average atomic mass of all contributing sublattices. The term -2 is included to account for broken chemical bonds.[183] The impact of lattice strain can be estimated from the difference in lattice parameters of TiNiSn (a ~5.9 Å) and $TiNi_2Sn$ (a ~ 6.1 Å). It is small compared to the impact of mass disorder, so has been omitted. This yields $\Gamma_{cal} = 0.07$ for the TiNiSn sample and increases to $\Gamma_{cal} = 0.21$ for the y = 0.1 sample. The experimental point defect scattering strength $\Gamma_{exp} = 0.06$ for parent TiNiSn, increases to $\Gamma_{exp} = 0.14(1)$ for 0.05 ≤ y ≤ 0.10, which have identical $\kappa_{lattice}$. The calculated Γ are found to be in good agreement with the experimental Γ_{exp} on the assumption that the interstitials form bonds and that these enhance the phonon scattering strength beyond that expected based on simple mass effects. In addition, the $\Gamma_{exp} = 0.06$ for TiNiSn is in good agreement with literature data for (Zr,Hf)NiSn, where interstitial Ni was assumed to reduce $\kappa_{lattice}$, yielding $\Gamma_{exp} = 0.03$-0.04.[184]

The ZT(T) is shown in Figure 3.8f. For y = 0, $ZT = 0.05$ at 323 K and increases to ZT = 0.37 at 673 K. The increase in S^2/ρ and reduction of $\kappa_{lattice}$ due to the introduction of excess Cu leads to $ZT = 0.09 – 0.12$ at 323 K (0.025 ≤ y ≤ 0.1), while a peak $ZT = 0.5 – 0.6$ is observed at 653 – 773 K. The reduction in $\kappa_{lattice}$ upon the introduction of the excess Cu is partially offset by the increased electronic contribution (LT/ρ), thereby limiting the ZT values. Nevertheless, the reported ZT values represent a 100% improvement over TiNiSn near room temperature and a 60% improvement in terms of peaks ZT.

The efficiency and the power output are important considerations for application of a material in a thermoelectric device. The efficiency (η) can be calculated using Equation 1.7, while the power output (ω) can be estimated using:[185]

$$\omega = \frac{PF_{device}(\Delta T)^2/2h}{\left(1+\frac{PF_{device}T_{hot}}{2\kappa_{device}}\right)+\sqrt{1+PF_{device}\bar{T}/\kappa_{device}}} \quad \text{Equation (3.2)}$$

Here, PF_{device} and κ_{device} are the average S^2/ρ and κ over the exploited temperature gradient, h is the length of the thermoelectric leg, $\Delta T = T_{hot} - T_{cold}$ and $\bar{T}$ is the average temperature. The temperature dependence of ZT_{device}, PF_{device}, the leg efficiencies and power output are shown in Figure 3.10. The ZT_{device} = 0.2 and 4.3% leg efficiency from ΔT = 450 K were observed for parent TiNiSn. For the Cu-doped samples, the ZT_{device} increases to 0.35, with η = 5.8-6.2% for the y = 0.025 and y = 0.05 samples, from the same ΔT (Figure 3.10a, b).

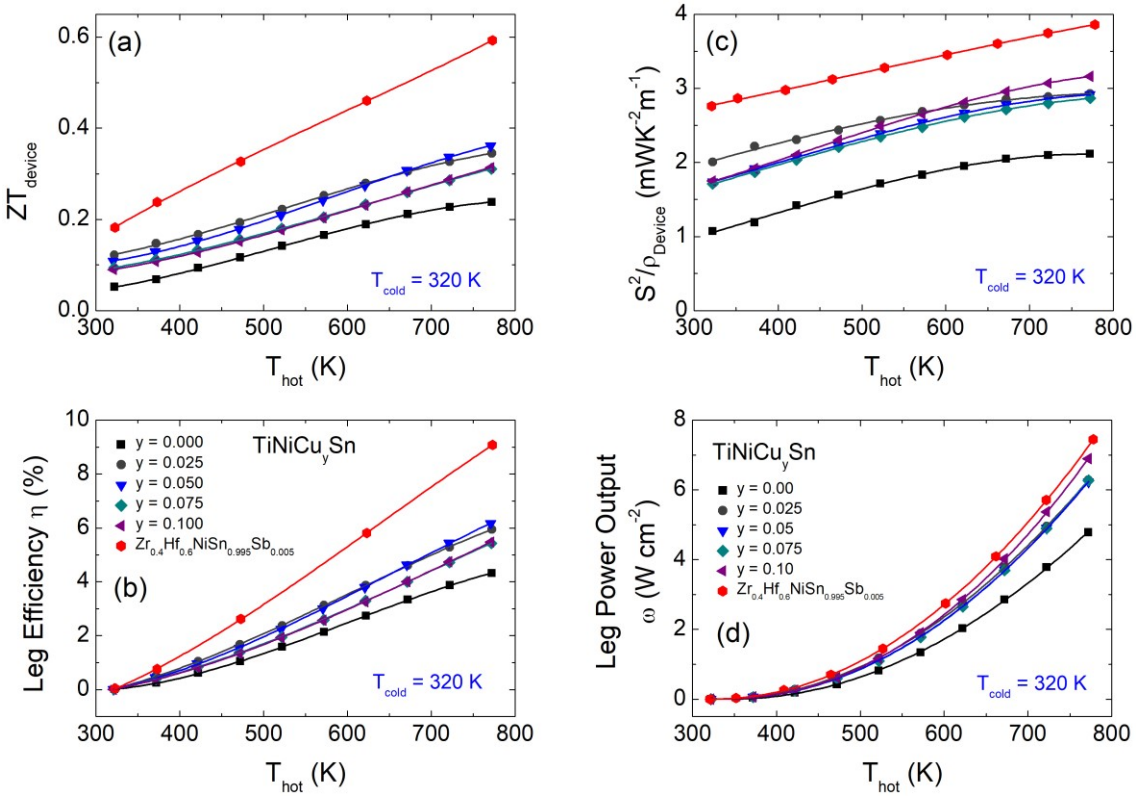

Figure 3.10. Temperature dependence of **(a)** ZT_{device}, **(b)** the efficiency (η), **(c)** PF_{device} and **(d)** the power output (ω) for the $TiNiCu_ySn$ samples as a function of hot-side temperature (T_{hot}). T_{cold} denotes the cold-side temperature. The data for the $Zr_{0.4}Hf_{0.6}NiSn_{0.995}Sb_{0.005}$ sample is representative of the best samples in the literature and was taken from Ref. 58.

As shown in Figure 3.10c, the magnitude of PF_{device} increases by 50% upon the introduction of excess Cu. This enables an improved leg power output, increasing from 5 W cm^{-2} (y = 0) to 7 W cm^{-2} (y = 0.1) from a 450 K gradient and using h = 0.2 cm (Figure

3.10d). The ZT_{device}, leg efficiency, PF_{device} and leg power output for a representative state-of-the-art $Zr_{0.4}Hf_{0.6}NiSn_{0.995}Sb_{0.005}$ alloy are shown for comparison in Figure 3.10.[58] This reveals that the $TiNiCu_ySn$ materials are competitive with the best half-Heuslers in terms of power output ($\omega \sim 7$ W cm^{-2}) but are characterised by a lower efficiency (6% versus 9%), due to the competing requirements for efficiency and power output. The former is linked to having a high ZT_{device} for which a low $\kappa(T)$ is essential, while power output relies on having a large PF_{device} but also on the magnitude of $\kappa(T)$ due to the coupled nature of the flow of heat and charge.[185] This illustrates that other performance indicators, such as power output, should be considered along ZT in judging the suitability of a thermoelectric material. We tested the thermoelectric properties under repeated cycling and did not observe any changes, which is critical for the construction of viable devices. Furthermore, a test where a large current density was forced through a $TiNiCu_{0.1}Sn$ sample at room temperature did not produce any changes in sample composition (for example, migration of Cu to the surface).

3.3.6. Discussion

Significant improvement in S^2/ρ and reduction of $\kappa_{lattice}$ have been achieved in $TiNiCu_ySn$ compositions. The samples are characterised by grain-by-grain compositional variations with a tendency towards the formation of either half-Heusler or full-Heusler compositions. Rietveld analysis revealed that Cu occupies normally vacant *4d* site of half-Heusler structure. In addition, 2-3% of excess Ni is spontaneously introduced on the *4d* site. Hall measurements have confirmed that the introduction of excess Cu leads to n-type doping and this optimises the S^2/ρ with increases observed over the entire 323 – 773 K temperature range. Recent computational work confirms initial suggestion that the Cu $4s^1$ electron is delocalised in the half-Heusler CB.[186] TEM supports the diffraction analysis that the grains contain randomly distributed excess metals. Some Cu segregation occurs at grain boundaries and this leads to the formation of "wetting-layers" enabling full densification and facile electronic transport. The absence of diffraction spot splitting in TEM precludes the presence of nanometre scale full-Heusler inclusions with different lattice parameters from the matrix. The only full-Heusler phases observed in microscopy are macroscopically segregated full-Heusler grains, which give rise to distinct diffraction peaks in X-ray powder diffraction and neutron powder diffraction. However, these are present in relatively small amounts for the $y \leq 0.1$ compositions.

The impact of the excess metals on the thermal transport is profound with a near 4-fold reduction in $\kappa_{lattice}$ for y = 0.05, compared to ~15 W m^{-1} K^{-1} for defect-free TiNiSn.[68, 180] The Callaway model revealed point defect as the main phonon scattering mechanism. It suggests that the reduction could be due to interstitial Ni and Cu metals. The improvement in the individual thermoelectric parameters results in a relatively flat $ZT(T)$ dependence, which enables improved energy harvesting efficiencies from lower grade waste heat. Our results are particularly significant as $TiNiCu_ySn$ alloys do not contain any toxic or expensive elements (such as Hf) and are produced using a simple processing route. These materials are therefore promising candidates for large-scale production.

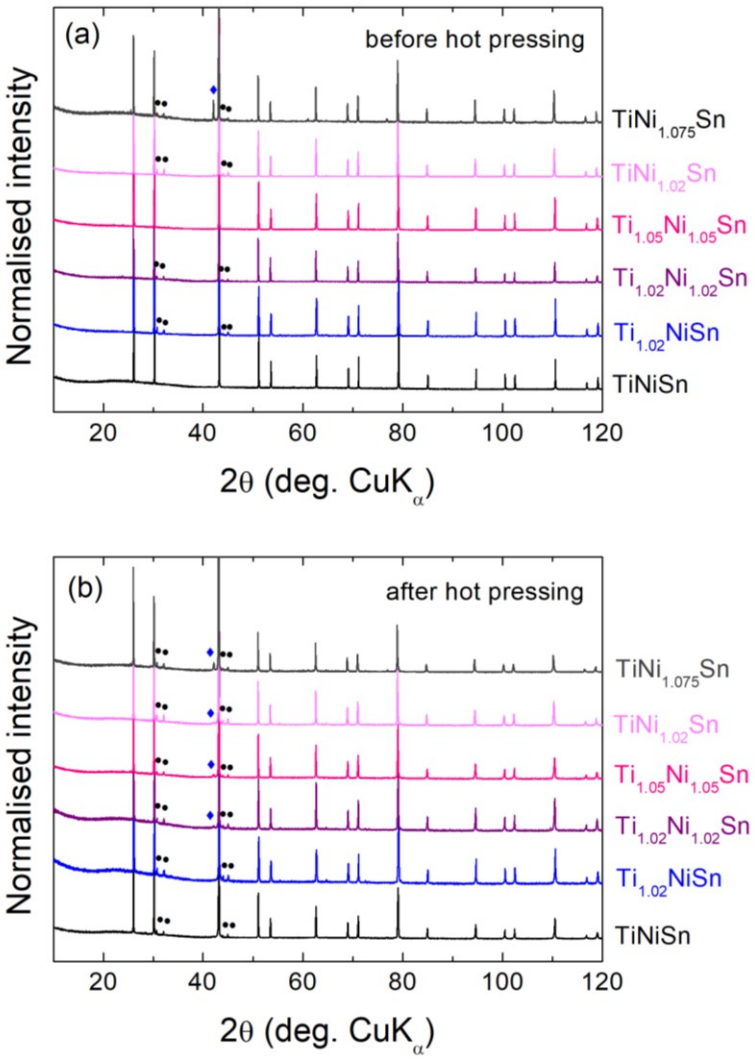

Figure 3.11. X-ray powder diffraction patterns for the $Ti_{1+x}Ni_{1+y}Sn$ samples **(a)** before and **(b)** after hot pressing. All main peaks can be indexed on the half-Heusler structure. Black circles are for elemental Sn, while the blue rhombus denotes $TiNi_2Sn$ (full-Heusler).

3.4. Off-stoichiometric $Ti_{1+x}Ni_{1+y}Sn$

As discussed above, the TiNiSn tends to spontaneously form as a Ni-rich composition. For this reason, a range of non-stoichiometric $Ti_{1+x}Ni_{1+y}Sn$ samples was prepared to investigate the possibility of preparing stoichiometric TiNiSn. This leads to the systematic formation of samples with excess Ni.

3.4.1. X-ray Powder Diffraction

XRD patterns of the $Ti_{1+x}Ni_{1+y}Sn$ samples are presented in Figure 3.11. Lattice parameters and weight fractions of identified phases are presented in Table 3.4. Rietveld analysis confirmed that all main Bragg reflections can be indexed on the half-Heusler structure (> 95 wt%) and small amount of elemental Sn. In addition, the hot-pressed $Ti_{1.02}Ni_{1.02}Sn$, $Ti_{1.05}Ni_{1.05}Sn$, $TiNi_{1.02}Sn$ and $TiNi_{1.075}Sn$ samples were found to contain minor full-Heusler $TiNi_2Sn$ phase, which was not present prior to hot pressing.

Table 3.4. Lattice parameters (*a*) and weight percentages (*wt%*) for the half-Heusler, full-Heusler and Sn phases, which were used during Rietveld refinement fit to X-ray powder diffraction data.

Composition	Half-Heusler		Full-Heusler		Sn		
	a (Å)	wt%	a (Å)	wt%	a (Å)	c (Å)	wt%
Before Hot-Pressing							
TiNiSn	5.9304(1)	100.0					
$Ti_{1.02}NiSn$	5.9292(1)	96.4(1)			5.8322(5)	3.1827(4)	3.6(1)
$Ti_{1.02}Ni_{1.02}Sn$	5.9316(1)	97.1(2)			5.8319(5)	3.1818(5)	2.9(2)
$Ti_{1.05}Ni_{1.05}Sn$	5.9343(1)	100.0					
$TiNi_{1.02}Sn$	5.9382(1)	95.4(1)			5.8339(3)	3.1828(2)	4.6(1)
$TiNi_{1.075}Sn$	5.9384(1)	89.8(1)	6.0803(1)	7.7(2)	5.8345(6)	3.1832(6)	2.5(2)
After Hot-Pressing							
TiNiSn	5.9307(1)	97.7(1)			5.8325(2)	3.1825(2)	2.3(1)
$Ti_{1.02}NiSn$	5.9311(1)	95.9(1)			5.8321(3)	3.1840(3)	4.1(1)
$Ti_{1.02}Ni_{1.02}Sn$	5.9352(1)	94.4(1)	6.084(1)	2.4(2)	5.8331(3)	3.1823(3)	3.2(1)
$Ti_{1.05}Ni_{1.05}Sn$	5.9344(1)	95.3(1)	6.0771(7)	2.8(1)	5.8317(4)	3.1823(3)	1.9(1)
$TiNi_{1.02}Sn$	5.9388(1)	93.8(1)	6.072(2)	2.1(3)	5.8333(2)	3.1820(1)	4.1(1)
$TiNi_{1.075}Sn$	5.9432(1)	92.8(1)	6.0745(3)	4.7(2)	5.8334(3)	3.1823(3)	2.5(1)

3.4.2. Neutron Powder Diffraction

Rietveld refinement was carried out on NPD data collected for the hot-pressed samples, with an aim to obtain the experimental compositions of half-Heusler phases.

Table 3.5. Lattice parameters (*a*), weight percentage (*wt%*), fractional site occupancies (*occ*), thermal displacement parameters (U_{iso}/Å^2) and refined compositions for the half-Heusler, full-Heusler, Ti and Sn phases that were used to fit the Polaris neutron powder diffraction data for the off-stoichiometric $Ti_{1+x}Ni_{1+y}Sn$ materials. Structural composition and lattice parameter (*a*) of HH phase evaluated using synchrotron X-ray diffraction (SXRD) and scanning electron microscopy with energy dispersive X-ray (SEM-EDX).

		TiNiSn	**$Ti_{1.02}NiSn$**	**$Ti_{1.02}Ni_{1.02}Sn$**	**$Ti_{1.05}Ni_{1.05}Sn$**	**$TiNi_{1.02}Sn$**
Half-Heusler Phase						
a (Å)		5.93100(4)	5.92951(4)	5.93364(3)	5.93380(3)	5.93607(3)
wt%		99.0(2)	93.7(2)	91.8(2)	91.4(1)	90.8(1)
v%		99.0	91.7	90.0	90.1	89.0
Ti (4a)	**Occ**	0.974(3)	0.978(3)	0.978(2)	0.978(2)	0.977(2)
	U_{iso}	0.00412(8)	0.00455(8)	0.00447(7)	0.00444(7)	0.00435(7)
Ni (4c)	**U_{iso}**	0.00407(4)	0.413(4)	0.00445(4)	0.00448(4)	0.00470(4)
Ni (4d)	**Occ**	0.025(1)	0.019(1)	0.038(1)	0.040(1)	0.058(1)
	U_{iso}	0.00407(4)	0.413(4)	0.00445(4)	0.000448(4)	0.00470(4)
Sn (4b)	**U_{iso}**	0.00394(7)	0.00387(6)	0.00403(6)	0.00405(5)	0.00415(5)
Refined composition		$Ti_{0.974(3)}Ni_{1.025(1)}Sn$	$Ti_{0.978(3)}Ni_{1.019(1)}Sn$	$Ti_{0.978(2)}Ni_{1.038(1)}Sn$	$Ti_{0.978(2)}Ni_{1.040(1)}Sn$	$Ti_{0.977(2)}Ni_{1.058(1)}Sn$
ρ_{HH} (g cm^{-3})		7.18	7.18	7.20	7.20	7.23
Full-Heusler Phase						
a (Å)				6.0717(7)	6.0753(3)	6.0622(9)
wt%				1.6(2)	3.5(1)	1.7(1)
Ti/Ni/Sn	**U_{iso}**			0.0014(6)	0.0058(4)	0.0001
Refined composition				$TiNi_2Sn$	$TiNi_2Sn$	$TiNi_2Sn$
ρ_{FH} (g cm^{-3})				8.427	8.412	8.467
Ti Phase						
a (Å)			2.9722(4)	2.9726(4)	2.9714(5)	2.9726(4)
c (Å)			4.545(1)	4.547(1)	4.548(1)	4.545(1)
wt%			3.8(2)	3.8(2)	3.3(1)	4.0(2)
Ti (2c)	**U_{iso}**		-0.0015(3)	0.005(1)	0.004(1)	0.006(1)
ρ_{Ti} (g cm^{-3})			4.575	4.572	4.575	4.574
Sn Phase						
a (Å)		5.8305(3)	5.8311(8)	5.8320(8)	5.829(2)	5.8311(6)
c (Å)		3.183(3)	3.1828(8)	3.1824(8)	3.188(2)	3.1811(6)
wt%		1.0(2)	2.5(2)	2.8(2)	1.8(2)	3.4(2)
Sn (4a)	**U_{iso}**	0.025	0.023(4)	0.019(3)	0.022(6)	0.018(2)
ρ_{Sn} (g cm^{-3})		7.285	7.285	7.283	7.279	7.285
Fit Statistics						
wR_p (%)	**bank 3**	2.43	2.93	2.58	2.44	2.46
	bank 4	1.92	2.19	2.14	1.88	1.94
	bank 5	1.77	1.97	1.96	1.75	1.87
R_p (%)	**bank 3**	2.69	2.64	2.49	2.43	2.42
	bank 4	3.38	4.02	4.11	3.64	3.96
	bank 5	2.62	2.88	2.76	2.59	2.71
Average composition		$Ti_{1.00}Ni_{1.05}Sn_{1.04}$	$Ti_{1.00}Ni_{0.98}Sn_{0.98}$	$Ti_{1.00}Ni_{1.01}Sn_{0.99}$	$Ti_{1.0}Ni_{1.04}Sn_{0.99}$	$Ti_{1.0}Ni_{1.01}Sn_{0.99}$
ρ_{exp} (gcm^{-3})		6.3(1)	6.6(1)	6.9(1)	6.5(1)	6.7(1)
ρ_{total} (gcm^{-3})		7.18(1)	7.03(1)	7.06(1)	7.11(1)	7.08(1)
Percentage density (%)		88%	94%	98%	92%	95%
Structural Composition and Lattice Parameter from SXRD and SEM-EDX						
SXRD		$TiNi_{1.03(2)}Sn$ a = 5.932(3) Å	$TiNi_{1.02(2)}Sn$ a = 5.930(4) Å	$TiNi_{1.05(2)}Sn$ a = 5.935(4) Å	$TiNi_{1.04(2)}Sn$ a = 5.934(4) Å	$TiNi_{1.06(2)}Sn$ a = 5.937(3) Å
SEM-EDX			$Ti_{0.98(1)}Ni_{0.954(8)}Sn$	$Ti_{0.98(2)}Ni_{0.96(1)}Sn$	$Ti_{0.99(1)}Ni_{0.98(1)}Sn$	$Ti_{0.98(1)}Ni_{0.99(1)}Sn$

Half-Heusler space group = $F\bar{4}3m$ – Ti: 4a (0,0,0), occ. refined; Ni(1): 4c (¼, ¼, ¼), occ. 1.00; Ni(2): (¾, ¾, ¾), occ. refined; Sn: 4b (½, ½, ½), occ. 1.00.

Full-Heusler space group = $Fm\bar{3}m$ – Ti: 4a (0,0,0), occ. 1.00; Ni: 8c (¼, ¼, ¼), occ. 1.00; Sn: 4b ((½, ½, ½), occ. 1.00.

Elemental Sn space group = $I41/amd$ (Origin 2) – Sn: 4a (0, ¾, ⅛), occ. 1.00.

Elemental Ti space group = $P63/mmc$ – Ti: 2c (⅓, ⅔, ¼), occ. 1.00.

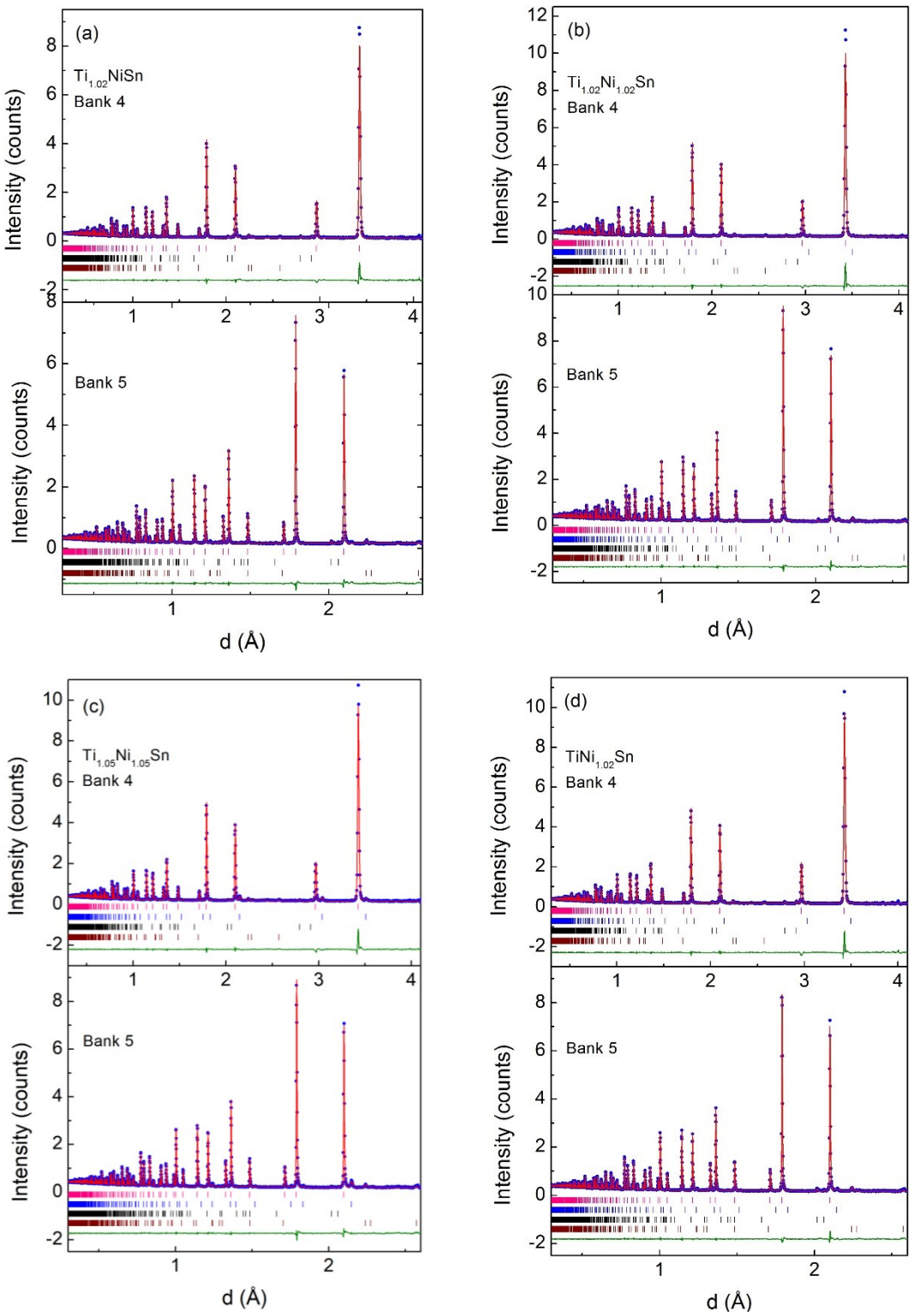

Figure 3.12. Observed (blue circles), calculated (red solid line) and difference (green solid line) Rietveld neutron powder diffraction profiles for **(a)** $Ti_{1.02}NiS$, **(b)** $Ti_{1.02}Ni_{1.02}Sn$, **(c)** $Ti_{1.05}Ni_{1.05}Sn$ and **(d)** $TiNi_{1.02}Sn$. Bragg markers correspond to the phases that were used to fit the pattern (pink: half-Heusler; blue: full-Heusler; black: Sn, brown: Ti). Banks 4 and 5 are the 90º and backscatter detector banks on the Polaris instrument.

Extended crystallographic information and fit statistics can be found in Table 3.5, while the final Rietveld fits are shown in Figure 3.12. In these fits, the occupancies of the *4a* (Ti), *4c* (Ni1) and *4d* (Ni2) sites were varied. This revealed a Ti occupancy of 0.978(2) for all compositions, while the Ni1 site remained fully occupied and was fixed in the final least squares cycles. The main difference between the samples lies in the Ni2-site content which varies between 0.019(1) and 0.058(1). This yields final fitted compositions for the $Ti_{1+x}Ni_{1+y}Sn$ samples of $Ti_{0.98}Ni_{1+y}Sn$ with $0.02 \leq y \leq 0.06$ (Table 3.5). The lattice parameter shows a smooth dependence on the refined amount of excess Ni, confirming the systematic change in structure as the composition is altered (Figure 3.13). Therefore, the excess Ni (y) that occupies vacant *4d* site of each phase can be calculated using following formula: $a_{NPD} = 0.21(3) \times Ni_{4d} + 5.925(1)$.

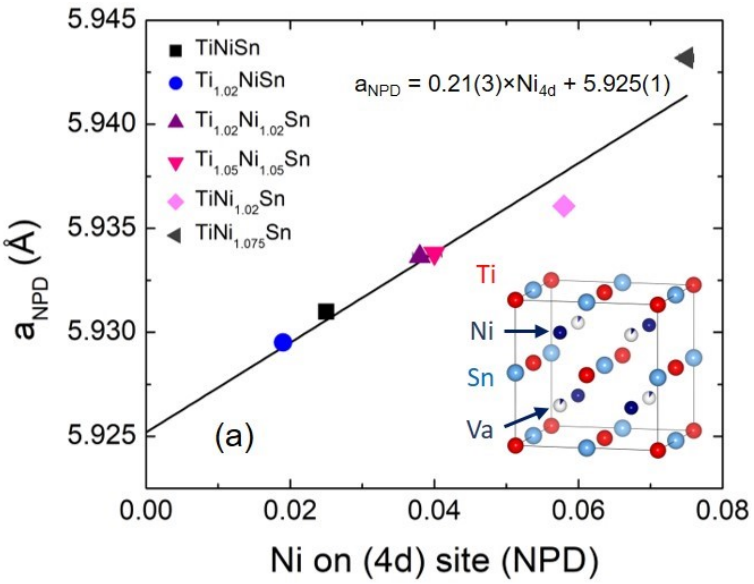

Figure 3.13. Lattice parameter of the half-Heusler phase against excess Ni on the (4d) site identified using neutron powder diffraction. The inset illustrates the half-Heusler structure, including the vacant (Va) site that is partially occupied with excess Ni2.

3.4.3. High-Resolution Synchrotron X-ray Diffraction Study

The SXRD data reveals interesting differences in crystal structure that are caused by hot pressing. As shown in Figure 3.14, the Bragg peaks of compositions prior to the hot pressing are highly symmetric suggesting homogeneous, "strain-free" materials. On the other hand, the Bragg reflections of hot pressed materials show asymmetry and strain-broadening towards higher d-spacing. Recently, Douglas *et. al.*[187] used peak asymmetry

to analyse the distribution of excess Ni within $TiNi_{1+y}Sn$. The peak broadening was fitted using two phases: one of them was "pure" TiNiSn, while the other allowed for Ni interstitials on the 4d site. Here, we extend this idea to model the data using multiple half-Heusler phases. The modified Thompson-Cox-Hastings (TCHZ) function offered by the TOPAS Academics software was used to describe the peak shape. A Si standard was initially evaluated and the resulting profile coefficient were used during the half-Heusler modelling, with exception of Lorentzian (*pky*) component. This coefficient was fixed at *pky* = 0.03, which was chosen as it describes the symmetric Bragg peaks of the samples prior to densification.

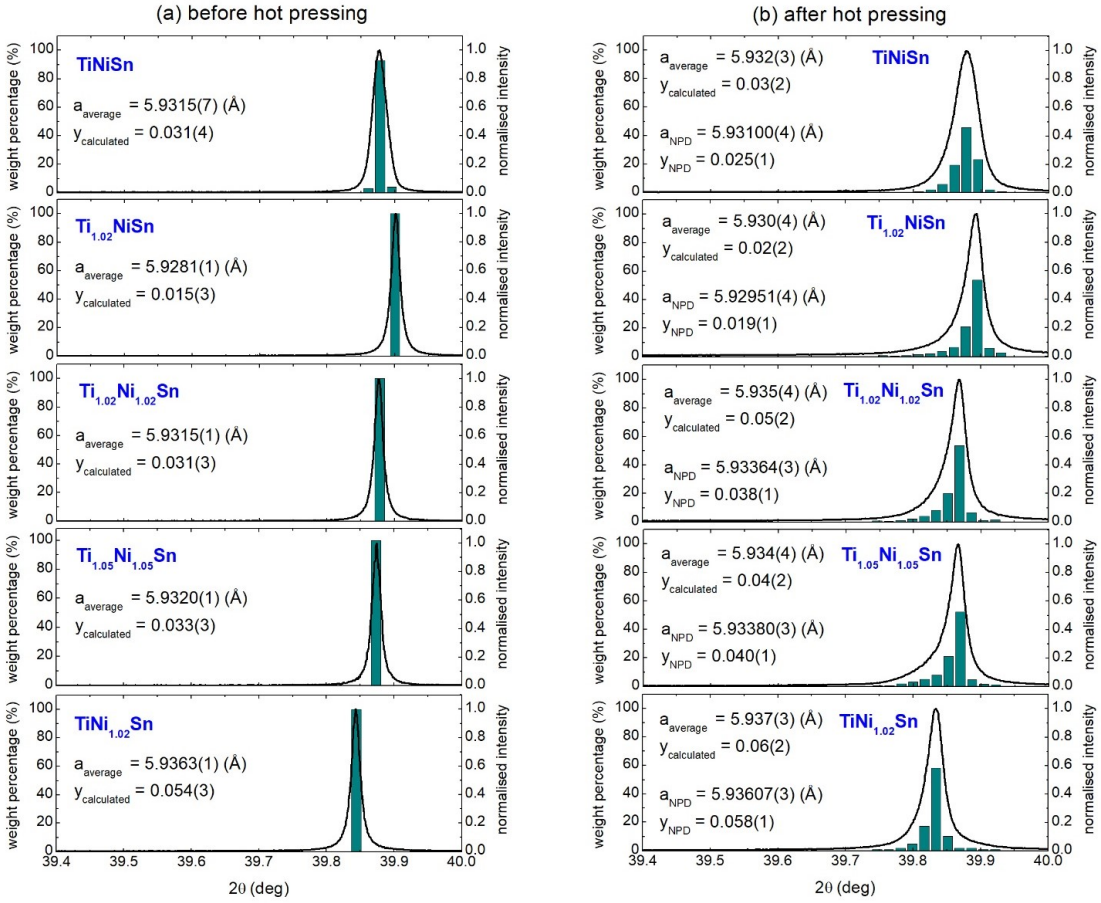

Figure 3.14. Close-up of a representative synchrotron X-ray powder diffraction half-Heusler reflection (422, black line) and the abundance of the half-Heusler phases used to fit the peak shape (green histograms) for the $Ti_{1+x}Ni_{1+y}Sn$ samples **(a)** before and **(b)** after hot pressing. The average lattice parameter ($a_{average}$) and amount of excess Ni ($y_{average}$) are shown for all samples. The lattice parameters (a_{NPD}) and Ni content (y_{NPD}) from NPD are given for comparison and are in excellent agreement.

The excess Ni (y) on the *4d* site of each phase was calculated using the following formula: $a_{NPD} = 0.21(3) \times Ni_{4d} + 5.925(1)$. Linear variation on lattice parameter (Δa) is assumed: $a_n = a_{high} + 0.1n(a_{low} - a_{high})$ where n is the phase number ($0 \leq n \leq 10$) and $\Delta a = 0.0025$Å.

The scale factor of each phase was evaluated from the Bragg reflection area and is shown in the form of histogram (blue columns in Figure 3.14). It is evident that samples prior to the hot pressing can be described using a single half-Heusler phase, while multiple phases are required to model broadening caused by hot pressing. The average lattice parameter ($a_{average}$) and average amount of excess Ni ($y_{average}$) were calculated for each half-Heusler composition. For comparison, the results attained from NPD experiment were included in the relevant panels, with all results presented in Table 3.5. The evaluated compositions are consistent with those obtained from NPD refinement. The average composition does not change upon hot pressing; the main impact is the distribution of the excess Ni, which become less homogeneous. Similarly to $TiNiCu_ySn$ compositions, the peak broadening is attributed to the segregation of Ni. This leads to grain-by-grain compositional variations, with individual grains tending towards either half-Heusler or full-Heusler compositions. Varying amount of excess Ni is trapped in half-Heusler grains resulting in a distribution of half-Heusler parameters. The broadening arises from incoherent summation over all diffracting grains.

3.4.4. Scanning Electron Microscopy

The BSE, SE images and EDX maps for two representative samples ($Ti_{1.05}Ni_{1.05}Sn$ and $TiNi_{1.02}Sn$) are shown in Figure 3.15. Significant amounts of elemental Sn are evident from these images, in agreement with the Rietveld analysis of diffraction data. For $TiNi_{1.02}Sn$ several small regions (~1-5 μm^2) corresponding to $TiNi_2Sn$ were observed, in keeping with the observation of this phase in XRD and NPD. No significant changes in the distribution of Ti, Ni and Sn were detected within the half-Heusler regions, which is as expected given the sensitivity and spatial resolution of the technique. The elemental mapping also revealed the presence of unreacted elemental Ti in these samples. This was not detected in XRD but was evident from the NPD data with a 3-4 wt% abundance (Table 3.5). The half-Heusler compositions obtained from the elemental mapping confirm the Ti and Sn occupancies obtained from the NPD data but show a systematically lower Ni content (Table 3.5). The EDX mapping was performed using internal standards, which can lead to the observed difference.

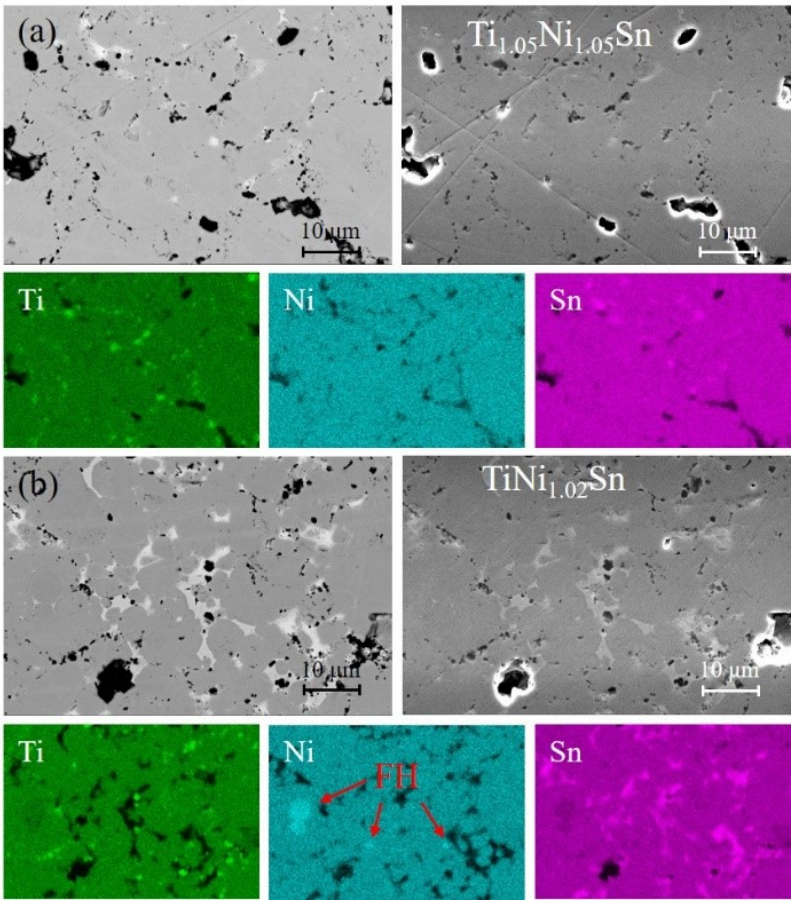

Figure 3.15. Backscattered electron (BSE) microscopy images (left), secondary electron (SE) microscopy images (right) and element-specific EDX maps for **(a)** $Ti_{1.05}Ni_{1.05}Sn$ and **(b)** $TiNi_{1.02}Sn$. The bright areas in the BSE images correspond to elemental Sn, while smaller dark regions correspond to elemental Ti. The $TiNi_{1.02}Sn$ sample contains several small full-Heusler ($TiNi_2Sn$) regions, which are most evident in the Ni elemental map.

3.4.5. Thermoelectric Properties

The temperature dependence of thermoelectric properties for the hot-pressed $Ti_{1+x}Ni_{1+y}Sn$ samples are shown in Figure 3.16. The negative values of S over the whole temperature range indicate n-type conduction. The magnitude of $S(T)$ increases up to about 550 K above which intrinsic carrier excitation occurs, leading to a reduction in magnitude of S. This is typical for TiNiSn due to its narrow band gap.[179]

The $\rho(T)$ are shown in Figure 3.16b and reveal semiconducting behaviour. Clear differences in magnitude are observed near room temperature (eg. 9.2 mΩ cm for $Ti_{1.02}NiSn$, 3.4 mΩ cm for TiNiSn and 3.7 mΩ cm for $TiNi_{1.02}Sn$). Similar values are observed above ~550 K, where intrinsic carrier excitation starts to dominate the electrical transport ($1.5 \leq \rho_{773\ K} \leq 2.0$ mΩ cm). The S^2/ρ are plotted in Figure 3.16c and show a

steady increase up to ~600-650 K with maximum values 2-3 mW m^{-1} K^{-2}, which are comparable to other published work.[101, 109, 129]

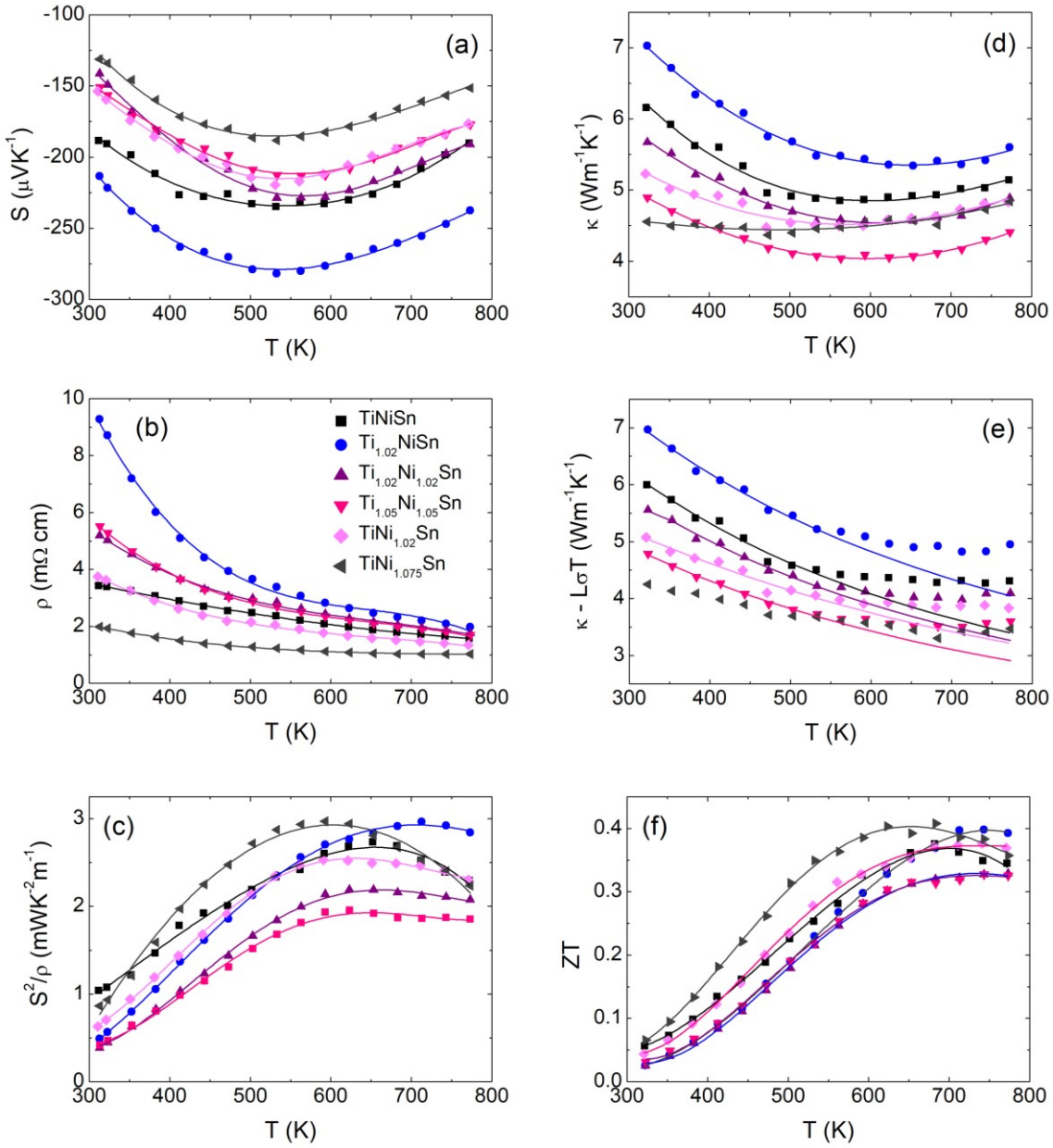

Figure 3.16. Temperature dependence of **(a)** the absolute Seebeck coefficient (S), **(b)** the electrical resistivity (ρ), **(c)** the thermoelectric power factor (S^2/ρ), **(d)** the total thermal conductivity (κ), **(e)** the lattice thermal conductivity ($\kappa - LT/\rho$) and **(f)** the figure of merit ZT for the $Ti_{1+x}Ni_{1+y}Sn$. The solid lines in panel (e) are Debye-Callaway fits in the 323-523 K interval.

The C_p for TiNiSn and the α of all synthesised materials are presented in Figure B2 (Appendix B). The C_p increases steadily with temperature up to 773 K. The α decreases with temperature until it reaches the intrinsic carrier excitation point (550 – 650 K), above which the values increase due to the bipolar transport of heat.[29] The $\kappa(T)$ for all investigated compounds are displayed in Figure 3.16d. The $\kappa(T)$ mimics the diffusivity and decreases up to 550 – 650 K, followed by an increase due to the bipolar contribution. The electronic thermal conductivity was calculated using $\kappa_{el} = LT/\rho$, where the Lorenz number L was estimated from $S(T)$ using Equation 2.30 and is shown in Figure B2 (Appendix B). The room temperature L values are similar for all samples and were kept constant during the κ_{el} calculations, over the whole temperature range. The calculated $\kappa - \kappa_{el}$ is shown in Figure 3.16e. A significant variation in magnitude is observed with values between 5-7 W m^{-1} K^{-1} at 323 K. We note that these values are lower than for stoichiometric ZrNiSn (κ = 17.2 W m^{-1} K^{-1}) and HfNiSn (κ = 14.5 W m^{-1} K^{-1}).[181]

Table 3.6. 323 – 550 K Callaway fit parameters for the off-stoichiometric $Ti_{1+x}Ni_{1+y}Sn$ samples. The *4d* site occupancy was taken from Rietveld fits to the neutron powder diffraction data. Γ and Γ_{exp} are calculated (Equation 3.1) and fitted point-defect scattering parameters.

Composition	*4d*-site occupancy	κ_{323K}-LT/ρ (W m^{-1} K^{-1})	Γ	Γ_{exp}
TiNiSn	$Ni_{0.025(1)}$	6.0	0.06	0.06
$Ti_{1.02}NiSn$	$Ni_{0.019(1)}$	7.0	0.04	0.04
$Ti_{1.02}Ni_{1.02}Sn$	$Ni_{0.038(1)}$	5.5	0.09	0.07
$Ti_{1.05}Ni_{1.05}Sn$	$Ni_{0.040(1)}$	4.8	0.09	0.10
$TiNi_{1.02}Sn$	$Ni_{0.058(1)}$	5.1	0.13	0.09

For all fits: B = 5 μm and $B_U = 2.1 \times 10^{-18}$ *S* K

The Callaway model (see Section 2.4.3.2 for details) was used to investigate the variation and magnitude of $\kappa_{lattice}$(T), An initial fit for TiNiSn using L = 5 μm yielded the Γ_{exp} = 0.06 and $B_U = 2.1 \times 10^{-18}$ S K^{-1}. For the remaining samples, L and B_U were kept fixed, while the point defect scattering pre-factor was used to quantify the differences between the samples. The high-quality fits are shown in Figure 3.16e, while the final fitted parameters are listed in Table 3.6. Variation in Γ_{exp} demonstrates that the reduction of $\kappa_{lattice}(T)$ is due to an increase in point defect scattering. The typical sources for point defect scattering are alloying, vacancies and interstitials. The values obtained here fall

between $0.04 < \Gamma_{exp} < 0.10$. The Γ calculated using the method described in Section 3.3.5 are found to be in good agreement with the experimental Γ_{exp}, confirming interstitials as a source of point defect scattering. The Γ_{exp} are large values that are comparable to those obtained from mixing of Ti, Zr and Hf on a single crystallographic site.[86] The large Γ_{exp} values demonstrate that the excess Ni in TiNiSn is highly effective at disrupting the thermal transport.

The temperature dependence of the figure of merit ZT is presented in Figure 3.16f. A gradual increase up to 550-723 K is observed, which coincides with the maximum in S^2/ρ (Figure 3.16c). The maximum ZT values are between $0.30 \leq ZT \leq 0.40$ at elevated temperature, while the room temperature values are between approximately $ZT = 0.03$ and $ZT = 0.06$.

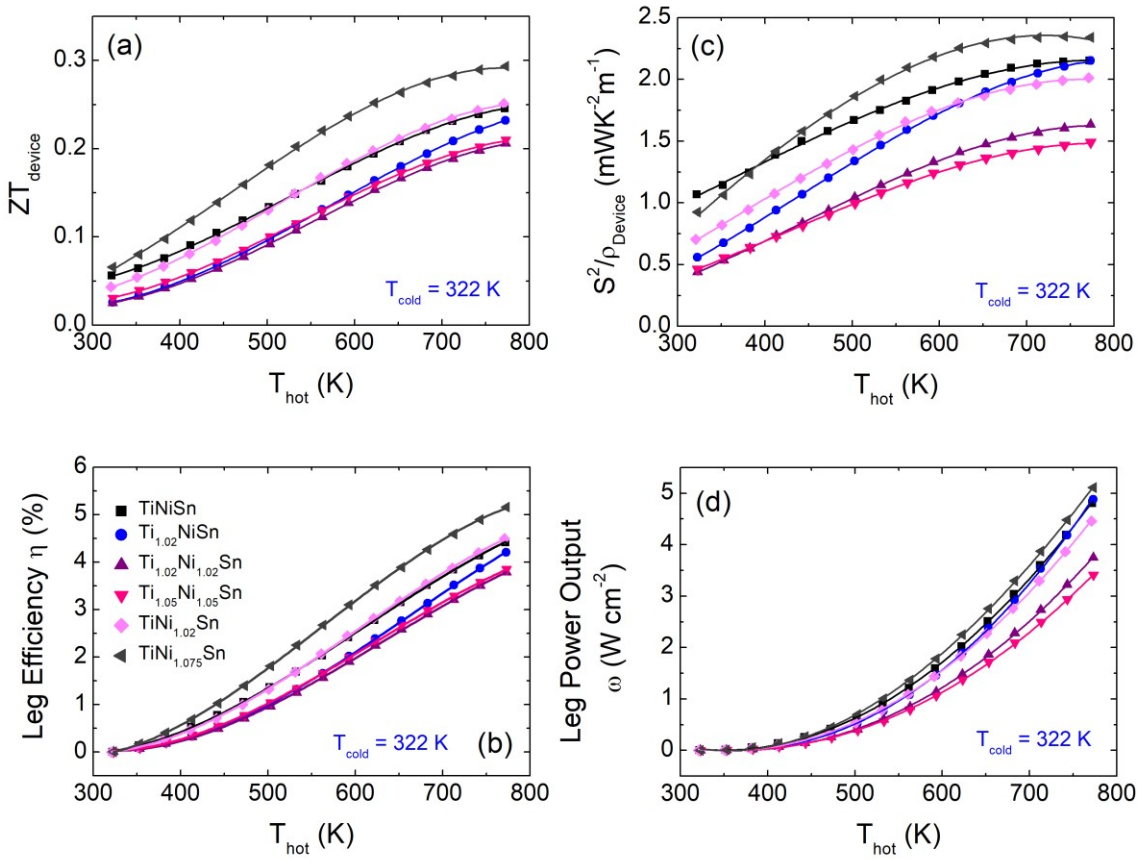

Figure 3.17. Temperature dependence of **(a)** ZT_{device} **(b)** the efficiency (η), **(c)** PF_{device} and **(d)** the power output (ω) for the $Ti_{1+x}Ni_{1+y}Sn$ samples as a function of hot-side temperature (T_{hot}). T_{cold} denotes the cold-side temperature.

The temperature dependence of ZT_{device}, PF_{device}, the leg efficiencies and leg power outputs are shown in Figure 3.17. The best ZT_{device} = 0.25 and 4.5% leg efficiency from a 450 K temperature gradient were observed for TiNiSn and $TiNi_{1.02}Sn$, while ZT_{device} = 0.3 and 5% efficiency were observed for $TiNi_{1.075}Sn$ from the same temperature gradient (Figure 3.17a, b). The PF_{device} are plotted in Figure 3.17c and reveals steady increase with maximum values 1.5 – 2.3 mW m^{-1} K^{-2} at 773 K. The leg power output varies from 3.5 W cm^{-2} for $Ti_{1.05}Ni_{1.05}Sn$ to 5 W cm^{-1} for $TiNi_{1.075}Sn$, TiNiSn and $Ti_{1.02}NiSn$ from a 450K temperature gradient and using length of thermoelectric leg of 0.2 cm (Figure 3.17d).

3.4.6. Discussion

The investigation of $Ti_{1+x}Ni_{1+y}Sn$ compositions reveals that it is difficult to prepare stoichiometric TiNiSn. Rietveld refinement of neutron powder diffraction data revealed that between 2-6% excess Ni occupies the *4d* site of the half-Heusler structure. The presence of full-Heusler and elemental Sn and Ti suggests that this may be caused by an incomplete reaction of the starting reagents. Computational studies indicate a limited solubility of excess Ni in the half-Heusler structure and suggest a segregation of the excess Ni into full-Heusler phases.[105, 115, 188] Analysis of the peak shapes of the high-resolution synchrotron X-ray diffraction data before and after hot pressing revealed a pronounced asymmetric broadening towards larger *d*-spacing upon consolidation. The symmetric peak shape prior to hot pressing is in keeping with a homogeneous distribution of the excess Ni. Hot pressing leads to the migration of excess Ni and the tendency to form either half-Heusler or full-Heusler compositions. At this point variations in local composition occur and these give rise to non-uniform strain and the observed peak broadening. Quantitative analysis reveals a 5-6 times increased compositional variation in the hot-pressed samples without altering the average composition of the half-Heusler phase.

The effect of Ni doping on the transport properties of TiNiSn was investigated by several groups.[60, 109, 178] Some authors[100, 116, 119] observed simultaneous enhancement of *S* with minor σ reduction upon introduction of excess Ni, explained by the formation of full-Heusler nano-inclusions. TEM analysis of $TiNiCu_ySn$ did not reveal any full-Heusler segregation, suggesting that introduction of excess metal influences transport properties of samples presented here in a different way. No simultaneous enhancement of *S* and σ was observed. Instead, the gradual decrease in *S* and ρ (consistent with carrier doping) were observed. This can be explained by the presence of randomly distributed excess Ni

on the interstitial *4d*-site, which act as an n-type dopant. Similarly to Cu-doped TiNiSn, excess Ni influences the thermal transport. Callaway fitting revealed that the $\kappa_{lattice}$ reduction is due to interstitial Ni metals. The Γ value increases with Ni content on the *4d*-site (Table 3.6) confirming interstitials as a source of point defect scattering.

3.5. Conclusions

The main focus of this Chapter was the investigation of the Cu-rich $TiNiCu_ySn$ half-Heuslers as well as to establish the effect of excess Ni on thermoelectric properties of TiNiSn. The presence of excess metal leads to a reduction of the $\kappa_{lattice}$ and enhanced S^2/ρ. Cu is a much more effective n-type dopant than Ni, leading to more dramatic change in ρ(T) and significant increase of S^2/ρ. Rietveld refinement of NPD data revealed that both, Ni and Cu occupy the normally vacant *4d*-site of half-Heusler matrix. However, Cu possesses an additional electron. This electron is transferred to the half-Heusler CB and is responsible for the transition to metallic behaviour upon Cu addition. An important conclusion from the TEM of $TiNiCu_ySn$ is that there is no evidence for nanoscale full-Heusler inclusions. Instead, Cu forms grain-by-grain compositional variations and Cu-rich grain boundaries. In both studies, the Callaway fitting suggests that the reduction of $\kappa_{lattice}$ is due to the presence of interstitial metals, which act as a point-defect centres of phonons. The materials power outputs are comparable to state-of-the-art half-Heusler alloys, but are characterised by lower efficiencies. High ZT_{device} require low $\kappa(T)$, while power output relies on having a large PF_{device} but also on the magnitude of $\kappa(T)$ due to the coupled nature of the flow of heat and charge.[185] However, compositions reported in this Chapter do not contain expensive elements (Zr and Hf). The synthesis protocol is straightforward and cost-effective, suggesting these samples are suitable candidates for large scale fabrication and application in thermoelectric generators. The findings presented in this Chapter form the basis of the work presented in the remaining part of this thesis. Chapter 4 explores the effect of excess Cu in single-phased $MNiCu_{0.075}Sn$ and multiphase $M_{0.5}M'_{0.5}NiCu_{0.075}Sn$ and $Ti_{0.5}Zr_{0.25}Hf_{0.25}NiCu_ySn$ ($0 \leq y \leq 0.075$) half-Heusler. Chapter 5 investigates the formation of Ni-rich $TiNi_{1+y}Sn$ (y = 0, 0.075 and 0.25) and multiphase $M_{0.5}M'_{0.5}NiSn$ samples during solid-state reaction. In addition, the distribution of excess Ni within the half-Heusler matrix was analysed using the pair distribution function method, which is discussed in Chapter 6.

Chapter 4 - Impact of excess Cu on the thermoelectric properties of $MNiCu_{0.075}Sn$, $M_{0.5}M'_{0.5}NiCu_{0.075}Sn$ (M = Ti, Zr, Hf) and $Ti_{0.5}Zr_{0.25}Hf_{0.25}NiCu_ySn$ ($0 \leq y \leq 0.075$)

4.1. Introduction

The investigation of a series of Cu-rich $MNiCu_{0.075}Sn$, $M_{0.5}M'_{0.5}NiCu_{0.075}Sn$ (M = Ti, Zr, Hf,) and $Ti_{0.5}Zr_{0.25}Hf_{0.25}NiCu_ySn$ ($0 \leq y \leq 0.075$) half-Heuslers was motivated by the promising properties of the $TiNiCu_ySn$ half-Heusler alloys. Detailed structural characterisation revealed that grain-by-grain compositional variations and the excess metal randomly distributed on the interstitial site of the TiNiSn matrix, can be used to enhance electrical properties and reduce the thermal conductivity. It was found that only a small amount of excess Cu (< 10%) is needed to achieve the optimal performance with the power factors $S^2/\rho = 2 - 4$ mW m^{-1} K^{-2} and lattice thermal conductivities $\kappa_{lattice}$ = 4-5 W m^{-1} K^{-1}. Another method to reduce $\kappa_{lattice}$ is the substitution of Ti with a heavier element such as Zr or Hf. In addition to the regular reduction of $\kappa_{lattice}$ due to alloying, so-called multiphase behaviour occurs. The multiphase behaviour, which occurs on the micrometre-scale is thought to be responsible for enhanced scattering of long-wavelength phonons.[63, 70-74] In 2005 a high ZT = 1.5 at 700 K for $Ti_{0.5}Zr_{0.25}Hf_{0.25}NiSn_{0.998}Sb_{0.002}$ was observed,[189] however this could not be reproduced and is categorised as unexplained.[78] Recently, ZT = 1.2 at 830 K was achieved in the n-type $Ti_{0.5}Zr_{0.25}Hf_{0.25}NiSn_{0.998}Sb_{0.002}$[71] and ZT = 1.2 at 983 K for the p-type $Ti_{0.25}Hf_{0.75}CoSb_{0.85}Sn_{0.15}$.[63] Therefore, the aim of this work was to investigate the effect of excess Cu on the microstructure and the thermoelectric properties of $MNiCu_ySn$ with mixtures of Ti, Zr and Hf. In the first part of this chapter, the single-phased $MNiCu_{0.075}Sn$ and multiphase $M_{0.5}M'_{0.5}NiCu_{0.075}Sn$ were investigated, while the second part focuses on multiphase $Ti_{0.5}Zr_{0.25}Hf_{0.25}NiCu_ySn$ with varying amount of Cu content. All prepared compositions were characterised using SXRD, NPD and electron microscopy.

4.2. Synthesis and Characterisation

Samples with the nominal composition of $MNiCu_{0.075}Sn$, $M_{0.5}M'_{0.5}NiCu_{0.075}Sn$ (M = Ti, Zr, Hf,) and $Ti_{0.5}Zr_{0.25}Hf_{0.25}NiCu_ySn$ ($0 \leq y \leq 0.075$) were prepared via solid-state reaction. Prepared samples were sealed in an evacuated quartz tube and initially annealed

at 850 °C for 24 hours. The samples were then re-homogenised and annealed at 850 °C for additional 2 weeks. The hot-pressing was carried out at 900 °C and 80 MPa for 20 minutes. One disk was used for the electrical properties measurement, while the second one for a diffusivity measurement. Additional batches of $MNiCu_{0.075}Sn$, $M_{0.5}M'_{0.5}NiCu_{0.075}Sn$ (M = Ti, Zr, Hf,) and $Ti_{0.5}Zr_{0.25}Hf_{0.25}NiCu_ySn$ (y = 0.025, 0.05 and 0.075) were prepared for SXRD and NPD experiments.

4.3. $MNiCu_{0.075}Sn$ and $M_{0.5}M'_{0.5}NiCu_{0.075}Sn$ (M = Ti, Zr, Hf,)

4.3.1. Neutron Powder Diffraction

NPD was performed to determine the composition of hot-pressed samples, as any deviation from the nominal value may have an impact on the thermoelectric properties. Rietveld fits for all materials are provided in Figure 4.1, with final compositions presented in Table 4.1 and detailed crystal structure information included in Appendix C.

Table 4.1. Lattice parameter (*a*) and weight percentage (*wt%*) for the half-Heusler, full-Heusler MNi_2Sn, Ti, Ni_3Sn_2 and CuSn phases, which were used during the Rietveld refinement for neutron powder diffraction data.

$MNiCu_{0.075}Sn$						
	Half-Heusler			**MNi_2Sn**	**Ti**	**Ni_3Sn_2**
	a (Å)	**wt%**	**Composition**	**wt%**	**wt%**	**wt%**
M =Ti	5.94603(4)	95.1(2)	$TiNi[Ni_{0.03}Cu_{0.072(1)}]Sn$		4.9(2)	
M = Zr	6.10864(3)	94.9(1)	$ZrNi[Cu_{0.022(1)}]Sn$			5.1(1)
M = Hf	6.07716(4)	96.7(1)	$HfNi[Cu_{0.023(1)}]Sn$	2.7(1)		0.5(2)
$M_{0.5}M'_{0.5}NiCu_{0.075}Sn$						
	Half-Heusler			**MNi_2Sn**		**CuSn**
	a (Å)	**wt%**	**Composition**	**wt%**		**wt%**
M = Ti, M' = Zr	6.03452(5)	99.3(1)	$Ti_{0.522(2)}Zr_{0.478(2)}Ni[Ni_{0.03}Cu_{0.061(2)}]Sn$			0.7(1)
M = Ti, M' = Hf	6.01314(4)	96.0(1)	$Ti_{0.473(2)}Hf_{0.527(2)}Ni[Cu_{0.036(1)}]Sn$	2.6(1)		0.9(1)
M = Zr, M' = Hf	6.09372(4)	96.8(1)	$Zr_{0.5}Hf_{0.5}Ni[Cu_{0.024(1)}]Sn$	2.4(1)		0.8(1)

4.3.1.1. $MNiCu_{0.075}Sn$ (M = Ti, Zr, Hf)

Rietveld fits to the NPD data of $MNiCu_{0.075}Sn$ are shown in Figure 4.1 (a-c). All main Bragg reflections were indexed to the half-Heusler structure. A small amount of $HfNi_2Sn$ (2.7(1) wt%) was identified for the M = Hf composition, while small amount (4.9(2) wt%) of elemental Ti was observed for the M = Ti sample. The half-Heusler phase was modelled using a metal-rich half-Heusler structure with the *4c* (¼, ¼, ¼) site fully occupied by Ni and excess Cu placed on the vacant *4d* (¾, ¾, ¾) site. The $TiNiCu_ySn$

series was discussed in Chapter 3 and with the final composition $TiNi_{1.03}Cu_{0.072}Sn$ attained for the M = Ti sample. Surprisingly, the free refinement of the occupancy of *4d* site in $ZrNiCu_{0.075}Sn$ and $HfNiCu_{0.075}Sn$ revealed that only 2.2 – 2.3% of Cu entered the half-Heusler matrix (Table 4.1). This is unexpectedly low and suggests the formation of Cu-containing impurities, which were not observed in the NPD data. Detailed electron microscopy analysis is required to investigate this further.

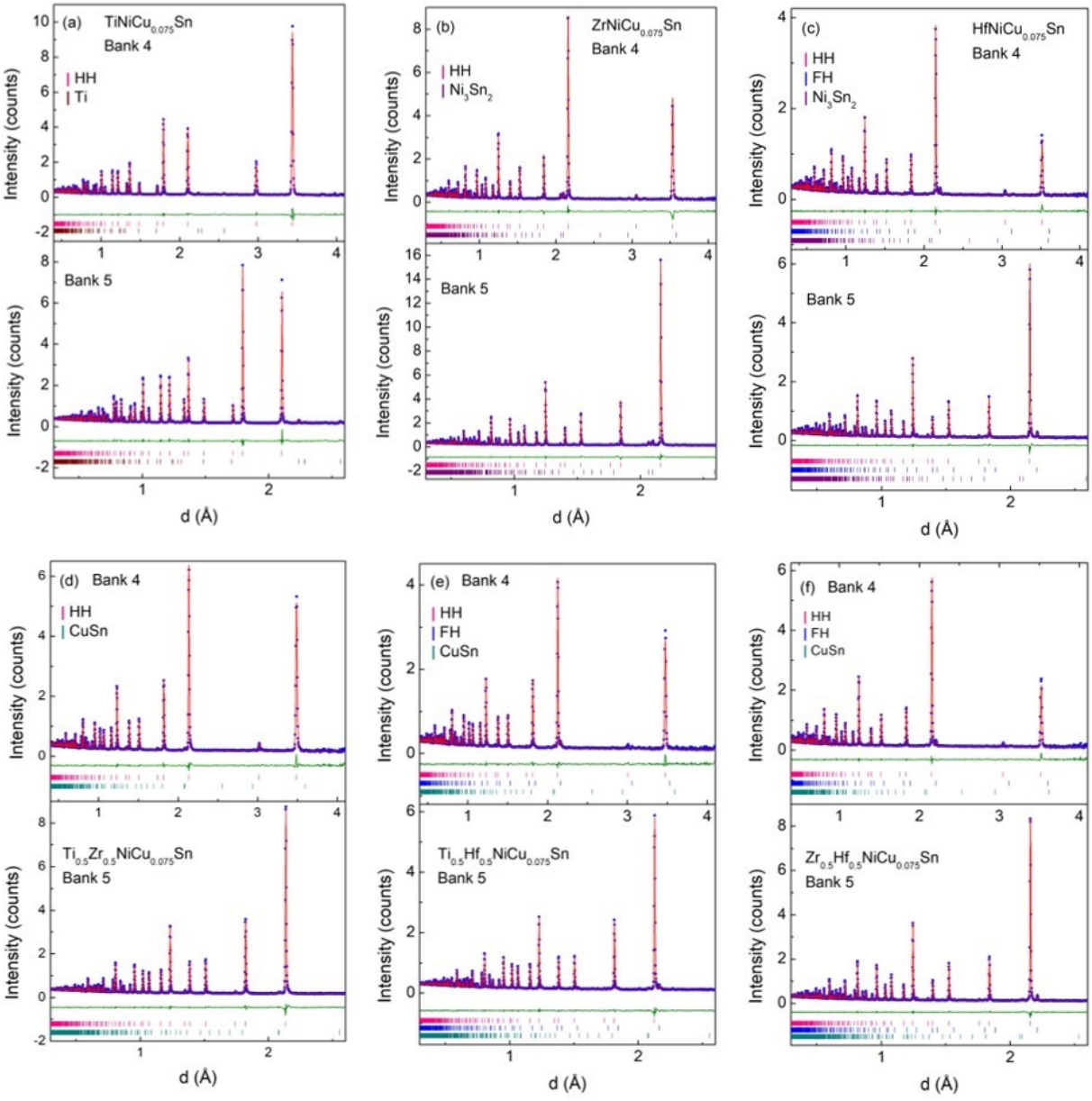

Figure 4.1. Observed (blue circles), calculated (red solid line) and difference (green solid line) Rietveld neutron powder diffraction profiles for **(a)** $TiNiCu_{0.075}Sn$, **(b)** $ZrNiCu_{0.075}Sn$, **(c)** $HfNiCu_{0.075}Sn$, **(d)** $Ti_{0.5}Zr_{0.5}NiCu_{0.075}Sn$, **(e)** $Ti_{0.5}Hf_{0.5}NiCu_{0.075}Sn$ and **(f)** $Zr_{0.5}Hf_{0.5}NiCu_{0.075}Sn$. Bragg markers correspond to the phases that were used to fit the pattern (pink: half-Heusler; blue: full-Heusler; brown: Ti, purple: Ni_3Sn_2 and light blue: CuSn). Banks 4 and 5 are the 90º and backscattered detector banks, respectively.

4.3.1.2. $M_{0.5}M'_{0.5}NiCu_{0.075}Sn$ (M = Ti, Zr, Hf)

The $M_{0.5}M'_{0.5}NiCu_{0.075}Sn$ compositions were investigated in a similar manner to the $MNiCu_{0.075}Sn$ samples. Analysis confirmed that the half-Heusler is the main phase, an additional full-Heusler phase was identified for $Ti_{0.5}Hf_{0.5}NiCu_{0.075}Sn$ and $Zr_{0.5}Hf_{0.5}NiCu_{0.075}Sn$, while CuSn (~1 wt%) was observed for all compositions. The starting point for Rietveld refinement was a stoichiometric $M_{0.5}M'_{0.5}NiCu_{0.075}Sn$ model. A constraint was applied to maintain 100% occupancy of *4a*, *4b* and *4c* site, while the Cu content on the normally vacant *4d* site was allowed to refine freely. In addition, a constraint was introduced for the thermal displacement parameters (U_{iso}) of half-Heusler phase: a single U_{iso} was used for M and M' elements, a single U_{iso} was used for Ni and Cu and a single U_{iso} was used for Sn. The refined occupancies have confirmed that nominal M:M' ratio was maintained. For $Ti_{0.5}Zr_{0.5}NiCu_{0.075}Sn$, 3% of excess Ni was observed, bringing the Cu content close to the nominal value (y = 0.063(1)). The Cu content for the remaining samples was lower (~2.5 – 3.5%), which can be explained by the formation of CuSn (0.7 – 0.9 wt%) impurity. Recently, Downie *et al*.[85] investigated $M_{0.5}M'_{0.5}NiSn$ compositions using NPD and found that 4 distinct half-Heusler phases were required to model $Ti_{0.5}Zr_{0.5}NiSn$ and $Ti_{0.5}Hf_{0.5}NiSn$, while a single half-Heusler phase was sufficient to describe $Zr_{0.5}Hf_{0.5}NiSn$. The above result suggests that Cu acts as a mineraliser, which improves the sintering of elemental precursors and formation of single-phased half-Heusler alloys. As can be seen from Figure 4.1 (d-f), all patterns are well described by the single half-Heusler phase, which represents an adequate powder average. The average experimental compositions are summarised in Table 4.1, while the refined lattice parameter and thermal displacement factor for each phase, along with the fit statistics, are given in Table C2 (Appendix C).

4.3.2. High-resolution Synchrotron X-ray Diffraction Study

SXRD was used to investigate peak broadening due to the compositional variations and to evaluate the impact of hot-pressing on the crystal structure of $MNiCu_{0.075}Sn$ and $M_{0.5}M'_{0.5}NiCu_{0.075}Sn$ compositions. Figure 4.2 shows the SXRD patterns for samples before and after hot pressing. The half-Heusler structure was analysed using the approach described in Section 3.4.3, with the number of half-Heusler phases n in the range $0 \leq n \leq 20$ and lattice parameter difference $\Delta a = 0.0025$ Å. Focusing on the M = Ti, Zr and Hf samples, the Bragg reflections for samples before hot-pressing are sharp and symmetric suggesting single phase, highly homogeneous, strain-free materials. On the other hand,

the Bragg peaks of hot-pressed $MNiCu_{0.075}Sn$ materials show slight broadening (FWHM increases upon hot pressing), suggesting a redistribution of excess Cu within the half-Heusler matrix (Figure 4.3). The segregation of Cu leads to grain-by-grain compositional variations. Individual grains tend towards either half-Heusler or full-Heusler compositions.

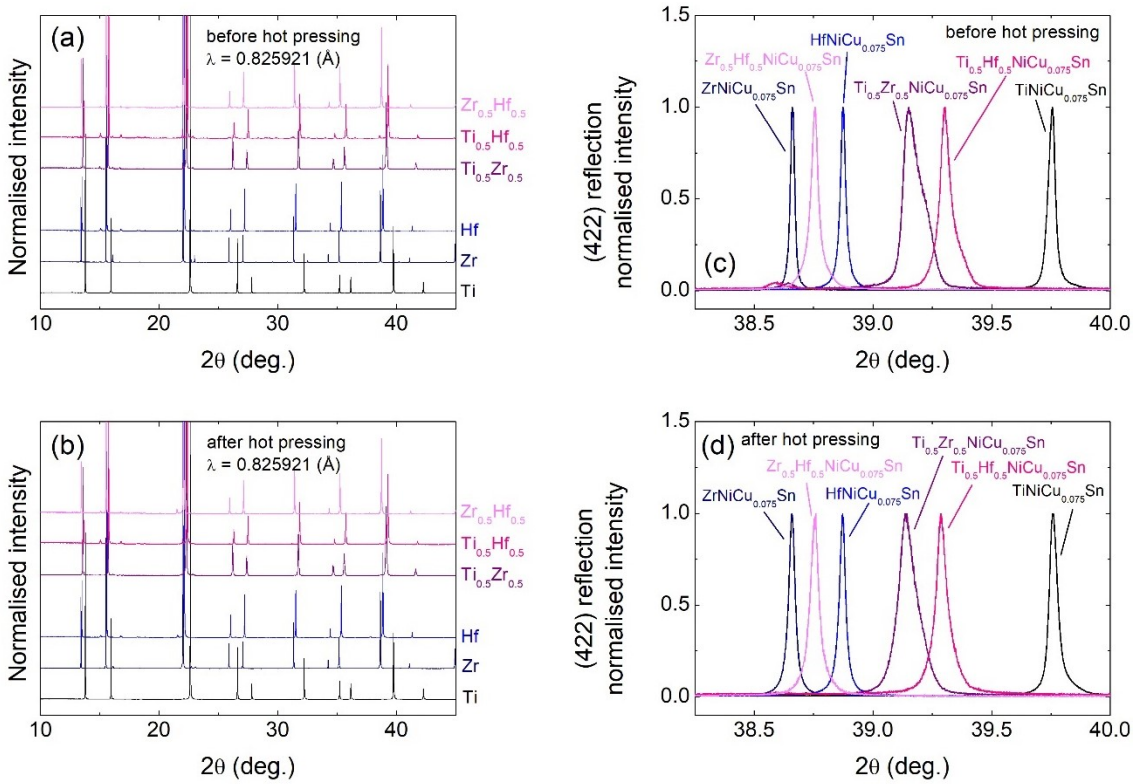

Figure 4.2. (a-b) High-resolution synchrotron X-ray powder diffraction patterns for $MNiCu_{0.075}Sn$ and $M_{0.5}M'_{0.5}NiCu_{0.075}Sn$ samples before and after hot-pressing. All main peaks can be indexed on the half-Heusler structure. **(c-d)** Close-up of the diffraction peak for the (422) half-Heusler reflection.

The NPD patterns collected for $M_{0.5}M'_{0.5}NiCu_{0.075}Sn$ samples were modelled using a single, Cu-rich phase. There was no evidence of peak broadening and formation of multiple half-Heusler phases. The SXRD revealed much more complicated compositional variation than indicated by the NPD. The main reflections for all $M_{0.5}M'_{0.5}NiCu_{0.075}Sn$ samples are significantly broader compared to $MNiCu_{0.075}Sn$ and had to be modelled using multiple half-Heusler phases (Figure 4.3). This suggests a complex microstructure that is not well described by the average model, offered by the powder diffraction techniques.

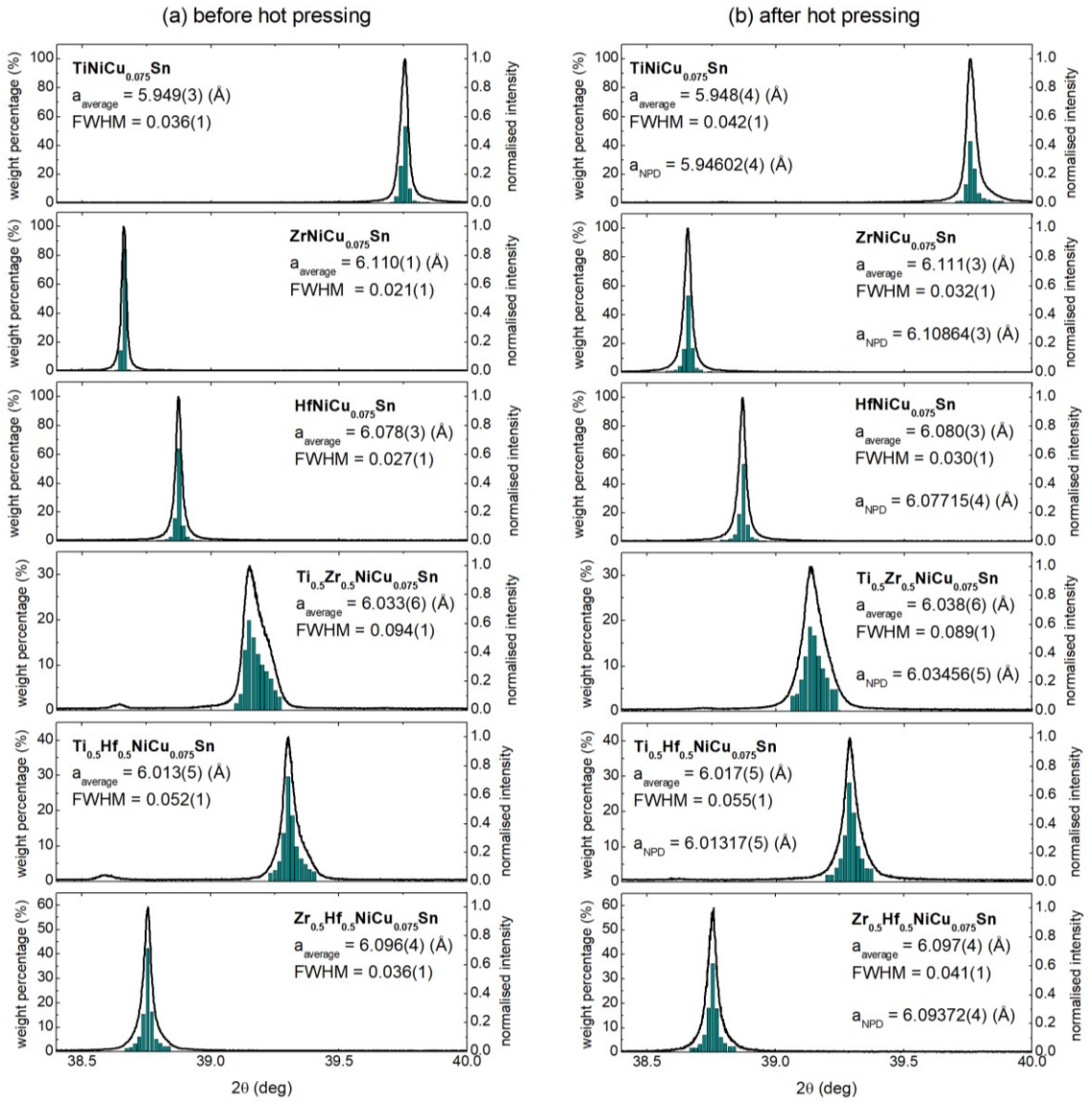

Figure 4.3. Close-up of a representative synchrotron X-ray powder diffraction half-Heusler reflection (422, black line) and the abundance of the half-Heusler phases used to fit the peak shape (green histograms) for the $MNiCu_{0.075}Sn$ and $M_{0.5}M'_{0.5}NiCu_{0.075}Sn$ samples **(a)** before and **(b)** after hot pressing. The average lattice parameter ($a_{average}$) is shown for all samples. The lattice parameters (a_{NPD}) from NPD is given for comparison and is in excellent agreement. The FWHM denotes the full width at half maximum.

The average lattice parameter ($a_{average}$) was calculated for each sample. For comparison, the results attained from NPD experiment are included in the relevant panels, showing excellent agreement. For all samples, the $a_{average}$ does not change upon hot-pressing, confirming that the crystal structure is not affected by consolidation. The main impact is the distribution of the excess Cu. Similarly to $TiNiCu_ySn$ series, the peak broadening is

attributed to the segregation of Cu and grain-by-grain compositional variations. Individual grains tend towards either half-Heusler or full-Heusler compositions, with varying amount of excess Cu trapped in the grains. The observed diffraction peaks arise from incoherent summation over all diffracting grains.

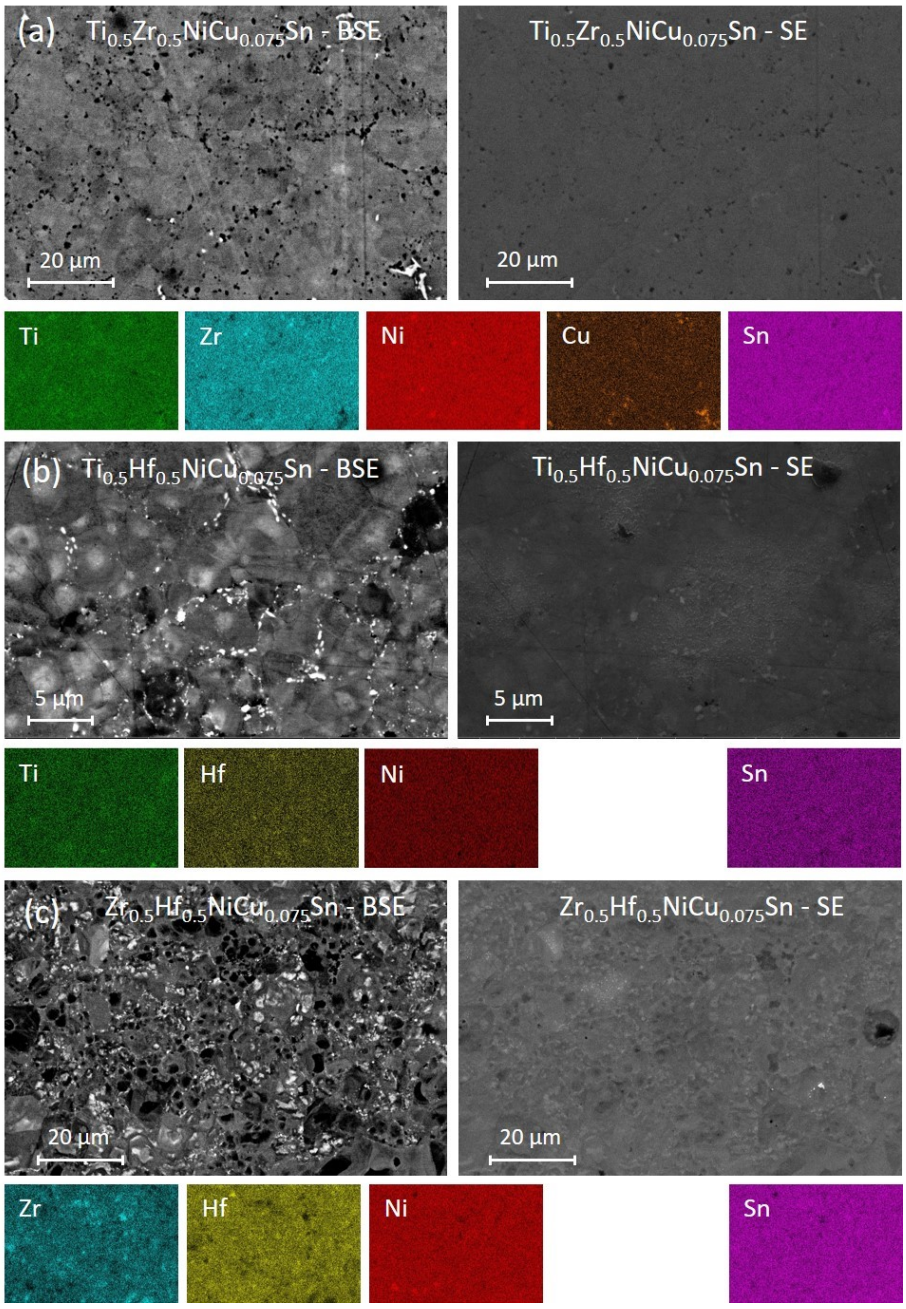

Figure 4.4. Backscattered electron (BSE) microscopy images (left), secondary electron (SE) microscopy images (right) and element-specific EDX maps for **(a)** $Ti_{0.5}Zr_{0.5}NiCu_{0.075}Sn$, **(b)** $Ti_{0.5}Hf_{0.5}NiCu_{0.075}Sn$ and **(c)** $Zr_{0.5}Hf_{0.5}NiCu_{0.075}Sn$.

4.3.3. Scanning Electron Microscopy

SEM and EDX were used to investigate the microstructure and composition of $Ti_{0.5}Zr_{0.5}NiCu_{0.075}Sn$, $Ti_{0.5}Hf_{0.5}NiCu_{0.075}Sn$ and $Zr_{0.5}Hf_{0.5}NiCu_{0.075}Sn$ samples. The morphology of $Ti_{0.5}Zr_{0.5}NiCu_{0.075}Sn$ is presented in Figure 4.4a. The image shows complex structure that consists of at least 3 half-Heusler phases. EDX mapping was used to estimate the compositions. It revealed Zr-rich, Ti-rich and (Ti,Zr)-mixed half-Heusler phases. No clear boundaries between phases are observed. The small white spots detected by BSE image are related to a Cu-rich phase (perhaps CuSn), suggesting incomplete reaction or poor mixing of elemental precursors. There is no evidence of voids or holes between the grains, consistent with full densification. The SEM-EDX images of $Ti_{0.5}Hf_{0.5}NiCu_{0.075}Sn$ are shown in Figure 4.4b. Analysis of BSE image and EDX maps revealed Hf-rich (white grains), (Ti,Hf)-mixed (grey region) and Ti-rich (dark grey area) half-Heusler phases. The dark (black) spots are identified as Ti-based alloys. Again, lack of voids and holes confirms full densification. Focusing on $Zr_{0.5}Hf_{0.5}NiCu_{0.075}Sn$, due to the lanthanide contraction, Zr and Hf have nearly the same atomic radii. Therefore ZrNiSn and HfNiSn are expected to be fully miscible, form solid solution and single phase (Zr,Hf)NiSn half-Heusler alloy.[70, 75-77, 190] However our data (Figure 4.4c) reveals that the morphology of $Zr_{0.5}Hf_{0.5}NiCu_{0.075}Sn$ is much more complex and single phase material is not formed. EDX analysis revealed Hf-rich (white grains), (Zr,Hf)-mixed (grey region) and Zr-rich (black area) half-Heusler phases. Such different crystal structure could be related to the solid-state synthesis protocol, which does not occur through the melt. Similarly to $Ti_{0.5}Zr_{0.5}NiCu_{0.075}Sn$ and $Ti_{0.5}Hf_{0.5}NiCu_{0.075}Sn$, no clear boundaries are observed between the phases. In addition, there is no evidence of voids or holes, consistent with full densification.

4.3.4. Thermoelectric Properties

The temperature dependence of S, ρ, S^2/ρ, κ, $\kappa - LT/\rho$ and ZT for the hot-pressed $MNiCu_{0.075}Sn$ and $M_{0.5}M'_{0.5}NiCu_{0.075}Sn$ (M = Ti, Zr, Hf) samples are shown in Figure 4.5. The thermoelectric properties of un-doped compositions are shown for comparison in Appendix D. All samples are n-type semiconductors, as indicated by the negative value of $S(T)$. The magnitude of S increases with temperature, reaching a maximum at ~650 K for $HfNiCu_{0.075}Sn$ and $Zr_{0.5}Hf_{0.5}NiCu_{0.075}Sn$. The ρ values follow the S values as expected, i.e., the higher the S value, the higher the ρ value. The temperature dependence of $\rho(T)$ changes upon Cu doping. The parent materials (see Figure D6, Appendix D) are non-

degenerate semiconductors with decreasing $\rho(T)$. The $\rho(T)$ for Cu-doped samples is characterised by metal-like conduction behaviour (Figure 4.5b). The introduction of Cu reduces the electrical resistivity of the material, acting as an effective n-type dopant.

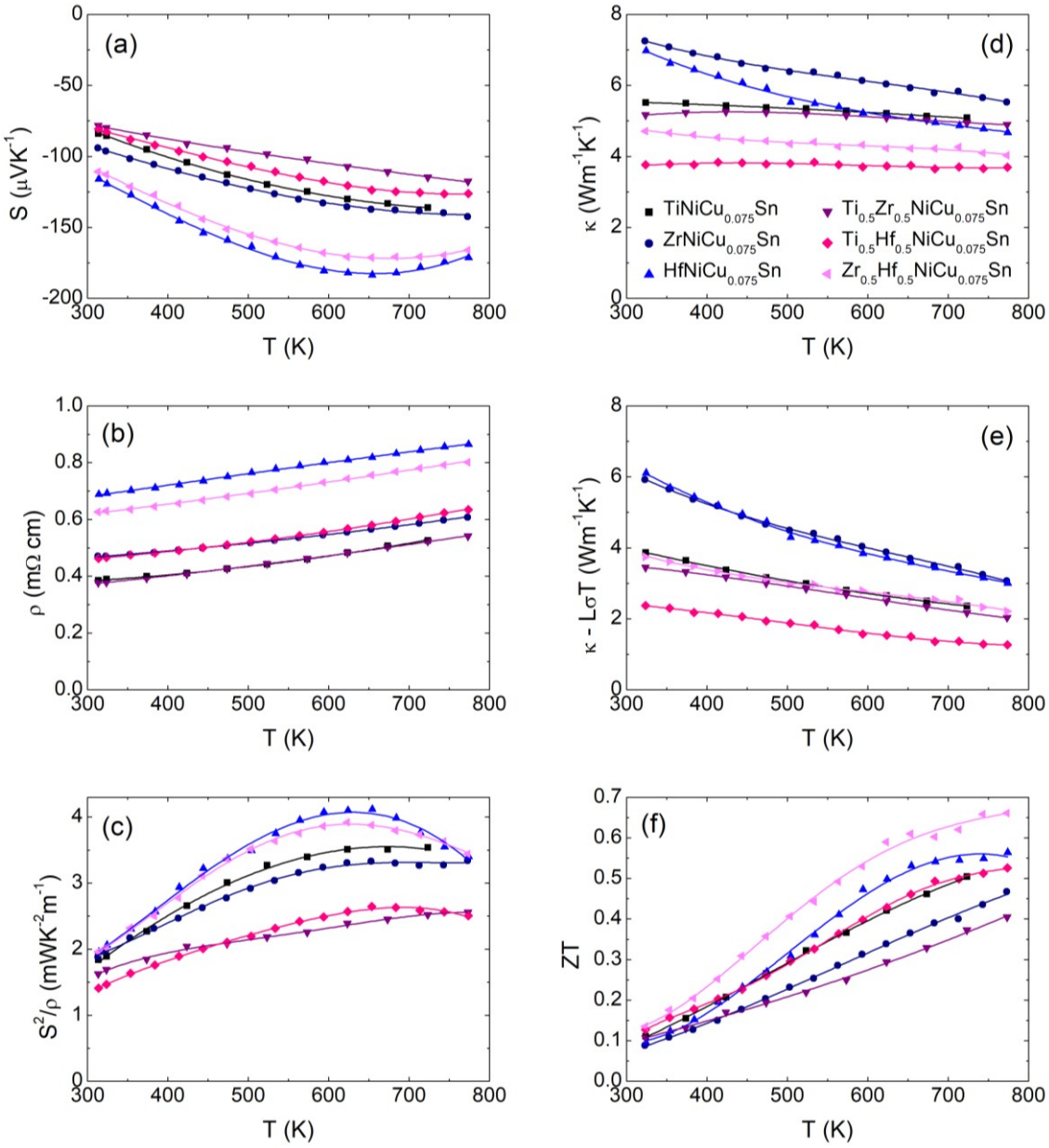

Figure 4.5. Temperature dependence of **(a)** the absolute Seebeck coefficient (S), **(b)** the electrical resistivity (ρ), **(c)** the thermoelectric power factor (S^2/ρ), **(d)** the total thermal conductivity (κ), **(e)** the lattice thermal conductivity ($\kappa - LT/\rho$) and **(f)** the figure of merit ZT for the $MNiCu_{0.075}Sn$ and $M_{0.5}M'_{0.5}NiCu_{0.075}Sn$ (M = Ti, Zr, Hf) compositions.

The Hall measurements confirmed efficient n-type doping. For all samples, the n increases between y = 0 and y = 0.075 (see Table 4.2). Focusing on the Cu-doped materials, n increases with the total *4d*-site occupancy. As a result, the S values decrease with the excess metal content. The S^2/ρ for all samples are shown in Figure 4.5c. The highest values S^2/ρ = 4.1 W m^{-1} K^{-1} at 653 K and S^2/ρ = 4.0 W m^{-1} K^{-1} at 623 K were observed for HfNiCu$_{0.075}$Sn and Zr$_{0.5}$Hf$_{0.5}$NiCu$_{0.075}$Sn, respectively. These samples are characterised by lowest n leading to the highest S values. The Ti$_{0.5}$Zr$_{0.5}$NiCu$_{0.075}$Sn and Ti$_{0.5}$Hf$_{0.5}$NiCu$_{0.075}$Sn display the lowest S^2/ρ, due to the highest n and lowest S.

The temperature dependence of C_p and α for the MNiCu$_{0.075}$Sn and M$_{0.5}$M'$_{0.5}$NiCu$_{0.075}$Sn compositions are presented in Figure C1 (Appendix C). The C_p of TiNiCu$_{0.1}$Sn (discussed in the previous Chapter) was used to evaluate the C_p for the compositions presented in this Section. The evaluated κ is presented in Figure 4.5d. The $\kappa(T)$ mimics the $\alpha(T)$. The $\kappa(T)$ of ZrNiCu$_{0.075}$Sn and HfNiCu$_{0.075}$Sn decreases as a function of temperature, whilst $\kappa(T)$ for TiNiCu$_{0.075}$Sn, Ti$_{0.5}$Zr$_{0.5}$NiCu$_{0.075}$Sn, Ti$_{0.5}$Hf$_{0.5}$NiCu$_{0.075}$Sn and Zr$_{0.5}$Hf$_{0.5}$NiCu$_{0.075}$Sn is lower and almost temperature independent. The lowest κ was observed for Ti$_{0.5}$Hf$_{0.5}$NiCu$_{0.075}$Sn, which is the result of the strongest alloying effect caused by Ti/Hf mass disorder.

Table 4.2. Room temperature carrier concentration (n), carrier mobility (μ) and lattice thermal conductivity ($\kappa_{323K} - LT/\rho$). The *4d* site occupancy for y = 0.075 compositions was taken from Rietveld fits to the neutron powder diffraction data. Γ_M and Γ_{Y2} are calculated disorder parameters on the M site (Equation 2.41) and on the interstitial *4d*-site (Equation 3.1), respectively, while Γ_{total} is sum of Γ_M and Γ_{Y2}.

Composition	y	n ($\times 10^{20}$ cm^{-3})	μ (cm^2 V^{-1}s^{-1})	*4d*-site occupancy	κ_{323K}-LT/ρ (W m^{-1} K^{-1})	Γ_M	Γ_{Y2}	Γ total
TiNiCu$_y$Sn	0.000	1.03	12.3	Ni$_{0.03}$	6.0	0	0.07	0.07
	0.075	14.60	12.9	Ni$_{0.03}$Cu$_{0.072}$	3.9	0	0.21	0.21
ZrNiCu$_y$Sn	0.000	0.26	21.0		9.1			
	0.075	5.67	25.2	Cu$_{0.022}$	5.9	0	0.04	0.04
HfNiCu$_y$Sn	0.000	0.95	37.8		6.6			
	0.075	3.52	24.5	Cu$_{0.023}$	6.1	0	0.04	0.04
Ti$_{0.5}$Zr$_{0.5}$NiCu$_y$Sn	0.000	0.42	26.1		3.4			
	0.075			Ni$_{0.03}$Cu$_{0.061}$	3.4	0.03	0.18	0.21
Ti$_{0.5}$Hf$_{0.5}$NiCu$_y$Sn	0.000	0.82	24.7		2.6			
	0.075	10.31	14.7	Cu$_{0.036}$	2.4	0.19	0.07	0.26
Zr$_{0.5}$Hf$_{0.5}$NiCu$_y$Sn	0.000				4.6			
	0.075	4.28	26.8	Cu$_{0.024}$	3.7	0.08	0.04	0.12

The room temperature Lorentz number (L = 1.86 to 2.00 × 10^8 $V^2 K^{-2}$) was estimated using Equation 2.33. The L values were kept constant during the κ_{el} calculations, over the whole temperature range. The LT/ρ is shown in Figure C1 (Appendix C), while the extracted $\kappa - LT/\rho$ is shown in Figure 4.5e. The $M_{0.5}M'_{0.5}NiCu_{0.075}Sn$ and $TiNiCu_{0.075}Sn$ show significantly lower $\kappa_{lattice}$ compared to $ZrNiCu_{0.075}Sn$ and $HfNiCu_{0.075}Sn$. With a value of 2.4 $Wm^{-1}K^{-1}$ at 323 K and 1.3 $Wm^{-1}K^{-1}$ at 773K for $Ti_{0.5}Hf_{0.5}NiCu_{0.075}Sn$, a reduction of 62% and 85%, respectively was achieved compared to $TiNiCu_{0.075}Sn$.

As shown in Chapter 3, the phonon scattering is dominated by point defect scattering. The point defect scattering for phonons can be created by the mass difference between the M metals and by the introduction of interstitial metals. The NPD for $MNiCu_{0.075}Sn$ and $M_{0.5}M'_{0.5}NiCu_{0.075}Sn$ samples has revealed that the excess metals (Ni and Cu) are present and occupy the vacant *4d*-sites in the half-Heusler structure. Therefore, to investigate the κ-LT/ρ, the disorder scattering parameter (Γ_{total}) was calculated by summing the mass disorder on the M-site (Γ_M) and the disorder parameters due to the interstitials (Γ_{Y2}), with results presented in Table 4.2. Focusing on the $M_{0.5}M'_{0.5}NiCu_ySn$ compositions, the atomic mass differences of Ti and Hf on the *4a*-site are larger than that of Ti and Zr or Zr and Hf. Consequently, the alloy scattering of $Ti_{0.5}Hf_{0.5}NiCu_{0.075}Sn$ is dominated by Γ_M. On the other hand, the Γ_{total} of $TiNiCu_{0.075}Sn$ and $Ti_{0.5}Zr_{0.5}NiCu_{0.075}Sn$ is dominated by Γ_{Y2}, due to the highest *4d*-site occupancy. As shown in Figure 4.6, the κ-LT/ρ decreases with Γ_{total}, confirming that the introduction of point defect centres is an efficient method to scatter phonons.

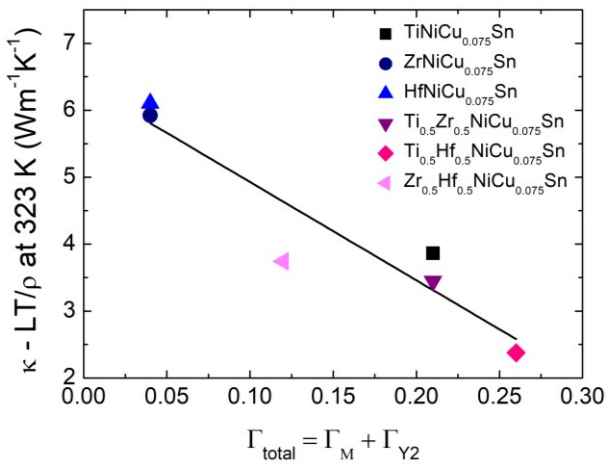

Figure 4.6. 323 K values of lattice thermal conductivity (κ-LT/ρ) as a function of total disorder scattering parameter (Γ_{total}).

The temperature dependence of *ZT* is shown in Figure 4.5f. The $Zr_{0.5}Hf_{0.5}NiCu_{0.075}Sn$ samples reaches *ZT* = 0.13 at 323 K and *ZT* = 0.66 at 773 K, due to its largest S^2/ρ and low $\kappa_{lattice}$. Although $Ti_{0.5}Hf_{0.5}NiCu_{0.075}Sn$ exhibits the lowest $\kappa_{lattice}$, poor electronic properties limit the *ZT*. The lowest *ZT* is observed for $ZrNiCu_{0.075}Sn$ (due to its high κ) and $Ti_{0.5}Zr_{0.5}NiCu_{0.075}Sn$ (caused by low S^2/ρ).

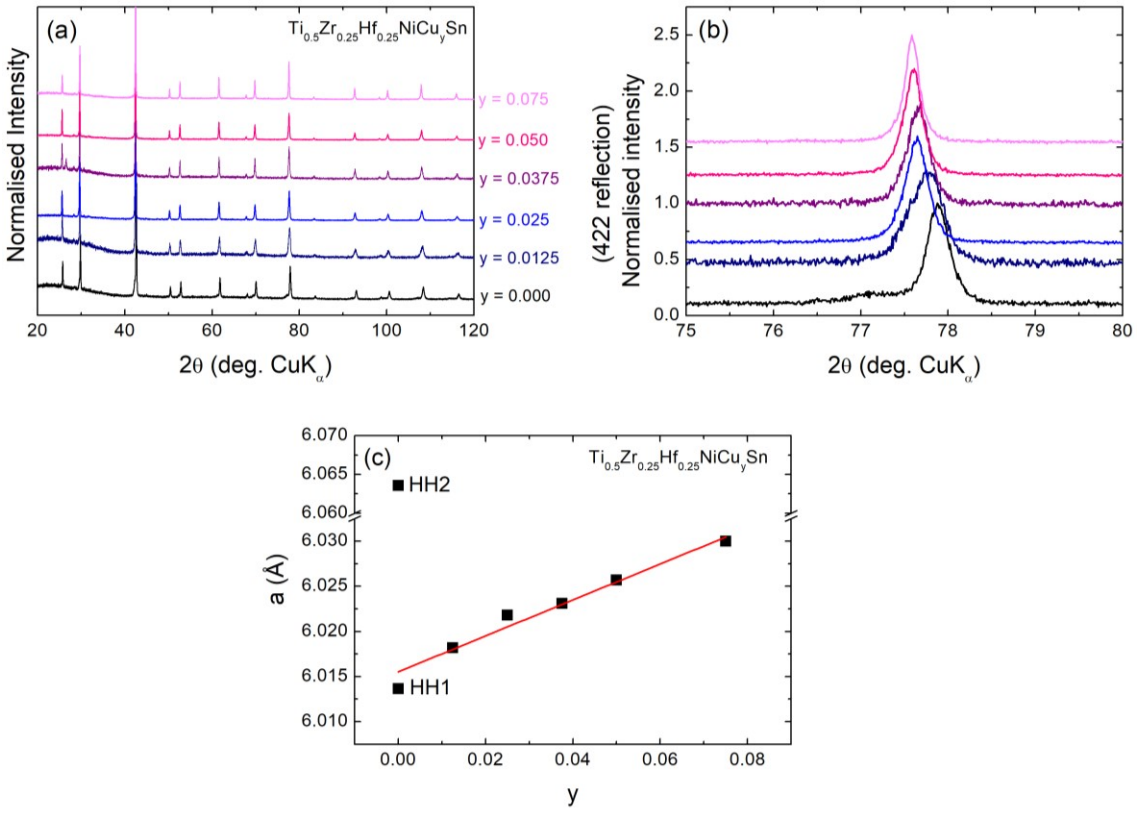

Figure 4.7. (a) X-ray powder diffraction patterns for the $Ti_{0.5}Zr_{0.25}Hf_{0.25}NiCu_ySn$ $0 \leq y \leq 0.075$. All main peaks can be indexed on the half-Heusler structure. **(b)** Close-up of the diffraction peak for the (422) half-Heusler reflection. **(c)** Lattice parameter of the half-Heusler phase as a function of nominal Cu content. HH1 and HH2 denote the half-Heusler phases which were used to fit diffraction pattern of y = 0 composition (see Table 4.3 for details)

4.4. $Ti_{0.5}Zr_{0.25}Hf_{0.25}NiCu_ySn$ ($0 \leq y \leq 0.075$)

4.4.1. X-ray Powder Diffraction

XRD data for the $Ti_{0.5}Zr_{0.25}Hf_{0.25}NiCu_ySn$ ($0 \leq y \leq 0.075$) half-Heuslers are presented in Figure 4.7a. All main diffraction peaks can be indexed to the cubic half-Heusler structure.

Rietveld refinement revealed that $Ti_{0.5}Zr_{0.25}Hf_{0.25}NiSn$ consists of a mixture of two half-Heusler phases, with different lattice parameters (a_{HH1} = 6.0137(1) Å and a_{HH2} = 6.0636(5) Å). This suggests that the Ti, Zr and Hf are not well-mixed. Interestingly, the Cu-rich materials could be fitted using a single, half-Heusler phase. In addition, the reflections become sharper and more symmetric with Cu content, suggesting Cu acts as a mineraliser that improves the homogenisation of Ti, Zr and Hf (Figure 4.7b). A small amount of $(Zr/Hf)O_2$ was observed for $y \geq 0.025$, while Sn was found in the y = 0.025 and 0.0375 compositions. As shown in the Figure 4.7c, the lattice parameter increases as a function of Cu content, confirming the introduction of excess Cu into the half-Heusler matrix. The details of Rietveld analysis are presented in Table 4.3.

Table 4.3. Lattice parameter (*a*) and weight percentage (*wt%*) for the half-Heusler, Sn and $(Zr/Hf)O_2$ phases, which were used during the Rietveld refinement fit to X-ray powder diffraction data.

y	Half-Heusler 1		Half-Heusler 2		Sn	$(Zr/Hf)O_2$
	a (Å)	wt%	a (Å)	wt%	wt%	wt%
0	6.0137(1)	84.1(1)	6.0636(5)	15.9(1)		
0.0125	6.0182(1)	100.0				
0.025	6.0218(1)	96.8(1)			0.7(2)	2.5(2)
0.0375*	6.0231(1)	94.8(1)			1.4(1)	3.8(3)
0.05	6.0257(1)	97.7(1)				2.3(2)
0.075	6.0300(1)	97.9(1)				2.1(2)

*contains graphite

4.4.2. Neutron Powder Diffraction

Rietveld fits to NPD data for $Ti_{0.5}Zr_{0.25}Hf_{0.25}NiCu_ySn$ (y = 0.025, 0.05 and 0.075) materials are shown in Figure 4.8. Analysis confirmed the formation of a single half-Heusler phase for all compositions, along with the presence of Ni_3Sn_2 (0.7 – 1.5 wt%) for y = 0.025 and 0.05 samples. The starting point for Rietveld refinement was a stoichiometric $Ti_{0.5}Zr_{0.25}Hf_{0.25}NiCu_ySn$ ($0 \leq y \leq 0.075$) model. A constraint was applied to maintain 100% occupancy of *4a*, *4b* and *4c* site, while the Cu content on the normally vacant *4d*-site was allowed to refine freely. This revealed similar amount of Ti, Zr and Hf for all compositions. The refined Cu content remains close to the nominal value (y), accounting for the main difference between the samples. In addition, the constraint was introduced for the thermal displacement parameters (U_{iso}) of the half-Heusler phase: a

single U_{iso} was used used for Ti, Zr and Hf, a single U_{iso} was used for Ni and Cu and a single U_{iso} was used for Sn. As can be seen from Figure 4.8, all patterns are well described by the single half-Heusler phase, which represents an adequate powder average. The average experimental compositions, the refined lattice parameter and the thermal motion factor for each alloy, along with the fit statistics, are given in Table 4.3 and Table C3 (Appendix C).

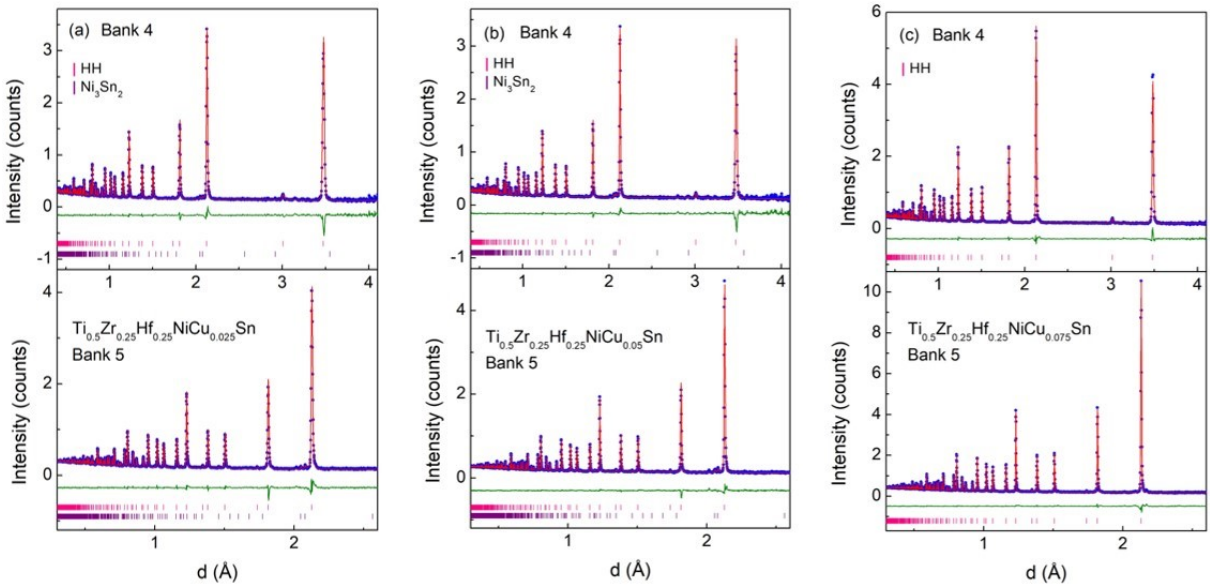

Figure 4.8. Observed (blue circles), calculated (red solid line) and difference (green solid line) Rietveld neutron powder diffraction profiles for (a) $Ti_{0.5}Zr_{0.25}Hf_{0.25}NiCu_{0.025}Sn$, (b) $Ti_{0.5}Zr_{0.25}Hf_{0.25}NiCu_{0.05}Sn$, and (c) $Ti_{0.5}Zr_{0.25}Hf_{0.25}NiCu_{0.075}Sn$. The Bragg markers correspond to the phases that were used to fit the pattern (pink is the half-Heusler and purple is Ni_3Sn_2). Banks 4 and 5 are the 90º and backscattered detector banks, respectively.

Table 4.3. Lattice parameter (*a*) and weight percentage (*wt%*) for the half-Heusler and Ni_3Sn_2 phases, which were used during the Rietveld refinement against neutron powder diffraction data.

y	**Half-Heusler $Ti_{0.5}Zr_{0.25}Hf_{0.25}NiCu_ySn$**			**Ni_3Sn_2**
	a (Å)	**wt%**	**Composition**	**wt%**
0.025	6.01528(8)	99.3(1)	$Ti_{0.515(3)}Zr_{0.242(1)}Hf_{0.242(1)}NiCu_{0.041(1)}Sn$	0.7(1)
0.050	6.01617(6)	98.5(1)	$Ti_{0.516(3)}Zr_{0.242(1)}Hf_{0.242(1)}NiCu_{0.049(2)}Sn$	1.5(1)
0.075	6.02732(5)	100	$Ti_{0.493(6)}Zr_{0.246(3)}Hf_{0.246(3)}NiCu_{0.073(1)}Sn$	

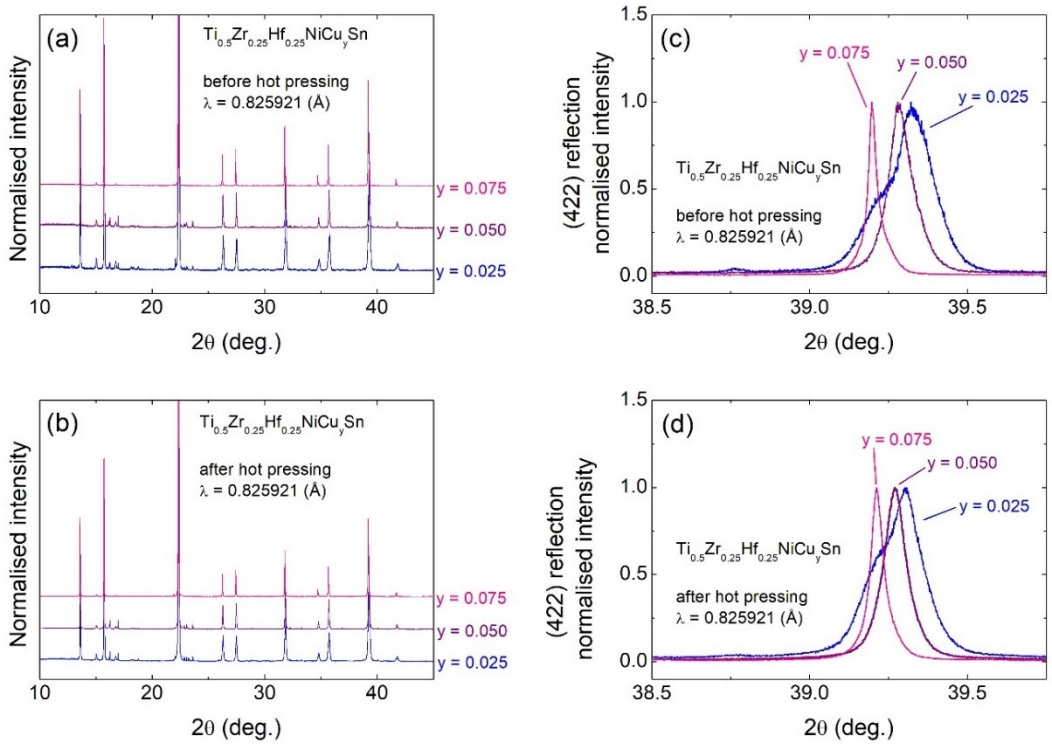

Figure 4.9. (a-b) High-resolution synchrotron X-ray powder diffraction patterns of samples before and after hot pressing. All main peaks can be indexed on the half-Heusler structure. **(c-d)** The diffraction peak for the (422) half-Heusler reflection.

4.4.3. High-Resolution Synchrotron X-ray Diffraction Study

The SXRD was used to investigate the peak broadening due to the compositional variations and to evaluate the impact of hot-pressing on the crystal structure of $Ti_{0.5}Zr_{0.25}Hf_{0.25}NiCu_ySn$ (y = 0.025, 0.05 and 0.075). Figure 4.9 shows the SXRD patterns for samples before and after hot pressing. It is evident from the peak positions that the main structure is related to the half-Heusler. In addition, the reflections become sharper and more symmetric as the Cu-doping increases from y = 0.025 to 0.075, suggesting Cu improves the homogenisation of Ti, Zr and Hf.

The peak shape was fitted using the approach discussed in Section 3.4.3, with the number of phases n in range $0 \leq n \leq 20$ and lattice parameter difference Δa = 0.0025 Å. It is evident from Figure 4.10 that as Cu content increases, the peaks become sharper and a smaller number of half-Heusler phases are required. In contrast, multiple half-Heusler phases are essential to describe the broadening of compositions with low amount of Cu (e.g. y = 0.025). The average lattice parameter ($a_{average}$) was calculated for each material. For comparison, the results from NPD experiment were included in the relevant panels,

showing excellent agreement. For all samples, the phase distribution and the $a_{average}$ do not change upon hot-pressing, confirming that the crystal structure is not affected by the consolidation.

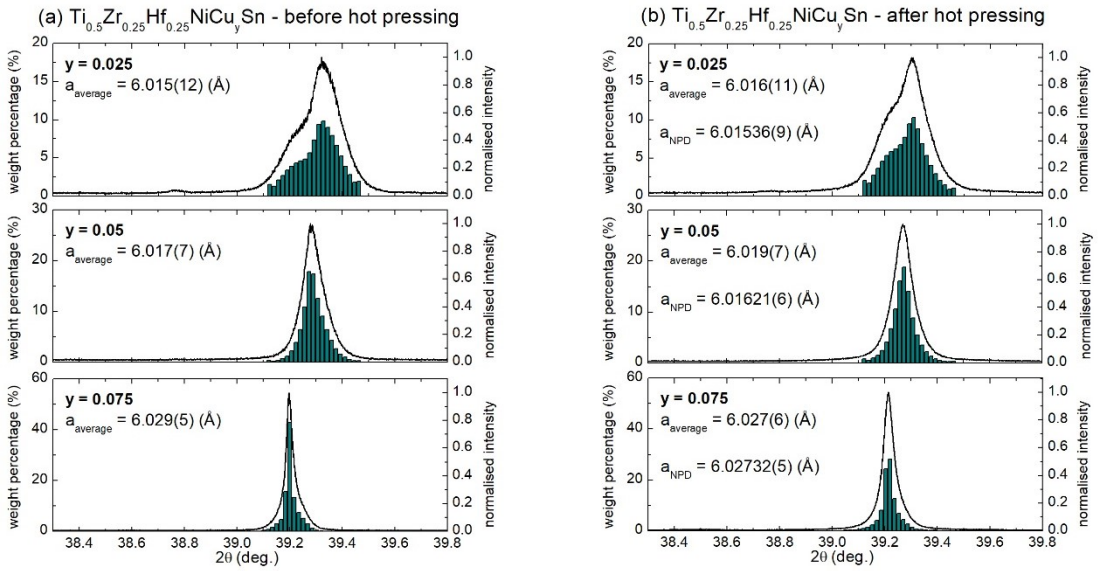

Figure 4.10. Close-up of a representative synchrotron X-ray powder diffraction half-Heusler reflection (422, black line) and the abundance of the half-Heusler phases used to fit the peak shape (green histograms) for the $Ti_{0.5}Zr_{0.25}Hf_{0.25}NiCu_ySn$ samples **(a)** before and **(b)** after consolidation. The average lattice parameter ($a_{average}$) was calculated using the scale factor for each identified phase. The lattice parameters (a_{NPD}) from neutron powder diffraction is given for comparison and is in excellent agreement.

4.4.4. Scanning Electron Microscopy

SEM-EDX was used to investigate the microstructure of $Ti_{0.5}Zr_{0.25}Hf_{0.25}NiCu_{0.075}Sn$. As for the $M_{0.5}M'_{0.5}NiCu_{0.075}Sn$ samples, morphology of the y = 0.075 composition is more complex, than inferred from diffraction studies. As shown in Figure 4.11, the sample consists of at least 3 half-Heusler phases. No clear boundaries between phases are observed. EDX mapping was used to estimate the compositions. It revealed Ti-rich and (Ti,Hf)-mixed and (Ti,Zr,Hf)-mixed half-Heusler phases. There is no evidence of voids or holes between the grains, consistent with full densification.

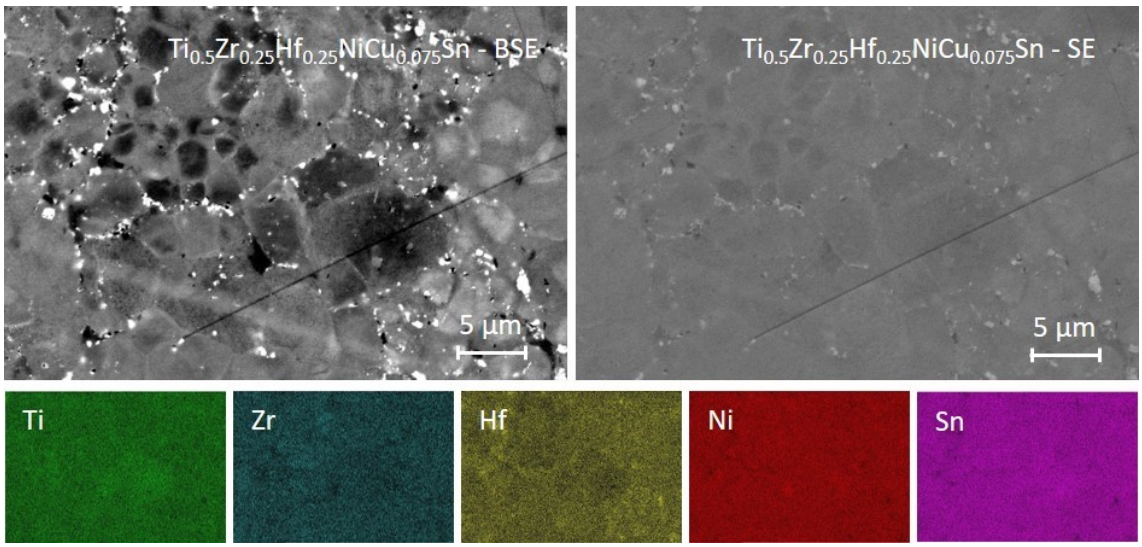

Figure 4.11. Backscattered electron (BSE) microscopy image (left), secondary electron (SE) microscopy image (right) and element-specific EDX maps for $Ti_{0.5}Zr_{0.25}Hf_{0.25}NiCu_{0.075}Sn$.

4.4.5. Thermoelectric Properties

The temperature dependence of S, ρ, S^2/ρ, κ, $\kappa - LT/\rho$ and ZT for the hot-pressed $Ti_{0.5}Zr_{0.25}Hf_{0.25}NiCu_ySn$ ($0 \leq y \leq 0.075$) compositions are shown in Figure 4.12. The magnitude of both S and ρ decrease sequentially with increasing Cu content. This suggests that excess Cu drastically increases the overall carrier density. This was confirmed by Hall measurements, with results presented in Figure 4.13. All samples are characterised by the negative sign of S, indicating n-type semiconducting behaviour and electrons as the major charge carriers. The $S(T)$ for all Cu-doped samples increases with increasing temperature and reaches a broad maximum at 650 – 750 K. A clear semiconducting temperature dependence of $\rho(T)$ is evident for the parent, $Ti_{0.5}Zr_{0.25}Hf_{0.25}NiSn$, whereas the Cu-rich samples exhibit metallic behaviour, which is indicative of high-levels of doping. As shown in Figure 4.12c, the power factors (S^2/ρ) for all compositions increase steadily and form a broad maximum at high temperature. The maximum S^2/ρ values were achieved for compositions with low Cu content ($0.0125 \leq y \leq 0.0375$), suggesting that only small amount of excess Cu is needed to achieve optimal electronic performance. For example, the S^2/ρ = 4.40 mW K^{-2} m^{-1} at 742 K for $Ti_{0.5}Zr_{0.25}Hf_{0.25}NiCu_{0.0375}Sn$ corresponds to ~75% increase compared to the y = 0 sample.

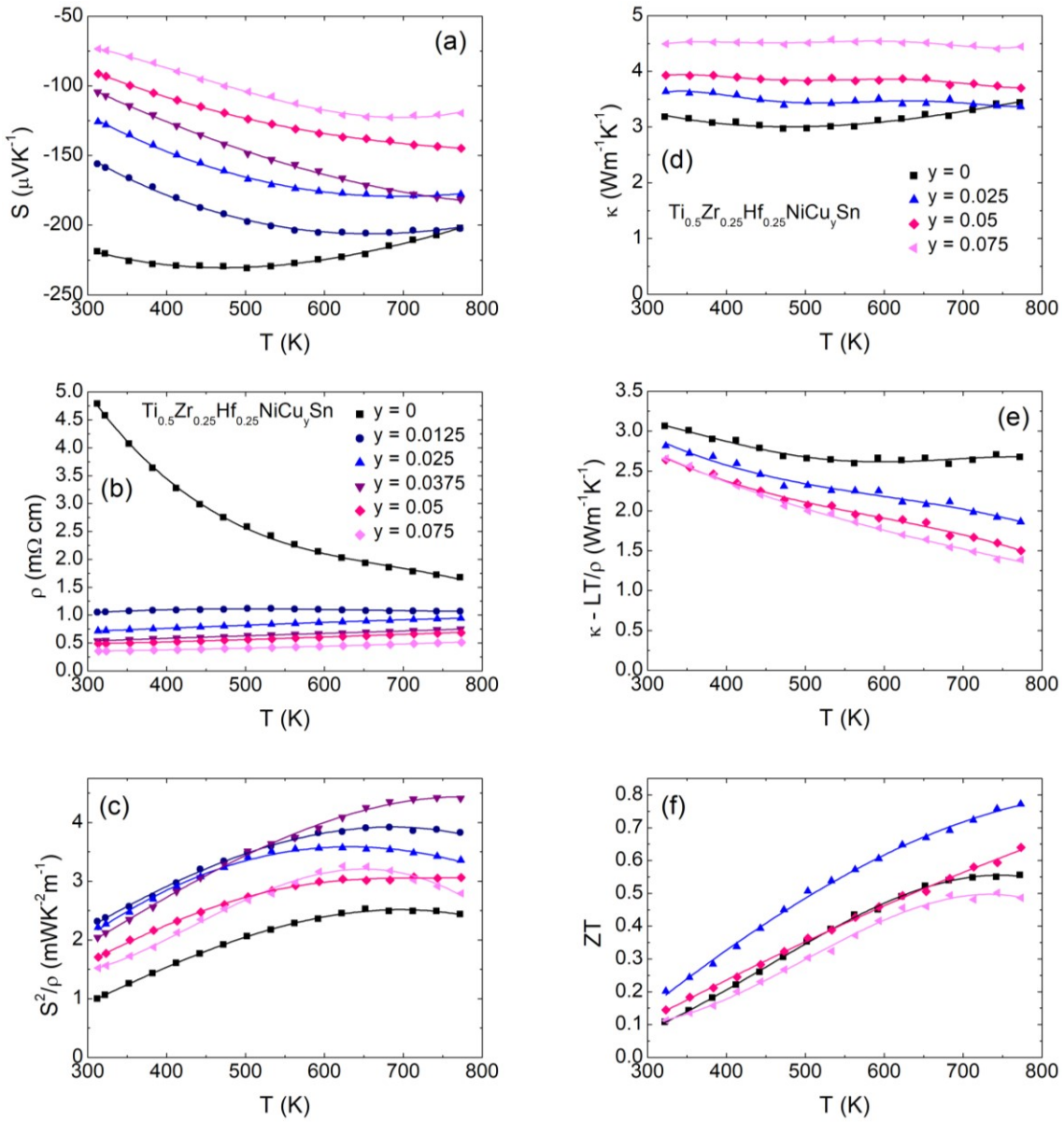

Figure 4.12. Temperature dependence of **(a)** the absolute Seebeck coefficient (S), **(b)** the electrical resistivity (ρ), **(c)** the thermoelectric power factor (S^2/ρ), **(d)** the total thermal conductivity (κ), **(e)** the lattice thermal conductivity ($\kappa - LT/\rho$) and **(f)** the figure of merit (ZT) for the $Ti_{0.5}Zr_{0.25}Hf_{0.25}NiCu_ySn$ ($0 \leq y \leq 0.075$).

Figure 4.13 shows the room temperature Hall measurement for $Ti_{0.5}Zr_{0.25}Hf_{0.25}NiCu_ySn$ alloys against nominal y. The carrier concentration (n_{RT}) increases linearly as a function of excess Cu, confirming Cu acts as effective n-type dopant. The increased carrier density is consistent with the change observed in ρ and S. Introduction of small amount of Cu (y = 0.0125) causes rapid increase in the carrier mobility (μ). However, as the Cu content is increased further (y > 0.0125), the μ decreases linearly. This may be caused by the

increase of the effective mass of carriers – see Equation 1.15. Equation 1.9 was used to obtain the value for the effective mass m^*. The S versus the n_{RT} is given in Figure 4.13c. The Pisarenko plot revealed increase of m^* with Cu content falling in 3.0 $m_e < m^* < 4.5$ m_e range. The m^* is consistent with the μ reduction upon Cu doping.

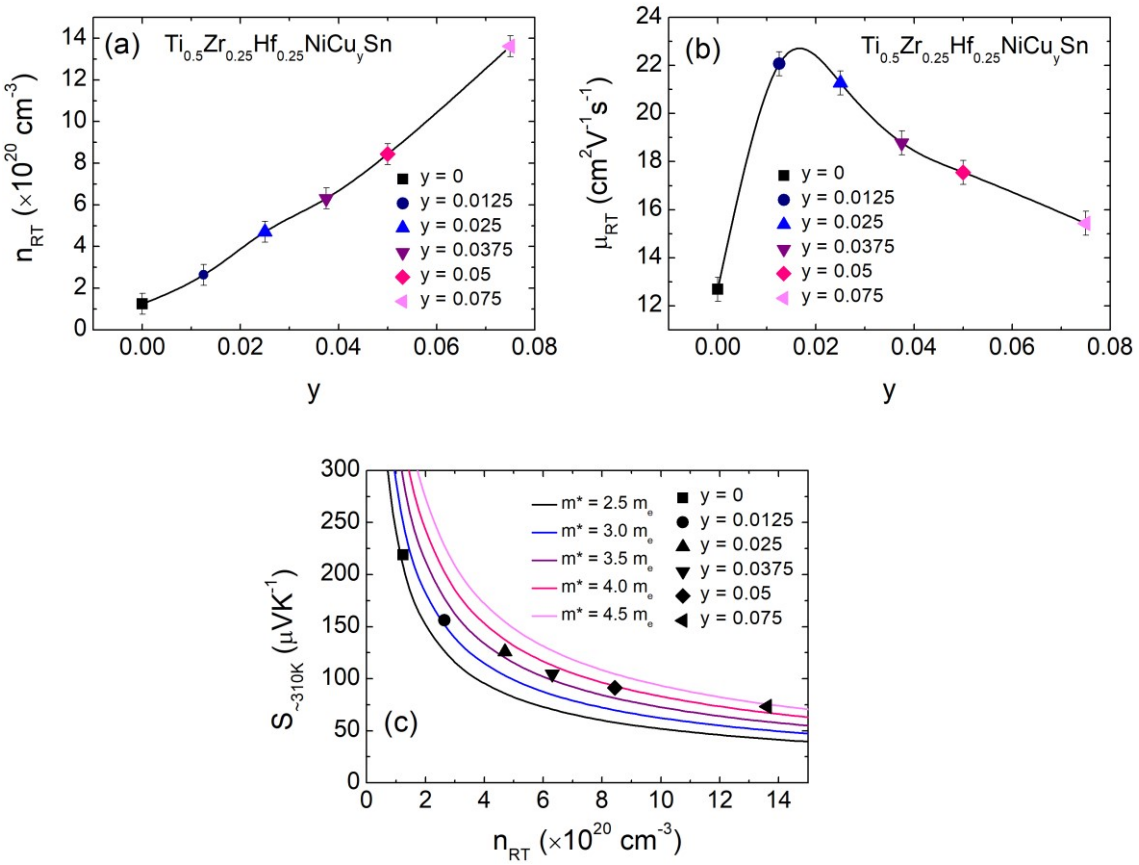

Figure 4.13. Room temperature values of **(a)** charge carrier concentration (n_{RT}) and **(b)** carrier mobility (μ_{RT}) as a function of nominal Cu (y) content in $Ti_{0.5}Zr_{0.25}Hf_{0.25}NiCu_ySn$. **(c)** Pisarenko plot: Seebeck coefficient (S) as a function of n_{RT}.

The C_p measured for parent $Ti_{0.5}Zr_{0.25}Hf_{0.25}NiSn$ was used to calculate the C_p for remaining Cu-doped compositions (see Figure C1, Appendix C). The $\alpha(T)$ was measured for all materials and is also presented in Appendix C. The evaluated κ is presented in Figure 4.12d. The $\kappa(T)$ mimics the $\alpha(T)$. Focusing on $Ti_{0.5}Zr_{0.25}Hf_{0.25}NiSn$. At 323 K it has the lowest κ = 3.2 W m^{-1} K^{-1} value, which decreases with temperature, reaches a minimum κ = 2.9 W m^{-1} K^{-1} at 473 K, above which it starts to increase. This suggests bipolar contribution and the presence of minority charge carriers (electron holes). The $\kappa(T)$ of Cu-doped compositions decreases slowly with increasing temperature. The

magnitude of κ increases with Cu content, with highest values reported for y = 0.075. The room temperature Lorentz number (L = 1.65 to 2.05 × 10^8 V^2 K^{-2}) was estimated using Equation 2.33. The L values were kept constant during the κ_{el} calculations, over the whole temperature range. The LT/ρ is shown in Figure C1 (Appendix C), while the extracted κ-LT/ρ is shown in Figure 4.5e. The introduction of Cu atoms has a significant effect on the $\kappa_{lattice}$. A reduction from 3.1 W m^{-1} K^{-1} (y = 0) to 2.6 – 2.8 W m^{-1} K^{-1} (0.025 ≤ y ≤ 0.075) was observed. The low values for Cu-rich members of the series are due to the rapid increase in κ_{el}. The sample with y = 0.075 reaches the lowest values of 2.6 W m^{-1} K^{-1} at 323 K and 1.4 W m^{-1} K^{-1} at 773 K, comparable to the values found by Rogl[98] for half-Heusler alloys prepared using a complex synthesis protocol.

Like $MNiCu_{0.075}Sn$ and $M_{0.5}M'_{0.5}NiCu_{0.075}Sn$ samples, the NPD revealed the presence of excess Cu on the vacant *4d*-site in the half-Heusler matrix. Therefore, to investigate the κ-LT/ρ of $Ti_{0.5}Zr_{0.25}Hf_{0.25}NiCu_ySn$ compositions, the disorder scattering parameter (Γ_{total}) was calculated by summing the mass disorder on the M-site (Γ_M) and the disorder parameters due to the interstitials (Γ_{Y2}), with results presented in Table 4.4. The M-site occupancy was the same for all materials, therefore the main difference between the samples arises from the *4d*-site occupancy. The Γ_{Y2} increases with the excess Cu content, suggesting that Cu acts as a point defect centres. As shown in Figure 4.14, the κ-LT/ρ decreases with Γ_{total}, confirming that the introduction of point defect centres is an efficient method to scatter phonons. To complete the analysis, $\kappa_{\text{lattice}}^{\text{calculated}}$ was evaluated using Equation 2.43. The calculated values are higher than expected, suggesting that point defect is not the only factor responsible for phonon scattering and the mechanism is more complicated.

Table 4.4. 323 K values of lattice thermal conductivity (κ_{323K} – LT/ρ) of $Ti_{0.5}Zr_{0.25}Hf_{0.25}NiCu_ySn$ compositions. The *4d*-site occupancy for 0.025 ≤ y ≤ 0.075 compositions was taken from Rietveld fits to the neutron powder diffraction data. Γ_M and Γ_{Y2} are calculated disorder parameters on the M-site and on the interstitial *4d*-site, respectively (Equation 2.41 and Equation 3.1), while Γ_{total} is sum of Γ_M and Γ_{Y2}. $\kappa_{\text{lattice}}^{\text{calculated}}$ was evaluated using Equation 2.43.

y	κ_{323K}-LT/ρ (W m^{-1} K^{-1})	*4d*-site occupancy	Γ_M	Γ_{Y2}	Γ_{total}	$\kappa_{\text{lattice}}^{\text{calculated}}$ (W m^{-1} K^{-1})
0.000	3.1		0.15	0	0.15	4.0
0.025	2.8	$Cu_{0.041(1)}$	0.15	0.08	0.23	3.4
0.050	2.6	$Cu_{0.049(1)}$	0.15	0.10	0.25	3.3
0.075	2.6	$Cu_{0.073(1)}$	0.15	0.14	0.29	3.1

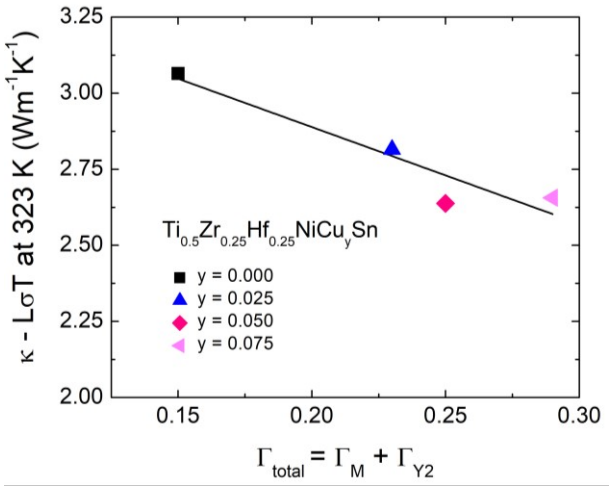

Figure 4.14. 323 K values of lattice thermal conductivity (κ-LT/ρ) as a function of total disorder scattering parameter (Γ_{total}).

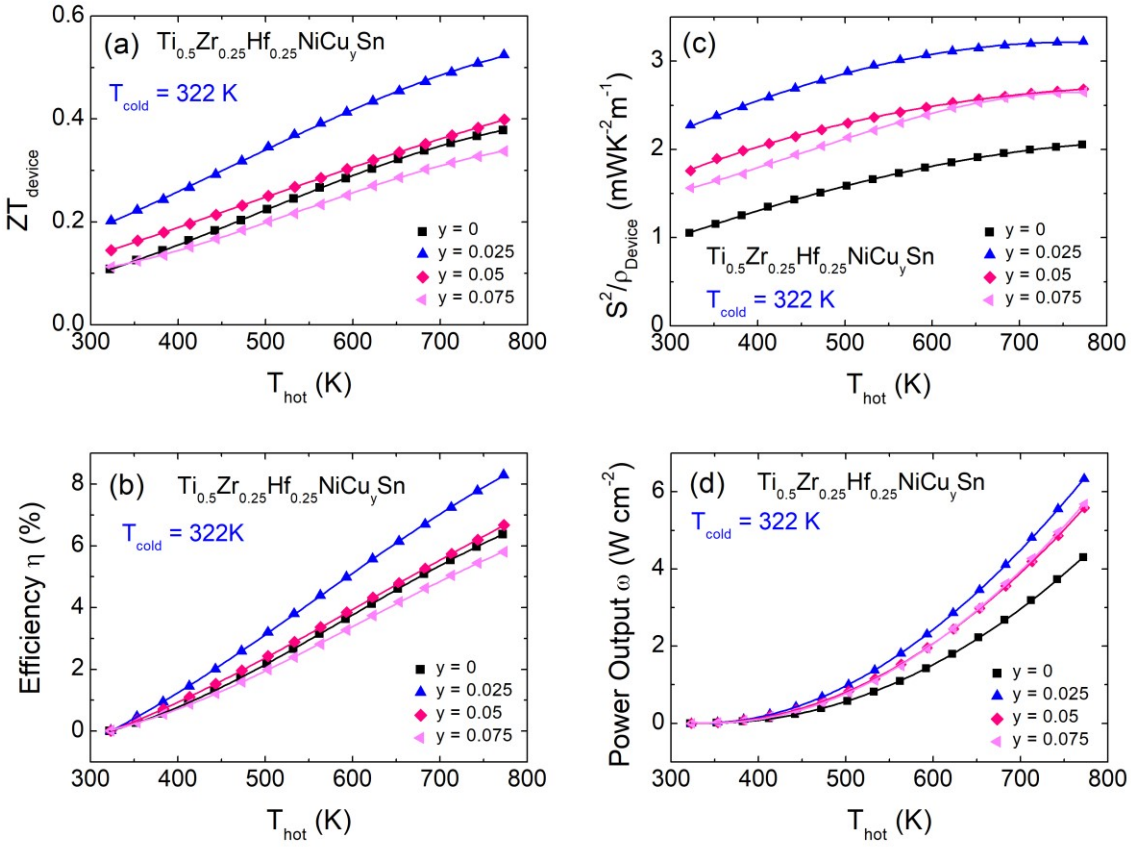

Figure 4.15. Temperature dependence of **(a)** ZT_{device} **(b)** the efficiency (η), **(c)** PF_{device} and **(d)** the power output (ω) for the $Ti_{0.5}Zr_{0.25}Hf_{0.25}NiCu_ySn$ samples as a function of hot-side temperature (T_{hot}). The cold-side temperature (T_{cold}) was assumed to be 323 K.

The temperature dependence of ZT is presented in Figure 4.12f. The combination of large S^2/ρ and low κ for y = 0.025 leads to the largest ZT = 0.2 at 323K and ZT = 0.77 at 773 K. This corresponds to 85% improvement near room temperature and 40% improvement in terms of maximum ZT compared with un-doped $Ti_{0.5}Zr_{0.25}Hf_{0.25}NiSn$.

The temperature dependence of ZT_{device}, PF_{device}, the leg efficiencies and leg power outputs are shown in Figure 4.15. This revealed ZT_{device} = 0.38 from a 450 K temperature gradient for $Ti_{0.5}Zr_{0.25}Hf_{0.25}NiSn$. Interestingly, significant enhancement was observed for y = 0.025 composition. Small Cu-doping (2.5%) leads to ZT_{device} = 0.52 and excellent 8.3% conversion efficiency. Such improvement is mainly due to the ZT ~0.2 at 323 K, which is comparable to the literature half-Heusler compositions.[56, 92] The PF_{device} increases by ~60% from 2.05 mW m^{-1} K^{-2} from 450 K gradient for y = 0 to 3.2 mW m^{-1} K^{-2} for the y = 0.025 sample (Figure 4.15c). As a result, the leg power output increases from 4.3 W cm^{-2} (y = 0) to 6.3 W cm^{-2} (y = 0.025) from ΔT = 450 K and using h = 0.2 cm (Figure 4.15d).

4.5. Discussion and Conclusions

The aim of this Chapter was to investigate the effect of excess Cu on the microstructure and the thermoelectric properties of $MNiCu_ySn$ compositions with the mixtures of Ti, Zr and Hf on the M-site. Focusing on $MNiCu_{0.075}Sn$ and $M_{0.5}M'_{0.5}NiCu_{0.075}Sn$ compositions. XRD and SEM confirmed that Cu was successfully introduced to the half-Heusler structure. The SXRD of $MNiCu_{0.075}Sn$ revealed peak broadening upon hot-pressing suggesting the redistribution of Cu within the half-Heusler structure. It was shown in Chapter 3 that in $TiNiCu_ySn$ this is attributed to the grain-by-grain compositional variations with individual Cu grains tending to form either half-Heusler or full-Heusler. We believe that similar mechanism is observed for $ZrNiCu_{0.075}Sn$ and $HfNiCu_{0.075}Sn$. The SXRD Bragg reflections for $M_{0.5}M'_{0.5}NiCu_{0.075}Sn$ are significantly broader than for $MNiCu_ySn$ suggesting much more complex compositional variation, due to the mixing of M metals. This is consistent with the SEM data. The evaluated average lattice parameter ($a_{average}$) confirms that for all compositions hot-pressing does not change the average crystal structure, however it affects the distribution of the excess Cu. Introduction of Cu leads to a change in the temperature dependence of $S(T)$ and $\rho(T)$, which is consistent with n-type doping. Improvements in S^2/ρ and reductions in $\kappa_{lattice}$ near room temperature have been achieved in $MNiCu_ySn$ and $M_{0.5}M'_{0.5}NiCu_ySn$ series, with highest ZT = 0.66 at 773 K reported for $Zr_{0.5}Hf_{0.5}NiCu_{0.075}Sn$.

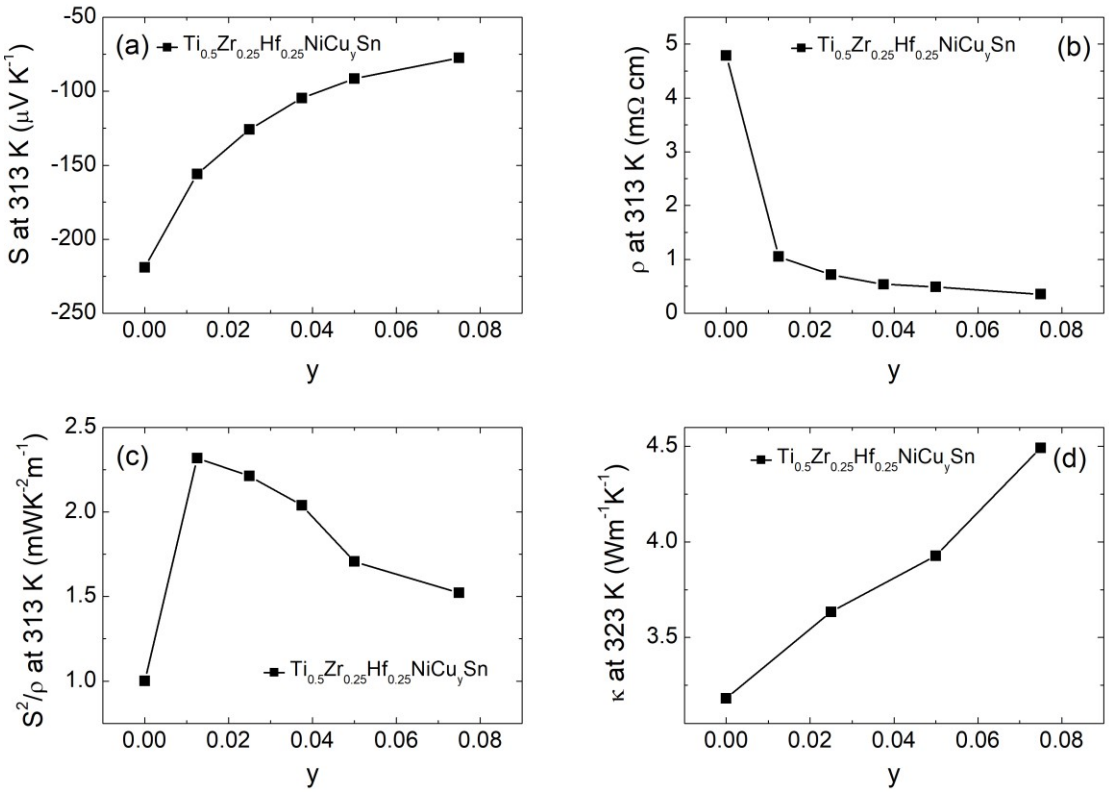

Figure 4.16. 312 K values of **(a)** Seebeck coefficient (S), **(b)** electrical resistivity (ρ), **(c)** power factor (S^2/ρ) and **(d)** thermal conductivity (κ) as a function of nominal Cu (y) content in $Ti_{0.5}Zr_{0.25}Hf_{0.25}NiCu_ySn$.

Summarising the $Ti_{0.5}Zr_{0.25}Hf_{0.25}NiCu_ySn$ half-Heusler alloys'. The diffraction studies confirmed the introduction of excess Cu into the half-Heusler structure. The SXRD revealed that Bragg reflections for $Ti_{0.5}Zr_{0.25}Hf_{0.25}NiCu_ySn$ become sharper and more symmetric upon Cu addition. This suggests the improvement in homogenisation of Ti, Zr and Hf. However, SEM suggests that these materials are not fully homogeneous, with some compositional variations observed. To establish the impact of excess Cu on the electronic and thermal transport properties, the S, ρ and S^2/ρ at 313 K and κ at 323 K were plotted against the nominal *4d*-site occupancy (Figure 4.16). The room temperature values of charge carrier concentration (n) and carrier mobility (μ) were shown in Figure 4.13. It is evident from both datasets that the electronic properties are strongly correlated to both, the n and μ. Linear increase of n upon Cu introduction explains the decrease of S and change in the magnitude of $\rho(T)$, with semiconducting value reported for y = 0 and metal-like behaviour for y > 0 compositions. Additionally, the trend in S^2/ρ (Figure 4.16c) mimics the observed rapid increase in μ with small Cu doping (y = 0.0125) and its further decrease with higher Cu content (y > 0.0125) – see Figure 4.13 b. This confirms that high

μ and n are essential to achieve high S^2/ρ. However, as shown by Pisarenko plot (Figure 4.13c) this may be difficult to accomplish as introduction of Cu leads to higher m^* values and reduced μ. Figure 4.16d presents the κ at 323 K as a function of nominal Cu content. The linear change with excess Cu is caused by the metallic nature of the sample and the rapid increase in κ_{el}. Despite the challenge of properties optimisation due to the competing nature of individual parameters, high ZT = 0.77 at 773 K was observed for $Ti_{0.5}Zr_{0.25}Hf_{0.25}NiCu_{0.025}Sn$

Chapter 5 - In-situ Neutron Powder Diffraction Monitoring of Half-Heusler Formation

5.1. Introduction

Formation of Ni-rich $MNi_{1+y}Sn$ and isovalent substitution on the M site by varying the ratio of Ti, Zr and Hf are important strategies used to enhance phonon scattering and improve thermoelectric properties of half-Heusler alloys. As discussed in Chapter 3, it is difficult to prepare pure, stoichiometric TiNiSn. This has been attributed to distinct differences in the melting points of constituent elements, as well as numerous binary phases that are present in the Ti-Ni-Sn phase diagram.[103, 109] Some intermediates have melting points significantly higher than TiNiSn (T_m = 1182 ºC) and therefore are much more stable. Moreover, the half-Heusler microstructure and formation of impurities depends strongly on the synthesis protocol. For example, TiNiSn prepared using solid-state reaction contains 2-3% of spontaneously formed excess Ni that occupies the normally vacant tetrahedral site.[129] This could be due to poor mixing of Ti, Ni and Sn leaving Ti and Sn unreacted, or oxidation of Ti.

The microstructure, formation and solubility limit of (Ti/Zr/Hf)NiSn also depends on the synthesis protocol. Populoh *et al.*[73] prepared $Ti_{0.37}Zr_{0.37}Hf_{0.26}NiSn$ using arc melting followed by annealing and observed a (Zr/Hf)-rich half-Heusler phase that due to higher melting point, solidifies first in the form of dendrites. The Ti-rich regions solidify later and fill in the interdendritic regions. A similar observation was made through detailed SEM/TEM and EDX study of a $Ti_{0.33}Zr_{0.33}Hf_{0.33}NiSn$ sample, which confirmed that Zr/Hf-rich grains are surrounded by a Ti-rich region with some evidence of full-Heusler $TiNi_2Sn$ segregation within Ti-rich domains.[72] The solid-state method does not proceed through the melt, therefore a completely different microstructure is obtained. Recently, Downie *et al.*[85, 134] prepared $M_{0.5}M'_{0.5}NiSn$ compositions using a solid-state synthesis protocol and did not observe the dendritic features, characteristic for arc-melted compositions. Instead a more continuous range of ($Ti_{1-x}Zr_xNiSn$) half-Heusler phases with $0.153 \leq x \leq 0.96$ was observed. $Ti_{0.5}Hf_{0.5}NiSn$ shows similar multiphase behaviour with semi-continuous $Ti_{1-x}Hf_xNiSn$ phases with x to be found in range $0.195 \leq x \leq 0.87$.[85]

Despite intense experimental and theoretical research over the past few decades, there is still not much known about the reaction mechanism of elemental precursors to form Ni-rich TiNiSn and multiphase half-Heusler alloys during solid-state reaction. An in-situ

NPD experiment was used to monitor the formation of $TiNi_{1+y}Sn$ (y = 0, 0.075 and 0.25), ZrNiSn and multiphase $Ti_{0.5}Zr_{0.5}NiSn$, $Ti_{0.5}Hf_{0.5}NiSn$, $Zr_{0.5}Hf_{0.5}NiSn$ and $Ti_{0.5}Zr_{0.25}Hf_{0.25}NiSn$ compositions. Using Rietveld analysis, the formation of a number of half-Heusler alloys was followed. It was observed that the formation of the half-Heusler structure from elemental powders is a complex, multi-step reaction.

5.2. Experimental Procedure and Characterisation

$TiNi_{1+y}Sn$ (y = 0, 0.075 and 0.25), ZrNiSn, $Ti_{0.5}Zr_{0.5}NiSn$, $Ti_{0.5}Hf_{0.5}NiSn$, $Zr_{0.5}Hf_{0.5}NiSn$ and $Ti_{0.5}Zr_{0.25}Hf_{0.25}NiSn$ samples were prepared from high purity elemental powders. Stoichiometric amounts of starting materials were thoroughly mixed using an agate mortar and pestle and cold-pressed using a 10-ton press into 13 mm diameter pellets. To avoid oxidation and evaporation of Sn, each sample was tightly wrapped in vanadium foil and placed in a ~10 mm diameter vanadium can.

In-situ NPD data were collected using the GEM instrument at the ISIS facility, Rutherford Appleton Laboratory. The sample was heated in a high-vacuum furnace up to 900 ºC with a ramp rate of 3 ºC/min. Data were continuously collected and binned in 10 minutes intervals, accounting for a 30 ºC temperature range. At 900 ºC each sample was held for 1.5 – 10 hours. Data continued to be collected during both, long annealing and cooling down, using the same collection procedure.

Physical property measurements were done on separately prepared samples, using the synthesis protocol discussed in previous Sections, with results presented in Appendix D.

5.3. $TiNi_{1+y}Sn$ (y = 0, 0.075, 0.25) series

Two-dimensional (2D) intensity contour maps of diffraction patterns for the formation of TiNiSn, $TiNi_{1.075}Sn$ and $TiNi_{1.25}Sn$ during heating at constant rate (3°C/min), followed by annealing at 900 °C and cooling down are shown in Figure 5.1. The solid red line indicates the temperature during the measurement, while dashed white lines denote the identified reaction regions (I-IV).

Rietveld analysis of the extracted data enabled the determination of intermediate phases and their weight percentages, with the results presented in Figure 5.2 and Figure 5.3. To confirm the accuracy of the Rietveld analysis, the percentage content of each element is also shown. At each key transformation (~230 ºC and 740 – 770 ºC) a depletion in Sn and

increase in Ti and Ni fractions are observed. As the reaction proceeds, the values plateau at constant values, consistent with the starting compositions. The decrease in Sn content is attributed to the melting of Sn and $Ni_{3+y}Sn_4$.

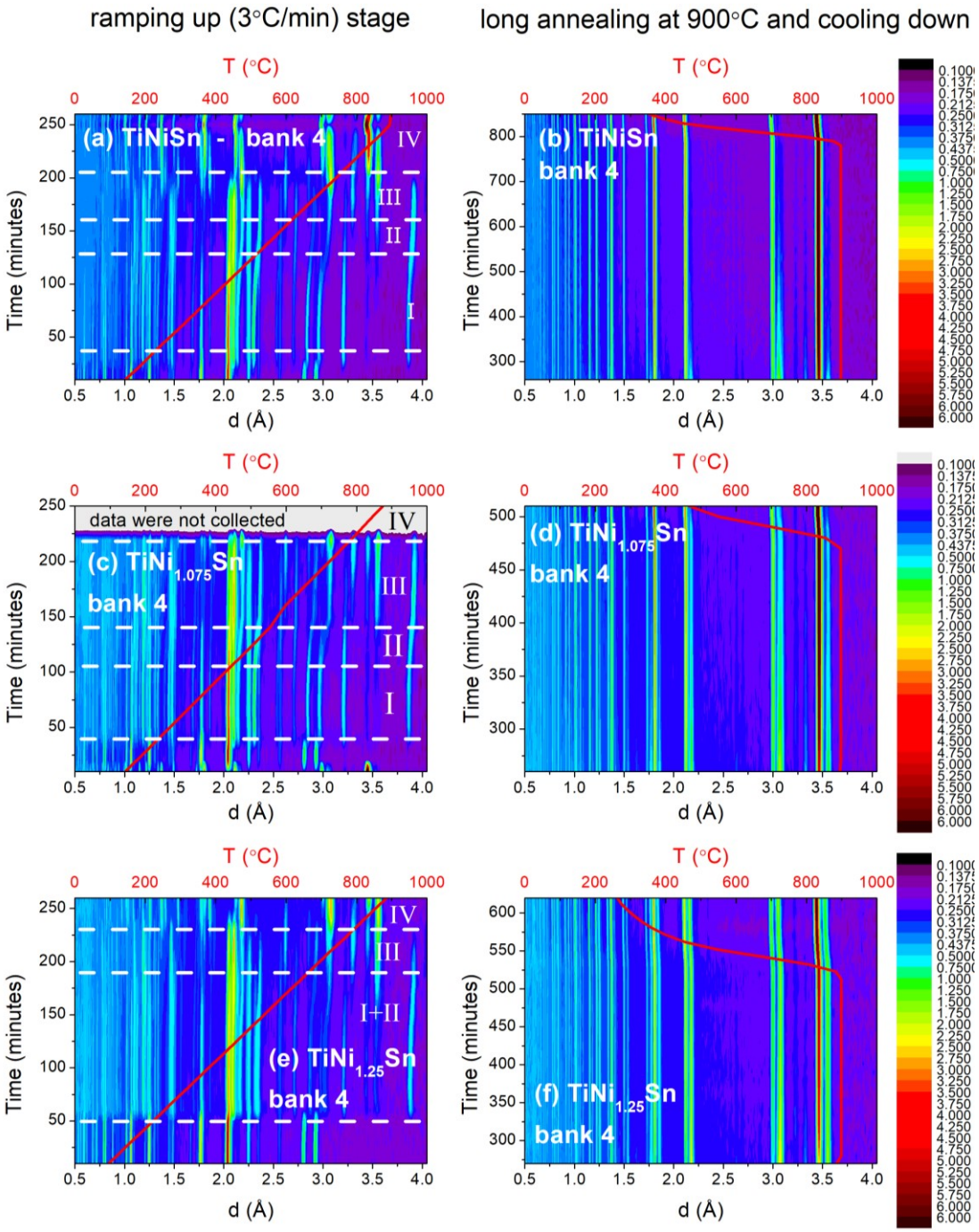

Figure 5.1. A two-dimensional colour map of neutron powder diffraction patterns for the formation of **(a,b)** TiNiSn, **(c,d)** $TiNi_{1.075}Sn$ and **(d,e)** $TiNi_{1.25}Sn$ during heating up, long annealing at 900 °C and cooling down. The red solid line indicates the temperature variation during the measurement. Rietveld refinement revealed 4 key reaction regions (denoted I-IV).

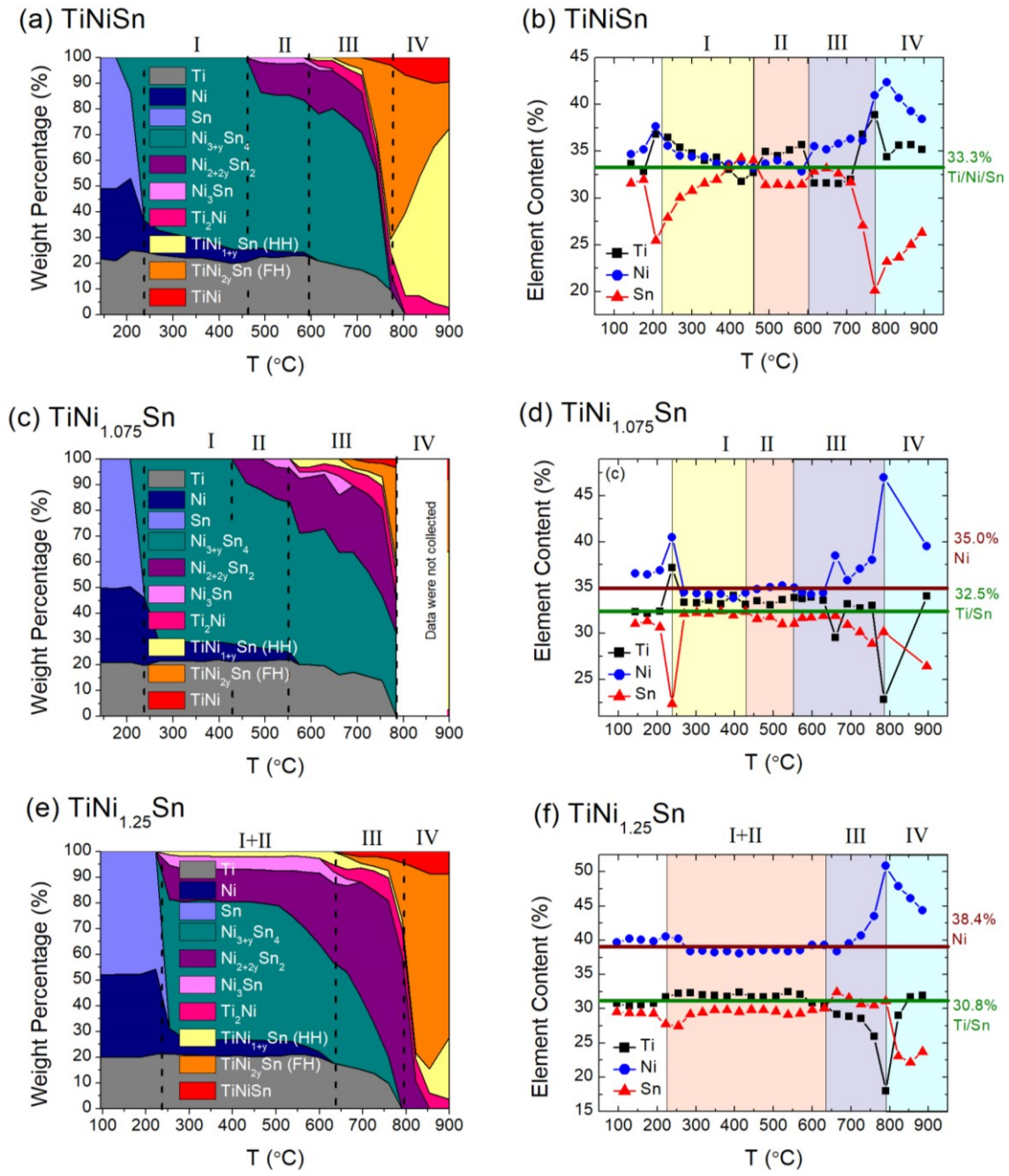

Figure 5.2. Weight percentage of the intermediate phases and percentage element content identified for the formation of **(a,b)** TiNiSn, **(c,d)** $TiNi_{1.075}Sn$ and **(e,f)** $TiNi_{1.075}Sn$ during heating at constant rate of 3 °C/min. The green and brown solid lines in (b), (d) and (f) denote ideal percentage element content. Rietveld refinement revealed 4 key reaction regions (denoted I-IV).

The Rietveld analysis of data collected during the ramping up step revealed 2 melting points and 4 reaction regions, labelled I-IV (Figure 5.2). The phases, which are involved

in this reaction are schematically shown in Figure 5.4. Detailed results for TiNiSn, $TiNi_{1.075}Sn$ and $TiNi_{1.25}Sn$ are shown in Table D1-D6 in Appendix D.

Focusing on TiNiSn. As can be seen in the 2D contour plot map (Figure 5.1 a-b), the first transformation at ~230 ºC corresponds to the melting of Sn (m_p = 231.9 ºC) and formation of a Ni_3Sn_4 binary phase, initiating the Region I. As the heating continues up to ~475 °C, the Ni_3Sn_4 reacts with molten Sn and a small amount of unreacted Ni is slowly introduced on the vacant *2c* (0, 0, 0.5) site to form $Ni_{3+y}Sn_4$. In Region II (identified from ~475 – 600 °C), the phase fraction of $Ni_{3+y}Sn_4$ decreases due to its further reaction with Ni and transformation into $Ni_{2+2y}Sn_2$ and Ni_3Sn. Surprisingly, elemental Ti does not react up to ~600 °C, commencing Region III. Above this point, the Ti gradually combines with the remaining Ni and Ni-Sn binaries to form Ti_2Ni and a small fraction of half-Heusler TiNiSn. The full-Heusler $TiNi_{2y}Sn$ (y ~ 0.9) and Ti_2Ni are also observed at this stage. The second key transformation occurs at 740 – 770 ºC and is related to the melting of Ni_3Sn_4 (m_p = 794.5 ºC).[191] The presence of liquid phase is evidenced by the sudden decrease of Sn and increase in Ti and Ni percentage contents (see Figure 5.2b). This point initiates the final Region IV that continues throughout ramping up to 900 °C and long annealing at this temperature. Here, the Ni-Sn binaries and Ti rapidly decrease and the half-Heusler and full-Heusler become dominant. Moreover, the weight fraction of Ti_2Ni reaches its maximum of ~8.0(2) wt% and a completely new TiNi phase appears, increases in content and reaches its maximum (~10.0(2) wt%) at ~870 ºC.

As shown in Figure 5.2, the formation of TiNiSn is complex and involves many intermediates. The Bragg reflections of all identified phases are shifted to higher *d*-spacing due to the continuous increase of unit cell parameters associated with the thermal expansion. $Ni_{3+y}Sn_4$ is the most Sn-rich phase, which crystalizes into a monoclinic unit cell (space group *C12/m1*) and exhibits a very broad compositional range. At room temperature, the $Ni_{3+y}Sn_4$ phase covers $0.080(5) \leq y \leq 0.60(2)$.[192] During ramping up, additional Ni enters the vacant *2c* (0, 0, ½) site (see Figure 5.4 for crystal structure). As the reaction proceeds, more Ni is introduced with a maximum y = 0.61 at ~650 ºC. Ni_3Sn_2, denoted as $Ni_{2+2y}Sn_2$ is another well-known and extensively studied composition. Equally to $Ni_{3+y}Sn_4$, it covers a wide compositional range ($0.35 < y < 0.59$).[193] During the heating step, the amount of Ni that occupies the *2d* site (⅓, ⅔, ¾) decreases with increasing temperature and reaches a minimum y = 0.30 at ~650 ºC (see Figure 5.4 for crystal structure).

Similar reaction mechanism and crystalline intermediates were observed for $TiNi_{1.075}Sn$ and $TiNi_{1.25}Sn$. Focussing on $TiNi_{1.075}Sn$, the first transformation occurs at ~230 ºC, which is related to the melting of Sn and formation of $Ni_{3+y}Sn_4$ binary phase, initiating Region I. As shown in Figure 5.2c, the fraction of $Ni_{3+y}Sn_4$ is comparable with the TiNiSn sample. As the temperature increases, the $Ni_{3+y}Sn_4$ slowly reacts with molten Sn and unreacted Ni gradually enters the *2c* (0, 0, ½) site. Due to the higher amount of excess Ni in the precursors mixture, a higher amount of Ni enters the *2c* site at lower temperature (e.g. y = 0 for TiNiSn at ~270 ºC – Table D1; y = 0.11 for $TiNi_{1.075}Sn$ at ~270 ºC – Table D3). In Region II (~445 – 555 °C), the fraction of $Ni_{3+y}Sn_4$ decreases rapidly due to further reaction with Ni and transformation into $Ni_{2+2y}Sn_2$ and Ni_3Sn. As expected, a higher amount of $Ni_{2+2y}Sn_2$ is formed, compared to TiNiSn. Similar to TiNiSn, the Ti precursor does not react at low temperatures. It remains intact up to ~575 ºC commencing Region III. At this point, it slowly reacts with Ni-Sn binaries to form Ti_2Ni and a half-Heusler phase. As the reaction proceeds, the Ti content decreases, the fraction of Ti_2Ni increases, while the amount of half-Heusler remains relatively constant. The full-Heusler $TiNi_{2y}Sn$ and TiNi form at ~690 ºC and ~720 ºC, respectively. Due to a problem with the neutron beam, we were unable to collect data in between ~800 – 890 ºC. Analysis of TiNiSn established that the key half-Heusler formation occurs at this stage. Investigation of data collected throughout the long annealing at 900 ºC, revealed the same intermediate phases as for TiNiSn (namely $TiNi_{1+y}Sn$, $TiNi_{2y}Sn$ and TiNi) suggesting similar reaction mechanism (see Figure 5.3c).

Figure 5.2 (e-f) summarise the in-situ NPD monitoring of $TiNi_{1.25}Sn$. The first transformation occurs at ~230 ºC, which corresponds to Sn melting. Contrasting with the TiNiSn and $TiNi_{1.075}Sn$ samples, $Ni_{3+y}Sn_4$ is not the only newly-grown phase at this point. As the amount of excess Ni in precursors mixture is significantly higher, $Ni_{2+2y}Sn_2$, Ni_3Sn and $TiNi_{1+y}Sn$ immediately form upon Sn melting (see Figure 5.2e), in essence merging Regions I and II. Again, elemental Ti remains intact up to ~630 – 660 °C. Its reaction with Ni-Sn binaries and formation of $TiNi_{2y}Sn$ full-Heusler, Ti_2Ni and TiNi initiates Region III. As the reaction proceeds, the Ti content decreases and completely disappears at ~760 ºC, while the fraction of Ti_2Ni increases and reaches maximum (10.1(2) wt%) at 790 ºC. A second key transformation is observed at ~790 °C indicating the Region IV. At this point $Ni_{3+y}Sn_4$ melts, while $TiNi_{2y}Sn$ and TiNi become dominant phases with a maximum content of ~76.0(2) wt% and 8.9(2) wt% recorded at ~850 ºC and 880 ºC, respectively. Above 880 ºC, the amount of full-Heusler and TiNi starts to decrease, indicating their reaction with molten Ni-Sn and formation of the half-Heusler phase.

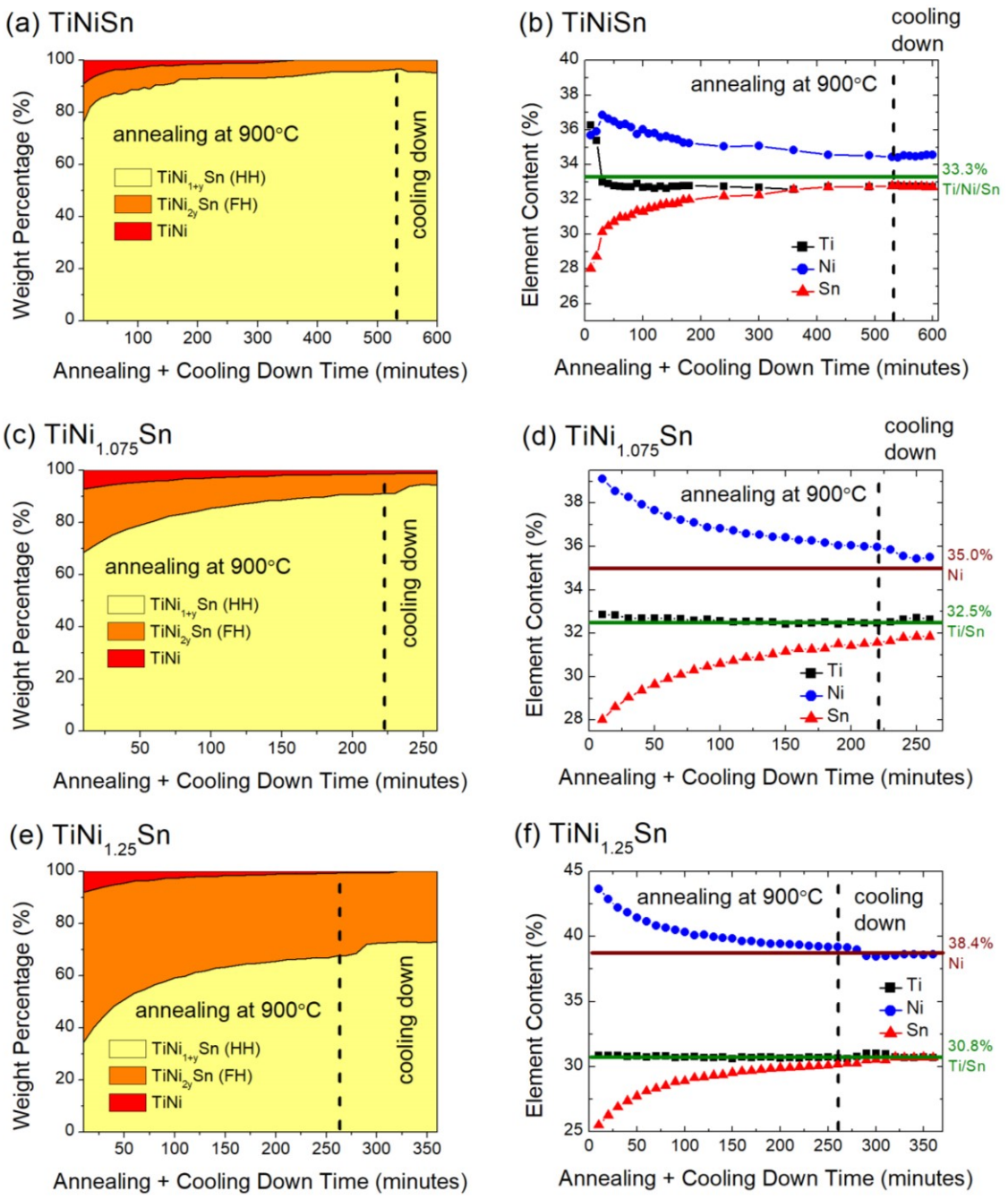

Figure 5.3. Weight percentage of the intermediate phases and percentage element content identified for the formation of **(a,b)** TiNiSn, **(c,d)** $TiNi_{1.075}Sn$ and **(e,f)** $TiNi_{1.075}Sn$ during annealing at 900 °C and cooling down. The green and brown solid lines in (b), (d) and (f) denote ideal percentage element content.

Long annealing is an essential step to improve the homogeneity of half-Heusler alloys as well as to reduce the amount of impurity phases. Figure 5.3 summarises reaction progress and intermediates involved during the annealing stage of TiNiSn, $TiNi_{1.075}Sn$ and $TiNi_{1.25}Sn$ formation. A similar mechanism was observed for all compositions, however

the amount of the target half-Heusler and intermediates depends on the amount of introduced excess Ni. Focusing on TiNiSn; long annealing enables the full-Heusler to react further with TiNi and "molten" Ni-Sn to form the target half-Heusler. As the reaction proceeds, the fraction of full-Heusler decreases from 14.8(2) wt% (10 minutes) to 3.5(2) wt% (after 9 hours), while the TiNi phase is reduced from 8.9(2) wt% to 0.9(2) wt% during 5 hours and then completely disappears. The percentage element content plateaus at constant value (~33 % for Ti, ~34% for Ni and ~33% for Sn), suggesting the equilibrium and system stabilisation (see Figure 5.3b). As no further transformation was observed, the sample was slowly cooled after total annealing time of 530 minutes. The data on cooling was recorded up to ~400 ºC. We found that at ~350 °C the TiNiSn consists of 95.2(2) wt% of TiNi[$Ni_{0.027(2)}$]Sn and 4.8(2) wt% of Ni-deficient $TiNi_{1.8}Sn$. This is not a surprising observation as Ni deficiencies in full-Heusler ($TiNi_{2-y}Sn$ denoted here as $TiNi_{2y}Sn$)[103, 115, 129] and metal-rich half-Heusler ($TiNi_{1+y}Sn$)[129, 178] are extensively studied.

As expected, a similar mechanism and the same intermediates as for TiNiSn (namely $TiNi_{1+y}Sn$, $TiNi_{2y}Sn$ and TiNi) were observed for $TiNi_{1.075}Sn$ and $TiNi_{1.25}Sn$ samples. For $TiNi_{1.075}Sn$ (Figure 5.3 c-d), the fraction of full-Heusler (24.1(2) wt% at 10 minutes) rapidly decreases during first 120 minutes of annealing (10.5(2) wt%), while a slower reduction rate (~0.27 wt% / 10 minutes) is observed above this point. A comparable trend is observed for TiNi – its content decreases from 7.1(2) wt% to 1.4(2) wt% after 210 minutes of annealing. The sample was cooled after 210 minutes of annealing. The mixture of 93.3(1) wt% of TiNi[$Ni_{0.061(2)}$]Sn, 4.5(2) wt% of Ni-deficient $TiNi_{1.80}Sn$ and 1.2(2) wt% of TiNi was observed at ~390 °C suggesting longer annealing is essential to complete the reaction.

Similar to the TiNiSn and $TiNi_{1.075}Sn$ compositions, long annealing of $TiNi_{1.25}Sn$ allows the full-Heusler to slowly react with TiNi and "molten Ni-Sn" to form the target half-Heusler alloy (see Figure 5.3e). The fraction of full-Heusler (57.6(2) wt% at 10 minutes) rapidly decreases during the first 120 minutes of annealing (36.7(2) wt%), while the half-Heusler content increases (34.0(2) wt% at 10 minutes; 61.1(2) wt% at 120 minutes). As the annealing proceeds, the fraction of full-Heusler is reduced further and half-Heusler content increases but with a much slower rate (~0.33 wt% / 10 minutes for full-Heusler and ~0.09 wt% / 10 minutes for half-Heusler). The fraction of TiNi decreases from 8.0(2) wt% to 0.9(2) wt% after 250 minutes of annealing and completely disappears during the cooling step.

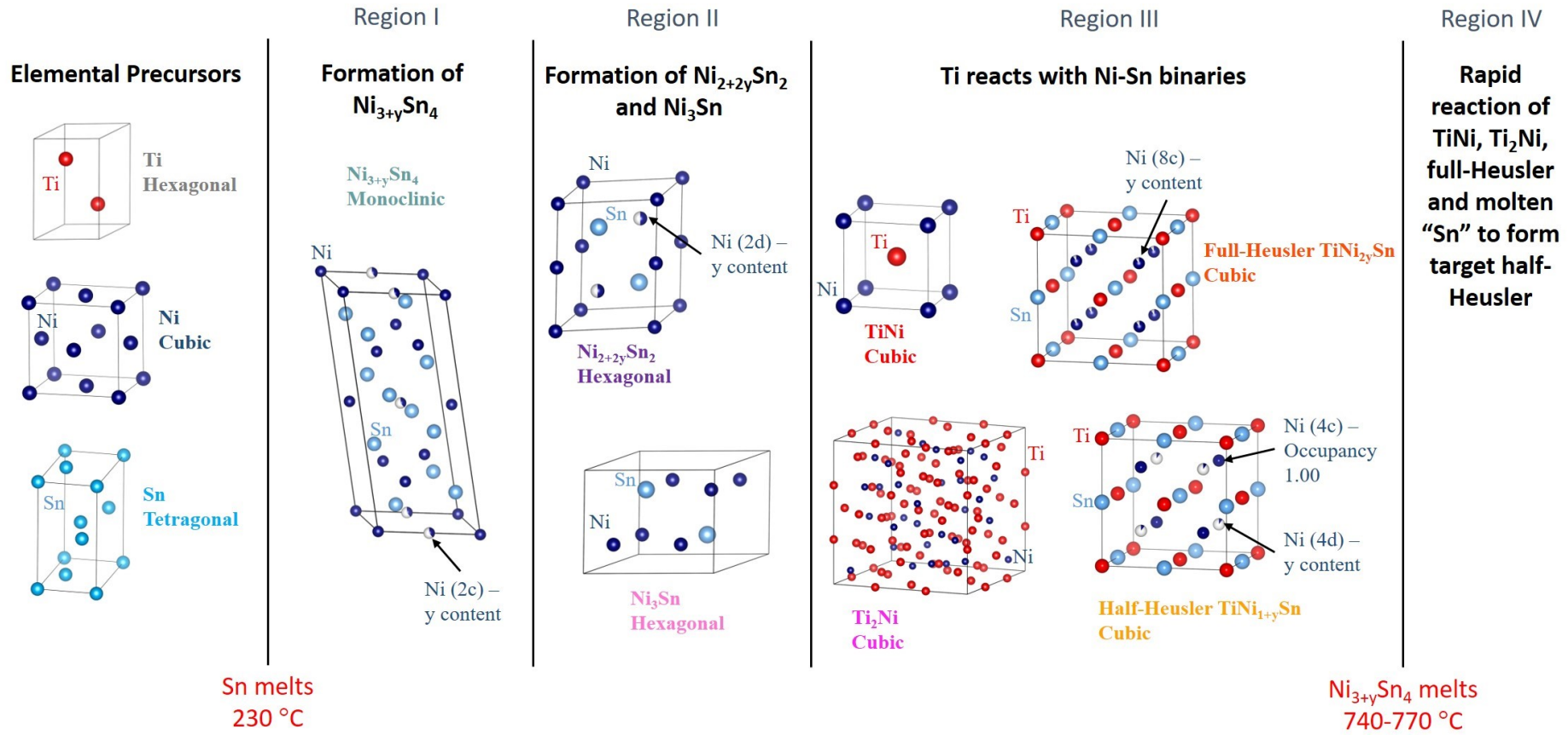

Figure 5.4. Rietveld refinement of NPD data revealed 2 melting points (at ~230°C and ~750-780 °C) and 4 reaction regions (labelled I-IV). At 230°C the Sn melts and $Ni_{3+y}Sn_4$ forms, initiating first region. In **Region I**: Ti remains intact and Ni slowly reacts with molten Sn and $Ni_{3+y}Sn_4$ by entering the normally vacant *2c* site of $Ni_{3+y}Sn_4$. In **Region II**: Ti remains intact, Ni reacts further with $Ni_{3+y}Sn_4$ and two new phases are formed ($Ni_{2+2y}Sn_2$ and Ni_3Sn). In **Region III**: Ti reacts with Ni-Sn binaries to form Ti-containing phases, namely: TiNi, Ti_2Ni, half-Heusler $TiNi_{1+y}Sn$ and full-Heusler $TiNi_{2y}Sn$. At ~750-780 °C, $Ni_{3+y}Sn_4$ melts initiating the final region. Throughout **Region IV**, the TiNi, Ti_2Ni, full-Heusler slowly reacts with molten Ni-Sn binary to form target half-Heusler material. This stage continues throughout the long annealing.

As expected, the $TiNi_{1.25}Sn$ contains the largest fraction of $TiNi_{2y}Sn$ phase, which can be easily explained by the highest amount of excess Ni (y = 0.25). We found that at ~260 °C, $TiNi_{1.25}Sn$ consists of 72.6(2) wt% of metal-rich $TiNi[Ni_{0.068(2)}]Sn$ and 27.4(2) wt% of Ni-deficient $TiNi_{1.88(4)}Sn$.

To complete the in-situ NPD experiment, the thermoelectric property measurements of $TiNi_{1+y}Sn$ (y = 0, 0.075 and 0.25) compositions were carried out on separately prepared samples. The results of XRD and measured properties are presented in Appendix D.

5.4. ZrNiSn and $Ti_{0.5}Zr_{0.25}Hf_{0.25}NiSn$

5.4.1. In-situ Neutron Powder Diffraction Monitoring

The results of in-situ NPD of ZrNiSn and $Ti_{0.5}Zr_{0.25}Hf_{0.25}NiSn$ are presented in Figure 5.5. For both systems, the first transformation occurs at ~230 – 260 ºC and is related to the melting of the Sn precursor. For $TiNi_{1+y}Sn$, the Sn melting is accompanied by the formation of Ni-Sn binaries. Interestingly, for ZrNiSn and $Ti_{0.5}Zr_{0.25}Hf_{0.25}NiSn$, the only phase formed at this temperature is the final product – a single half-Heusler phase. This is a surprising observation, as multiple intermediates were identified throughout the synthesis protocol of $TiNi_{1+y}Sn$ and $M_{0.5}M'_{0.5}NiSn$ (M = Ti, Zr, Hf) compositions, with half-Heusler phases formed mainly at high temperatures. To investigate the above trend further, the pressure inside the high-vacuum furnace ($P_{average}$) was plotted against the total experiment time (solid green line in Figure 5.5 b and e). The $P_{average}$ is the average pressure of 10 minutes-long collection scans that account for 30ºC temperature range. The $P_{average}$ remains relatively constant during the experiments, though significant increase is observed at ~230 – 260 ºC suggesting a strong exothermic process. Recently Su et al.[194] investigated the self-propagating high-temperature synthesis (SPS) as an alternative method for preparing high purity thermoelectric compounds. In SPS, the sample's combustion is initiated through the point-heating that creates combustion wave. The heat liberated in one section of sample is sufficient to maintain the reaction in the neighbouring sections. This technique has been tried with ZrNiSn, producing a single-phase material. In our opinion, the ZrNiSn and $Ti_{0.5}Zr_{0.25}Hf_{0.25}NiSn$ were prepared through a similar self-propagating process (SPS). In powder form, Zr is highly flammable. At ~230 ºC, Sn has molten creating a heating point within the sample. Once started, a wave of exothermic reaction swept through the sample, forming single-phase half-Heusler. The Zr combustion and build-up of pressure within the vanadium can, created an environment suitable self-propagating combustion reaction. The entire process

was likely completed within a few seconds. Visual inspection of samples directly after the in-situ experiment (Figure 5.6) revealed that $Ti_{0.5}Zr_{0.5}NiSn$, $Ti_{0.5}Hf_{0.5}NiSn$ and $Zr_{0.5}Hf_{0.5}NiSn$ (discussed below) are in powdered form, which is characteristic for laboratory prepared samples. However, $Ti_{0.5}Zr_{0.25}Hf_{0.25}NiSn$ and ZrNiSn look like molten ingots typical of e.g. arc-melted compositions. The reacted ZrNiSn material following the combustion was rather porous, therefore it was ground and hot-pressed to achieve near theoretical density. Same procedure was applied for $Ti_{0.5}Zr_{0.25}Hf_{0.25}NiSn$.

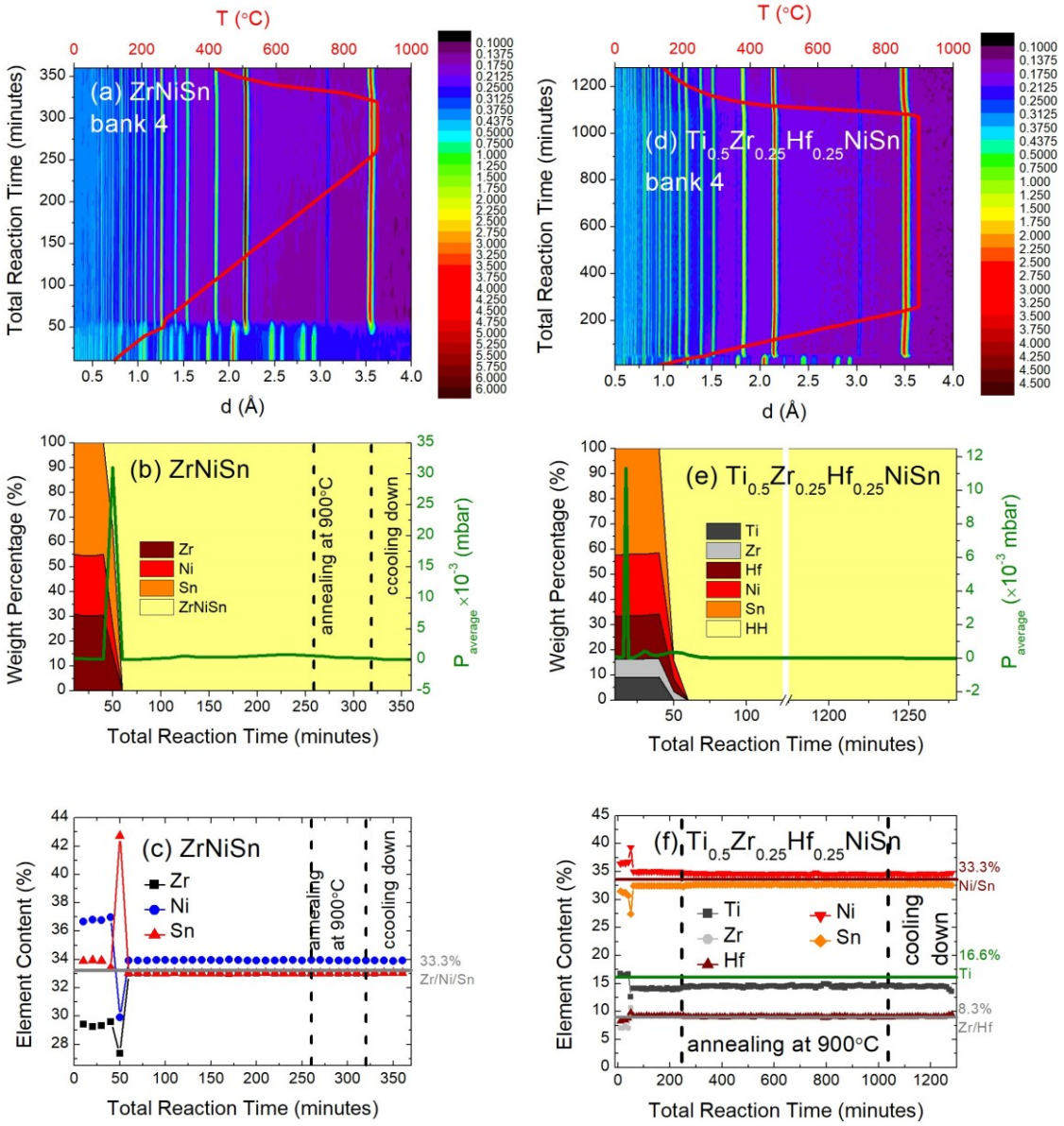

Figure 5.5. A two-dimensional intensity colour plot of neutron powder diffraction patterns, weight percentage of the intermediate phases and percentage element content identified for the formation of **(a-c)** ZrNiSn and **(d-f)** $Ti_{0.5}Zr_{0.25}Hf_{0.25}NiSn$ during heating at constant rate of 3 °C/min, annealing at 900 °C and cooling down. The grey, green and brown solid lines in (c) and (f) denote ideal percentage element content. The green solid line in panels (b) and (d) represents the average pressure ($P_{average}$) inside the furnace.

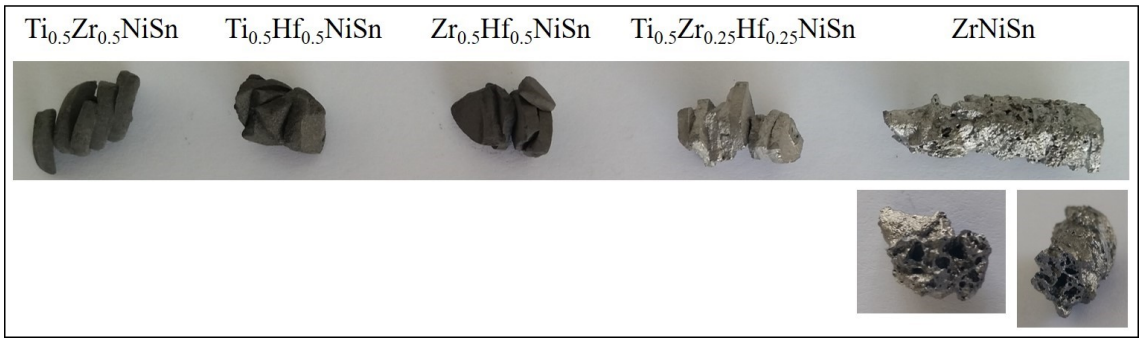

Figure 5.6. Visual comparison of samples after in-situ NPD experiment.

5.4.2. Thermoelectric Properties

The thermoelectric properties of the ZrNiSn and $Ti_{0.5}Zr_{0.25}Hf_{0.25}NiSn$ compositions are shown in Figure 5.7. For comparison, the transport properties of ZrNiSn and $Ti_{0.5}Zr_{0.25}Hf_{0.25}NiSn$, synthesised using the solid-state reaction (SSR) are also included. The C_p for SSR ZrNiSn and $Ti_{0.5}Zr_{0.25}Hf_{0.25}NiSn$ (shown in Appendix D) were used to evaluate thermal transport of SPS samples. The temperature dependence of α and LT/ρ are also shown in Appendix D.

Focussing first on the ZrNiSn composition. Both, SPS and SSR samples are characterised by negative sign of S indicating n-type conduction and electrons as the major charge carriers (Figure 5.7a). Similar S values are observed at low temperature (S_{314K} = -241 μV K^{-1} for SPS and S_{314K} = -238 μV K^{-1} for SSR). As temperature increases, significantly higher S is reported for SSR composition (S_{max} = -321 μVK^{-1} at 464 K for SSR and S_{max} = -269 μV K^{-1} at 443 K for SPS). The $\rho(T)$ decreases as a function of temperature suggesting semiconducting behaviour with higher values recorded for ZrNiSn (SSR). However, the $\rho(T)$ of SPS sample is more metallic than SSR ZrNiSn. The dramatic changes in S and ρ can be explained by excess Ni. Our previous work[85] revealed that SSR ZrNiSn forms stoichiometric half-Heusler matrix with no evidence of Ni interstitials. The final composition of SPS ZrNiSn contains 2.5% of spontaneously formed excess Ni on the *4d*-site, suggesting it acts as n-type dopant. The $S^2/\rho(T)$ are shown in Figure 5.7c. The S^2/ρ of ZrNiSn (SPS) is higher at low temperatures (S^2/ρ_{314} = 0.8 mW K^{-2} m^{-1}) compared with SSR sample (S^2/ρ_{314} = 0.5 mW K^{-2} m^{-1}). Rapid increase of S^2/ρ with temperature and similar maximum S^2/ρ_{max} = 2.0 – 2.1 mW K^{-2} m^{-1} were observed for both samples, confirming that spontaneous Ni doping does not reduce the electronic transport.

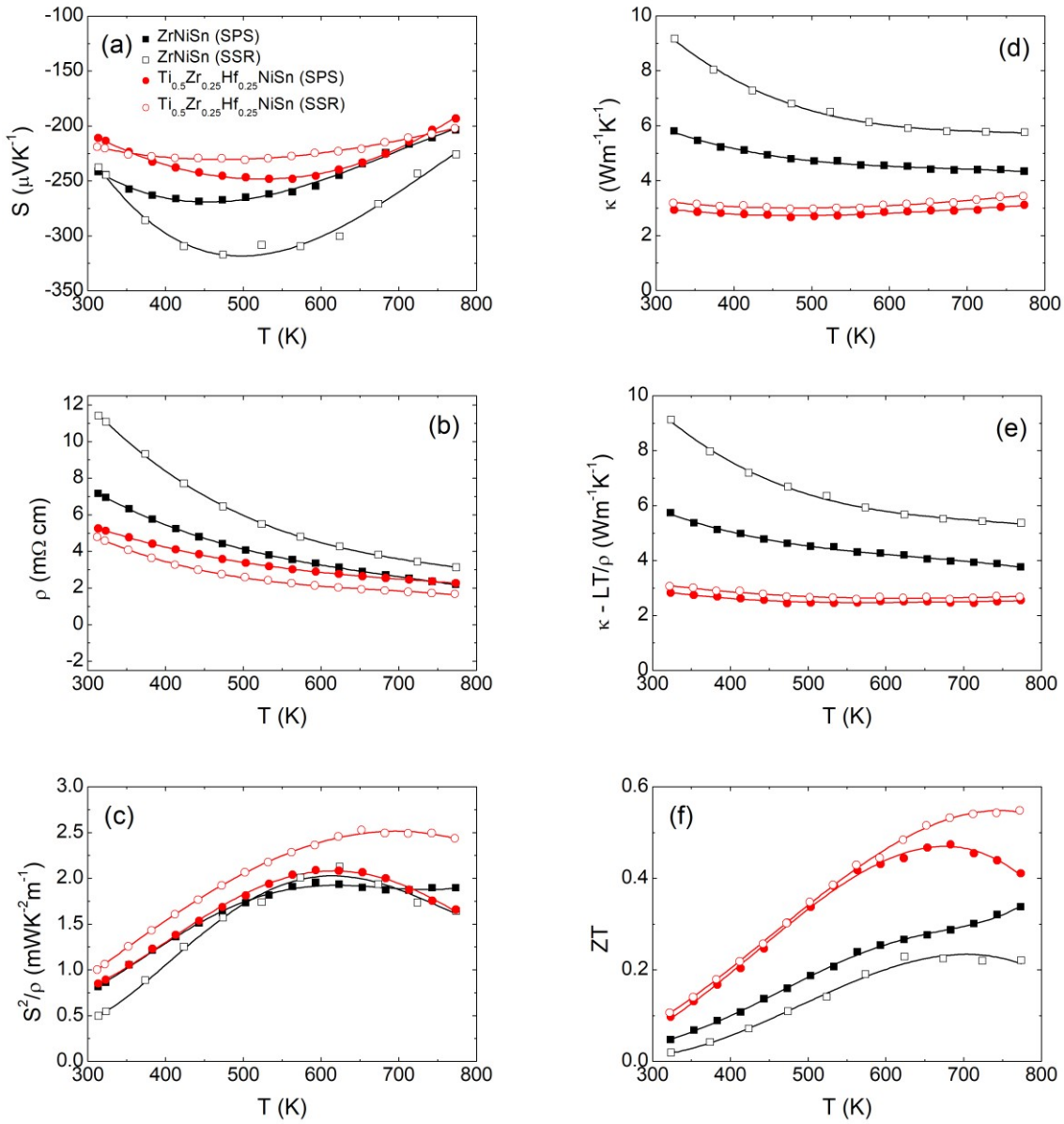

Figure 5.7. Temperature dependence of **(a)** the absolute Seebeck coefficient (S), **(b)** the resistivity (ρ), **(c)** the thermoelectric power factor (S^2/ρ), **(d)** the total thermal conductivity (κ), **(e)** the lattice thermal conductivity (κ-LT/ρ) and **(f)** figure of merit (ZT) for ZrNiSn and $Ti_{0.5}Zr_{0.25}Hf_{0.25}NiSn$ that were prepared through self-propagating high-temperature synthesis (SPS). ZrNiSn and $Ti_{0.5}Zr_{0.25}Hf_{0.25}NiSn$ that were prepared through standard solid-state reaction (SSR) are shown for comparison.

The $\kappa(T)$ mimics the temperature dependence of α. Typical semiconducting behaviour is observed for both materials: κ decreases until ~620 K, without significant changes above this point (Figure 5.7d). Lower κ values over the whole temperature range are observed for the SPS sample. It is clear from Figure 5.7e that κ-LT/ρ of the SPS sample is

significantly reduced compared to the SSR sample. As discussed in previous Chapters, interstitial Ni enhances strength of point defect scattering, which is responsible for the reduction of $\kappa_{lattice}$. Spontaneous formation of Ni-rich half-Heusler matrix in the SPS sample explains the above trend. The $ZT(T)$ is summarised in Figure 5.7f. It is evident that the synthesis protocol has influenced the thermoelectric properties of ZrNiSn. Significantly higher ZT values over the whole temperature range are observed for the SPS sample. The $ZT = 0.05$ at 323 K and $ZT_{max} = 0.33$ at 773 K are improved compared to the SSR sample ($ZT = 0.02$ at 324 K and $ZT_{max} = 0.22$ at 624 K). The reported values are slightly lowered when compared to ZrNiSn that was recently investigated by Su ($ZT =$ 0.38 at 629 K).[194]

Focussing on $Ti_{0.5}Zr_{0.25}Hf_{0.25}NiSn$, negative sign of S confirms n-type conduction (Figure 5.7a). Similar S at low temperature ($S_{314K} = -211$ μV K^{-1} for SPS and $S_{314K} = -219$ μVK^{-1} for SSR) were observed. Interestingly the $S(T)$ curve of the SPS sample is more parabolic (with higher values) compared with more linear trend seen for SSR composition. Similar ρ temperature dependence is recorded, with slightly lower values for SSR $Ti_{0.5}Zr_{0.25}Hf_{0.25}NiSn$ (see Figure 5.7b). The SSR composition exhibits higher S^2/ρ over the whole temperature range. The maximum S^2/ρ are 2.1 mW K^{-2} m^{-1} at 603 K and 2.5 mW K^{-2} m^{-1} at 642 K for SPS and SSR compositions, respectively. The $\kappa(T)$ mimics the $\alpha(T)$ with almost identical $\kappa(T)$ trends observed for SPS and SSR samples. Relatively constant values over the whole temperature range were observed for both materials. The $\kappa_{lattice}$ mimics the $\kappa(T)$ dependence, with very similar, relatively constant values over the whole temperature range (see Figure 5.7e). As shown in Chapter 4, the phonon scattering in multiphase materials largely depends on the mass difference between M metals. Any excess Ni has a secondary impact on the $\kappa_{lattice}$. Similar $\kappa_{lattice}$ of SPS and SSR materials suggest similar final compositions. Both, SPS and SSR compositions show relatively high ZT near RT ($ZT_{322K} = 0.10$ and $ZT_{323K} = 0.11$, respectively). As temperature rises, ZT of SSR sample increases and reaches $ZT_{max} = 0.55$ at 773 K. The SPS $Ti_{0.5}Zr_{0.25}Hf_{0.25}NiSn$ reaches its maximum at lower temperature ($ZT_{max} = 0.47$ at 683 K), above which the reduction is observed.

5.5. $Ti_{0.5}Zr_{0.5}NiSn$, $Ti_{0.5}Hf_{0.5}NiSn$ and $Zr_{0.5}Hf_{0.5}NiSn$

In the final part of this chapter, the formation of $Ti_{0.5}Zr_{0.5}NiSn$, $Ti_{0.5}Hf_{0.5}NiSn$ and $Zr_{0.5}Hf_{0.5}NiSn$ was monitored. The thermoelectric properties of the $M_{0.5}M'_{0.5}NiSn$ and an

additional MNiSn (M = Ti, Zr, Hf) were measured on separately prepared samples with results summarised in Appendix D.

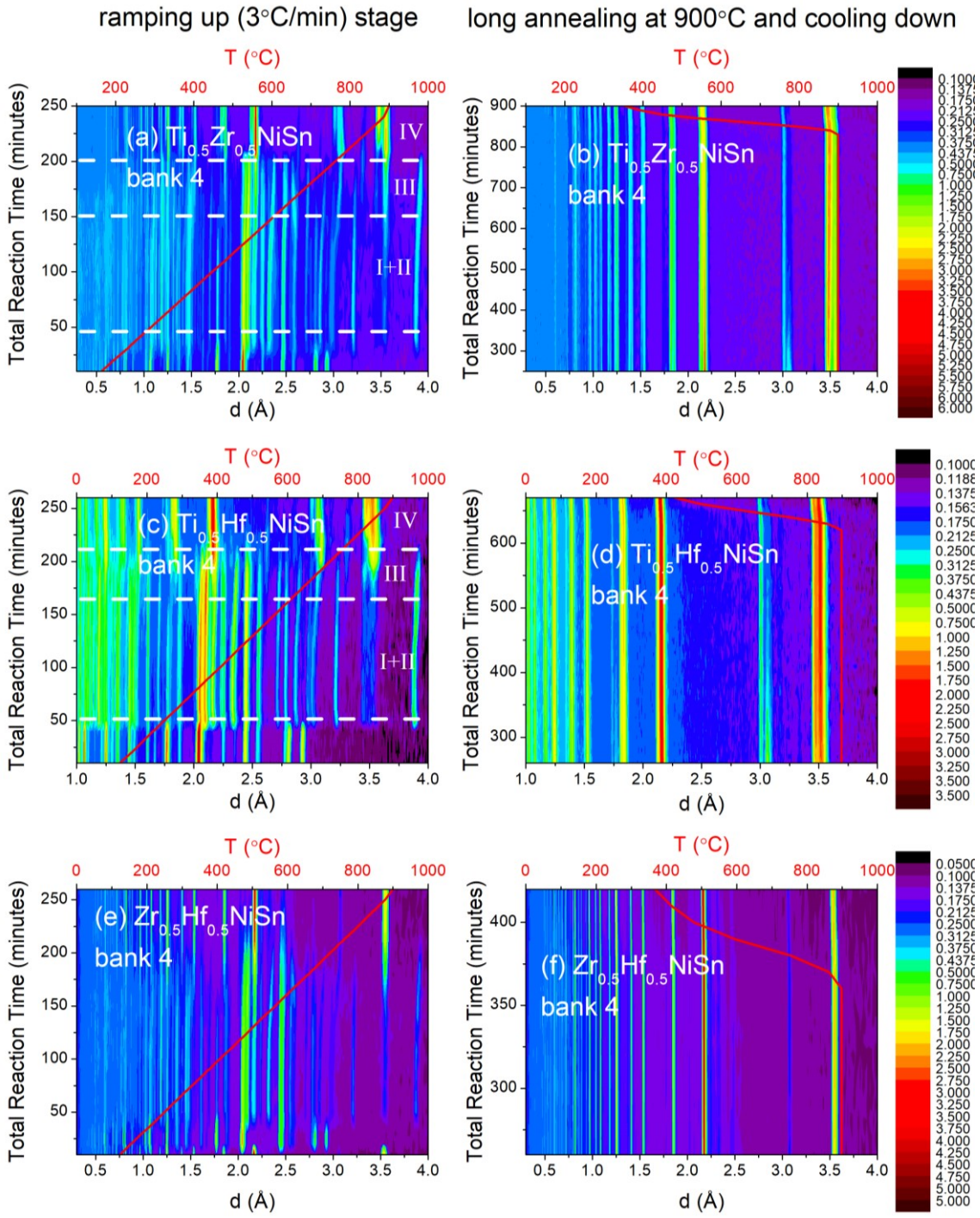

Figure 5.8. A two-dimensional colour map of neutron powder diffraction patterns for the formation of **(a,b)** $Ti_{0.5}Zr_{0.5}NiSn$, **(c,d)** $Ti_{0.5}Hf_{0.5}NiSn$ and **(d,e)** $Zr_{0.5}Hf_{0.5}NiSn$ during heating up, long annealing at 900 °C and cooling down. The red solid line indicates the temperature variation during the measurement. Rietveld refinement revealed 4 key reaction regions (denoted I-IV).

The 2D intensity colour plot maps of in-situ NPD data for $Ti_{0.5}Zr_{0.5}NiSn$, $Ti_{0.5}Hf_{0.5}NiSn$ and $Zr_{0.5}Hf_{0.5}NiSn$ are shown in Figure 5.8. Detailed results of Rietveld analysis are presented in Tables D8-D12 (Appendix D). Three distinct half-Heusler phases (denoted as HH1, HH2 and HH3) were identified during the formation of $Ti_{0.5}Zr_{0.5}NiSn$ and $Ti_{0.5}Hf_{0.5}NiSn$ samples, while a single half-Heusler phase (HH1) was identified for the $Zr_{0.5}Hf_{0.5}NiSn$ composition. The identified phases were labelled in order of appearance with temperature. The temperatures at which each half-Heusler phase was first formed and its compositional evolution are summarised in Table 5.1.

Table 5.1. Composition of half-Heusler phases at their formation temperatures, composition at 900 °C and after annealing at 900 °C.

		$Ti_{0.5}Zr_{0.5}NiSn$	**$Ti_{0.5}Hf_{0.5}NiSn$**	**$Zr_{0.5}Hf_{0.5}NiSn$**
HH1	Formation temperature and composition	~260 °C ZrNiSn	~280 °C HfNiSn	~250 °C $Zr_{0.5}Hf_{0.5}Ni_{1.06(1)}Sn$
	Composition at 900 °C	ZrNiSn	HfNiSn	$Zr_{0.5}Hf_{0.5}Ni_{1.02(1)}Sn$
	Composition after annealing	ZrNiSn	HfNiSn	$Zr_{0.5}Hf_{0.5}Ni_{1.01(1)}Sn$
HH2	Formation temperature and composition	~635 °C TiNiSn	~280 °C TiNiSn	
	Composition at 900 °C	$Ti_{0.87(1)}Zr_{0.13(1)}Ni_{1.04(1)}Sn$	$Ti_{0.47(1)}Hf_{0.53(1)}NiSn$	
	Composition after annealing	$T_{0.89(1)}Zr_{0.11(1)}Ni_{1.03(1)}Sn$	$Ti_{0.48(1)}Hf_{0.52(1)}NiSn$	
HH3	Formation temperature and composition	~885 °C $Ti_{0.29(1)}Zr_{0.71(1)}NiSn$	~815 °C $Ti_{0.89(1)}Hf_{0.11(1)}Sn$	
	Composition at 900 °C	$Ti_{0.36(1)}Zr_{0.64(1)}NiSn$	$Ti_{0.92(1)}Hf_{0.08(1)}Ni_{1.03(1)}Sn$	
	Composition after annealing	$Ti_{0.47(1)}Zr_{0.53}Ni_{1.02(1)}Sn$	$Ti_{0.93(1)}Hf_{0.07(1)}Ni_{1.03(1)}Sn$	

Focusing on $Ti_{0.5}Zr_{0.5}NiSn$ and $Ti_{0.5}Hf_{0.5}NiSn$; Rietveld analysis of the extracted data enabled determination of intermediates involved in the half-Heusler formation, with results presented in Figure 5.9. Similarly to the $TiNi_{1+y}Sn$ compositions, 2 melting points and 4 reaction regions (I-IV) were identified (see Figure 5.4). The first transformation is observed at ~230 °C, where mixture of Ni-Sn binary phases ($Ni_{3+y}Sn_4$, Ni_3Sn_2, Ni_3Sn) is observed, which is similar for $TiNi_{1.25}Sn$ but unlike for TiNiSn and $TiNi_{1.075}Sn$, where only Ni_3Sn_4 is formed upon Sn melting. In addition, small fraction of ZrNiSn – HH1 (~4.5(2) wt%) was formed in $Ti_{0.5}Zr_{0.5}NiSn$, while 3.0(2) wt% of HfNiSn (HH1) and 1.5(2) wt% of TiNiSn (HH2) were observed for $Ti_{0.5}Hf_{0.5}NiSn$, suggesting the merging of Regions I and II. This is rather surprising as in TiNiSn and $TiNi_{1.075}Sn$, the half-Heusler phase was not formed until 570 – 600 °C. A possible explanation is that a self-propagating combustion reaction was initiated upon Sn melting, however it failed here and the more

regular solid-state route has taken over. At this stage, the majority of Ti, Zr and Hf remain in the elemental form.

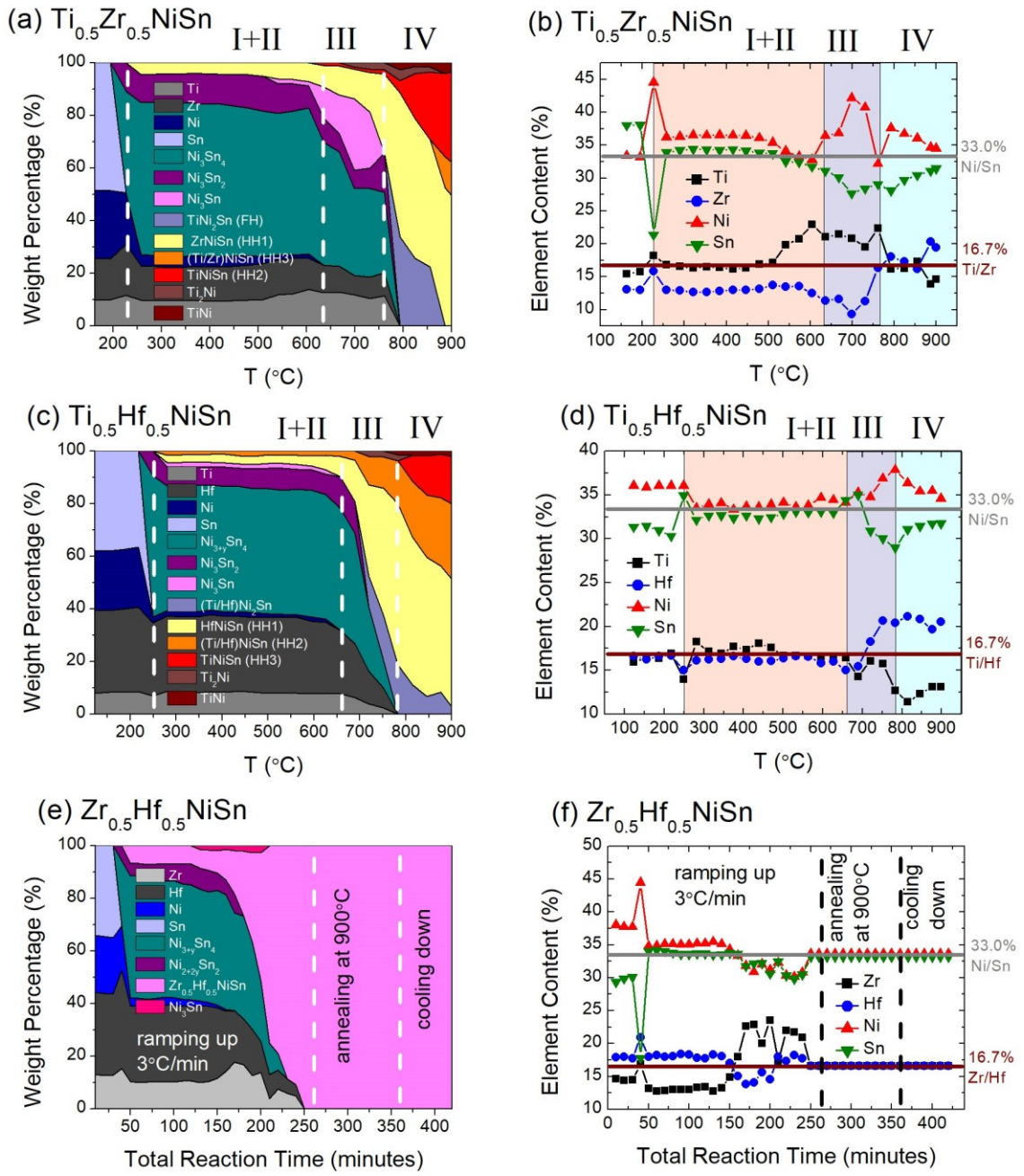

Figure 5.9. Weight percentage of the intermediate phases and percentage element content identified for the formation of **(a,b)** $Ti_{0.5}Zr_{0.5}NiSn$, **(c,d)** $Ti_{0.5}Hf_{0.5}NiSn$ and **(e,f)** $Zr_{0.5}Hf_{0.5}NiSn$ during heating at constant rate of 3 °C/min. The grey and brown solid lines in (b), (d) and (f) denote ideal percentage element content. Rietveld refinement revealed 4 key reaction regions (denoted I-IV).

For $Ti_{0.5}Zr_{0.5}NiSn$ (see Figure 5.9 a-b), the amount of Ni_3Sn_2 and HH1 is relatively constant up to ~510 – 540 ºC, while the $Ni_{3+y}Sn_4$ content does not change significantly up to ~600 ºC. Above this point, the fraction of $Ni_{3+y}Sn_4$ and Ni_3Sn_2 decreases, which is related to the formation of Ni_3Sn and the gradual growth of HH1 phase. At ~635 ºC, the Ni precursor completely disappears and small fraction (~0.9(2) wt%) of HH2 is formed, initiating Region III. During further heating, the amount of elemental Zr is further reduced, Ti_2Ni is recorded at ~700 ºC and Ni_3Sn reaches its maximum (27.0(2) wt% at 700 ºC).

For $Ti_{0.5}Hf_{0.5}NiSn$ (see Figure 5.9 c-d), a small percentage of Ni_3Sn (~1.6(2) wt%) is observed at significantly lower temperature (~280 ºC), compared with $Ti_{0.5}Zr_{0.5}NiSn$. The fractions of $Ni_{3+y}Sn_4$, Ni_3Sn_2, Ni_3Sn, Ti, Hf, HH1 and HH2 are relatively constant up to ~660 ºC. At this point the Ni and Ni_3Sn are no longer observed while Ni_3Sn_2 reaches its maximum (~11.9(2) wt%), initiating Region III. Comparable to $Ti_{0.5}Zr_{0.5}NiSn$ system, Ti_2Ni is detected at ~720 ºC, though a significant fraction of full-Heusler $Ti_{1-x}Hf_xNi_2Sn$ (x = 0.05(1)) is also recorded at this temperature.

The second key transformation is observed at 760-790 °C, which is related to the melting of $Ni_{3+y}Sn_4$. In $Ti_{0.5}Zr_{0.5}NiSn$ system, melting of $Ni_{3+y}Sn_4$ causes rapid reaction of Ni-Sn binaries, Ti and Zr to form large amount (~34.4(2) wt%) of full-Heusler $Ti_{1-x}Zr_xNi_{2y}Sn$ ($0.08(1) < x < 0.16(1)$; $y \sim 0.75$). Moreover, HH1 becomes the dominant phase, Ti_2Ni reaches its maximum (4.1(2) wt%) and TiNi intermediate is formed. As the heating continues the full-Heusler reacts with molten Ni-Sn, Ti_2Ni and TiNi. The amount of HH2 rapidly increases and HH3 is formed ~885 ºC. Throughout further heating up to the target 900 ºC and long annealing, the amount of HH1 and HH2 slowly decreases, TiNi is reduced and disappears after ~300 minutes of long annealing, while the fraction of HH3 increases, becoming the dominant phase (Figure 5.10 a-b). As the reaction rate was significantly reduced, sample was cooled down after total annealing time of 590 minutes.

Similar phase evolution was observed for $Ti_{0.5}Hf_{0.5}NiSn$. At 780 – 810 ºC full-Heusler and HH1 reach a maximum (18.8(2) wt% and 61.2(2) wt%, respectively), while HH3 forms. As the reaction proceeds the full-Heusler content decreases, while HH3 rapidly grows in quantity. Long annealing enables further reaction between all half-Heusler phases, TiNi and molten Ni-Sn (Figure 5.10 c-d). The HH1 content decreases quickly, the fraction of HH3 remains relatively constant (~18.5 – 21 wt%) and HH2 becomes main phase. TiNi that was formed ~780 ºC is no longer observed after 220 minutes of annealing time. The investigated system was cooled down after total annealing time of 360 minutes.

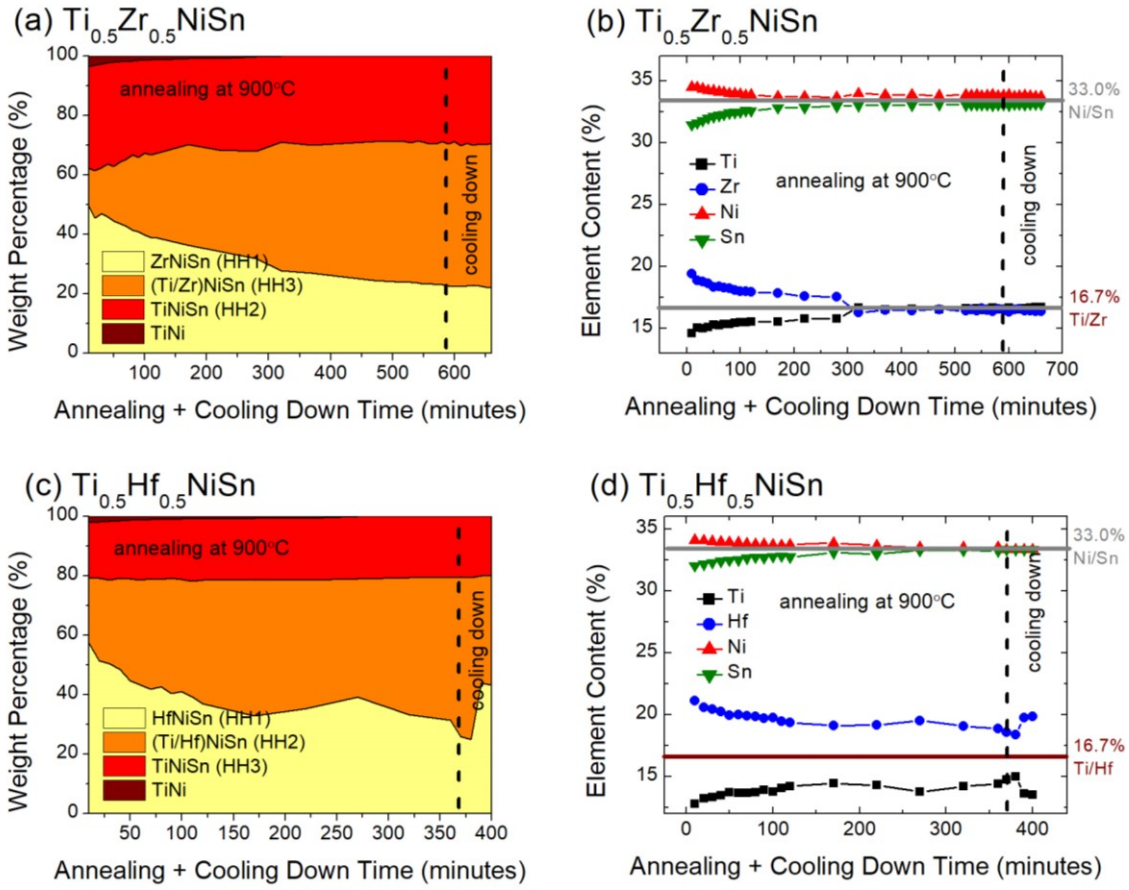

Figure 5.10. Weight percentage of the intermediate phases and percentage element content identified for the formation of **(a,b)** $Ti_{0.5}Zr_{0.5}NiSn$ and **(c,d)** $Ti_{0.5}Hf_{0.5}NiSn$ during annealing at 900 °C and cooling down. The grey and brown solid lines in (b) and (d) denote ideal percentage element content.

Investigation of $Zr_{0.5}Hf_{0.5}NiSn$ (Figure 5.9 e-f) revealed a slightly different mechanism. Sn melting initiates reaction similar to self-propagating synthesis. However, the formation of the half-Heusler proceeds more gradually compared to ZrNiSn and $Ti_{0.5}Zr_{0.25}Hf_{0.25}NiSn$. Like $Ti_{0.5}Zr_{0.5}NiSn$ and $Ti_{0.5}Hf_{0.5}NiSn$, $Ni_{3+y}Sn_4$ (46.5(2) wt%), Ni_3Sn_2 (5.0(2) wt%) and half-Heusler $Zr_{0.5}Hf_{0.5}Ni_{1+y}Sn$ (7.0(2) wt%) were formed immediately upon Sn melting, with relatively constant fractions up to ~600 ºC. In addition, small fraction (~1.3(2) wt%) of Ni_3Sn intermediate is observed at ~500 ºC. Above ~600 ºC, the amount of $Ni_{3+y}Sn_4$ decreases rapidly and Ni_3Sn_2 disappears, which is associated with rapid growth (similar to SPS) of the main $Zr_{0.5}Hf_{0.5}Ni_{1+y}Sn$ phase. At ~780 ºC, $Ni_{3+y}Sn_4$ melts and combines with remaining amount of Zr and Hf precursors, with single phase $Zr_{0.5}Hf_{0.5}Ni_{1+y}Sn$ observed at ~875 ºC. As no significant changes were observed during annealing, the sample was cooled down after 100 minutes.

The different mechanism can be related to the lack of Ti in the reaction mixture. Investigation of Ti-containing systems shows that Ti tends to react with Ni and Ni-Sn phases to form Ti_2Ni and TiNi, while there is no evidence for Zr- and Hf- containing binaries. Zr and Hf precursors are either accommodated in elemental form, within full-Heusler ($Ti_{1-x}Zr_xNi_2Sn$ and $Ti_{1-x}Hf_xNi_2Sn$) or in half-Heusler phases.

5.6. Discussion

From a detailed analysis of in-situ NPD data, a reaction progress of the half-Heusler formation was proposed. It was observed that the sintering of elemental precursors occurs through a complex, multi-step reaction. Focusing first on Ni-rich $TiNi_{1+y}Sn$ (y = 0, 0.075 and 0.25) compositions, Rietveld analysis revealed 2 melting points and 4 reaction regions (labelled I-IV). During heating, the melting of Sn (~230 ºC) is accompanied by the formation of a number of Ni-Sn binary phases. This first transformation step strongly depends on the amount of excess Ni (y in $TiNi_{1+y}Sn$) that is present. Sequential Rietveld analysis revealed that for the TiNiSn, Ni_3Sn_4 is formed upon Sn melting. To accommodate unreacted Ni, Ni_3Sn_4 transforms into $Ni_{3+y}Sn_4$. This phase is particularly interesting, as elemental Ni is gradually introduced into the vacant *2c* (0, 0, ½) site. As the reaction proceeds, $Ni_{3+y}Sn_4$ reacts further with elemental Ni leading to the formation of $Ni_{2+2y}Sn$ and Ni_3Sn. The reaction of $TiNi_{1.075}Sn$ is slightly different. More Ni is accommodated into $Ni_{3+y}Sn_4$ site at low temperature and throughout further heating, higher fractions of $Ni_{2+2y}Sn_2$ and Ni_3Sn intermediates are formed. For $TiNi_{1.25}Sn$, the first transformation also occurs at the melting of Sn. However, $Ni_{3+y}Sn_4$ is not the only newly-grown phase. Here, the amount of excess Ni was large enough to allow crystallisation of $Ni_{2+2y}Sn_2$, Ni_3Sn and $TiNi_{1+y}Sn$ at about 250 ºC. Due to the competing nature of these phases, a smaller fraction of $Ni_{3+y}Sn_4$ was formed and remains reduced during further heating.

Rietveld analysis also revealed that Ti does not react at low temperatures. It remains intact up to ~570 ºC and as the temperature rises it gradually combines with Ni and Ni-Sn binaries to form a Ni-deficient full-Heusler ($TiNi_{2y}Sn$), Ti_2Ni and TiNi. Although the target half-Heusler starts to crystallise at around ~570 – 600 ºC (y = 0 and 0.075) or 250 ºC (y = 0.25), largescale formation requires further heating to 900 ºC and prolonged annealing. The half-Heusler formation occurs in 700 – 900 ºC temperature range. At ~750 – 780 °C, $Ni_{3+y}Sn_4$ melts and full-Heusler becomes the dominant phase. As the reaction proceeds, the full-Heusler reacts with molten Ni-Sn, TiNi and Ti_2Ni phases to form the

half-Heusler phase. The fraction of full-Heusler decreases slowly with reaction time, while the amount of half-Heusler increases.

In-situ NPD was also used to monitor the formation of ZrNiSn and $Ti_{0.5}Zr_{0.25}NiSn$. For both systems, the first transformation occurs at ~230 – 260 ºC (Sn melting). Interestingly, the final half-Heusler alloys were immediately formed at this stage. A literature search[194] and visual inspection of the prepared materials, suggest that these samples were prepared through a rapid self-propagating high-temperature synthesis. At ~230 ºC, Sn has molten creating heating point within the sample. Once started, the exothermic combustion wave swept through the sample, leading to the formation of single-phase half-Heusler. The Zr combustion and the closed environment within the vanadium can, created an environment suitable for spontaneous reaction of reactants to form the final product. The entire process was likely completed within a few seconds. Unfortunately, the spontaneous self-propagating synthesis was not reproduced in the laboratory, though this experiment and literature results[194] indicates that this is a promising synthesis method that should be investigated further.

In-situ NPD monitoring of $M_{0.5}M'_{0.5}NiSn$ (M = Ti, Zr, Hf) revealed a similar, complex sequence, however the mechanism is slightly different. For the Ti-containing compositions ($Ti_{0.5}Zr_{0.5}NiSn$ and $Ti_{0.5}Hf_{0.5}NiSn$), Sn melting initiates the formation of Ni-Sn binaries and small fraction of half-Heusler phases – ZrNiSn for $Ti_{0.5}Zr_{0.5}NiSn$ and HfNiSn and TiNiSn for $Ti_{0.5}Hf_{0.5}NiSn$. For both samples, Ti remains intact up to ~570-600 °C above which it reacts with Ni and Ni-Sn binaries to form Ti_2Ni, TiNi and full-Heusler intermediates. Similarly to $TiNi_{1+y}Sn$, large scale half-Heusler formation occurs upon melting of $Ni_{3+y}Sn_4$ and its gradual reaction with full-Heusler and TiNi phases. For $Zr_{0.5}Hf_{0.5}NiSn$, the melting of Sn also causes the formation of Ni-Sn binaries and main half-Heusler phases. However, as the reaction proceeds the fraction of half-Heusler phases increases more rapidly, compared to $Ti_{0.5}Zr_{0.5}NiSn$ and $Ti_{0.5}Hf_{0.5}NiSn$ samples.

Such a different mechanism can be related to the lack of Ti in the reaction mixture. For all $M_{0.5}M'_{0.5}NiSn$ samples, the Zr and Hf precursors do not form any binary phases. Zr and Hf are either accommodated in elemental form, within full-Heusler ($Ti_{1-x}Zr_xNi_2Sn$ and $Ti_{1-x}Hf_xNi_2Sn$) or in half-Heusler phases, whereas Ti forms binary phases (Ti_2Ni and TiNi). This suggests that the atomic size difference between Ti and Zr/Hf is not the only factor affecting the formation of multiphase half-Heusler alloys.

Concluding, this study reveals that there are differences in the formation of half-Heusler materials with and without Ti. For all $TiNi_{1+y}Sn$ and $M_{0.5}M'_{0.5}NiSn$ samples, Ni-Sn binaries are formed upon Sn melting. Focusing on samples containing Ti, at ~570-600 °C Ti forms TiNi and Ti_2Ni intermediates, which do not react further until higher temperatures. In contrast, in samples with Zr and Hf, there is a lack of Zr- and Hf-containing binaries suggesting that these phases are formed at higher temperatures and do not contribute to the half-Heusler formation. For all compositions, main half-Heusler formation is initiated by the melting of Ni_3Sn_4. At this point, quantities of Zr and Hf that are in elemental form and those partially incorporated in half-Heusler and full-Heusler phases react with Ni-Sn binaries and the amount of target half-Heusler phases rapidly increases. For $TiNi_{1+y}Sn$ samples, Ni_3Sn_4 melting initiates the reaction between already formed Ti-Ni and Ni-Sn binaries, and the full-Heusler phase becomes the dominant phase that reacts further to form the target half-Heusler. The formation of Ti_2Ni and TiNi and the subsequent complex reaction mechanism may explain why it is difficult to prepare impurity-free, stoichiometric TiNiSn as well as the multiphase behaviour observed in $Ti_{1-x}Zr_xNiSn$ and $Ti_{1-x}Hf_xNiSn$ samples, as reported in the literature.

Chapter 6 - Distribution of Excess Ni within the Half-Heusler Matrix Investigated Using Pair Distribution Function Analysis

6.1. Introduction

In a standard powder diffraction experiment, the crystal structure is obtained solely from the position and intensity of the Bragg reflections. This analysis provides information on the average structure, omitting information on local disorder, which is determined through the study of diffuse scattering. In the total scattering, both the Bragg and diffuse scattering are analysed simultaneously.[156] It has recently been shown that total scattering can provide information on the local arrangements and positions of atoms within the crystal structure. The Fourier transform of the total scattering data produces a pair distribution function (PDF). The PDF describes the interatomic distances within the crystal volume. Opposite to the average structural information attained from the Bragg data, the position and shape of PDF peaks informs on the local environment surrounding each atom.

TiNiSn-based alloys tend to spontaneously form Ni-rich composition, with 2-3% of excess Ni occupying the normally vacant *4d*-site of half-Heusler matrix. Unfortunately, there is still little known about the arrangement of excess Ni within the crystal structure. To address this issue, the atomic configurations of stoichiometric TiNiSn and intentionally Ni-doped $TiNi_{1.05}Sn$ were investigated using the total scattering. Reverse Monte Carlo (RMC) modelling that implements a large 3D box with atoms was used to simultaneously model the PDF and Bragg profiles. Rietveld refinement revealed the presence of Ni on the normally vacant *4d*-site of half-Heusler matrix (1.4(1)% for TiNiSn and 5.9(1)% for $TiNi_{1.05}Sn$). The excellent fit to the Bragg pattern provided information on the average structure, however it does not assess the local arrangements around the atoms. Introduction of Ni into a half-Heusler causes local distortions in the regular lattice of atoms, by moving neighbouring host atoms away from their ideal positions. The total scattering data provided information on the local atomic arrangement, with details presented in this part of thesis.

6.2. Experimental Procedure

The TiNiSn and $TiNi_{1.05}Sn$ samples were prepared on 10 g scale using a solid-state synthesis protocol, which was discussed in Section 3.2. Total neutron scattering

experiments were performed on the POLARIS powder diffractometer at ISIS. Samples were loaded into vanadium cans with inner diameter of 0.8 cm. To ensure good statistical quality, the data for each sample were collected at room temperature for 8 hours of neutron beam time. For normalisation purposes, data were also collected from an empty can, the empty instrument and a vanadium rod. The Mantid software[149] was used to correct, normalise and combine data from the 3008 detectors. The total scattering data were reduced and corrected using standard methods in the GudrunN software.[195] Corrected data were Fourier transformed to obtain the PDF using the SToG program, distributed as part of the RMCProfile package[166] with a Q_{max} = 40 Å^{-1}. PDF is also referred to as the $G(r)$ and these terms are used interchangeably. The theoretical total scattering functions of Ni-rich $TiNi_{1+y}Sn$ ($0 \leq y \leq 1$) half-Heusler were calculated from the crystallographic Information File (CIF) using PDFgui software.[196] The Reverse Monte Carlo (RMC) modelling of the total scattering data was performed with the RMCProfile program. The RMC refinements were performed using configurations consisting 10×10×10 supercell of the cubic half-Heusler unit cell. For the final fits, the refinements were constrained by fitting of the $G(r)$, low-r $G(r)$ range and Bragg profile. Each final model (atom swap and grey atom – see later for details) was repeated 20 times. All figures present fits attained after a run time of 12 hours. The neutron scattering lengths for this study are b_{Ti} = -3.4 fm, b_{Ni} = 10.3 fm and b_{Sn} = 6.2 fm, providing excellent scattering contrast between constituent elements. Due to the negative scattering length of Ti, the contribution of Ti containing bonds will have opposite signs compared with non-Ti bonds, resulting in partial cancellation of the observed intensity. To distinguish, Ni atoms which occupy the *4c*- and *4d*-site are denoted as Ni1 and Ni2, respectively. The χ^2 RMC shows the total value that consists of χ^2 values from different data sets: χ^2-$G(r)$ is goodness of fit for full r-range $G(r)$ function ($0 \leq r \leq 29.6$ Å), χ^2-$G(r)$_2 corresponds to the goodness of fit for $G(r)$ function with r in range $0 \leq r \leq 3.6$ Å, while χ^2-Bragg describes the quality of fit to Bragg pattern.

6.3. X-ray and Neutron Powder Diffraction

XRD patterns of parent TiNiSn and Ni-doped $TiNi_{1.05}Sn$ were collected to investigate the phase purity of the prepared compositions. Rietveld analysis confirmed the formation of half-Heusler phase, with an increase of the lattice parameter upon Ni doping.[109, 129] Rietveld analysis of NPD data was used to attain the experimental composition of the HH phase. In these fits, the occupancies of the Ti (*4a*), Ni1 (*4c*) and Sn (*4b*) sites were fixed.

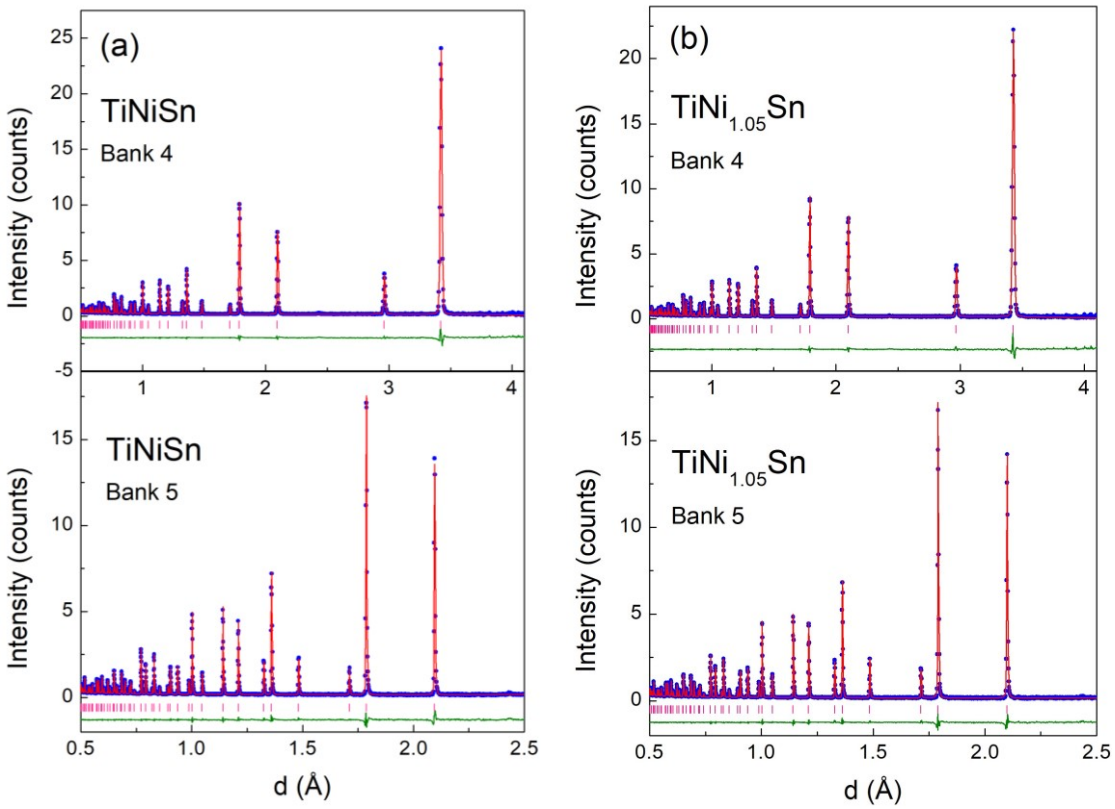

Figure 6.1. Observed (blue circles), calculated (red solid line) and difference (green solid line) Rietveld neutron powder diffraction profiles for **(a)** TiNiS and **(b)** $TiNi_{1.05}Sn$. Pink Bragg markers correspond to the half-Heusler phase that was used to fit the pattern.

Table 6.1. Lattice parameters (a), fractional site occupancies (occ), thermal displacement parameters (U_{iso}/Å^2) and refined compositions for the half-Heusler phase used to fit the Polaris neutron powder diffraction data for TiNiSn and $TiNi_{1.05}Sn$.

		TiNiSn	**$TiNi_{1.05}Sn$**
Half-Heusler Phase			
a (Å)		5.9262(1)	5.9358(1)
Ti (4a)	**U_{iso}**	0.00448(9)	0.00409(8)
Ni1 (4c)	**U_{iso}**	0.00429(5)	0.00490(5)
Ni2 (4d)	**Occ**	0.014(1)	0.059(1)
	U_{iso}	0.00429(5)	0.00490(5)
Sn (4b)	**U_{iso}**	0.00372(6)	0.00384(6)
Refined composition		$TiNi_{1.014(1)}Sn$	$TiNi_{1.059(1)}Sn$
Fit Statistics			
wR_p (%)	**bank 3**	3.65	3.61
	bank 4	3.62	3.41
	bank 5	3.52	3.87
R_p (%)	**bank 3**	5.15	5.10
	bank 4	6.35	6.13
	bank 5	3.31	7.61

Half-Heusler space group = $F\bar{4}3m$ – Ti: 4a (0,0,0), occ. 1.00; Ni(1): 4c (¼, ¼, ¼), occ. 1.00; Ni(2): (¾, ¾, ¾), occ. refined; Sn: 4b (½, ½, ½), occ. 1.00.

The amount of Ni2 on the *4d*-site was allowed to refine freely and accounts for the main difference between analysed materials. This revealed a Ni2 occupancy 0.014(1) for TiNiSn and 0.059(1) for $TiNi_{1.05}Sn$. The crystallographic information and fit statistics are shown in Table 6.1, while the final Rietveld fits are shown in Figure 6.1.

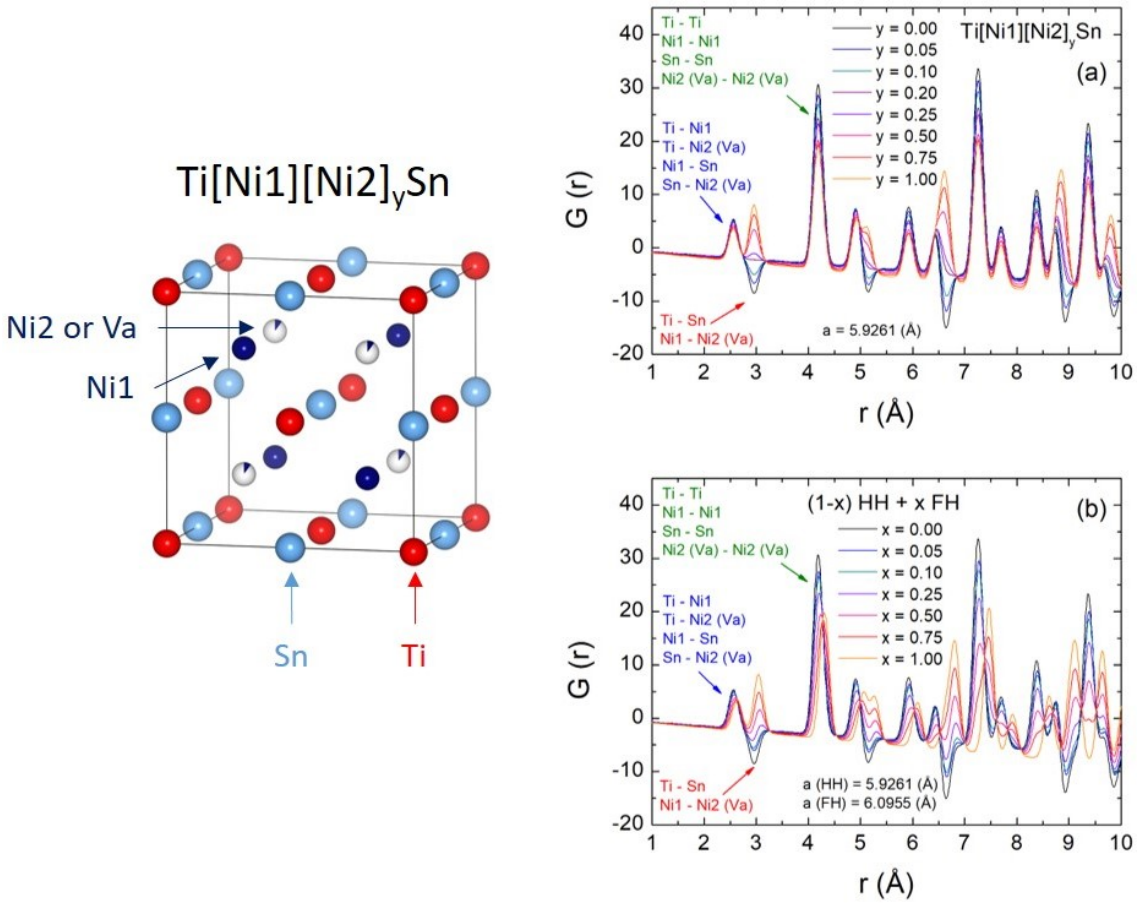

Figure 6.2. Theoretical total scattering functions calculated using the PDFGui software. **(a)** Evolution of $G(r)$ with excess Ni (y) content on *4d*-site of the $TiNi_{1+y}Sn$ half-Heusler structure. Constant lattice parameter a (HH) = 5.9261 Å was assumed. Equivalent to randomly distributed Ni. **(b)** Evolution of $G(r)$ with amount of distinct full-Heusler phase. Corresponding to half-Heusler matrix with distinct full-Heusler phase that has a different cell size. The crystal structure of half-Heusler was added for clarity. Va denotes vacancy.

6.4. Theoretical PDF Functions

The computational and experimental studies of Ni-doped $TiNi_{1+y}Sn$ suggest that up to 8% of excess Ni can be statistically distributed within the half-Heusler matrix before distinct full-Heusler ($TiNi_2Sn$) is formed. The theoretical total scattering functions of Ni-rich $TiNi_{1+y}Sn$ ($0 \leq y \leq 1$) half-Heusler alloys were calculated using the PDFgui software.[196]

In the first model, increasing amount of excess Ni2 was introduced into the *4d*-site of half-Heusler Ti[Ni1][Ni2]$_y$Sn matrix, assuming no expansion of unit cell with Ni-doping. Here excess Ni is randomly distributed within the matrix and its introduction does not lead to formation of distinct full-Heusler phase. As shown in Figure 6.2a, the introduction of excess Ni has an effect on all $G(r)$ peaks. Interestingly, the most significant change is observed at 2.8 – 3.0 Å, which is related to the Ti – Sn and Ni1- Ni2 interactions. As discussed above, negative scattering length of Ti results in the negative $G(r)$ peaks. As the amount of excess Ni2 is slowly increased, the Ti – Sn interaction is cancelled out by the positive Ni1 – Ni2 set. It is evident that 20% doping will result in complete cancelation of Ti – Sn peak. Further increase of excess Ni will result in the growth of Ni1 – Ni2 peak.

In the second model, the $G(r)$ functions of TiNi$_{1+y}$Sn system that forms half-Heusler matrix and distinct full-Heusler phase with different lattice parameter, were calculated. The introduction of distinct full-Heusler influences all $G(r)$ peaks (Figure 6.2b). As the half-Heusler content decreases, the Ti – Sn interaction is cancelled out by the positive Ni1 – Ni2 set. Interestingly, at least 50% of full-Heusler phase must be present for complete cancellation of Ti-Sn contribution.

6.5. Reverse Monte Carlo Modelling

The Rietveld refined crystal structures of TiNiSn and TiNi$_{1.05}$Sn (see Section 6.3) were starting points to construct the initial models for the RMC simulations. From the refined average composition and unit cell (TiNi$_{1.014}$Sn and TiNi$_{1.059}$Sn, respectively), a simulation box with a size of 10 × 10 × 10 was constructed. In the initial fit, the arrangement of the atoms reflects the average crystal structure of the system. Every atom will be on its ideal position, with no positional variations associated with thermal vibrations.

The RMC models do not use space group symmetry, therefore, to keep a model physically realistic, it is necessary to use constraints to incorporate additional information about the structure. The distance-window constraint specifies the closest and furthest distance two atoms can come together or be apart. By defining the configuration space, the model retains a logical atomic network. Unless otherwise stated, all refinements employed a distance window constraint. The refinement process was allowed to continue until no improvement in the fit was observed.

Figure 6.3 shows the experimental $G(r)$ and Bragg patterns for TiNiSn and TiNi$_{1.05}$Sn. Similar to the predicted functions (see section 6.4), excess Ni affects all $G(r)$ peaks. The

peak amplitudes are dampened as a function of *r*. Moreover, a systematic shift of the peak position was observed, which is consistent with the increase in lattice parameters. The difference curve (green line) shows that there are clear differences for small changes in excess Ni content.

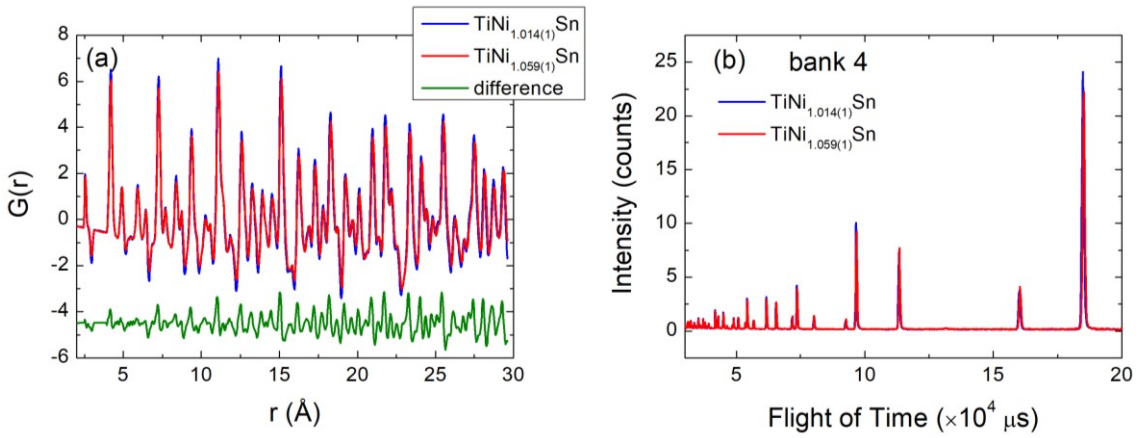

Figure 6.3. (a) Total radial distribution function $G(r)$ and **(b)** Bragg pattern for TiNiSn and $TiNi_{1.05}Sn$. The blue line is TiNiSn, while red line corresponds to $TiNi_{1.05}Sn$. Green line denotes the difference between the measured patterns.

6.5.1. Stoichiometric TiNiSn Model

Firstly, TiNiSn and $TiNi_{1.05}Sn$ were investigated using a stoichiometric TiNiSn model consisting of a 10 × 10 × 10 supercell containing 12000 atoms (4000 Ti, 4000 Ni, 4000 Sn). Initial refinements were performed by fitting the Bragg pattern and $G(r)$ function simultaneously. The $G(r)$ was fitted using $D(r)$ fit type (see Equation 2.24), with $r < 29.6$ Å. This model described well for large r values. However closer inspection revealed that the shape of the 2nd $G(r)$ peak (for both materials) was very poorly fitted (data not shown). To overcome this problem, an additional $G(r)$ function (denoted as $G(r)\_2$) was added. The $G(r)\_2$ covers the low-r range ($0 < r < 3.60$ Å) and was modelled with a $G(r)$ fit type (see Equation 2.22-2.23). This improved the modelling of the peak at ~3.0 Å slightly. However, it did not fully resolve the issue (see Figure 6.4). The high χ^2 values suggest that the stoichiometric TiNiSn model is insufficient to describe the TiNiSn and $TiNi_{1.05}Sn$.

As discussed in Section 6.4, peak at ~3.0 Å corresponds to Ti-Sn and Ni1-vacancy pair contributions. It was shown that the peak intensity is strongly affected by the Ni1-Ni2

contribution that occurs for Ni-rich compositions. The positive Ni1-Ni2 interaction is "used" to cancel out the negative Ti-Sn set and attain the correct shape of $G(r)$ peak. This observation is thus in keeping with the presence of excess Ni, observed in the Rietveld fits. To confirm the above observation, excess Ni2 was added to the simulation box.

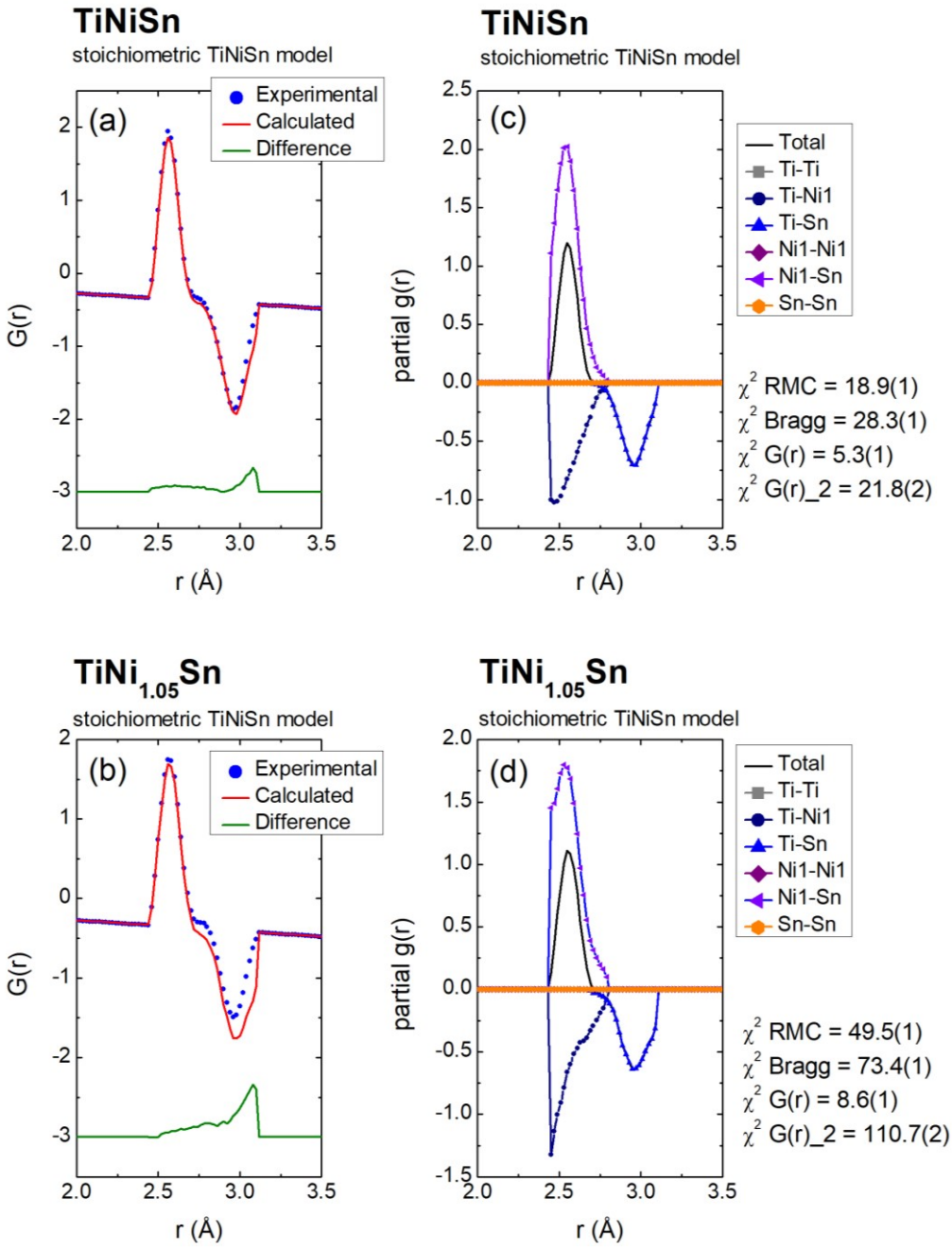

Figure 6.4. Comparison of the $G(r)$ for the stoichiometric TiNiSn model and the experimental $G(r)$ data for **(a)** TiNiSn and **(b)** $TiNi_{1.05}Sn$. The partial $G(r)$ functions for **(c)** TiNiSn and **(d)** $TiNi_{1.05}Sn$.

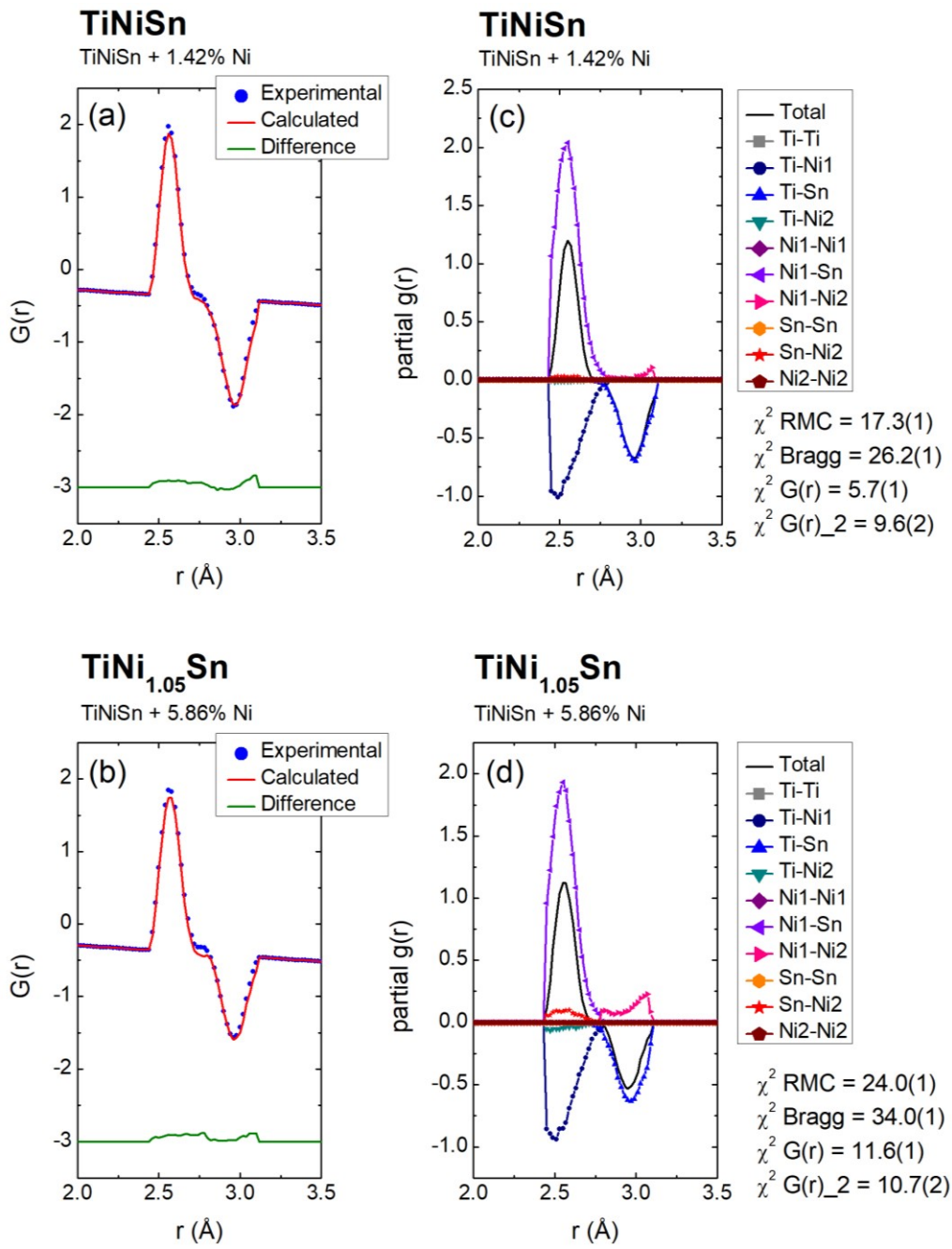

Figure 6.5. Comparison between measured and calculated $G(r)$ functions of TiNiSn with random excess Ni2 model applied for TiNiSn and $TiNi_{1.05}Sn$: **(a, b)** the total correlation function $G(r)$ and **(c, d)** the partial $G(r)$ functions.

6.5.2. TiNiSn with Excess Ni

In the 2nd model excess Ni (denoted as Ni2 - 1.4(1)% for TiNiSn and 5.9(1)% for $TiNi_{1.05}Sn$) was introduced and randomly distributed on the *4d*-site, with the RMC fitting results presented in Figure 6.5. The $TiNi_{1.05}Sn$ sample was chosen for discussion as the

contribution of the excess Ni is easier to observe, however similar features are found for TiNiSn composition.

The RMC modelling of $TiNi_{1.05}Sn$ was performed using a 10 × 10 × 10 supercell containing 12234 atoms (4000 Ti, 4000 Ni1, 4000 Sn and 234 Ni2). It is evident from Figure 6.5c that introduction of excess Ni2 significantly improves the G(r) fit. Moreover, the quality of all fitted functions is significantly improved, which is evident from lower χ^2 values. This confirms the observation from the Rietveld analysis that excess Ni is present in the structure. In the next section, the spatial distribution of the excess Ni is explored.

6.5.3. TiNiSn with Excess Ni – Atom Swap Modelling

To establish the arrangement of Ni2 within the simulation box, an atom swap function was added. Here, vacancies and Ni2 atoms, which occupy the *4d*-site were allowed to swap positions. The swap probability was chosen as 0.2, which means that 20% of all attempted movements are atom swaps, while the remaining moves correspond to atom displacements. Both, TiNiSn and $TiNi_{1.05}Sn$ were modelled using the same approach. RMC modelling was performed using configurations consisting of a 10 × 10 × 10 supercell with the following atoms:

-**TiNiSn**: 4000 Ti, 4000 Ni1, 4000 Sn, 57 Ni2 and 3943 vacancy sites;
-**$TiNi_{1.05}Sn$**: 4000 Ti, 4000 Ni1, 4000 Sn, 234 Ni2 and 3766 vacancy sites.

The Bragg pattern, $G(r)$ ($0 \leq r \leq 29.6$ Å) and $G(r)\_2$ ($0 \leq r \leq 3.5$) functions were fitted simultaneously. The $G(r)$ was fitted using a $D(r)$ fit type, while $G(r)\_2$ was modelled with a $G(r)$ fit type. Low χ^2 values were attained for the individual functions with the final fit statistics presented in Table 6.2. The fitted $G(r)$ function, Bragg pattern and partial $G(r)$ functions for TiNiSn and $TiNi_{1.05}Sn$ are presented in Figure 6.6 and Figure 6.7, respectively. As can be seen, the quality of the fit is extremely good, demonstrating that both systems are well described using the atom swap model. By collapsing the RMC model onto the unit cell and showing the refined 10 × 10 × 10 simulation box, the arrangement of the excess Ni can be visualised. In the condensed cell, "clouds" of atoms represent the distribution of atoms around the average positions. The atomic configuration snapshot for TiNiSn and $TiNi_{1.05}Sn$ compositions is presented in Figure 6.8. Images (a) and (d) show that Ni2 is present within the vacancy clouds (occupying *4d*-site). The supercell presentation (panels b-c for TiNiSn and e-f for $TiNi_{1.05}Sn$), revealed a random

distribution of the Ni2 within the simulation box. There is no evidence for Ni2 to form any short-range clustering or long-range ordering. From these fits, the Ni2 arrangement is therefore random.

Table 6.2. The quality of the RMC fits for TiNiSn and $TiNi_{1.05}Sn$. Two approaches were applied, namely atom swap and grey atom, which are discussed in the text.

	TiNiSn		**$TiNi_{1.05}Sn$**	
Model	Atom Swap	Grey Atom	Atom Swap	Grey Atom
χ^2 RMC	16.04(2)	16.17(2)	16.84(4)	17.17(3)
χ^2 Bragg	26.88(6)	26.93(5)	29.39(7)	29.73(5)
χ^2 G(r)	7.2(1)	7.21(7)	5.71(9)	5.75(7)
χ^2 G(r)_2	8.4(2)	10.84(9)	10.3(1)	13.7(3)
Ni2 arrangement	Random	Random	Random	Random

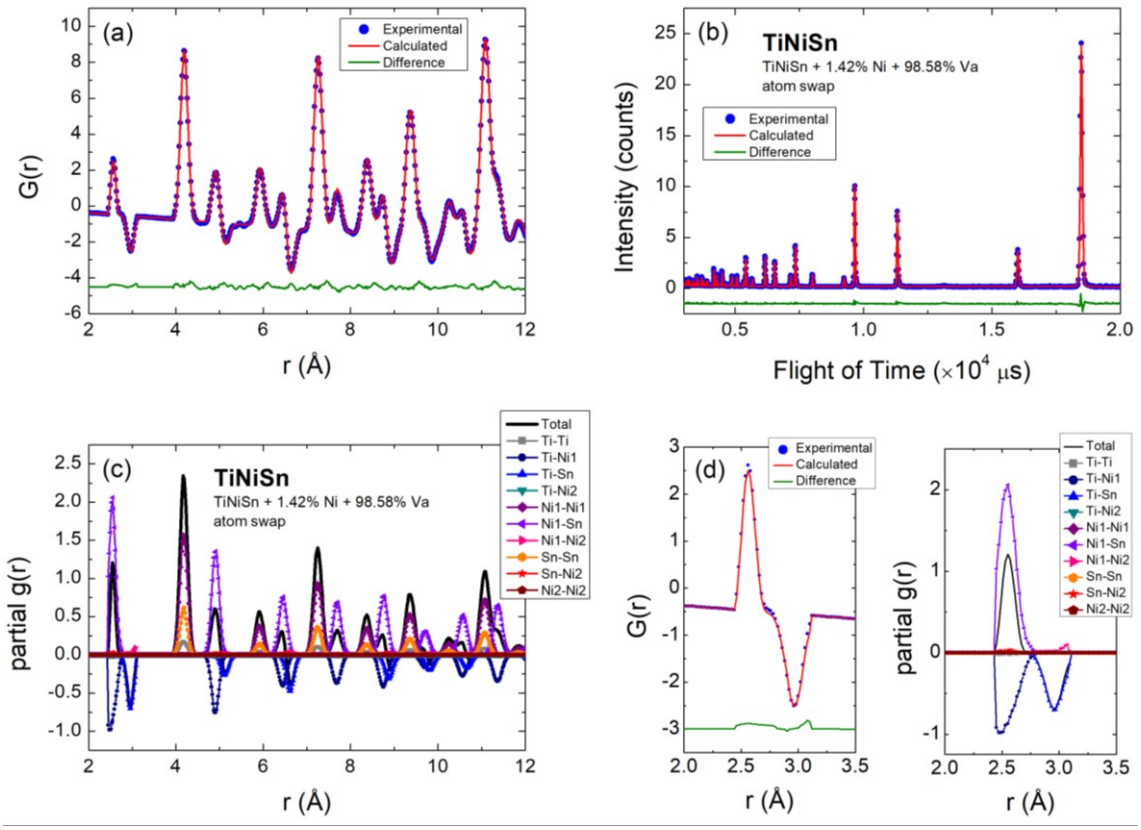

Figure 6.6. (a) The fitted pair distribution function G(r), **(b)** the fitted Bragg pattern, **(c)** the partial G(r) and **(d)** close up of the G(r) and partial G(r) functions for TiNiSn.

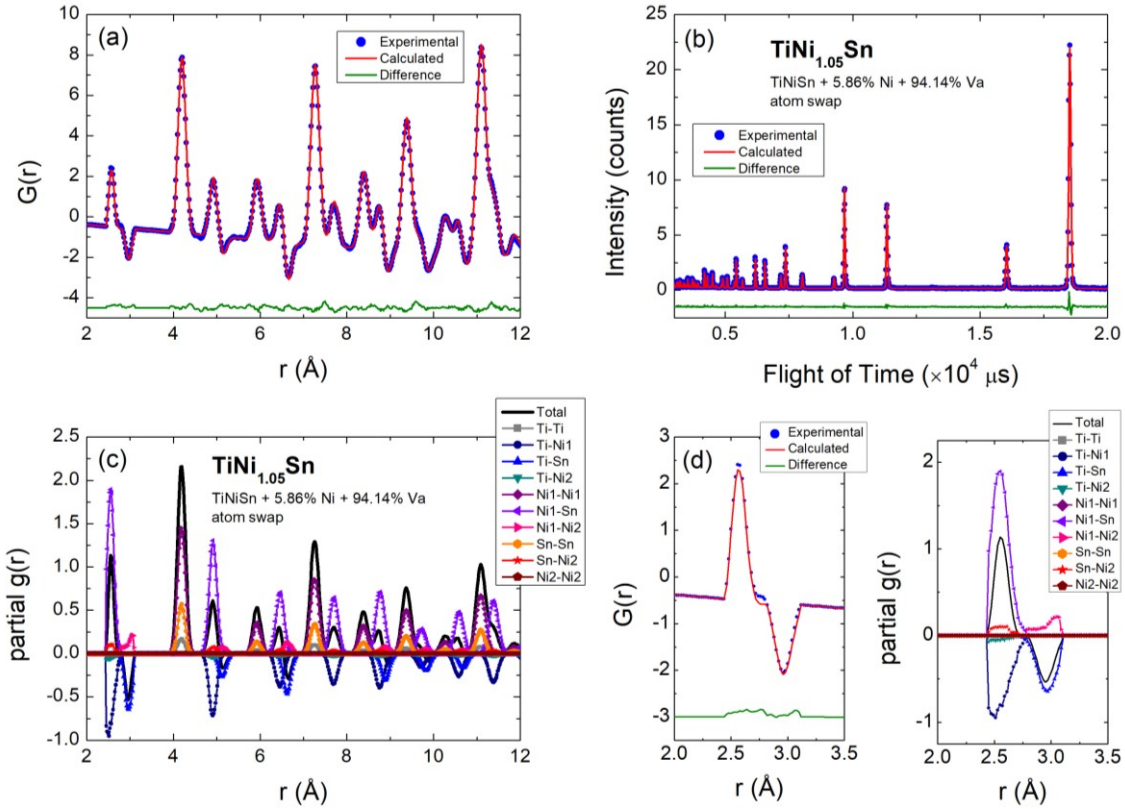

Figure 6.7. (a) The fitted pair distribution function G(r), **(b)** the fitted Bragg pattern, **(c)** the partial G(r) and **(d)** close up of the G(r) and partial G(r) functions for $TiNi_{1.05}Sn$.

6.5.4. TiNiSn with Excess Ni – Grey Atom Model

To confirm the random arrangement of Ni2 within the simulation box, a grey atom model was used. In this model, the *G*(*r*), *G*(*r*)_2 and Bragg datasets of TiNiSn and $TiNi_{1.05}Sn$ were modelled using a 10 × 10 × 10 box containing 4000 Ti, 4000 Ni1, 4000 Sn and 4000 grey atoms on the *4d*-site. The grey atom has a compositionally weighted average scattering length of Ni2 and vacancies. Figure 6.9 shows the fitted *G*(*r*) and Bragg profile for TiNiSn and $TiNi_{1.05}Sn$, while fit statistics are presented in Table 6.1. The χ^2 values are comparable to the atom swap model (see Table 6.1), supporting the random arrangement of Ni2. For the grey atom model, the visualisation of the 10 × 10 × 10 simulation box will not provide information on the arrangement of atoms. To overcome this problem, the partial *G*(*r*) functions of the grey atom model were compared to the partial *G*(*r*) functions of known Ni2 arrangement. Therefore, the *G*(*r*) for Ni1-Ni1, Ni1-grey atom and grey atom – grey atom interactions were plotted in Figure 6.10 and compared with the *G*(*r*) functions (Ni1-Ni1, Ni1-Ni2, Ni2-Ni2) of the atom swap model. As discussed above, the Ni1-Ni2 interaction strongly affects the shape of the second *G*(*r*) peak. Inspection of

Figure 6.11 revealed that the peak positions for atom swap and grey atom model are the same, suggesting that a random Ni2 arrangement is more probable outcome.

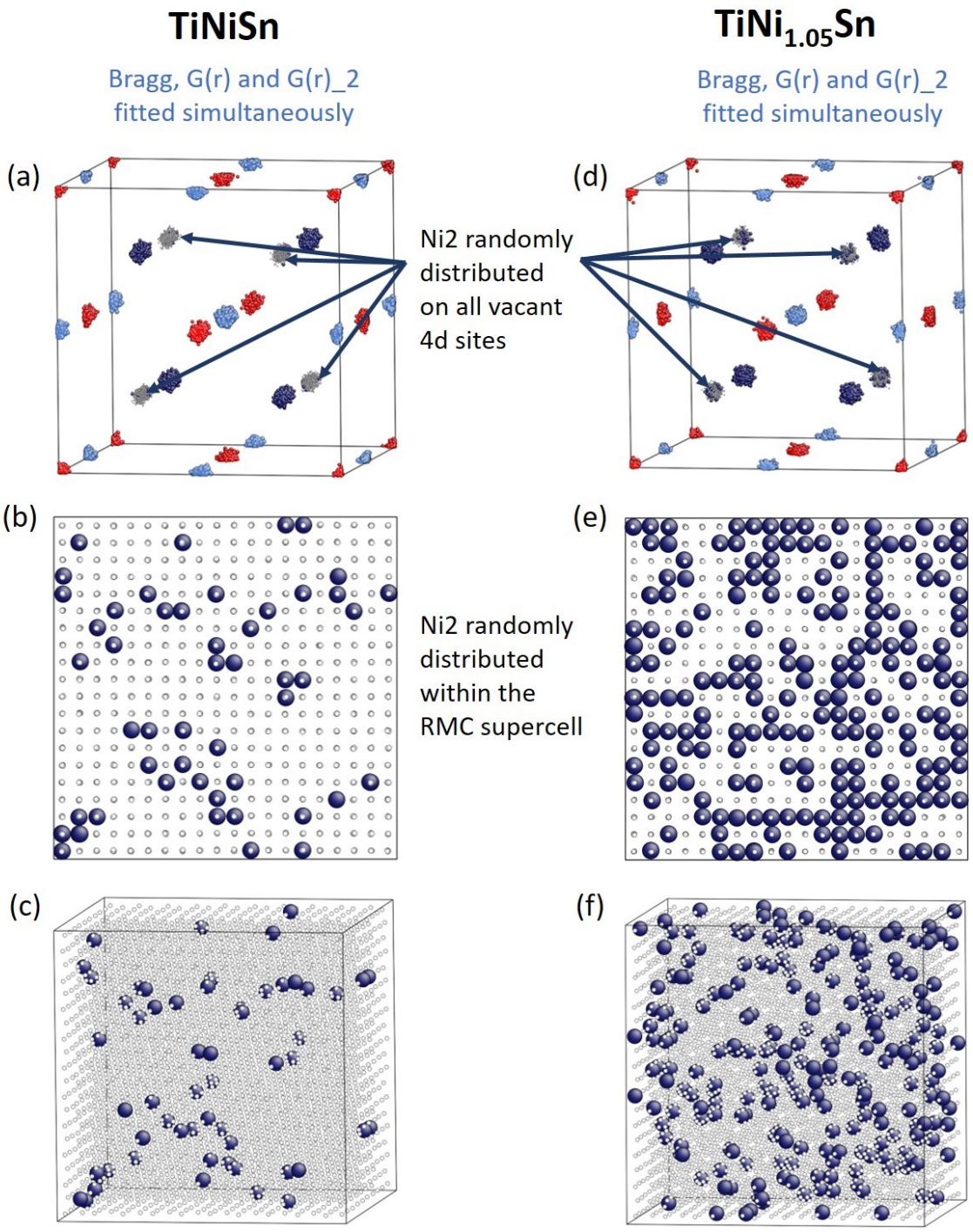

Figure 6.8. (a, d) RMC configuration condensed onto the original cubic cell. **(b, c, e, f)** Ni2/vacancy distribution in the 10 × 10 × 10 supercell. Red spheres are Ti, dark blue correspond to Ni1 and Ni2, light blue are Sn and grey are vacancies. For clarity, Ti, Ni1 and Sn were omitted for the supercell images b, c, e, f.

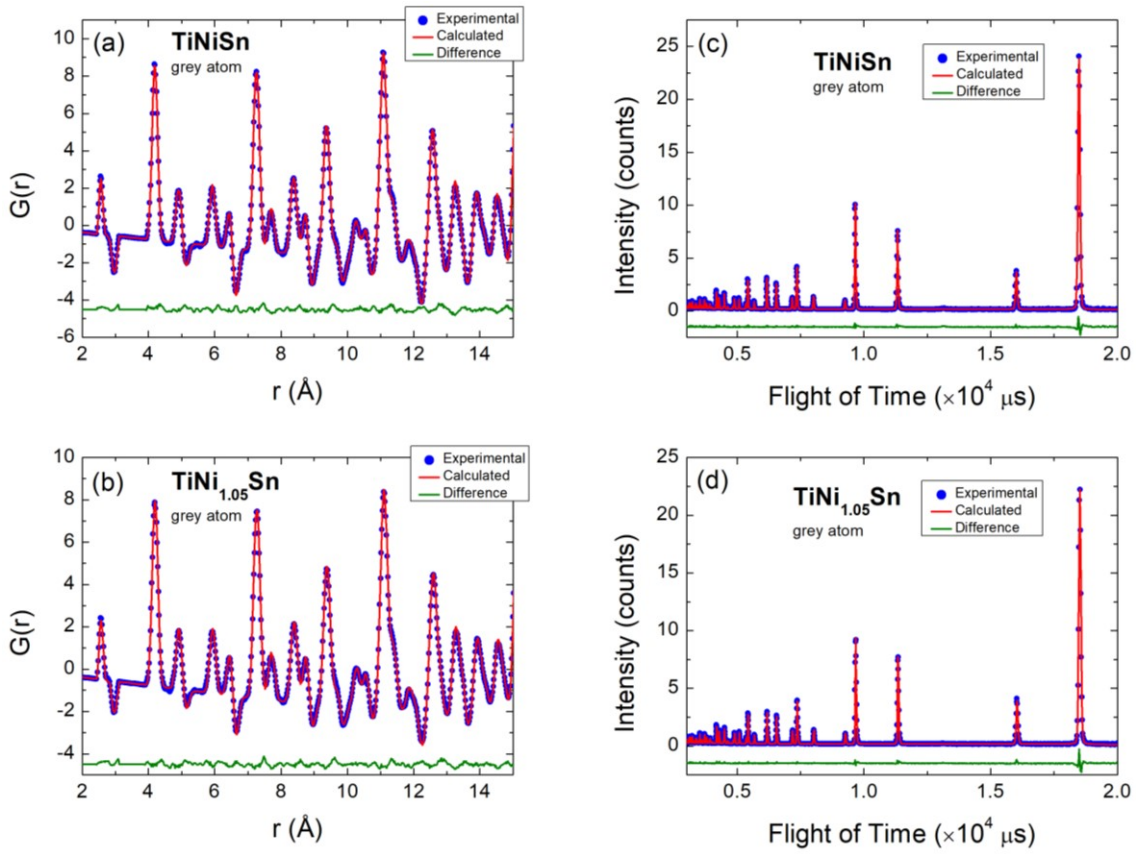

Figure 6.9. (a, b) The fitted pair distribution function $G(r)$ and **(c, d)** the fitted Bragg pattern for TiNiSn and $TiNi_{1.05}Sn$, attained with grey atom model.

6.6. Discussion

As shown in the previous Chapters, TiNiSn-based half-Heusler alloys tend to spontaneously form with a Ni-rich matrix. Computational and experimental results suggest that small amounts of excess Ni (< 8%) can be statistically distributed within the structure before phase segregation to TiNiSn and full-Heusler $TiNi_2Sn$ phase is observed.[103, 105, 115, 188] Rietveld analysis of diffraction data provides information about average crystal structure of the investigated material, omitting details of the local atomic distribution. Thus, refinement against neutron total scattering data using a RMC modelling approach was used to gain insight into the arrangement of excess Ni within TiNiSn and $TiNi_{1.05}Sn$. Rietveld refinement to NPD data revealed 1.4(1)% of Ni within TiNiSn and 5.9(1)% of excess Ni in $TiNi_{1.05}Sn$. Simultaneous RMC modelling of total scattering data and Bragg pattern revealed that both materials form half-Heusler matrix with statistical, randomly distributed excess Ni2. This was proved by two different models – the atom swap feature implemented in RMCProfile as well as the grey atom model.

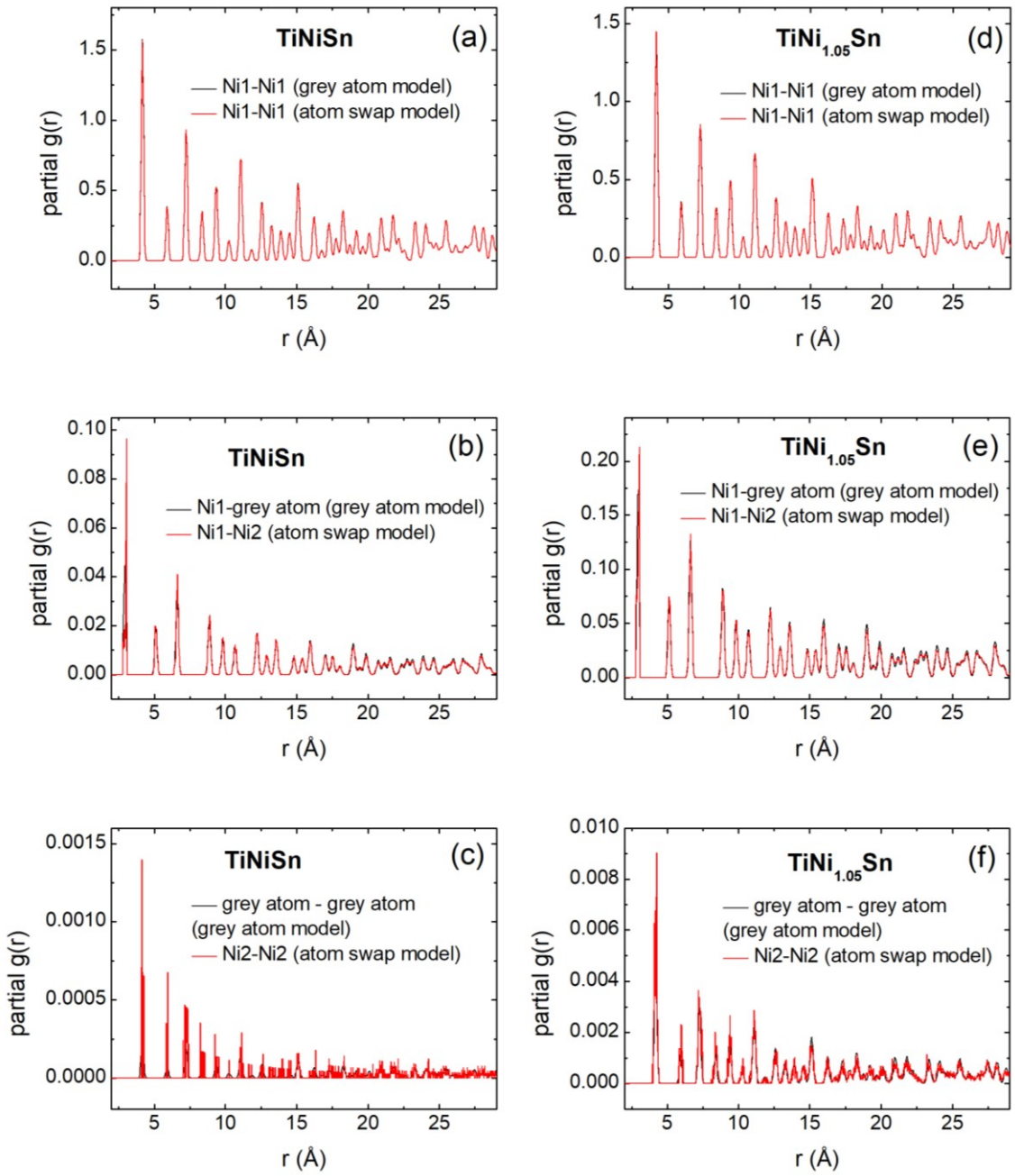

Figure 6.11. Comparison of partial G(r) functions that were attained using atom swap and grey atom models. **(a, d)** G(r) for Ni1-Ni1 interaction, **(b, e)** G(r) for Ni1-Ni2 (or Ni1-grey atom) and **(c, f)** G(r) for Ni2-Ni2 (or grey atom-grey atom).

It is worth noting that the random Ni2 arrangement is consistent with the TEM data for $TiNiCu_ySn$ compositions. The microscopy study shown in Chapter 3 revealed that excess metal (Cu and Ni) randomly occupy the interstitial *4d*-sites.

Chapter 7 - Conclusions

The MNiSn, MCoSb (M = Ti, Zr, Hf) and FeNbSb half-Heusler compounds are promising n- and p-type thermoelectric materials. Alloying on any of the three occupied sublattices and the introduction of excess metal on the vacant interstitial site are excellent strategies to manipulate the electronic and thermal transport to enhance the thermoelectric figure of merit *ZT*. The work shown in Chapters 3 and 4 investigated the effect of processing and introduction of excess metal on the structure and thermoelectric properties of MNiSn-based materials. In addition, the solid-state reaction used to synthesise the half-Heusler alloys was studied using in-situ NPD experiment (Chapter 5). In the final results section (Chapter 6), total scattering was used to gain insight into the arrangement of excess Ni within TiNiSn structure.

7.1. Chapter 3 – $TiNiCu_ySn$ ($0 \leq y \leq 0.25$) and off-stoichiometric $Ti_{1+x}Ni_{1+y}Sn$

The focus of Chapter 3 was a detailed investigation of Cu-rich $TiNiCu_ySn$ and off-stoichiometric $Ti_{1+x}Ni_{1+y}Sn$ half-Heusler compounds. The crystal structure of the prepared compositions was investigated using XRD, SXRD and NPD techniques. Electron microscopy was used to gain detailed insight into their microstructure. The S, ρ, κ and Hall coefficient were also measured to establish the structure-properties relationship.

Rietveld analysis of XRD and NPD data for $TiNiCu_ySn$ ($0 \leq y \leq 0.25$) revealed that up to 10% of Cu can be introduced into the normally vacant *4d*-site. In addition, spontaneous formation of ~3% interstitial Ni on the same sublattice was identified. NPD suggests a random distribution of Cu and Ni across the half-Heusler matrix. TEM revealed grain-by-grain compositional variations with a tendency towards the formation of full-Heusler grains. No evidence for nanoscale full-Heusler inclusions is observed. Instead, the excess metal is randomly distributed on the interstitial sites. In addition, Cu partially segregates at grain boundaries, forming Cu "wetting layers". This enables full densification and facile electronic transport, which was confirmed by Hall coefficient measurement. In addition, the introduction of excess Cu leads to a significantly lowered $\kappa_{lattice}$. This is explained by the presence of interstitials, which acts as phonon scattering centres. The improvement in the individual properties results in *ZT* enhancement. For y = 0, *ZT* = 0.05

at 323 K increases to ZT = 0.37 at 673 K, while for Cu-rich samples, ZT = 0.09-0.12 at 323 K increases to a peak ZT = 0.5-0.6 at 653-773 K.

The off-stoichiometric $Ti_{1+x}Ni_{1+y}Sn$ series was synthesised to investigate the impact of spontaneously formed excess Ni that was observed in $TiNiCu_ySn$. The second aim was to check if it is possible to prepare stoichiometric (1:1:1) TiNiSn. The NPD revealed the presence of 2-6% of excess Ni on the interstitial site, with all investigated compositions becoming Ni-rich. SXRD revealed changes in the crystal structure upon hot pressing. A symmetric peak shape was observed for samples before hot-pressing, while an asymmetric broadening towards larger *d*-spacing was identified for hot-pressed samples. The symmetric peak shape suggests a homogeneous distribution of the excess Ni, while the broadening can be explained by the Ni redistribution and tendency towards formation of full-Heusler grains. Unfortunately, elemental Ti and Sn were also observed, which may be caused by an incomplete reaction of the starting reagents. This could affect the thermoelectric properties. Spontaneous formation of Ni-rich half-Heusler matrix has a beneficial effect on the thermoelectric properties. Hall measurements confirmed that Ni acts as a weak carrier dopant which improves electronic transport. In addition, Ni interstitials effectively disrupt the thermal transport, lowering $\kappa_{lattice}$ and yielding ZT = 0.40 at a relatively low temperature of 600 – 700 K.

The results presented in Chapter 3 are particularly interesting as both series do not contain any toxic or expensive elements (such as Hf) and are produced using a simple processing route. Therefore, these materials are promising for large-scale production and applications.

7.2. Chapter 4 – Multiphase Cu-doped half-Heusler compounds

The findings presented in Chapter 3, formed the basis of the work shown in the remaining parts of this thesis. Focusing on Chapter 4, which explored effect of excess Cu on the crystal structure and thermoelectric properties of multiphase and MNiSn (M = Ti, Zr, Hf) half-Heusler compounds. The powder diffraction techniques combined with electron microscopy revealed multiphase behaviour for all $M_{0.5}M'_{0.5}NiCu_{0.075}Sn$ and $Ti_{0.5}Zr_{0.25}Hf_{0.25}NiCu_ySn$ samples, while the $MNiCu_{0.075}Sn$ compositions form a single phase half-Heusler matrix. Unfortunately, the structural studies revealed the presence of impurities such as elemental Sn, Ni_3Sn_2 or ZrO_2, suggesting an incomplete reaction of starting reagents. This may affect the thermoelectric properties. The Hall measurements

confirmed that Cu acts as an effective n-type dopant, which improves electronic transport. The combination of alloying on the M site and introduction of interstitial Cu leads to low $\kappa_{lattice}$. Simultaneous improvement of S^2/ρ and reduction of κ leads to significantly enhanced ZT values, with ZT = 0.77 at 773 K observed for $Ti_{0.5}Zr_{0.25}Hf_{0.25}NiCu_{0.025}Sn$.

7.3. Chapter 5 – In-situ Neutron Powder Diffraction Experiment

In-situ NPD was used to monitor the formation of various half-Heusler compositions. Sequential Rietveld analysis of NPD data, which were collected during heating up, annealing and cooling down, revealed a complex, multi-step reaction, which involves numerous intermediates. Two key transformations are related to the melting of Sn and Ni_3Sn_4, driving the formation of target half-Heusler composition. Elemental Ti remains intact up to ~600°C, above which it slowly reacts with Ni-Sn binaries to form $TiNi_2Sn$, Ti_2Ni and TiNi. Zr and Hf also remain intact up to ~600°C, however above this point they do not form any binary phases. Instead they form Ni-deficient full-Heusler ($Ti_{1-x}Zr_xNi_2Sn$ and $Ti_{1-x}Hf_xNi_2Sn$) or half-Heusler phases. Lack of Zr- and Hf-containing binary phases is surprising as synthetic routes, which proceed through the melt contain large number of binary impurities. In addition, the investigation of ZrNiSn and $Ti_{0.5}Zr_{0.25}Hf_{0.25}NiSn$ revealed self-propagating high-temperature synthesis as a potential, fast route to prepare half-Heusler complexes.

7.4. Chapter 6 – Application of Pair Distribution Function

Pair distribution function (PDF) analysis has been applied to many amorphous, low-crystallinity compounds, but it has never been used to study half-Heusler compounds. Here, PDF analysis was successfully applied to study the structure and distribution of excess Ni in TiNiSn and $TiNi_{1.05}Sn$. It revealed random distribution of excess Ni within the half-Heusler matrix, which is in keeping with our experimental results. This confirms that small amount of Ni can be introduced into the interstitial site prior to the formation of distinct full-Heusler phase.

7.5. Summary and Further Work

XRD, SXRD, NPD and electron microscopy revealed that half-Heusler is main phase for all prepared compositions. These techniques also exposed the presence of impurity

phases, suggesting incomplete synthesis protocol. The impurities may significantly affect the thermoelectric properties, demonstrating the need for better synthesis protocols. This thesis confirms that half-Heusler compounds are difficult to prepare impurity-free or in stoichiometric ratio. Finding new technique or manipulation of current approach should be investigated to achieve better samples. In-situ NPD of ZrNiSn and $Ti_{0.5}Zr_{0.25}Hf_{0.25}NiSn$ suggests self-propagating high temperature synthesis as a new, fast route to achieve "cleaner" samples. Such protocol should be studied using available laboratory equipment and extended to other compositions. The integration of ball-milling into samples preparation to improve homogeneity is another technique worth to investigate.

Throughout this work, investigation of $\kappa_{lattice}$ revealed that interstitials and alloying on the M-site are responsible for the phonon scattering and $\kappa_{lattice}$ reduction. The 323 K values of $\kappa_{lattice}$, the calculated mass-disorder parameter on the *M* site (Γ_M) and on the interstitial site (Γ_{Y2}) for most of the samples discussed in this thesis are summarised in Table 7.1. The $\kappa_{lattice}$ as a function of Γ_{total} is shown in Figure 7.1. It is evident that $\kappa_{lattice}$ decreases with Γ_{total} confirming that introduction of point defect centres is effective method to scatter phonons. To complete this analysis, $\kappa_{lattice}^{calculated}$ was estimated using Equation 2.43. Focusing on $TiNiCu_ySn$ and the off-stoichiometric $Ti_{1+x}Ni_{1+y}Sn$ samples, introduction of excess metal (Ni and Cu) increases the Γ_{Y2} component. The $\kappa_{lattice}^{calculated}$ is found to be similar to the experimental values, confirming that the $\kappa_{lattice}$ reduction is mainly due to the presence of the excess metal on the interstitial *4d*-site. For the $M_{0.5}M'_{0.5}NiCu_{0.075}Sn$ and the $Ti_{0.5}Zr_{0.25}Hf_{0.25}NiCu_ySn$ samples, the introduction of excess metal is combined with alloying on the M-site. Such approach has a dramatic effect on $\kappa_{lattice}$ with the lowest values reported for $Ti_{0.5}Hf_{0.5}NiCu_{0.075}Sn$ and Cu-rich $Ti_{0.5}Zr_{0.25}Hf_{0.25}NiCu_ySn$ samples. However, $\kappa_{lattice}^{calculated}$ for these samples is higher than experimental values, suggesting that the point defect is not the only factor responsible for phonon scattering. It is likely that the mechanism is more complicated and there are other factors contributing to $\kappa_{lattice}$ reduction. SEM revealed complicated microstructure, which is likely to be important. Therefore, it would be useful to investigate other phonon scattering mechanisms and develop a new model that would help to understand their impact on $\kappa_{lattice}$. TEM analysis, could provide more detailed insight into the microstructure and compositional homogeneity of these samples, which may significantly influence thermal transport.

Chapter 6 presents PDF analysis as an alternative technique, which can be used to gain insight into the crystal structure and distribution of excess metal on the vacant interstitial site of half-Heusler matrix. The compositions investigated in this thesis were not hot-

pressed. The synchrotron X-ray diffraction and electron microscopy studies shown in Chapter 3 suggest clustering of excess Ni upon hot pressing. Therefore, it may be vital to investigate the TiNiSn and $TiNi_{1.05}Sn$ samples after consolidation to check if the purely statistical distribution of any excess Ni is maintained. In addition, such analysis could be extended to other compositions, particularly multiphase half-Heusler materials. The investigation of multiphase samples using PDF could help to determine the inter-dependence of multiple phases and establish more detailed structure-properties relationships. This technique could also be applied to MCoSb and NbFeSb-based systems, which show promising thermoelectric properties and are p-type counterparts to MNiSn.

Table 7.1. The 323 K values lattice thermal conductivity ($\kappa_{323K} - LT/\rho$) of selected compositions discussed in this thesis. The *4d*-site occupancy was taken from Rietveld fits to the neutron powder diffraction data. Γ_M and Γ_{Y2} are calculated disorder parameters on the *M* site and on the interstitial *4d*-site, respectively (Equation 2.41 and Equation 3.1), while Γ_{total} is sum of Γ_M and Γ_{Y2}. $\kappa_{\text{lattice}}^{\text{calculated}}$ was evaluated using Equation 2.43.

	***4d*-site occupancy**	**κ_{323K}-LT/ρ (W m^{-1} K^{-1})**	**Γ_M**	**Γ_{Y2}**	**Γ total**	**$\kappa_{\text{lattice}}^{\text{calculated}}$ (Wm^{-1}K^{-1})**
$TiNiCu_ySn$ samples – Chapter 3						
TiNiSn	$Ni_{0.030}$	6.0	0	0.07	0.07	5.7
$TiNiCu_{0.025}Sn$	$Ni_{0.03}Cu_{0.018}$[a)]	4.5	0	0.11	0.11	4.8
$TiNiCu_{0.05}Sn$	$Ni_{0.03}Cu_{0.033(1)}$	4.0	0	0.14	0.14	4.3
$TiNiCu_{0.075}Sn$	$Ni_{0.03}Cu_{0.072(1)}$	3.9	0	0.21	0.21	3.7
$TiNiCu_{0.1}Sn$	$Ni_{0.03}Cu_{0.073(1)}$	4.2	0	0.21	0.21	3.7
off-stoichiometric $Ti_{1+x}Ni_{1+y}Sn$ samples – Chapter 3						
$Ti_{1.02}NiSn$	$Ni_{0.019(1)}$	7.0	0	0.04	0.04	6.7
$Ti_{1.02}Ni_{1.02}Sn$	$Ni_{0.038(1)}$	5.5	0	0.09	0.09	5.3
$Ti_{1.05}Ni_{1.05}Sn$	$Ni_{0.040(1)}$	4.8	0	0.09	0.09	5.2
$TiNi_{1.02}Sn$	$Ni_{0.058(1)}$	5.1	0	0.13	0.13	4.5
$MNiCu_{0.075}Sn$ and $M_{0.5}M'_{0.5}NiCu_{0.075}Sn$ samples – Chapter 4						
$TiNiCu_{0.075}Sn$	$Ni_{0.03}Cu_{0.072(1)}$	3.9	0	0.21	0.21	3.7
$ZrNiCu_{0.075}Sn$	$Cu_{0.022(1)}$	5.9	0	0.04	0.04	6.4
$HfNiCu_{0.075}Sn$	$Cu_{0.023(1)}$	6.1	0	0.04	0.04	6.7
$Ti_{0.5}Zr_{0.5}NiCu_{0.075}Sn$	$Ni_{0.03}Cu_{0.061(1)}$	3.4	0.03	0.18	0.21	3.6
$Ti_{0.5}Hf_{0.5}NiCu_{0.075}Sn$	$Cu_{0.036(1)}$	2.4	0.19	0.07	0.26	3.3
$Zr_{0.5}Hf_{0.5}NiCu_{0.075}Sn$	$Cu_{0.024(1)}$	3.7	0.08	0.04	0.12	4.4
$Ti_{0.5}Zr_{0.25}Hf_{0.25}NiCu_ySn$ samples – Chapter 4						
$Ti_{0.5}Zr_{0.25}Hf_{0.25}NiSn$		3.1	0.15	0	0.15	4.0
$Ti_{0.5}Zr_{0.25}Hf_{0.25}NiCu_{0.025}Sn$	$Cu_{0.041(1)}$	2.8	0.15	0.08	0.23	3.4
$Ti_{0.5}Zr_{0.25}Hf_{0.25}NiCu_{0.05}Sn$	$Cu_{0.049(1)}$	2.6	0.15	0.10	0.25	3.3
$Ti_{0.5}Zr_{0.25}Hf_{0.25}NiCu_{0.075}Sn$	$Cu_{0.073(1)}$	2.6	0.15	0.14	0.29	3.1

[a)] interpolated value

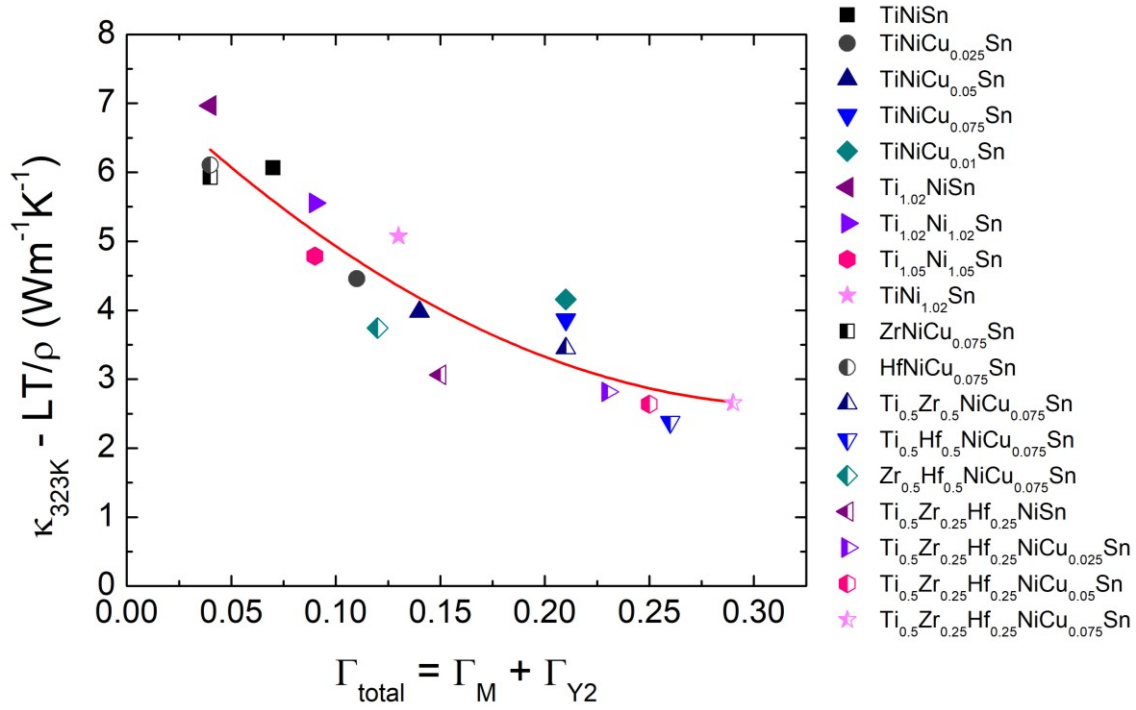

Figure 7.1. 323 K values of lattice thermal conductivity (κ-LT/ρ) as a function of total disorder scattering parameter (Γ_{total}) for selected samples discussed in this thesis.

References

1. A. K. Pandey, V. V. Tyagi, J. A. L. Selvaraj, N. A. Rahim and S. K. Tyagi, *Renewable & Sustainable Energy Reviews*, 2016, **53**, 859-884.
2. S. Sinha and S. S. Chandel, *Renewable & Sustainable Energy Reviews*, 2015, **50**, 755-769.
3. A. Tummala, R. K. Velamati, D. K. Sinha, V. Indraja and V. H. Krishna, *Renewable & Sustainable Energy Reviews*, 2016, **56**, 1351-1371.
4. A. Murugesan, C. Umarani, R. Subramanian and N. Nedunchezhian, *Renewable & Sustainable Energy Reviews*, 2009, **13**, 653-662.
5. M. H. Elsheikh, D. A. Shnawah, M. F. M. Sabri, S. B. M. Said, M. H. Hassan, M. B. A. Bashir and M. Mohamad, *Renewable & Sustainable Energy Reviews*, 2014, **30**, 337-355.
6. G. J. Tan, L. D. Zhao and M. G. Kanatzidis, *Chemical Reviews*, 2016, **116**, 12123-12149.
7. W. He, G. Zhang, X. X. Zhang, J. Ji, G. Q. Li and X. D. Zhao, *Applied Energy*, 2015, **143**, 1-25.
8. L. E. Bell, *Science*, 2008, **321**, 1457-1461.
9. C. Han, Z. Li and S. X. Dou, *Chinese Science Bulletin*, 2014, **59**, 2073-2091.
10. P. Ball and T. Caillat, *Mrs Bulletin*, 2013, **38**, 446-447.
11. T. M. Tritt, H. Boettner and L. Chen, *Mrs Bulletin*, 2008, **33**, 366-368.
12. Fitriani, R. Ovik, B. D. Long, M. C. Barma, M. Riaz, M. F. M. Sabri, S. M. Said and R. Saidur, *Renewable & Sustainable Energy Reviews*, 2016, **64**, 635-659.
13. S. Chen and Z. F. Ren, *Materials Today*, 2013, **16**, 387-395.
14. J. W. G. Bos and R. A. Downie, *Journal of Physics-Condensed Matter*, 2014, **26**, 433201.
15. A. K. Cheetham and P. Day, *Solid State Chemistry: Techniques*, Oxford University Press, Oxford, 1987.
16. S. B. Riffat and X. L. Ma, *Applied Thermal Engineering*, 2003, **23**, 913-935.
17. H. J. Goldsmid, *Introduction to Thermoelectricity*, Springer, Berlin, 2010.
18. G. J. Snyder, *The Electrochemical Society Interface*, 2008, **17**, 54-56.
19. F. J. DiSalvo, *Science*, 1999, **285**, 703-706.
20. G. J. Snyder and E. S. Toberer, *Nature Materials*, 2008, **7**, 105-114.

21. D. Kraemer, B. Poudel, H. P. Feng, J. C. Caylor, B. Yu, X. Yan, Y. Ma, X. W. Wang, D. Z. Wang, A. Muto, K. McEnaney, M. Chiesa, Z. F. Ren and G. Chen, *Nature Materials*, 2011, **10**, 532-538.
22. P. Atkins, T. Overton, J. Rourke, M. Weller and F. Armstrong, *Shriver & Atkins' Inorganic Chemistry*, Oxford University Press, 5th edn., 2010.
23. A. Blackman, S. E. Bottle, S. Schmid, M. Mocerino and U. Wille, *Chemistry*, John Wiley & Sons Australia, 2008.
24. A. R. West, *Solid State Chemistry and its Applications - Student Edition*, John Wiley & Sons, 2nd edn., 2014.
25. J. R. Sootsman, D. Y. Chung and M. G. Kanatzidis, *Angewandte Chemie-International Edition*, 2009, **48**, 8616-8639.
26. Z. M. Gibbs, H. S. Kim, H. Wang and G. J. Snyder, *Applied Physics Letters*, 2015, **106**, 022112.
27. H. J. Goldsmid and J. W. Sharp, *Journal of Electronic Materials*, 1999, **28**, 869-872.
28. E. S. Toberer, A. F. May and G. J. Snyder, *Chemistry of Materials*, 2010, **22**, 624-634.
29. T. M. Tritt, ed., *Thermal Conductivity: Theory, Properties and Applications*, Kluwer Academic, New York, 2004.
30. H. S. Kim, Z. M. Gibbs, Y. L. Tang, H. Wang and G. J. Snyder, *Apl Materials*, 2015, **3**, 041506.
31. E. S. Toberer, A. Zevalkink and G. J. Snyder, *Journal of Materials Chemistry*, 2011, **21**, 15843-15852.
32. X. Zhang and L.-D. Zhao, *Journal of Materiomics*, 2015, **1**, 92-105.
33. L. D. Hicks and M. S. Dresselhaus, *Physical Review B*, 1993, **47**, 12727-12731.
34. M. S. Dresselhaus, G. Chen, M. Y. Tang, R. G. Yang, H. Lee, D. Z. Wang, Z. F. Ren, J. P. Fleurial and P. Gogna, *Advanced Materials*, 2007, **19**, 1043-1053.
35. J. P. Heremans, M. S. Dresselhaus, L. E. Bell and D. T. Morelli, *Nat Nano*, 2013, **8**, 471-473.
36. *Thermoelectrics Handbook: Macro to Nano*, CRC Press, Boca Raton, 1st edn., 2006.
37. X. Shi, L. Chen and C. Uher, *International Materials Reviews*, 2016, **61**, 379-415.
38. G. S. Nolas, J. Poon and M. Kanatzidis, *Mrs Bulletin*, 2006, **31**, 199-205.
39. L.-D. Zhao, S.-H. Lo, Y. Zhang, H. Sun, G. Tan, C. Uher, C. Wolverton, V. P. Dravid and M. G. Kanatzidis, *Nature*, 2014, **508**, 373-377.

40. Q. Zhang, E. K. Chere, J. Sun, F. Cao, K. Dahal, S. Chen, G. Chen and Z. Ren, *Advanced Energy Materials*, 2015, **5**, 1500360-n/a.
41. C.-L. Chen, H. Wang, Y.-Y. Chen, T. Day and G. J. Snyder, *Journal of Materials Chemistry A*, 2014, **2**, 11171-11176.
42. S. R. Popuri, M. Pollet, R. Decourt, F. D. Morrison, N. S. Bennett and J. W. G. Bos, *Journal of Materials Chemistry C*, 2016, **4**, 1685-1691.
43. K. F. Hsu, S. Loo, F. Guo, W. Chen, J. S. Dyck, C. Uher, T. Hogan, E. K. Polychroniadis and M. G. Kanatzidis, *Science*, 2004, **303**, 818-821.
44. M. Beekman, D. T. Morelli and G. S. Nolas, *Nature Materials*, 2015, **14**, 1182-1185.
45. M. Rull-Bravo, A. Moure, J. F. Fernandez and M. Martin-Gonzalez, *RSC Advances*, 2015, **5**, 41653-41667.
46. T. Graf, C. Felser and S. S. P. Parkin, *Progress in Solid State Chemistry*, 2011, **39**, 1-50.
47. R. A. Degroot, F. M. Mueller, P. G. Vanengen and K. H. J. Buschow, *Physical Review Letters*, 1983, **50**, 2024-2027.
48. J. Schmitt, Z. M. Gibbs, G. J. Snyder and C. Felser, *Materials Horizons*, 2015, **2**, 68-75.
49. C. G. Fu, T. J. Zhu, Y. T. Liu, H. H. Xie and X. B. Zhao, *Energy & Environmental Science*, 2015, **8**, 216-220.
50. C. G. Fu, S. Q. Bai, Y. T. Liu, Y. S. Tang, L. D. Chen, X. B. Zhao and T. J. Zhu, *Nature Communications*, 2015, **6**, 8144.
51. F. Casper, T. Graf, S. Chadov, B. Balke and C. Felser, *Semiconductor Science and Technology*, 2012, **27**, 063001.
52. W. G. Zeier, J. Schmitt, G. Hautier, U. Aydemir, Z. M. Gibbs, C. Felser and G. J. Snyder, *Nature Reviews Materials*, 2016, **1**, 16032.
53. A. Page, C. Uher, P. F. Poudeu and A. Van der Ven, *Physical Review B*, 2015, **92**, 174102
54. T. J. Zhu, C. G. Fu, H. H. Xie, Y. T. Liu and X. B. Zhao, *Advanced Energy Materials*, 2015, **5**, 1500588.
55. K. Bartholomé, B. Balke, D. Zuckermann, M. Köhne, M. Müller, K. Tarantik and J. König, *Journal of Electronic Materials*, 2014, **43**, 1775-1781.
56. C. Yu, T. J. Zhu, R. Z. Shi, Y. Zhang, X. B. Zhao and J. He, *Acta Materialia*, 2009, **57**, 2757-2764.

57. G. Joshi, X. Yan, H. Z. Wang, W. S. Liu, G. Chen and Z. F. Ren, *Advanced Energy Materials*, 2011, **1**, 643-647.
58. L. Chen, S. Gao, X. Zeng, A. M. Dehkordi, T. M. Tritt and S. J. Poon, *Applied Physics Letters*, 2015, **107**, 041902.
59. M. Gurth, G. Rogl, V. V. Romaka, A. Grytsiv, E. Bauer and P. Rogl, *Acta Materialia*, 2016, **104**, 210-222.
60. R. A. Downie, R. I. Smith, D. A. MacLaren and J.-W. G. Bos, *Chemistry of Materials*, 2015, **27**, 2449–2459.
61. X. A. Yan, G. Joshi, W. S. Liu, Y. C. Lan, H. Wang, S. Lee, J. W. Simonson, S. J. Poon, T. M. Tritt, G. Chen and Z. F. Ren, *Nano Letters*, 2011, **11**, 556-560.
62. C. Fu, T. Zhu, Y. Liu, H. Xie and X. Zhao, *Energy & Environmental Science*, 2015, **8**, 216-220.
63. E. Rausch, B. Balke, J. M. Stahlhofen, S. Ouardi, U. Burkhardt and C. Felser, *Journal of Materials Chemistry C*, 2015, **3**, 10409-10414.
64. A. Tavassoli, F. Failamani, A. Grytsiv, G. Rogl, P. Heinrich, H. Müller, E. Bauer, M. Zehetbauer and P. Rogl, *Acta Materialia*, 2017, **135**, 263-276.
65. H. Hohl, A. P. Ramirez, W. Kaefer, K. Fess, C. Thurner, C. Kloc and E. Bucher, *MRS Proceedings*, 1997, **478**.
66. X. Yan, W. S. Liu, H. Wang, S. Chen, J. Shiomi, K. Esfarjani, H. Z. Wang, D. Z. Wang, G. Chen and Z. F. Ren, *Energy & Environmental Science*, 2012, **5**, 7543-7548.
67. G. Joshi, T. Dahal, S. Chen, H. Z. Wang, J. Shiomi, G. Chen and Z. F. Ren, *Nano Energy*, 2013, **2**, 82-87.
68. S. N. H. Eliassen, A. Katre, G. K. H. Madsen, C. Persson, O. M. Lovvik and K. Berland, *Physical Review B*, 2017, **95**, 045202
69. H. Geng and H. Zhang, *Journal of Applied Physics*, 2014, **116**, 033708.
70. E. Rausch, B. Balke, S. Ouardi and C. Felser, *Physical Chemistry Chemical Physics*, 2014, **16**, 25258-25262.
71. M. Schwall and B. Balke, *Physical Chemistry Chemical Physics*, 2013, **15**, 1868-1872.
72. K. Galazka, S. Populoh, L. Sagarna, L. Karvonen, W. J. Xie, A. Beni, P. Schmutz, J. Hulliger and A. Weidenkaff, *Physica Status Solidi a-Applications and Materials Science*, 2014, **211**, 1259-1266.
73. S. Populoh, M. H. Aguirre, O. C. Brunko, K. Galazka, Y. Lu and A. Weidenkaff, *Scripta Materialia*, 2012, **66**, 1073-1076.

74. Y. F. Liu and P. F. P. Poudeu, *Journal of Materials Chemistry A*, 2015, **3**, 12507-12514.
75. R. He, H. S. Kim, Y. C. Lan, D. Z. Wang, S. Chen and Z. F. Ren, *Rsc Advances*, 2014, **4**, 64711-64716.
76. R. Akram, Y. G. Yan, D. W. Yang, X. Y. She, G. Zheng, X. L. Su and X. F. Tang, *Intermetallics*, 2016, **74**, 1-7.
77. S. Chen, K. C. Lukas, W. S. Liu, C. P. Opeil, G. Chen and Z. F. Ren, *Advanced Energy Materials*, 2013, **3**, 1210-1214.
78. S. R. Culp, S. J. Poon, N. Hickman, T. M. Tritt and J. Blumm, *Applied Physics Letters*, 2006, **88**, 042106.
79. Y. Kimura, H. Ueno and Y. Mishima, *Journal of Electronic Materials*, 2009, **38**, 934-939.
80. E. Rausch, M. V. Castegnaro, F. Bernardi, M. C. M. Alves, J. Morais and B. Balke, *Acta Materialia*, 2016, **115**, 308-313.
81. A. Page, A. Van der Ven, P. F. P. Poudeu and C. Uher, *Journal of Materials Chemistry A*, 2016, **4**, 13949-13956.
82. J. Yang, H. M. Li, T. Wu, W. Q. Zhang, L. D. Chen and J. H. Yang, *Advanced Functional Materials*, 2008, **18**, 2880-2888.
83. L. Chaput, J. Tobola, P. Pecheur and H. Scherrer, *Physical Review B*, 2006, **73**, 7.
84. D. F. Zou, S. H. Xie, Y. Y. Liu, J. G. Lin and J. Y. Li, *Journal of Applied Physics*, 2013, **113**, 193705.
85. R. A. Downie, S. A. Barczak, R. I. Smith and J. W. G. Bos, *Journal of Materials Chemistry C*, 2015, **3**, 10534-10542.
86. J. Yang, G. P. Meisner and L. Chen, *Applied Physics Letters*, 2004, **85**, 1140-1142.
87. L. D. Chen, X. Y. Huang, M. Zhou, X. Shi and W. B. Zhang, *Journal of Applied Physics*, 2006, **99**, 064305.
88. H. H. Xie, H. Wang, Y. Z. Pei, C. G. Fu, X. H. Liu, G. J. Snyder, X. B. Zhao and T. J. Zhu, *Advanced Functional Materials*, 2013, **23**, 5123-5130.
89. P. G. Klemens, *Physical Review*, 1960, **119**, 507-509.
90. L. Romaka, Y. Stadnyk, A. Horyn, M. G. Shelyapina, V. S. Kasperovich, D. Fruchart, E. K. Hlil and P. Wolfers, *Journal of Alloys and Compounds*, 2005, **396**, 64-68.
91. S. Bhattacharya, A. L. Pope, R. T. Littleton, T. M. Tritt, V. Ponnambalam, Y. Xia and S. J. Poon, *Applied Physics Letters*, 2000, **77**, 2476-2478.

92. K. S. Kim, Y.-M. Kim, H. Mun, J. Kim, J. Park, A. Y. Borisevich, K. H. Lee and S. W. Kim, *Advanced Materials*, 2017, 1702091.
93. Y. Lei, C. Cheng, Y. Li, R. D. Wan and M. Wang, *Ceramics International*, 2017, **43**, 9343-9347.
94. C. Uher, J. Yang and G. P. Meisner, presented in part at the 18th International Conference on Thermoelectrics, 1999.
95. H.-H. Xie, C. Yu, T.-J. Zhu, C.-G. Fu, G. Jeffrey Snyder and X.-B. Zhao, *Applied Physics Letters*, 2012, **100**, 254104.
96. J. Krez, J. Schmitt, G. J. Snyder, C. Felser, W. Hermes and M. Schwind, *Journal of Materials Chemistry A*, 2014, **2**, 13513-13518.
97. H. Zhang, Y. Wang, K. Dahal, J. Mao, L. Huang, Q. Zhang and Z. Ren, *Acta Materialia*, 2016, **113**, 41-47.
98. G. Rogl, P. Sauerschnig, Z. Rykavets, V. V. Romaka, P. Heinrich, B. Hinterleitner, A. Grytsiv, E. Bauer and P. Rogl, *Acta Materialia*, 2017, **131**, 336-348.
99. E. Lkhagvasuren, S. Ouardi, G. H. Fecher, G. Auffermann, G. Kreiner, W. Schnelle and C. Felser, *Aip Advances*, 2017, **7**, 045010.
100. Y. F. Liu, P. Sahoo, J. P. A. Makongo, X. Y. Zhou, S. J. Kim, H. Chi, C. Uher, X. Q. Pan and P. F. P. Poudeu, *Journal of the American Chemical Society*, 2013, **135**, 7486-7495.
101. C. S. Birkel, J. E. Douglas, B. R. Lettiere, G. Seward, N. Verma, Y. C. Zhang, T. M. Pollock, R. Seshadri and G. D. Stucky, *Physical Chemistry Chemical Physics*, 2013, **15**, 6990-6997.
102. Y. W. Chai, T. Oniki and Y. Kimura, *Acta Materialia*, 2015, **85**, 290-300.
103. V. V. Romaka, P. Rogl, L. Romaka, Y. Stadnyk, N. Melnychenko, A. Grytsiv, M. Falmbigl and N. Skryabina, *Journal of Solid State Chemistry*, 2013, **197**, 103-112.
104. V. V. Romaka, P. Rogl, L. Romaka, Y. Stadnyk, A. Grytsiv, O. Lakh and V. Krayovskii, *Intermetallics*, 2013, **35**, 45-52.
105. K. Kirievsky, Y. Gelbstein and D. Fuks, *Journal of Solid State Chemistry*, 2013, **203**, 247-254.
106. K. Kirievsky, M. Shlimovich, D. Fuks and Y. Gelbstein, *Physical Chemistry Chemical Physics*, 2014, **16**, 20023-20029.
107. T. Morimura, M. Hasaka and M. Yoshimoto, *Journal of Alloys and Compounds*, 2006, **416**, 155-159.

108. J. E. Douglas, C. S. Birkel, M. S. Miao, C. J. Torbet, G. D. Stucky, T. M. Pollock and R. Seshadri, *Applied Physics Letters*, 2012, **101**, 183902.
109. J. E. Douglas, C. S. Birkel, N. Verma, V. M. Miller, M. S. Miao, G. D. Stucky, T. M. Pollock and R. Seshadri, *Journal of Applied Physics*, 2014, **115**, 043720.
110. J. E. Douglas, M. P. Echlin, W. C. Lenthe, R. Seshadri and T. M. Pollock, *Apl Materials*, 2015, **3**, 096107.
111. Y. W. Chai and Y. Kimura, *Applied Physics Letters*, 2012, **100**, 033114.
112. Y. Kimura, C. Asami, Y. W. Chai and Y. Mishima, *Materials Science Forum*, 2010, **654-656**, 2795-2798.
113. Y. W. Chai and Y. Kimura, *Acta Materialia*, 2013, **61**, 6684-6697.
114. Y. W. Chai, T. Oniki, T. Kenjo and Y. Kimura, *Journal of Alloys and Compounds*, 2016, **662**, 566-577.
115. D. T. Do, S. D. Mahanti and J. J. Pulikkoti, *Journal of Physics-Condensed Matter*, 2014, **26**, 275501.
116. J. P. A. Makongo, D. K. Misra, X. Y. Zhou, A. Pant, M. R. Shabetai, X. L. Su, C. Uher, K. L. Stokes and P. F. P. Poudeu, *Journal of the American Chemical Society*, 2011, **133**, 18843-18852.
117. J. P. A. Makongo, D. K. Misra, J. R. Salvador, N. J. Takas, G. Y. Wang, M. R. Shabetai, A. Pant, P. Paudel, C. Uher, K. L. Stokes and P. F. P. Poudeu, *Journal of Solid State Chemistry*, 2011, **184**, 2948-2960.
118. P. Sahoo, Y. F. Liu, J. P. A. Makongo, X. L. Su, S. J. Kim, N. Takas, H. Chi, C. Uher, X. Q. Pan and P. F. P. Poudeu, *Nanoscale*, 2013, **5**, 9419-9427.
119. Y. F. Liu, J. P. A. Makongo, A. Page, P. Sahoo, C. Uher, K. Stokes and P. F. P. Poudeu, *Journal of Solid State Chemistry*, 2016, **234**, 72-86.
120. S. V. Faleev and F. Leonard, *Physical Review B*, 2008, **77**, 214304
121. K. Biswas, J. Q. He, I. D. Blum, C. I. Wu, T. P. Hogan, D. N. Seidman, V. P. Dravid and M. G. Kanatzidis, *Nature*, 2012, **489**, 414-418.
122. K. Biswas, J. Q. He, Q. C. Zhang, G. Y. Wang, C. Uher, V. P. Dravid and M. G. Kanatzidis, *Nature Chemistry*, 2011, **3**, 160-166.
123. A. Bhardwaj, N. S. Chauhan, B. Sancheti, G. N. Pandey, T. D. Senguttuvan and D. K. Misra, *Physical Chemistry Chemical Physics*, 2015, **17**, 30090-30101.
124. H. Muta, T. Kanemitsu, K. Kurosaki and S. Yamanaka, *Materials Transactions*, 2006, **47**, 1453-1457.
125. H. Hazama, R. Asahi, M. Matsubara and T. Takeuchi, *Journal of Electronic Materials*, 2010, **39**, 1549-1553.

126. H. Hazama, M. Matsubara and R. Asahi, *Journal of Electronic Materials*, 2012, **41**, 1730-1734.
127. H. Hazama, M. Matsubara, R. Asahi and T. Takeuchi, *Journal of Applied Physics*, 2011, **110**, 063710.
128. R. A. Downie, D. A. MacLaren, R. I. Smith and J. W. G. Bos, *Chemical Communications*, 2013, **49**, 4184-4186.
129. R. A. Downie, R. I. Smith, D. A. MacLaren and J.-W. G. Bos, *Chemistry of Materials*, 2015.
130. M. Gurth, A. Grytsiv, J. Vrestal, V. V. Romaka, G. Giester, E. Bauer and P. Rogl, *Rsc Advances*, 2015, **5**, 92270-92291.
131. C. S. Birkel, W. G. Zeier, J. E. Douglas, B. R. Lettiere, C. E. Mills, G. Seward, A. Birkel, M. L. Snedaker, Y. C. Zhang, G. J. Snyder, T. M. Pollock, R. Seshadri and G. D. Stucky, *Chemistry of Materials*, 2012, **24**, 2558-2565.
132. R. A. Downie, S. R. Popuri, H. P. Ning, M. J. Reece and J. W. G. Bos, *Materials*, 2014, **7**, 7093-7104.
133. N. Verma, J. E. Douglas, S. Kramer, T. M. Pollock, R. Seshadri and C. G. Levi, *Metallurgical and Materials Transactions a-Physical Metallurgy and Materials Science*, 2016, **47A**, 4116-4127.
134. R. A. Downie, D. A. MacLaren and J. W. G. Bos, *Journal of Materials Chemistry A*, 2014, **2**, 6107-6114.
135. M. Eckert, *Annalen Der Physik*, 2012, **524**, A83-A85.
136. *Powder Diffraction: Theory and Practice*, RSC Publishing, 2008.
137. L. E. Smart and E. A. Moore, *Solid State Chemistry: An Introduction*, CRC Press, Taylor & Francis Group, 4th edn., 2012.
138. R. J. D. Tilley, *Crystals and Crystal Structures*, John Wiley & Sons, 2006.
139. C. Hammond, *The basics of crystallography and diffraction*, Oxford University Press, Oxford, 3rd edn., 2009.
140. W. Clegg, *X-ray Crystallography*, Oxford University Press, 2nd edn., 2015.
141. V. K. Pecharsky and P. Y. Zavalij, *Fundamentals of Powder Diffraction and Structural Characterization of Materials*, Springer, 2nd edn., 2009.
142. M. Hellenbrandt, *Crystallography Reviews*, 2004, **10**, 17-22.
143. W. Clegg, A. Blake, J., J. Cole, M., J. Evans, S. O., S. Parsons, D. Watkin, J. and P. Main, *Crystal structure analysis: principles and practice*, OUP, 2nd edn., 2009.
144. S. P. Thompson, J. E. Parker, J. Potter, T. P. Hill, A. Birt, T. M. Cobb, F. Yuan and C. C. Tang, *Review of Scientific Instruments*, 2009, **80**, 075107.

145. N. Tartoni, S. P. Thompson, C. C. Tang, B. L. Willis, G. E. Derbyshire, A. G. Wright, S. C. Jaye, J. M. Homer, J. D. Pizzey and A. M. T. Bell, *Journal of Synchrotron Radiation*, 2008, **15**, 43-49.
146. E. H. Kisi and C. J. Howard, *Applications of neutron powder diffraction*, Oxford University Press, 2008.
147. V. F. Sears, *Neutron News*, 1992, **3**, 26-37.
148. http://www.isis.stfc.ac.uk/instruments/polaris/, (accessed 09.03.2017).
149. O. Arnold, J. C. Bilheux, J. M. Borreguero, A. Buts, S. I. Campbell, L. Chapon, M. Doucet, N. Draper, R. Ferraz Leal, M. A. Gigg, V. E. Lynch, A. Markvardsen, D. J. Mikkelson, R. L. Mikkelson, R. Miller, K. Palmen, P. Parker, G. Passos, T. G. Perring, P. F. Peterson, S. Ren, M. A. Reuter, A. T. Savici, J. W. Taylor, R. J. Taylor, R. Tolchenov, W. Zhou and J. Zikovsky, *Nuclear Instruments and Methods in Physics Research Section A: Accelerators, Spectrometers, Detectors and Associated Equipment*, 2014, **764**, 156-166.
150. A. C. Hannon, *Nuclear Instruments & Methods in Physics Research Section a-Accelerators Spectrometers Detectors and Associated Equipment*, 2005, **551**, 88-107.
151. H. M. Rietveld, *Acta Crystallographica*, 1967, **22**, 151-152.
152. H. M. Rietveld, *Journal of Applied Crystallography*, 1969, **2**, 65-71.
153. A. K. Cheetham and A. L. Goodwin, *Nature Materials*, 2014, **13**, 760-762.
154. G. Will, *Powder Diffraction: The Rietveld Method and the Two Stage Method to Determine and Refine Crystal Structures from Powder Diffraction Data*, Springer - Verlag Berlin Heidelberg, 1st edn., 2006.
155. R. A. Young, *The Rietveld Method*, Oxford University Press, 1st edn., 1993.
156. T. Egami and S. J. L. Billinge, *Underneath the Bragg Peaks: Structural Analysis of Complex Materials, 2nd Edition*, 2012, **16**, 1-481.
157. S. J. L. Billinge, *Journal of Solid State Chemistry*, 2008, **181**, 1695-1700.
158. D. A. Keen, *Journal of Applied Crystallography*, 2001, **34**, 172-177.
159. T. Proffen and H. Kim, *Journal of Materials Chemistry*, 2009, **19**, 5078-5088.
160. M. G. Tucker, M. T. Dove and D. A. Keen, *Journal of Applied Crystallography*, 2001, **34**, 780-782.
161. D. A. Keen, M. G. Tucker and M. T. Dove, *Journal of Physics-Condensed Matter*, 2005, **17**, S15-S22.
162. C. A. Young and A. L. Goodwin, *Journal of Materials Chemistry*, 2011, **21**, 6464-6476.

163. A. C. Larson and R. B. Von Dreele, *General Structure Analysis System (GSAS)*, Los Alamos National Laboratory Report LAUR 86-748, 2000.
164. B. H. Toby, *Journal of Applied Crystallography*, 2001, **34**, 210-213.
165. A. A. Coelho, J. S. O. Evans, I. R. Evans, A. Kern and S. Parsons, *Powder Diffraction*, 2011, **26**, S22-S25.
166. M. G. Tucker, D. A. Keen, M. T. Dove, A. L. Goodwin and Q. Hui, *Journal of Physics-Condensed Matter*, 2007, **19**, 335218.
167. H. J. Wu, F. S. Zheng, D. Wu, Z. H. Ge, X. Y. Liu and J. Q. He, *Nano Energy*, 2015, **13**, 626-650.
168. R. F. Egerton, *Physical Principles of Electron Microscopy: An Introduction to TEM, SEM and AEM*, Springer Science + Business Media, Inc, 1st edn., 2005.
169. Y. Leng, *Materials Characterization: Introduction to Microscopic and Spectroscopic Methods*, Willey-VCH Verlag GmbH & Co., 2nd edn., 2013.
170. A. F. May and G. J. Snyder, in *Thermoelectrics and its Energy Harvesting*, ed. D. M. Rowe, CRC press, Boca Raton, 2012, ch. 11.
171. A. F. May, D. J. Singh and G. J. Snyder, *Physical Review B*, 2009, **79**, 153101.
172. H. H. Xie, H. Wang, C. G. Fu, Y. T. Liu, G. J. Snyder, X. B. Zhao and T. J. Zhu, *Scientific Reports*, 2014, **4**, 6888.
173. W. Liu, H. Chi, H. Sun, Q. Zhang, K. Yin, X. Tang, Q. Zhang and C. Uher, *Physical Chemistry Chemical Physics*, 2014, **16**, 6893-6897.
174. S. F. Corbin and D. M. Turriff, in *Characterization of Materials*, John Wiley & Sons, Inc., 2012.
175. J. Callaway, *Physical Review*, 1959, **113**, 1046-1051.
176. J. Yang, L. Xi, W. Qiu, L. Wu, X. Shi, L. Chen, J. Yang, W. Zhang, C. Uher and D. J. Singh, *Npj Computational Materials*, 2016, **2**, 15015.
177. A. Petersen, S. Bhattacharya, T. M. Tritt and S. J. Poon, *Journal of Applied Physics*, 2015, **117**, 035706.
178. C. S. Birkel, J. E. Douglas, B. R. Lettiere, G. Seward, Y. C. Zhang, T. M. Pollock, R. Seshadri and G. D. Stucky, *Solid State Sciences*, 2013, **26**, 16-22.
179. C. Colinet, P. Jund and J. C. Tedenac, *Intermetallics*, 2014, **46**, 103-110.
180. L. Andrea, G. Hug and L. Chaput, *Journal of Physics-Condensed Matter*, 2015, **27**, 425401.
181. C. Uher, J. Yang, S. Hu, D. T. Morelli and G. P. Meisner, *Phys. Rev. B*, 1999, **59**, 8615-8621.
182. J. Shiomi, K. Esfarjani and G. Chen, *Physical Review B*, 2011, **84**, 104302.

183. C. A. Ratsifaritana and P. G. Klemens, *International Journal of Thermophysics*, 1987, **8**, 737-750.
184. Y. T. Liu, H. H. Xie, C. G. Fu, G. J. Snyder, X. B. Zhao and T. J. Zhu, *Journal of Materials Chemistry A*, 2015, **3**, 22716-22722.
185. D. Narducci, *Applied Physics Letters*, 2011, **99**, 102104.
186. D. Fuks, G. Komisarchik, M. Kaller and Y. Gelbstein, *Journal of Solid State Chemistry*, 2016, **240**, 91-100.
187. J. E. Douglas, P. A. Chater, C. M. Brown, T. M. Pollock and R. Seshadri, *Journal of Applied Physics*, 2014, **116**, 163514.
188. A. Page, C. Uher, P. F. Poudeu and A. Van der Ven, *Phys. Rev. B*, 2015, **92**, 174102.
189. S. Sakurada and N. Shutoh, *Applied Physics Letters*, 2005, **86**, 082105.
190. S. R. Culp, J. W. Simonson, S. J. Poon, V. Ponnambalam, J. Edwards and T. M. Tritt, *Applied Physics Letters*, 2008, **93**, 022105.
191. A. Lis, C. Kenel and C. Leinenbach, *Metallurgical and Materials Transactions a-Physical Metallurgy and Materials Science*, 2016, **47A**, 2596-2608.
192. S. Furuseth and H. Fjellvag, *Acta Chemica Scandinavica Series a-Physical and Inorganic Chemistry*, 1986, **40**, 695-700.
193. H. Fjellvag and A. Kjekshus, *Acta Chemica Scandinavica Series a-Physical and Inorganic Chemistry*, 1986, **40**, 23-30.
194. X. L. Su, F. Fu, Y. G. Yan, G. Zheng, T. Liang, Q. Zhang, X. Cheng, D. W. Yang, H. Chi, X. F. Tang, Q. J. Zhang and C. Uher, *Nature Communications*, 2014, **5**, 4908.
195. A. K. Soper and E. R. Barney, *Journal of Applied Crystallography*, 2011, **44**, 714-726.
196. C. L. Farrow, P. Juhas, J. W. Liu, D. Bryndin, E. S. Bozin, J. Bloch, T. Proffen and S. J. L. Billinge, *Journal of Physics-Condensed Matter*, 2007, **19**, 335219.

Appendix A

Appendix contains supplementary information for Chapters 3-5.

Table A1. Experimental density (d), crystallographic density ($d_{crystal}$), percentage density (*%density*), experimental total thermal conductivity (κ_p) at 323 K and porosity corrected thermal conductivity (κ) at 323 K for selected samples discussed in this thesis. κ was calculated using the Equation 2.35.

	d (g cm^{-3})	$d_{crystal}$ (g cm^{-3})	%density	$\kappa_{p,323K}$ (W m^{-1} K^{-1})	κ_{323K} (W m^{-1} K^{-1})
$TiNiCu_ySn$ samples – Chapter 3					
$TiNiSn$	6.3(1)	7.18(1)	88%	5.2	6.2
$TiNiCu_{0.025}Sn$	6.2(1)	7.19(1)	87%	4.3	5.3
$TiNiCu_{0.05}Sn$	6.7(1)	7.23(1)	92%	4.6	5.1
$TiNiCu_{0.075}Sn$	7.1(1)	7.27(1)	97%	5.6	5.8
$TiNiCu_{0.10}Sn$	7.1(1)	7.30(1)	97%	6.0	6.2
off-stoichiometric $Ti_{1+x}Ni_{1+y}Sn$ samples – Chapter 3					
$Ti_{1.02}NiSn$	6.6(1)	7.03(1)	94%	6.5	7.0
$Ti_{1.02}Ni_{1.02}Sn$	6.9(1)	7.06(1)	98%	5.5	5.7
$Ti_{1.05}Ni_{1.05}Sn$	6.5(1)	7.11(1)	92%	4.4	4.9
$TiNi_{1.02}Sn$	6.7(1)	7.08(1)	95%	4.9	5.2
$MNiCu_{0.075}Sn$ and $M_{0.5}M'_{0.5}NiCu_{0.075}Sn$ samples – Chapter 4					
$TiNiCu_{0.075}Sn$	7.1(1)	7.27(1)	97%	5.6	5.8
$ZrNiCu_{0.075}Sn$	7.8(1)	7.95(1)	98%	7.1	7.2
$HfNiCu_{0.075}Sn$	10.2(1)	10.66(1)	96%	6.6	7.0
$Ti_{0.5}Zr_{0.5}NiCu_{0.075}Sn$	7.3(1)	7.60(1)	96%	4.9	5.2
$Ti_{0.5}Hf_{0.5}NiCu_{0.075}Sn$	8.7(1)	8.99(1)	97%	3.6	3.7
$Zr_{0.5}Hf_{0.5}NiCu_{0.075}Sn$	9.1(1)	9.28(1)	98%	4.5	4.7
$Ti_{0.5}Zr_{0.25}Hf_{0.25}NiCu_ySn$ samples – Chapter 4					
$Ti_{0.5}Zr_{0.25}Hf_{0.25}NiSn$	8.1(1)	8.18(1)	99%	3.1	3.1
$Ti_{0.5}Zr_{0.25}Hf_{0.25}NiCu_{0.025}Sn$	8.2(1)	8.24(1)	100%	3.6	3.6
$Ti_{0.5}Zr_{0.25}Hf_{0.25}NiCu_{0.05}Sn$	8.2(1)	8.27(1)	100%	3.9	3.9
$Ti_{0.5}Zr_{0.25}Hf_{0.25}NiCu_{0.075}Sn$	8.2(1)	8.29(1)	100%	4.5	4.5
$MNiSn$ and $M_{0.5}M'_{0.5}NiSn$ samples – Chapter 5 + Appendix D					
$TiNiSn$	6.3(1)	7.18(1)	88%	5.2	6.2
$ZrNiSn$	7.6(1)	7.83(1)	97%	8.7	9.2
$HfNiSn$	10.0(1)	10.35(1)	97%	6.5	6.7
$Ti_{0.5}Zr_{0.5}NiSn$	7.1(1)	7.46(1)	95%	3.3	3.5
$Ti_{0.5}Hf_{0.5}NiSn$	8.9(1)	8.93(1)	100%	2.8	2.8
$Zr_{0.5}Hf_{0.5}NiSn$	8.7(1)	9.18(1)	95%	4.4	4.7
$TiNi_{1+y}Sn$ samples – Chapter 5 + Appendix D					
$TiNiSn$	6.3(1)	7.18(1)	88%	5.2	6.2
$TiNi_{1.075}Sn$	7.0(1)	7.30(1)	96%	4.3	4.5
$TiNi_{1.25}Sn$	6.7(1)	7.51(1)	90%	4.6	5.3
$ZrNiSn$ and $Ti_{0.5}Zr_{0.25}Hf_{0.5}NiSn$ (prepared using the self-propagated high temperature synthesis + hot-pressing) – Chapter 5					
$ZrNiSn$	6.8(1)	7.83(1)	87%	4.8	5.8
$Ti_{0.5}Zr_{0.25}Hf_{0.25}NiSn$	7.5(1)	8.18(1)	92%	2.6	2.9

Appendix B

Appendix contains supplementary information for Chapter 3.

TiNiCu$_y$Sn series: The thermal diffusivity (α) and heat capacity (C_p) for TiNiCu$_y$Sn are shown in FigureB1.

Off-stoichiometric Ti$_{1+x}$Ni$_{1+y}$Sn: The heat capacity (C_p), thermal diffusivity (α) and electronic component of thermal conductivity (LT/ρ) for off-stoichiometric Ti$_{1+x}$Ni$_{1+y}$Sn are shown in Figure B2.

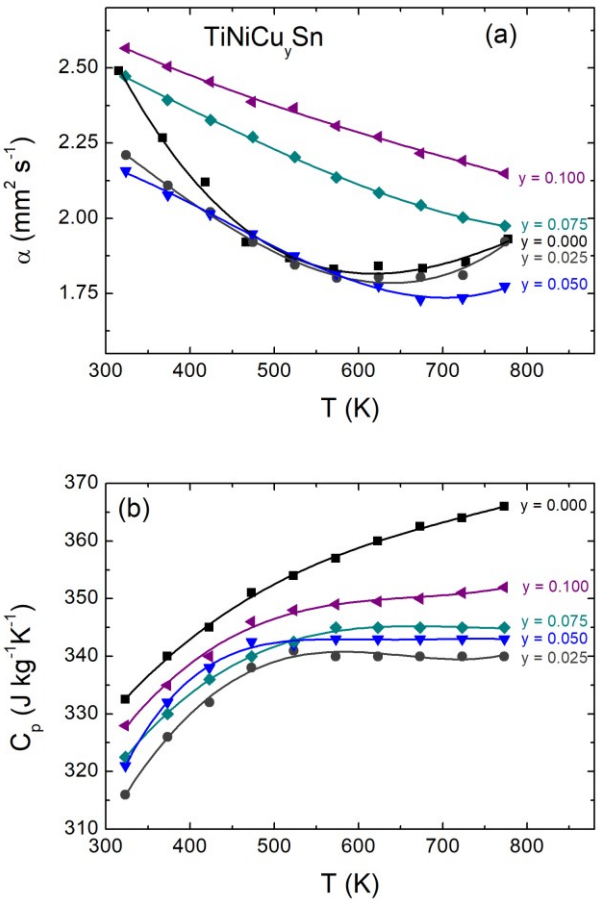

Figure B1. Temperature dependence of **(a)** the thermal diffusivity (α) and **(b)** the heat capacity (C_p) for the TiNiCu$_y$Sn samples.

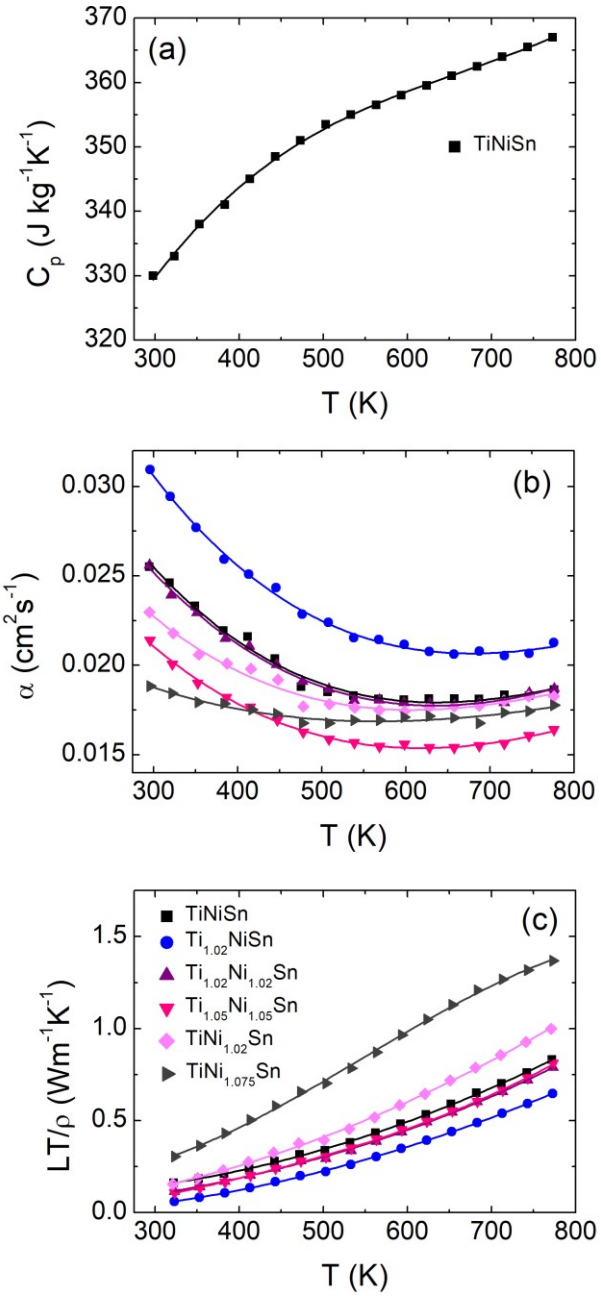

Figure B2. Temperature dependence of **(a)** the heat capacity (C_p) for stoichiometric TiNiSn, **(b)** the thermal diffusivity (α) and **(c)** the electronic thermal conductivity (LT/ρ) for $Ti_{1+x}Ni_{1+y}Sn$ compositions.

Appendix C

Appendix contains supplementary information for Chapter 4.

$MNiCu_{0.075}Sn$ and $M_{0.5}M'_{0.5}MiCu_{0.075}Sn$ series: The Rietveld refined structural parameters, compositions and fit statistics for neutron powder diffraction data are summarised in Table C1-C2. The calculated heat capacity (C_p), thermal diffusivity (α) and evaluated electronic component of thermal conductivity (LT/ρ) for $MNiCu_{0.075}Sn$, $M_{0.5}M'_{0.5}NiCu_{0.075}Sn$ are shown in Figure C1.

$Ti_{0.5}Zr_{0.25}Hf_{0.25}NiCu_ySn$ series: The Rietveld refined structural parameters, compositions and fit statistics for neutron powder diffraction data are summarised in Table C3. The heat capacity (C_p), thermal diffusivity (α) and calculated electronic component of thermal conductivity (LT/ρ) for $Ti_{0.5}Zr_{0.25}Hf_{0.25}NiCu_ySn$ are shown in Figure C1.

Table C1. Lattice parameters (*a*), weight percentage (*wt%*), volume percentage (*v%*), fractional site occupancies (*occ*), thermal displacement parameters (U_{iso}/Å^2) and refined compositions for the half-Heusler, full-Heusler, Ti and Ni_3Sn_2 phases that were used to fit the Polaris neutron powder diffraction data for $MNiCu_{0.075}Sn$ (M = Ti, Zr, Hf) materials.

$MNiCu_{0.075}Sn$		**M = Ti**	**M = Zr**	**M = Hf**
Half-Heusler Phase				
a (Å)		5.94603(4)	6.10864(3)	6.07716(4)
wt%		95.1(2)	94.9(1)	96.7(1)
v%		92.4(2)	95.4(1)	96.3(1)
Ti/Zr/Hf (4a)	**Occ**	Ti (4a) 1.00	Zr (4a) 1.00	Hf (4a) 1.00
	U_{iso}	0.00498(7)	0.0036(7)	0.0038(2)
Ni (4c)	**U_{iso}**	0.00534(5)	0.00428(4)	0.00455(6)
Ni / Cu (4d)	**Occ**	0.03 / 0.072(1)	0.00 / 0.022(1)	0.00 / 0.023(1)
	U_{iso}	0.00534(5)	0.00428(4)	0.00455(6)
Sn (4b)	**U_{iso}**	0.00458(6)	0.0044(36)	0.0044(2)
Refined composition		$TiNi_{1.03}Cu_{0.072(1)}Sn$	$ZrNiCu_{0.022(1)}Sn$	$HfNiCu_{0.023(1)}Sn$
ρ_{HH} (g cm^{-3})		7.319	7.868	10.575
Full-Heusler Phase				
a (Å)				6.2385(3)
wt%				2.7(1)
v%				2.9(1)
Ti/Zr/Hf (4a)	**U_{iso}**			Hf (4a) 0.0086(5)
Ni (8c)	**Occ**			1.00
	U_{iso}			0.0086(5)
Sn (4b)	**U_{iso}**			0.0086(5)
Refined composition				$HfNi_2Sn$
ρ_{FH} (g cm^{-3})				11.342
Ti Phase				
a (Å)		2.9649(4)		
c (Å)		4.568(1)		
v (Å^3)		34.78(1)		
wt%		4.9(2)		
v%		7.6(2)		
Ti (2c)	**U_{iso}**	0.008(1)		
ρ_{Ti} (g cm^{-3})		4.574		
$Ni_{2+2x}Sn_2$ (Ni_3Sn_2) Phase				
a (Å)			4.1305(2)	4.1488(9)
c (Å)			5.1733(4)	5.175(1)
v (Å^3)			76.436(7)	77.09(7)
wt%			5.1(1)	0.5(1)
v%			4.6(1)	0.8(1)
Ni (2a)	**U_{iso}**		0.013(5)	0.005(2)
Ni (2d)	**U_{iso}**		0.013(5)	0.005(2)
Sn (2c)	**U_{iso}**		0.013(5)	0.005(2)
$P_{Ni2+2xSn}$ (g cm^{-3})			8.668	8.901
Fit Statistics				
wR_p (%)	**bank 3**	2.90	3.03	2.75
	bank 4	2.13	2.34	2.17
	bank 5	2.28	2.44	2.37
R_p (%)	**bank 3**	2.68	2.90	2.77
	bank 4	3.43	3.67	3.43
	bank 5	3.09	3.11	3.13
Average composition		$Ti_{1.00}Ni_{0.951}Cu_{0.067}Sn_{0.924}$	$Zr_{1.00}Ni_{1.133}Cu_{0.022}Sn_{1.097}$	$Hf_{1.00}Ni_{1.049}Cu_{0.022}Sn_{1.013}$

Half-Heusler space group = $F\bar{4}3m$ – M (Ti, Zr, Hf): 4a (0,0,0), occ. 1.00; Ni(1): 4c (¼, ¼, ¼), occ. 1.00; Ni(2) / Cu: 4d (¾, ¾, ¾), occ. 0.03 / refined; Sn: 4b (½, ½, ½), occ. 1.00.

Full-Heusler space group = $Fm\bar{3}m$ – M (Ti, Zr, Hf): 4a (0,0,0), occ. 1.00; Ni: 8c (¼, ¼, ¼), occ. 1.00; Sn: 4b ((½, ½, ½), occ. 1.00.

Elemental Ti space group = $P63/mmc$ – Ti: 2c (⅓, ⅔, ¼), occ. 1.00.

Ni_3Sn_2 space group = $P63/mmc$ – Ni(1): 2a (0,0,0), occ. 1.00; Ni(2): 2d (⅓, ⅔, ¼), occ. 0.5; Sn: (2c) (⅓, ⅔, ¾), occ. 1.00

Table C2. Lattice parameters (*a*), weight percentage (*wt%*), volume percentage (*v%*), fractional site occupancies (*occ*), thermal displacement parameters (U_{iso}/Å^2) and refined compositions for the half-Heusler, full-Heusler and CuSn phases that were used to fit the Polaris neutron powder diffraction data for $M_{0.5}M'_{0.5}NiCu_{0.075}Sn$ (M = Ti, Zr, Hf) materials.

$M_{0.5}M'_{0.5}NiCu_{0.075}Sn$		M = Ti, M' = Zr	M = Ti, M' = Hf	M = Zr, M' = Hf
Half-Heusler Phase				
a (Å)		6.03452(5)	6.01314(4)	6.09372(4)
wt%		99.3(1)	96.0(1)	96.8(1)
v%		99.3(1)	96.5(1)	96.8(1)
Ti/Zr/Hf (4a)	**Occ**	Ti / Zr 0.522(2) / 0.478(2)	Ti / Hf 0.473(2) / 0.527(2)	Zr / Hf 0.5 / 0.5
	U_{iso}	0.0060(3)	0.0014(3)	0.0055(3)
Ni (4c)	**U_{iso}**	0.0065(1)	0.0047(1)	0.00446(5)
Ni / Cu (4d)	**Occ**	0.03 / 0.061(2)	0.00 / 0.036(1)	0.00 / 0.024(1)
	U_{iso}	0.0065(1)	0.0047(1)	0.00446(5)
Sn (4b)	**U_{iso}**	0.0041(2)	0.0082(3)	0.0028(3)
Refined composition		$Ti_{0.522(2)}Zr_{0.478(2)}Ni_{1.03}Cu_{0.061(2)}Sn$	$Ti_{0.473(2)}Hf_{0.527(2)}Ni_{1.00}Cu_{0.036(1)}Sn$	$Zr_{0.50}Hf_{0.50}Ni_{1.00}Cu_{0.024(1)}Sn$
ρ_{HH} (g cm^{-3})		7.605	9.055	9.211
Full-Heusler Phase				
a (Å)			6.1189(3)	6.2479(3)
wt%			2.6(1)	2.4(1)
v%			2.5(1)	2.2(1)
Ti/Zr/Hf (4a)	**Occ**		Ti / Hf 0.64(1) / 0.36(1)	Zr / Hf 0.5 / 0.5
	U_{iso}		0.0064(5)	0.0074(5)
Ni (8c)	**Occ**		1.00	1.00
	U_{iso}		0.0064(5)	0.0074(5)
Sn (4b)	**U_{iso}**		0.0064(5)	0.0074(5)
Refined composition			$Ti_{0.64(1)}Hf_{0.36(1)}Ni_2Sn$	$Zr_{0.50}Hf_{0.50}Ni_2Sn$
ρ_{FH} (g cm^{-3})			9.579	10.102
CuSn Phase				
a (Å)		4.1556(8)	4.1478(8)	4.177(1)
c (Å)		5.111(2)	5.111(2)	5.071(2)
v (Å^3)		76.43(3)	76.12(2)	76.63(4)
wt%		0.7(1)	0.9(1)	0.8(1)
v%		0.7(1)	1.0(1)	1.0(1)
Cu (2a)	**U_{iso}**	0.002(2)	0.005(2)	0.005(3)
Sn (2c)	**U_{iso}**	0.002(2)	0.005(2)	0.005(3)
P_{CuSn} (g cm^{-3})		7.919	7.948	7.898
Fit Statistics				
wR_p (%)	**bank 3**	2.54	2.84	2.62
	bank 4	2.15	2.11	2.10
	bank 5	2.13	2.13	2.17
R_p (%)	**bank 3**	2.63	3.01	2.75
	bank 4	3.37	3.83	3.63
	bank 5	2.87	3.08	2.92
Average composition		$Ti_{0.518}Zr_{0.475}Ni_{1.023}Cu_{0.068}Sn_{1.0}$	$Ti_{0.472}Hf_{0.517}Ni_{1.015}Cu_{0.045}Sn_{1.0}$	$Zr_{0.495}Hf_{0.495}Ni_{1.013}Cu_{0.033}Sn_{1.0}$

Half-Heusler space group = $F\bar{4}3m$ – M (Ti, Zr, Hf): 4a (0,0,0), occ. refined; Ni(1): 4c (¼, ¼, ¼), occ. 1.00; Ni(2) / Cu: 4d (¾, ¾, ¾), occ. 0.03 / refined; Sn: 4b (½, ½, ½), occ. 1.00.
Full-Heusler space group = $Fm\bar{3}m$ – M (Ti, Zr, Hf): 4a (0,0,0), occ. 1.00; Ni: 8c (¼, ¼, ¼), occ. 1.00; Sn: 4b ((½, ½, ½), occ. 1.00.
CuSn space group = $P63/mmc$ – Cu: 2a (0,0,0), occ. 1.00; Sn: 2c (⅓, ⅔, ¼), occ. 1.00.

Table C3. Lattice parameters (*a*), weight percentage (*wt%*), volume percentage (*v%*), fractional site occupancies (*occ*), thermal displacement parameters (U_{iso}/Å^2) and refined compositions for the half-Heusler and $Ni_{2+2x}Sn_2$ phases that were used to fit the Polaris neutron powder diffraction data collected for $Ti_{0.5}Zr_{0.25}Hf_{0.25}NiCu_ySn$ materials.

		y = 0.025	**y = 0.05**	**y = 0.075**
Half-Heusler				
a (Å)		6.01528(8)	6.01617(6)	6.02732(5)
wt%		99.3(1)	98.5(1)	100
v%		99.4(1)	98.5(1)	100
Ti/Zr/Hf	**Occ**	0.515(3) / 0.242(1) / 0.242(1)	0.516(3) / 0.242(1) / 0.242(1)	0.493(6) / 0.246(3) / 0.246(3)
4(a)	**U_{iso}**	0.0011(5)	0.0030(5)	0.0054(4)
Ni(4c)	**U_{iso}**	0.0050(1)	0.0053(1)	0.0056(1)
Cu (4d)	**Occ**	0.041(2)	0.049(2)	0.073(2)
	U_{iso}	0.0050(1)	0.0053(1)	0.0056(1)
Sn (4b)	**U_{iso}**	0.0071(4)	0.0058(4)	0.0046(2)
ρ_{HH} (g cm^{-3})		8.241	8.378	8.252
Ni_3Sn_2				
a (Å)		4.0976(8)	4.1161(5)	
c (Å)		5.131(1)	5.1236(9)	
v (Å^3)		74.61(2)	75.18(1)	
wt%		0.7(1)	1.5(1)	
v%		0.6(1)	1.5(1)	
Ni (2a)	**U_{iso}**	0.008(2)	0.008(1)	
Ni (2d)	**U_{iso}**	0.008(2)	0.008(1)	
Sn (2c)	**U_{iso}**	0.008(2)	0.008(1)	
ρ (g cm^{-3})		9.203	9.131	
Fit Statistics				
χ^2(Rietveld)		4.050	1.884	3.507
wR_p	**bank 3**	3.16	2.97	2.96
(%)	**bank 4**	2.47	2.21	2.29
	bank 5	2.43	2.08	1.99
R_p	**bank 3**	3.26	3.24	3.05
(%)	**bank 4**	4.22	4.40	3.41
	bank 5	3.54	3.11	2.90

Half-Heusler space group = $F\bar{4}3m$ – M (Ti, Zr, Hf): 4a (0,0,0), occ. refined; Ni(1): 4c (¼, ¼, ¼), occ. 1.00; Ni(2) / Cu: 4d (¾, ¾, ¾), occ. 0.03 / refined; Sn: 4b (½, ½, ½), occ. 1.00.
Ni_3Sn_2 space group = $P63/mmc$ – Ni(1): 2a (0,0,0), occ. 1.00; Ni(2): 2d (⅓, ⅔, ¼), occ. 0.50; Sn: (2c) (⅓, ⅔, ¾), occ. 1.00.

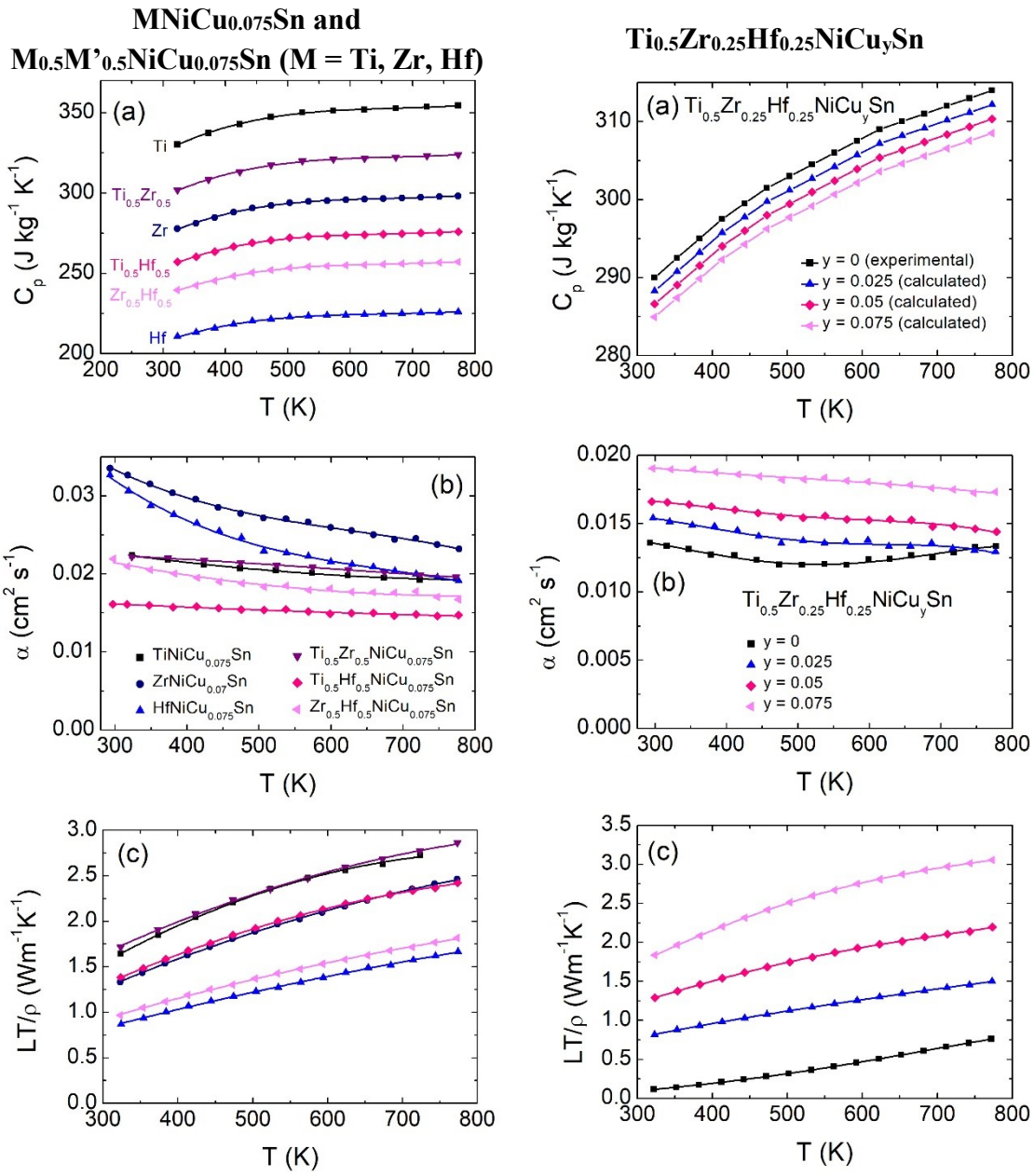

Figure C1. Temperature dependence of **(a)** heat capacity (C_p), **(b)** the thermal diffusivity (α) and **(c)** the electronic thermal conductivity (LT/ρ) for $MNiCu_{0.075}Sn$, $M_{0.5}M'_{0.5}NiCu_ySn$ and $Ti_{0.5}Zr_{0.25}Hf_{0.25}NiCu_ySn$ series.

Appendix D

Appendix contains supplementary information for Chapter 5.

$TiNi_{1+y}Sn$ (y = 0, 0.075 and 0.25): Results of Rietveld refinements to in-situ neutron powder diffraction data are shown in Tables D1-D6. The thermoelectric properties measurements of TiNiSn, $TiNi_{1.075}Sn$ and $TiNi_{1.25}Sn$ samples were done on separately prepared samples. X-ray powder diffraction patterns for samples before and after hot pressing are presented in Figure D1, while the results of Rietveld refinements are shown in Table D7. The thermoelectric properties are summarised in Figure D2 and Figure D3.

ZrNiSn and $Ti_{0.5}Zr_{0.25}Hf_{0.25}NiSn$: The heat capacity ($C_p$), the thermal diffusivity (α) and calculated electronic component of thermal conductivity (LT/ρ) of ZrNiSn and $Ti_{0.5}Zr_{0.25}Hf_{0.25}NiSn$ are presented in Figure D4.

$M_{0.5}M'_{0.5}NiSn$ (M = Ti, Zr, Hf): Results of Rietveld refinements to neutron powder diffraction data are shown in Tables D8-D12. The thermoelectric properties measurements of MNiSn and $M_{0.5}M'_{0.5}NiSn$ samples were done on separately prepared samples. X-ray powder diffraction patterns for samples after in-situ NPD experiment, after long annealing (before hot-pressing) and after hot-pressing are presented in Figure D5, while the results of Rietveld refinements are shown in Table D13 and Table D14. The thermoelectric properties are summarised in Figure D6 and Figure D7.

Table D1. *TiNiSn* –Weight percentage (*wt%*) of intermediate phases that were identified during the heating up of elemental precursors to form target TiNiSn alloy, determined through Rietveld analysis. *T* (°C) denotes the average temperature of 30°C measurement steps, y represents the Ni (*2c*) site occupancy of $Ni_{3+y}Sn_4$, Ni (*2d*) site occupancy of $Ni_{2+2y}Sn_2$, Ni (*4d*) site occupancy of $TiNi_{1+y}Sn$ and Ni (*8d*) site occupancy of $TiNi_{2y}Sn$. (f) denotes the atomic occupancy that was fixed (not allowed to refine). The standard deviation for the *wt%* is 0.2, while for the Ni content (y) it is 0.005.

T (ºC)	Ti	Ni	Sn	$Ni_{3+y}Sn_4$		$Ni_{2+2y}Sn_2$		Ni_3Sn	Ti_2Ni	$TiNi_{1+y}Sn$		$TiNi_{2y}Sn$		TiNi
	wt%	wt%	wt%	wt%	y	wt%	y	wt%	wt%	wt%	y	wt%	y	wt%
142.8	21.8	27.5	50.7											
175.5	21.2	27.8	51.1											
207.0	25.2	28.0	33.5	13.3	0.0 (f)									
237.6	24.4	12.0		63.5	0.0 (f)									
269.5	23.3	9.7		67.1	0.0 (f)									
301.0	22.7	8.8		68.5	0.040									
332.6	22.0	8.2		69.8	0.042									
364.2	22.2	7.3		70.5	0.054									
396.0	21.1	6.2		72.7	0.082									
427.3	20.0	5.5		74.4	0.126									
458.6	20.7	4.7		74.6	0.194									
490.2	22.7	3.3		60.6	0.230	11.5	0.579	1.9						
521.6	22.4	2.4		60.9	0.339	12.1	0.700	2.3						
552.9	22.8	1.7		60.7	0.417	12.3	0.626	2.4						
584.2	23.2	1.0		59.2	0.509	14.5	0.418	2.0						
615.6	21.0			57.2	0.567	16.9	0.368	1.7	1.9	1.2	0.0 (f)			
647.0	19.8			60.4	0.617	14.7	0.305	0.9	3.1	1.2	0.0 (f)			
678.5	18.4			57.3	0.617	15.3	0.311		4.7	1.7	0.0 (f)	2.6	0.9 (f)	
709.8	17.3			53.6	0.627	15.6	0.310		6.5	2.3	0.0 (f)	4.5	0.9 (f)	
741.2	14.7			41.0	0.592	3.8	0.337		7.3	3.6	0.0 (f)	28.3	0.9 (f)	1.3
772.5	9.7					6.9	0.50 (f)		7.8	5.1	0.0 (f)	67.7	0.9 (f)	2.8
803.6									7.6	32.1	0.048	53.5	0.9 (f)	6.8
834.7									7.3	46.1	0.056	38.2	0.9 (f)	8.3
866.0				(2)					4.6	60.6	0.058	24.8	0.9 (f)	10.0
894.0									2.9	69.7	0.062	18.1	0.9 (f)	9.4

Table D2. *TiNiSn* – Weight percentage (*wt%*) of intermediate phases that were identified during the annealing and cooling down of elemental precursors to form target TiNiSn alloy, determined through Rietveld analysis. *T* (°C) denotes the average temperature of 30°C measurement steps, while y represents Ni (4d) site occupancy of $TiNi_{1+y}Sn$ and Ni (*8d*) site occupancy of $TiNi_{2y}Sn$. (f) denotes the atomic occupancy that was fixed (not allowed to refine). The standard deviation for the *wt%* is 0.2, while for the Ni content (y) it is 0.005.

Long annealing					
Time (minutes)	**$TiNi_{1+y}Sn$**		**$TiNi_{2y}Sn$**		**TiNi**
	wt%	**y**	**wt%**	**y**	**wt%**
10	76.3	0.059	14.8	0.9 (f)	8.9
20	82.2	0.061	10.7	0.9 (f)	7.1
30	84.3	0.061	9.8	0.9 (f)	5.9
40	85.8	0.061	9.1	0.9 (f)	5.1
50	86.5	0.059	9.3	0.9 (f)	4.3
60	87.4	0.055	8.9	0.9 (f)	3.7
70	87.0	0.055	9.3	0.9 (f)	3.6
80	87.6	0.050	9.0	0.9 (f)	3.4
90	88.9	0.051	7.9	0.9 (f)	3.2
100	88.6	0.050	8.6	0.9 (f)	2.9
110	89.6	0.041	7.9	0.9 (f)	2.5
120	89.1	0.044	8.8	0.9 (f)	2.3
130	90.7	0.043	7.0	0.9 (f)	2.2
140	90.5	0.045	7.6	0.9 (f)	1.9
150	91.0	0.041	6.9	0.9 (f)	2.1
160	91.2	0.041	6.7	0.9 (f)	2.0
170	92.6	0.040	5.7	0.9 (f)	1.7
180	92.8	0.040	5.6	0.9 (f)	1.6
240	93.4	0.036	5.5	0.9 (f)	1.1
300	93.1	0.035	6.1	0.9 (f)	0.9
360	94.0	0.035	6.0	0.9 (f)	
420	95.5	0.027	4.5	0.9 (f)	
490	95.8	0.028	4.1	0.9 (f)	
530	96.5	0.028	3.5	0.9 (f)	
Cooling down					
T (ºC)	**$TiNi_{1+y}Sn$**		**$TiNi_{2y}Sn$**		**TiNi**
	wt%	**y**	**wt%**	**y**	**wt%**
897.0	96.5	0.027	3.5	0.9 (f)	
877.5	96.6	0.028	3.4	0.9 (f)	
792.1	95.7	0.027	4.3	0.9 (f)	
660.0	95.7	0.025	4.3	0.9 (f)	
537.0	59.8	0.025	4.2	0.9 (f)	
447.0	95.6	0.026	4.4	0.9 (f)	
392.5	95.4	0.027	4.6	0.9 (f)	
352.5	95.2	0.027	4.8	0.9 (f)	

Table D3. *$TiNi_{1.075}Sn$* – Weight percentage (*wt%*) of intermediate phases that were identified during the heating up of elemental precursors to form target $TiNi_{1.075}Sn$ alloy, determined through Rietveld analysis. *T* (°C) denotes the average temperature of 30°C measurement steps, y represents the Ni (*2c*) site occupancy of $Ni_{3+y}Sn_4$, Ni (*2d*) site occupancy of $Ni_{2+2y}Sn_2$, Ni (*4d*) site occupancy of $TiNi_{1+y}Sn$ and Ni (*8d*) site occupancy of $TiNi_{2y}Sn$. (f) denotes the atomic occupancy that was fixed (not allowed to refine). Data was not collected during heating stage in temperature range ~800 – 890 ºC. The standard deviation for the *wt%* is 0.2, while for the Ni content (y) it is 0.005.

T (ºC)	Ti	Ni	Sn	$Ni_{3+y}Sn_4$		$Ni_{2+2y}Sn_2$		Ni_3Sn	Ti_2Ni	$TiNi_{1+y}Sn$		$TiNi_{2y}Sn$		TiNi
	wt%	wt%	wt%	wt%	y	wt%	y	wt%	wt%	wt%	y	wt%	y	wt%
143.0	21.0	29.1	49.9											
175.0	20.8	28.9	50.3											
207.0	21.1	29.4	49.5											
238.1	19.8	26.1		54.0	0.136									
269.6	21.5	7.5		71.0	0.107									
301.6	21.4	7.3		71.2	0.103									
333.1	21.7	7.3		71.0	0.103									
363.9	21.3	7.2		71.5	0.109									
396.1	22.0	7.0		70.9	0.124									
427.6	21.3	7.0		71.7	0.145									
458.3	21.7	6.0		63.1	0.154	9.2	0.50 (f)							
491.0	21.4	5.1		61.6	0.224	11.9	0.50 (f)	3.1						
522.1	21.9	3.8		58.9	0.335	12.3	0.50 (f)	3.6						
553.3	22.0	2.8		58.4	0.412	13.1	0.50 (f)	2.5						
574.7	20.1			51.3	0.605	21.2	0.360	1.9	1.8	3.2	0.0 (f)			
597.7	20.1			51.6	0.605	21.4	0.352	1.4	2.0	3.0	0.0 (f)			
628.9	19.7			53.2	0.629	21.3	0.333	7.6	2.6	1.8	0.0 (f)			
660.1	16.1			47.6	0.653	22.2	0.321		3.6	2.8	0.0 (f)			
691.4	17.3			46.4	0.641	26.0	0.311		5.6	1.1	0.0 (f)	3.5	1.0 (f)	
722.7	15.5			40.8	0.638	30.0	0.304		7.2	1.9	0.0 (f)	3.4	1.0 (f)	1.1
754.1	13.9			32.9	0.662	33.9	0.294		9.0	3.5	0.0 (f)	5.2	1.0 (f)	1.6
784.7				32.2	0.646	13.2	0.250		9.8	4.0	0.0 (f)	37.5	1.0 (f)	3.2
816.1 847.5	Data were not collected													
895.5									2.5	61.4	0.060	28.1	0.870	8.0

Table D4. *$TiNi_{1.075}Sn$* – Weight percentage (*wt%*) of intermediate phases that were identified during the annealing and cooling down of elemental precursors to form target $TiNi_{1.075}Sn$ alloy, determined through Rietveld analysis. *T* (°C) denotes the average temperature of 30°C measurement steps, while y represents Ni (*4d*) site occupancy of $TiNi_{1+y}Sn$ and Ni (*8d*) site occupancy of $TiNi_{2y}Sn$. The standard deviation for the *wt%* is 0.2, while for the Ni content (y) it is 0.005.

Long annealing					
Time (minutes)	**$TiNi_{1+y}Sn$**		**$TiNi_{2y}Sn$**		**TiNi**
	wt%	**y**	**wt%**	**y**	**wt%**
10	68.7	0.064	24.2	0.878	7.1
20	72.1	0.061	21.6	0.873	6.2
30	75.1	0.066	19.5	0.883	5.4
40	77.3	0.064	17.8	0.881	4.9
50	79.1	0.063	16.4	0.880	4.5
60	80.7	0.063	15.3	0.875	4.0
70	82.5	0.063	13.8	0.889	3.7
80	83.2	0.064	13.5	0.882	3.3
90	84.3	0.064	12.5	0.869	3.2
100	85.5	0.064	11.7	0.895	2.8
110	86.1	0.067	11.3	0.887	2.6
120	87.0	0.063	10.6	0.900	2.4
130	87.7	0.066	9.9	0.901	2.4
140	88.5	0.065	9.4	0.909	2.1
150	88.7	0.068	9.5	0.892	1.8
160	89.3	0.067	9.0	0.890	1.7
170	89.7	0.068	8.5	0.893	1.7
180	89.9	0.066	8.3	0.875	1.8
190	90.6	0.064	8.1	0.899	1.3
200	90.7	0.065	7.7	0.882	1.6
210	90.7	0.066	8.0	0.864	1.4
Cooling down					
T (ºC)	**$TiNi_{1+y}Sn$**		**$TiNi_{2y}Sn$**		**TiNi**
	wt%	**y**	**wt%**	**y**	**wt%**
798.8	91.1	0.066	7.6	0.871	1.3
631.5	91.3	0.059	7.4	0.893	1.2
506.3	93.6	0.061	5.1	0.840	1.3
440.0	92.8	0.060	4.4	0.734	2.8
390.4	93.4	0.061	5.4	0.724	1.2

Table D5. *$TiNi_{1.25}Sn$* – Weight percentage (*wt%*) of intermediate phases that were identified during the heating up of elemental precursors to form target $TiNi_{1.25}Sn$ alloy, determined through Rietveld analysis. *T* (°C) denotes the average temperature of 30°C measurement steps, y represents the Ni (*2c*) site occupancy of $Ni_{3+y}Sn_4$, Ni (*2d*) site occupancy of $Ni_{2+2y}Sn_2$, Ni (*4d*) site occupancy of $TiNi_{1+y}Sn$ and Ni (*8d*) site occupancy of $TiNi_{2y}Sn$. (f) denotes the atomic occupancy that was fixed (not allowed to refine). The standard deviation for the *wt%* is 0.2, while for the Ni content (y) it is 0.005.

T (ºC)	Ti	Ni	Sn	$Ni_{3+y}Sn_4$		$Ni_{2+2y}Sn_2$		Ni_3Sn	Ti_2Ni	$TiNi_{1+y}Sn$		$TiNi_{2y}Sn$		TiNi
	wt%	wt%	wt%	wt%	y	wt%	y	wt%	wt%	wt%	y	wt%	y	wt%
95.7	20.1	31.8	48.0											
127.8	19.9	32.3	47.8											
158.4	20.0	32.2	47.7											
190.2	20.2	32.1	47.7											
222.3	21.1	33.1	45.8											
254.4	21.3	9.8		50.2	0.346	13.3	0.50 (f)	4.1		1.3	0.0 (f)			
285.2	20.9	6.5		53.1	0.377	12.6	0.50 (f)	5.0		1.9	0.0 (f)			
316.7	20.7	6.4		53.8	0.367	12.4	0.50 (f)	5.0		1.7	0.0 (f)			
348.3	20.4	6.5		54.0	0.366	12.2	0.459	5.0		1.9	0.0 (f)			
379.8	20.3	6.5		53.6	0.372	12.6	0.459	4.9		2.2	0.0 (f)			
411.7	20.8	6.4		53.2	0.375	12.8	0.476	4.8		2.0	0.0 (f)			
442.8	20.2	6.4		53.7	0.382	12.7	0.486	4.9		2.1	0.0 (f)			
474.6	20.3	6.2		53.2	0.387	13.2	0.440	5.2		1.9	0.0 (f)			
505.9	20.4	5.8		52.7	0.434	13.4	0.446	5.6		2.0	0.0 (f)			
537.5	21.1	4.9		48.8	0.487	17.8	0.386	5.7		1.7	0.0 (f)			
568.8	20.9	3.4		45.5	0.549	22.1	0.388	5.9		2.2	0.0 (f)			
600.3	20.0	2.0		41.9	0.606	27.8	0.374	5.5		2.8	0.0 (f)			
631.6	17.7			39.3	0.651	30.8	0.352	4.5	2.7	5.1	0.0 (f)			
663.0	16.5			36.4	0.654	33.8	0.341	2.6	3.7	4.9	0.0 (f)	1.0	1.0 (f)	1.0
695.1	15.2			28.5	0.690	44.4	0.322		5.4	2.0	0.0 (f)	2.4	1.0 (f)	2.1
726.5	13.6			19.2	0.707	52.1	0.306		7.5	1.9	0.0 (f)	3.9	1.0 (f)	1.8
759.4	10.0			10.1	0.759	60.6	0.303		9.0	2.8	0.0 (f)	4.7	1.0 (f)	2.7
790.2						59.6	0.309		10.1	4.0	0.0 (f)	21.9	0.954	4.4
822.1						10.8	0.262		8.5	2.4	0.0 (f)	71.9	0.952	6.4
853.6									6.1	9.4	0.0 (f)	76.0	0.928	8.5
884.8									3.6	24.2	0.063	63.3	0.901	8.9

Table D6. *$TiNi_{1.25}Sn$* – Weight percentage (*wt%*) of intermediate phases that were identified during the annealing and cooling down of elemental precursors to form target $TiNi_{1.25}Sn$ alloy, determined through Rietveld analysis. *T* (°C) denotes the average temperature of 30°C measurement steps, while y represents Ni (*4d*) site occupancy of $TiNi_{1+y}Sn$ and Ni (*8d*) site occupancy of $TiNi_{2y}Sn$. The standard deviation for the *wt%* is 0.2, while for the Ni content (y) it is 0.005.

Long annealing					
Time (minutes)	**$TiNi_{1+y}Sn$**		**$TiNi_{2y}Sn$**		**TiNi**
	wt%	**y**	**wt%**	**y**	**wt%**
10	34.4	0.062	57.6	0.908	8.0
20	40.1	0.060	53.0	0.908	6.9
30	44.5	0.062	49.6	0.902	5.9
40	48.4	0.065	46.5	0.913	5.1
50	50.7	0.062	44.7	0.907	4.6
60	53.1	0.065	43.1	0.910	3.8
70	54.6	0.066	41.7	0.901	3.6
80	56.5	0.065	40.2	0.906	3.4
90	57.7	0.066	39.6	0.909	2.7
100	59.0	0.066	38.2	0.911	2.7
110	59.7	0.067	37.9	0.895	2.4
120	61.2	0.070	36.7	0.914	2.1
130	61.7	0.069	36.3	0.910	2.0
140	62.7	0.069	35.3	0.915	2.0
150	63.3	0.073	35.1	0.913	1.6
160	63.8	0.070	34.6	0.904	1.6
170	64.5	0.073	34.0	0.908	1.5
180	64.6	0.071	34.0	0.901	1.4
190	65.1	0.070	33.5	0.899	1.3
200	65.5	0.072	33.4	0.907	1.1
210	66.0	0.070	32.9	0.910	1.1
220	66.2	0.074	32.8	0.906	0.9
230	66.6	0.073	32.4	0.901	1.0
240	66.8	0.073	32.2	0.902	0.9
250	66.7	0.071	32.4	0.896	0.9
Cooling down					
T (ºC)	**$TiNi_{1+y}Sn$**		**$TiNi_{2y}Sn$**		**TiNi**
	wt%	**y**	**wt%**	**y**	**wt%**
846.9	66.7	0.075	32.4	0.904	0.9
742.7	67.5	0.068	31.9	0.913	0.7
612.7	67.7	0.064	31.7	0.910	0.5
497.6	68.4	0.068	30.9	0.903	0.7
427.5	72.0	0.065	27.2	0.909	0.7
379.7	72.3	0.065	27.0	0.917	0.7
343.0	72.6	0.066	26.7	0.931	0.7
314.0	72.8	0.065	27.2	0.945	
288.9	73.1	0.066	26.9	0.939	
269.0	72.8	0.065	27.2	0.935	
257.6	72.6	0.068	27.4	0.941	

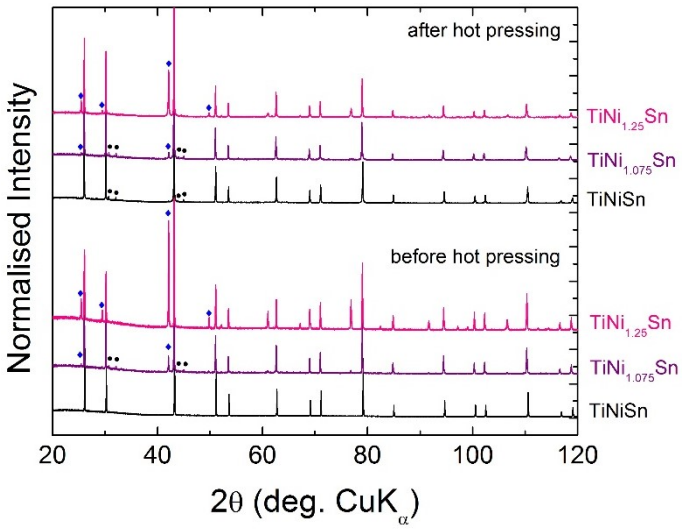

Figure D1. *$TiNi_{1+y}Sn$*: X-ray diffraction patterns of separately prepared samples before and after hot pressing. All main peaks can be indexed as the half-Heusler structure. Black circles show elemental Sn impurity, while blue rhombus denote $TiNi_2Sn$ (full-Heusler) phase.

Table D7. *$TiNi_{1+y}Sn$*: Lattice parameter (*a*) and weight percentage (*wt%*) for the half-Heusler, full-Heusler and Sn phases, which were used during the Rietveld refinement fit to X-ray powder diffraction data of samples prepared separately for thermoelectric properties measurement.

Composition	Half-Heusler		Full-Heusler		Sn
	a (Å)	wt%	a (Å)	wt%	wt%
Before Hot Pressing					
TiNiSn	5.9304(1)	100.0			
$TiNi_{1.075}Sn$	5.9384(1)	89.8(2)	6.0803(1)	7.7(2)	2.5(2)
$TiNi_{1.25}Sn$	5.9391(1)	62.4(2)	6.0801(1)	37.6(2)	
After Hot Pressing					
TiNiSn	5.9307(1)	97.7(1)			2.3(1)
$TiNi_{1.075}Sn$	5.9432(1)	92.9(1)	6.0745(3)	4.7(2)	2.4(1)
$TiNi_{1.25}Sn$	5.9401(1)	73.7(2)	6.0770(1)	26.3(2)	

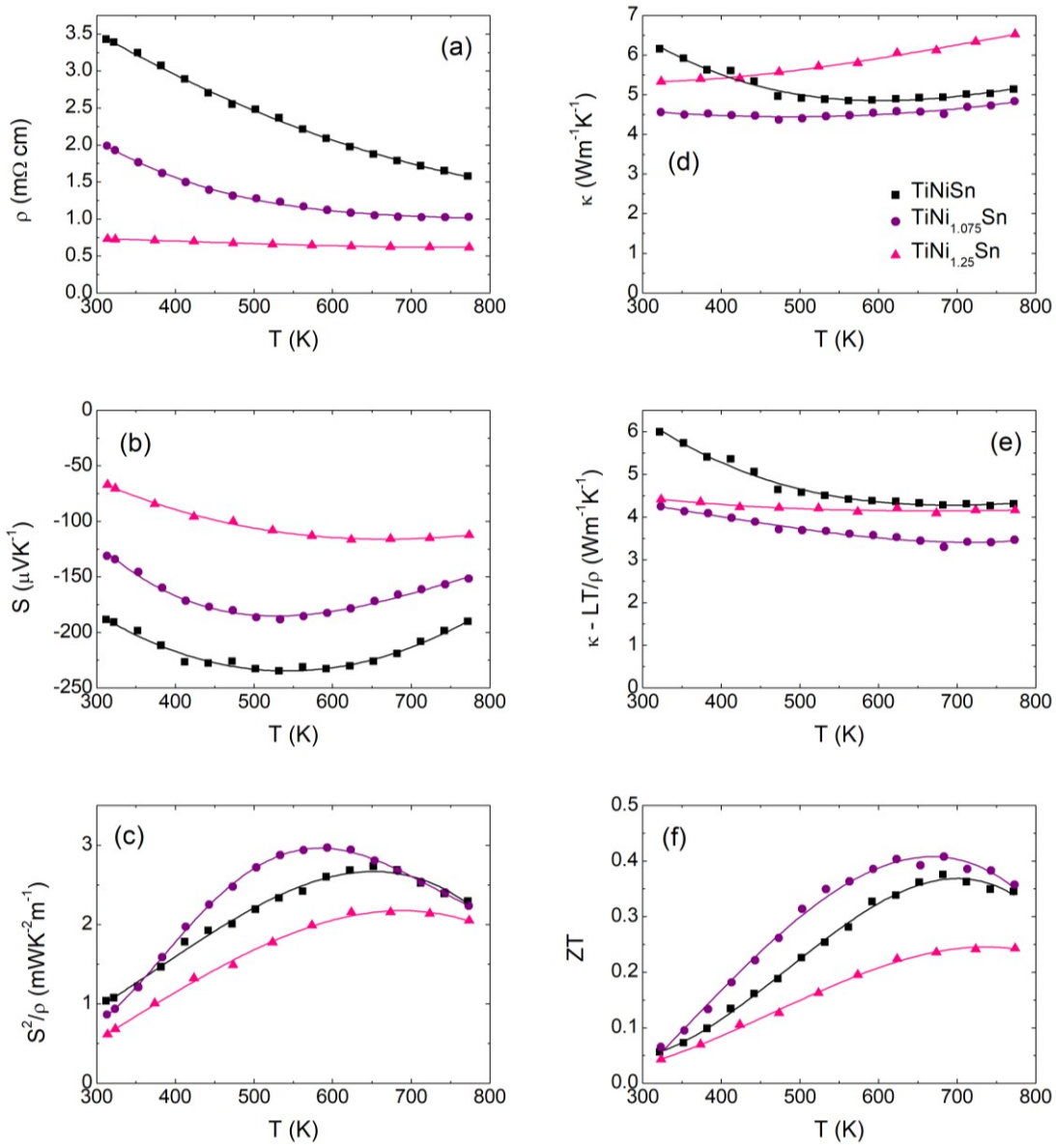

Figure D2. *TiNi$_{1+y}$Sn*: Temperature dependence of **(a)** the absolute Seebeck coefficient (*S*), **(b)** the resistivity (ρ), **(c)** the thermoelectric power factor (S^2/ρ), **(d)** the total thermal conductivity (κ), **(e)** the lattice thermal conductivity (κ-LT/ρ) and **(f)** figure of merit (*ZT*) for various TiNi$_{1+y}$Sn (y = 0, 0.075, 0.25) materials

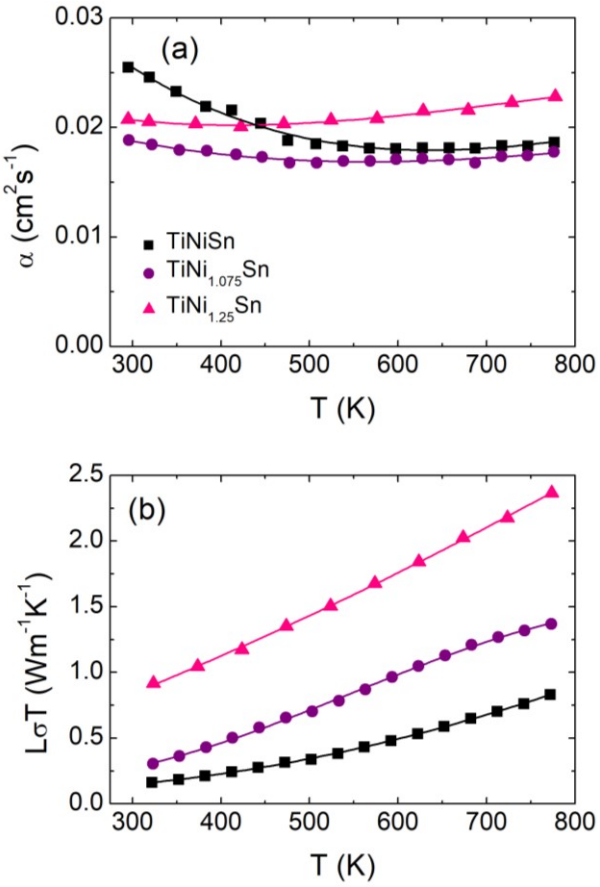

Figure D3. *$TiNi_{1+y}Sn$*: Temperature dependence of **(a)** the thermal diffusivity (α) and **(b)** the electronic thermal conductivity ($L\sigma T$) for $TiNi_{1+y}Sn$ (y = 0, 0.075 and 0.25).

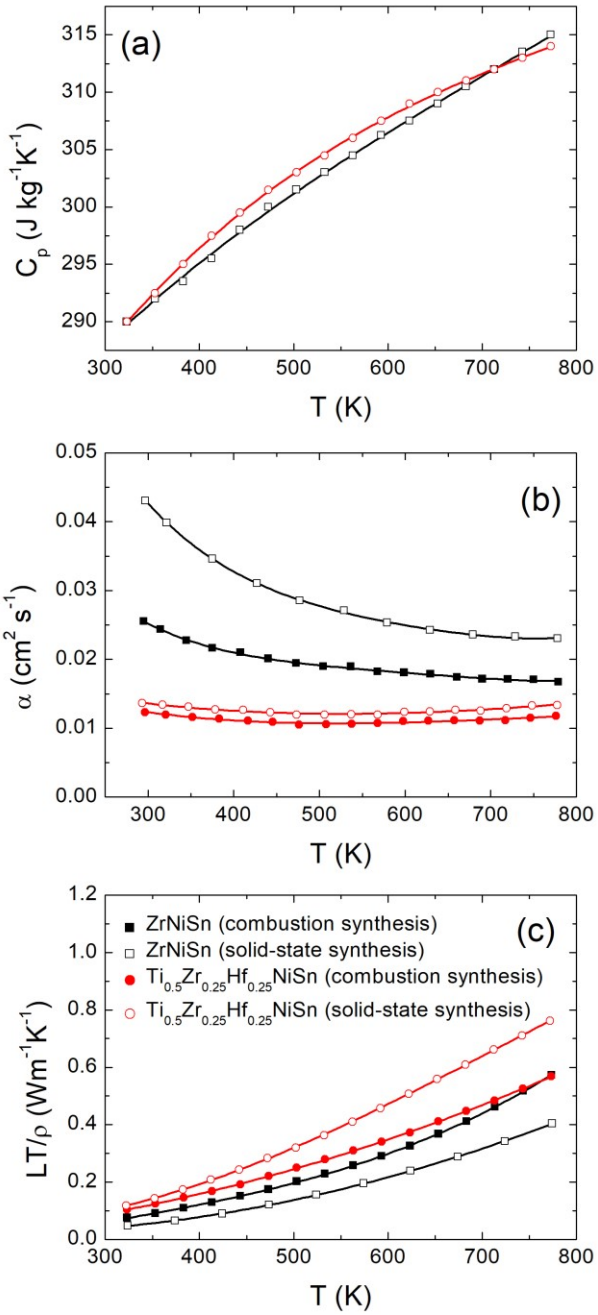

Figure D4. *ZrNiSn and $Ti_{0.5}Zr_{0.25}Hf_{0.25}NiSn$:* Temperature dependence of **(a)** heat capacity (C_p), **(b)** the thermal diffusivity (α) and **(c)** the electronic thermal conductivity (LT/ρ) for ZrNiSn and $Ti_{0.5}Zr_{0.25}Hf_{0.25}NiSn$ prepared using solid-state protocol and self-propagation high temperature synthesis.

Table D8. *$Ti_{0.5}Zr_{0.5}NiSn$* – Weight percentage (*wt%*) of intermediate phases that were identified during the heating up of elemental precursors to form target $Ti_{0.5}Zr_{0.5}NiSn$ alloy, determined through Rietveld analysis. *T* (°C) denotes the average temperature of 30°C measurement steps, y represents Ni (*2c*) site occupancy of $Ni_{3+y}Sn_4$, Ni (*4d*) site occupancy of $TiNi_{1+y}Sn$ and Ni (*8d*) site occupancy of full-Heusler (FH), while x denotes Zr content on (*4a*) site of half-Heusler (HH) phase and (*4a*) site of full-Heusler (FH) phase. The standard deviation for the *wt%* is 0.2, while for the Ni content (y) and for the M content (x) it is 0.005.

Ramping up (3ºC/min)																						
T (ºC)	Ti	Zr	Ni	Sn	$Ni_{3+y}Sn_4$		Ni_3Sn_2	Ni_3Sn	$Ti_{1-x}Zr_xNi_{2y}Sn$ (FH)			Ti_2Ni	TiNi	HH1 $Ti_{1x}Zr_xNi_{1+y}Sn$			HH3 $Ti_{1-x}Zr_xNi_{1+y}Sn$			HH2 $Ti_{1-x}Zr_xNiSn$		
	wt%	wt%	wt%	wt%	wt%	y	wt%	wt%	wt%	x	y	wt%	wt%	wt%	x	y	wt%	x	y	wt%	x	y
163.0	9.8	15.8	25.9	48.6																		
194.8	10.0	15.7	25.7	48.6																		
226.8	11.7	19.4	19.6		38.6	0.142	10.8															
257.7	9.9	13.1	4.2		57.7	0.218	10.7							4.4	1.0	0						
289.5	9.7	13.0	4.1		58.2	0.208	10.8							4.2	1.0	0						
321.0	9.6	12.7	4.1		58.2	0.199	11.1							4.3	1.0	0						
352.5	9.7	12.8	4.1		58.2	0.203	11.2							4.0	1.0	0						
384.1	9.6	12.9	4.1		57.7	0.209	11.6							4.1	1.0	0						
415.8	9.5	13.0	4.0		58.2	0.225	11.2							4.2	1.0	0						
446.9	9.6	13.1	3.9		57.1	0.229	12.0							4.3	1.0	0						
478.7	9.9	13.3	3.5		56.2	0.255	12.7							4.4	1.0	0						
510.0	10.1	13.6	2.8		55.3	0.282	13.1							5.2	1.0	0						
541.5	11.8	13.3	1.9		53.9	0.337	11.2	2.0						6.0	1.0	0						
572.8	12.4	13.3	1.2		54.7	0.417	10.4	1.8						6.2	1.0	0						
604.2	13.9	11.9	1.6		55.6	0.464	8.3	1.6						7.2	1.0	0						
635.6	12.6	10.4			46.9	0.493	9.1	11.9						8.2	1.0	0				0.9	0	0
667.4	12.9	9.8			43.6	0.534	6.9	14.6						11.1	1.0	0				1.2	0	0
698.4	12.0	7.3			33.0	0.590	7.1	27.0				1.6		11.3	1.0	0				0.9	0	0
730.6	10.4	8.2			33.7	0.626	7.9	21.2				2.4		15.1	1.0	0				1.2	0	0
761.3	11.6	8.7			30.7	0.693	14.7					2.7		30.2	1.0	0				1.5	0	0
792.7									33.8	0.162	0.754	4.0	2.7	54.8	1.0	0				4.7	0.085	0
824.1									25.8	0.087	0.773	2.7	1.4	53.0	1.0	0				17.2	0.124	0
855.4									22.6	0.101	0.720	1.8	1.5	48.2	1.0	0				25.9	0.136	0
886.5													4.1	52.5	1.0	0	11.9	0.709	0	31.5	0.134	0
899.9													3.3	49.6	1.0	0	12.8	0.638	0	34.4	0.131	0

Table D9. *$Ti_{0.5}Zr_{0.5}NiSn$* – Weight percentage (*wt%*) of intermediate phases that were identified during the annealing and cooling down of elemental precursors to form target $Ti_{0.5}Zr_{0.5}NiSn$ alloy, determined through Rietveld analysis. *T* (°C) denotes the average temperature of 30°C measurement steps, x and y represents Zr content on (*4a*) site and Ni (*4d*) site occupancy of half-Heusler (HH), respectively. The standard deviation for the *wt%* is 0.2, while for the Ni content (y) and for the M content (x) it is 0.005.

Long annealing										
Time	**HH1 – $Ti_{1-x}Zr_xNi_{1+y}Sn$**			**HH3 – $Ti_{1-x}Zr_xNi_{1+y}Sn$**			**HH2 – $Ti_{1-x}Zr_xNi_{1+y}Sn$**			**TiNi**
(min)	**wt%**	**x**	**y**	**wt%**	**x**	**y**	**wt%**	**x**	**y**	**wt%**
10	49.6	1.0	0	12.8	0.638	0	34.4	0.131	0.0404	3.3
20	45.6	1.0	0	15.8	0.651	0	35.6	0.124	0.0445	3.0
30	47.0	1.0	0	15.5	0.580	0	34.9	0.117	0.0421	2.6
40	46.0	1.0	0	17.7	0.555	0	34.1	0.109	0.0412	2.3
50	44.6	1.0	0	18.3	0.547	0	35.1	0.112	0.0437	2.0
60	43.7	1.0	0	20.7	0.545	0	33.7	0.104	0.0382	1.9
70	42.7	1.0	0	22.8	0.544	0	32.8	0.095	0.0384	1.7
80	41.5	1.0	0	25.3	0.528	0	31.7	0.095	0.0342	1.5
90	40.9	1.0	0	25.2	0.534	0	32.5	0.098	0.0334	1.4
100	39.9	1.0	0	27.5	0.521	0	31.3	0.093	0.0360	1.4
110	39.1	1.0	0	27.8	0.534	0	32.0	0.095	0.0285	1.2
120	38.8	1.0	0	28.6	0.530	0	31.4	0.091	0.0325	1.2
170	36.3	1.0	0	33.9	0.522	0	29.0	0.080	0.0304	0.8
220	34.4	1.0	0	34.2	0.535	0	30.8	0.092	0.0315	0.7
280	31.8	1.0	0	36.2	0.537	0	31.8	0.105	0.0321	0.5
320	27.8	1.0	0	43.2	0.475	0.051	29.0	0.105	0.0275	
370	27.0	1.0	0	43.1	0.501	0.036	29.9	0.108	0.0310	
420	25.8	1.0	0	44.8	0.504	0.037	29.4	0.109	0.0305	
470	24.6	1.0	0	46.6	0.516	0.026	28.8	0.107	0.0312	
520	24.0	1.0	0	47.3	0.516	0.031	28.8	0.108	0.0350	
530	23.9	1.0	0	46.9	0.520	0.030	29.2	0.116	0.0302	
540	23.7	1.0	0	47.8	0.514	0.031	28.4	0.108	0.0305	
550	23.3	1.0	0	47.6	0.534	0.019	29.0	0.107	0.0388	
560	23.6	1.0	0	46.8	0.525	0.023	29.6	0.114	0.0358	
570	23.1	1.0	0	47.3	0.526	0.026	29.6	0.112	0.0392	
580	23.1	1.0	0	48.3	0.527	0.022	28.7	0.112	0.0344	
590	22.8	1.0	0	47.6	0.531	0.022	29.6	0.113	0.0373	
Cooling down										
T (ºC)	**HH1 – $Ti_{1-x}Zr_xNi_{1+y}Sn$**			**HH2 – $Ti_{1-x}Zr_xNi_{1+y}Sn$**			**HH3 – $Ti_{1-x}Zr_xNi_{1+y}Sn$**			**TiNi**
	wt%	**x**	**y**	**wt%**	**x**	**y**	**wt%**	**x**	**y**	**wt%**
899.9	22.8	1.0	0	47.6	0.531	0.0217	29.6	0.1133	0.0373	
845.7	22.6	1.0	0	48.7	0.522	0.0274	28.7	0.1083	0.0367	
737.1	22.6	1.0	0	47.3	0.535	0.0197	30.2	0.1229	0.0301	
603.0	22.8	1.0	0	47.9	0.537	0.0162	29.3	0.1121	0.0372	
488.7	22.8	1.0	0	47.2	0.525	0.0243	30.0	0.1229	0.0331	
420.0	22.6	1.0	0	47.8	0.528	0.0188	29.6	0.1149	0.0339	
373.5	22.2	1.0	0	48.0	0.530	0.0194	29.7	0.1150	0.0308	
338.2	22.0	1.0	0	48.6	0.533	0.0156	29.4	0.1090	0.0349	

Table D10. *$Ti_{0.5}Hf_{0.5}NiSn$* – Weight percentage (*wt%*) of intermediate phases that were identified during the heating up of elemental precursors to form target $Ti_{0.5}Hf_{0.5}NiSn$ alloy, determined through Rietveld analysis. *T* (°C) denotes the average temperature of 30°C measurement steps, y represents Ni (*2c*) site occupancy of $Ni_{3+y}Sn_4$, Ni (*4d*) site occupancy of $TiNi_{1+y}Sn$ and Ni (*8d*) site occupancy of full-Heusler (FH), while x denotes Hf content on (*4a*) site of half-Heusler (HH) phase and Hf content on (*4a*) site of full-Heusler (FH) phase. The standard deviation for the *wt%* is 0.2, while for the Ni content (y) and for the M content (x) it is 0.005.

Ramping up (3°C/min)																					
T (°C)	**Ti**	**Hf**	**Ni**	**Sn**	**$Ni_{3+y}Sn_4$**		**Ni_3Sn_2**	**Ni_3Sn**	**FH $Ti_{1-x}Hf_xNi_2Sn$**		**Ti_2Ni**	**TiNi**	**HH1 $Ti_{1-x}Hf_xNi_{1+y}Sn$**			**HH2 $Ti_{1-x}Hf_xNi_{1+y}Sn$**			**HH3 $Ti_{1-x}Hf_xNi_{1+y}Sn$**		
	wt%	**wt%**	**wt%**	**wt%**	**wt%**	**y**	**wt%**	**wt%**	**wt%**	x	**wt%**	**wt%**	**wt%**	**x**	**y**	**wt%**	**x**	**y**	**wt%**	**x**	**y**
123.3	8.1	31.6	22.5	37.8																	
155.0	8.5	31.0	22.6	37.9																	
187.2	8.4	31.7	22.6	37.3																	
217.3	8.7	32.0	22.7	36.6																	
249.3	7.0	27.9	2.2		53.7	0.393	9.3														
281.1	8.8	28.6	2.0		47.3	0.326	7.1	1.6					3.0	1.0	0	1.5	0	0			
312.5	8.3	28.8	2.0		48.2	0.332	6.8	1.7					2.8	1.0	0	1.5	0	0			
343.9	8.2	28.9	2.0		47.9	0.325	7.1	1.8					2.8	1.0	0	1.3	0	0			
375.6	8.6	29.3	1.8		47.5	0.325	6.9	1.6					3.0	1.0	0	1.2	0	0			
406.9	8.4	28.7	1.7		47.8	0.333	7.2	1.8					3.2	1.0	0	1.2	0	0			
438.4	8.7	28.4	1.9		47.6	0.339	6.9	1.6					3.1	1.0	0	1.8	0	0			
469.7	8.4	28.4	1.9		47.1	0.342	7.4	1.7					3.2	1.0	0	1.9	0	0			
501.2	8.0	28.7	1.6		47.5	0.370	7.7	1.8					3.2	1.0	0	1.5	0	0			
532.5	7.9	28.9	1.4		47.1	0.396	8.3	1.7					3.2	1.0	0	1.6	0	0			
564.0	7.9	28.9	1.0		47.8	0.439	7.4	1.9					3.5	1.0	0	1.6	0	0			
595.3	7.8	27.5	1.6		48.3	0.470	7.8	1.3					3.9	1.0	0	1.8	0	0			
626.5	8.0	27.0	1.2		47.3	0.496	7.7	1.6					5.5	1.0	0	1.7	0	0			
657.7	7.8	24.2			46.3	0.537	11.9						7.8	1.0	0	2.0	0	0			
688.8	6.4	20.5			42.0	0.583	11.9						15.8	1.0	0	3.4	0	0			
720.0	3.9	12.5			24.2	0.628			11.8	0.054	1.9		34.7	1.0	0	10.9	0.452	0			
751.3	2.6	7.5			10.5	0.706			17.3	0.092	2.1		48.2	1.0	0	11.8	0.492	0			
782.7									18.8	0.121	2.3	1.3	61.2	1.0	0	16.4	0.455	0			
814.2									11.3	0.116		1.6	56.2	1.0	0	21.1	0.602	0	9.9	0.106	0
845.4									6.8	0.110		1.7	52.8	1.0	0	23.7	0.617	0	14.9	0.111	0
876.1									8.3	0.166		1.1	48.0	1.0	0	25.9	0.577	0	16.6	0.108	0
898.3									2.9	0.138		2.0	48.5	1.0	0	28.6	0.610	0	18.0	0.113	0

Table D11. *$Ti_{0.5}Hf_{0.5}NiSn$* – Weight percentage (*wt%*) of intermediate phases that were identified during the annealing and cooling down of elemental precursors to form target $Ti_{0.5}Hf_{0.5}NiSn$ alloy, determined through Rietveld analysis. *T* (°C) denotes the average temperature of 30°C measurement steps, x and y represents Hf content on (*4a*) site and Ni (*4d*) site occupancy of half-Heusler (HH), respectively. The standard deviation for the *wt%* is 0.2, while for the Ni content (y) and for the M content (x) it is 0.005.

Long annealing										
Time (min)	**HH1 – $Ti_{1-x}Hf_xNi_{1+y}Sn$**			**HH2 – $Ti_{1-x}Hf_xNi_{1+y}Sn$**			**HH3 – $Ti_{1-x}Hf_xNi_{1+y}Sn$**			**TiNi**
	wt%	**x**	**y**	**wt%**	**x**	**y**	**wt%**	**x**	**y**	**wt%**
10	57.5	1.0	0	22.0	0.528	0	18.6	0.084	0.028	2.0
20	51.4	1.0	0	27.8	0.559	0	19.0	0.085	0.031	1.8
30	50.4	1.0	0	28.3	0.570	0	19.8	0.081	0.032	1.5
40	48.7	1.0	0	30.5	0.560	0	19.5	0.078	0.032	1.4
50	44.8	1.0	0	34.3	0.576	0	19.8	0.078	0.036	1.2
60	43.4	1.0	0	35.2	0.599	0	20.3	0.083	0.031	1.2
70	41.8	1.0	0	37.2	0.600	0	20.0	0.077	0.031	1.0
80	42.6	1.0	0	36.2	0.590	0	20.3	0.080	0.025	0.9
90	40.5	1.0	0	38.7	0.591	0	19.9	0.078	0.024	0.9
100	41.0	1.0	0	37.9	0.596	0	20.3	0.079	0.026	0.8
110	39.2	1.0	0	39.0	0.597	0	21.0	0.081	0.016	0.7
120	37.1	1.0	0	41.6	0.599	0	20.6	0.084	0.024	0.8
170	33.0	1.0	0	45.8	0.608	0	20.8	0.075	0.039	0.5
220	35.5	1.0	0	43.3	0.596	0	20.8	0.079	0.027	0.5
270	39.2	1.0	0	39.9	0.579	0	20.9	0.081	0.029	
320	33.3	1.0	0	46.1	0.593	0	20.6	0.080	0.027	
360	31.4	1.0	0	48.0	0.598	0	20.6	0.073	0.034	
Cooling down										
T (ºC)	**HH1 – $Ti_{1-x}Hf_xNi_{1+y}Sn$**			**HH2 – $Ti_{1-x}Hf_xNi_{1+y}Sn$**			**HH3 – $Ti_{1-x}Hf_xNi_{1+y}Sn$**			**TiNi**
	wt%	**x**	**y**	**wt%**	**x**	**y**	**wt%**	**x**	**y**	**wt%**
898.9	31.4	1.0	0	47.6	0.531	0	20.6	0.084	0.028	
857.1	26.0	1.0	0	48.7	0.522	0	20.3	0.096	0.000	
750.4	25.0	1.0	0	47.3	0.535	0	20.5	0.096	0.000	
619.1	43.9	1.0	0	47.9	0.537	0	19.9	0.077	0.000	
499.2	43.3	1.0	0	47.2	0.525	0	19.9	0.074	0.000	

Table D12. *$Zr_{0.5}Hf_{0.5}NiSn$* – Weight percentage (*wt%*) of intermediate phases that were identified during the heating up of elemental precursors to form target $Zr_{0.5}Hf_{0.5}NiSn$ alloy, determined through Rietveld analysis. *T* (°C) denotes the average temperature of 30°C measurement steps, y represents Ni (*2c*) site occupancy of $Ni_{3+4}Sn_4$ and Ni content on (*4d*) site of half-Heusler (HH) phase. The standard deviation for the *wt%* is 0.2, while for the Ni content (y) it is 0.005.

Ramping up (3ºC/min)										
T (ºC)	**Zr**	**Hf**	**Ni**	**Sn**	**$Ni_{3+y}Sn_4$**		**Ni_3Sn_2**	**Ni_3Sn**	**$Zr_{0.5}Hf_{0.5}Ni_{1+y}Sn$**	
	wt%	**wt%**	**wt%**	**wt%**	**wt%**	**y**	**wt%**	**wt%**	**wt%**	**y**
123.9	13.0	31.2	21.8	34.0						
154.5	12.7	31.2	21.6	34.5						
186.0	12.8	30.8	21.6	34.8						
219.5	15.4	37.4	16.8		24.7	0.118	5.7			
249.8	10.5	28.7	2.9		46.5	0.221	4.6		6.7	0.057
281.3	10.1	29.1	2.9		46.7	0.213	4.5		6.7	0.031
312.7	10.2	28.6	2.9		45.6	0.215	5.7		7.0	0.043
344.1	10.3	28.9	2.9		44.6	0.212	6.5		6.9	0.055
375.7	10.3	29.3	2.9		44.2	0.216	6.5		6.9	0.043
407.1	10.3	29.2	2.9		44.5	0.236	6.2		6.9	0.053
438.6	10.6	28.4	2.7		43.8	0.233	7.5		6.9	0.070
470.0	10.7	28.3	2.5		43.6	0.263	8.0		6.9	0.071
501.5	10.1	29.1	2.0		42.4	0.314	7.9	1.3	7.2	0.049
532.9	10.4	28.5	1.4		42.1	0.358	8.1	1.6	7.8	0.026
565.0	11.8	26.7	1.0		43.6	0.392	6.6	1.7	8.6	0.022
595.7	14.3	22.8	0.7		43.6	0.420	5.7	1.4	11.6	0.013
627.0	17.9	19.5			37.1	0.451	7.2	1.7	16.6	0.029
658.5	16.8	17.4			39.0	0.523		2.0	24.8	0.017
689.9	12.8	17.4			33.4	0.576		2.6	33.8	0.018
721.3	13.9	11.6			23.1	0.606		2.6	48.8	0.011
752.7	4.0	9.2			11.9	0.722			75.0	0.013
784.1	7.6	7.1			6.5	0.737			78.9	0.011
815.5	5.9	5.6							88.5	0.011
846.5	4.9	4.3							90.8	0.011
877.5									100.0	0.015
898.6									100.0	0.016

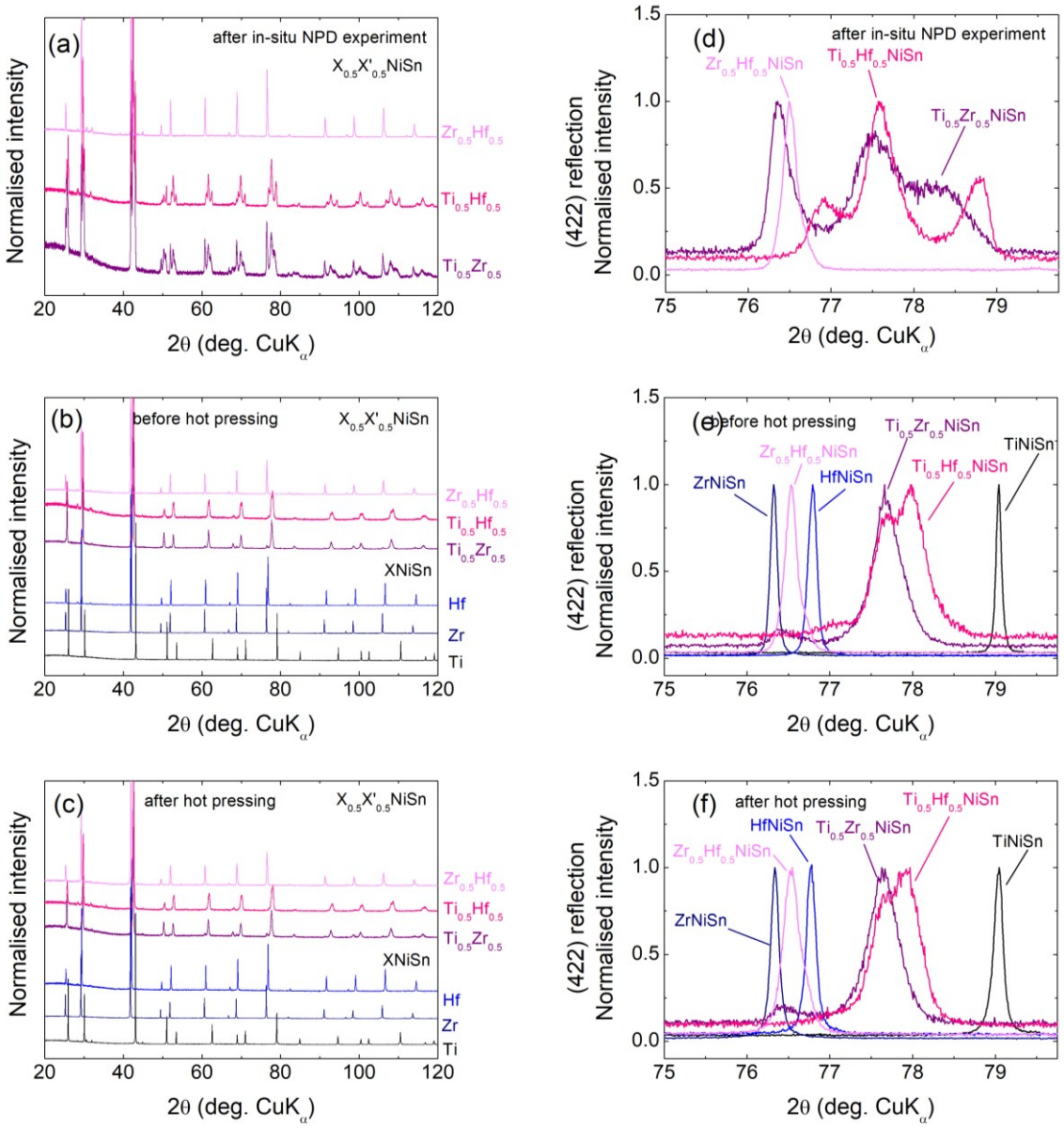

Figure D5. *MNiSn and $M_{0.5}M'_{0.5}$NiSn*: **(a-c)** Laboratory X-ray powder diffraction patterns of samples after in-situ NPD, long annealing and hot-pressing. All main peaks can be indexed on the half-Heusler structure. **(d-f)** The diffraction peak for the (422) half-Heusler reflection.

Table D13. *MNiSn and $M_{0.5}M'_{0.5}NiSn$*: Lattice parameters (*a*) and weight percentages (*wt%*) of half-Heusler phases, which were used during the Rietveld refinement of TiNiSn, ZrNiSn and HfNiSn samples, before and after hot-pressing.

Composition	Half-Heusler		$(Zr/Hf)O_2$
	a (Å)	wt%	wt%
Before hot-pressing			
TiNiSn	5.9304(1)	100	
ZrNiSn	6.1077(1)	100	
HfNiSn	6.0764(1)	95.5(2)	4.5(2)
After hot-pressing			
TiNiSn*	5.9307(1)	97.8(1)	
ZrNiSn♦	6.1068(1)	98.3(2)	
HfNiSn	6.0774(1)	100	

*contains Sn; ♦contains Ni_3Sn_4

Table D14. *MNiSn and $M_{0.5}M'_{0.5}NiSn$*: Lattice parameters (*a*) and weight percentages (*wt%*) of half-Heusler phases, which were used during the Rietveld refinement of $Ti_{0.5}Zr_{0.5}NiSn$, $Ti_{0.5}Hf_{0.5}NiSn$ and $Zr_{0.5}Hf_{0.5}NiSn$ samples following in-situ NPD experiment (equivalent of 3 – 10 hours of annealing), long annealing (2 weeks) and hot-pressing.

Composition	Half-Heusler 1		Half-Heusler 2		Half-Heusler 3		$(Zr/Hf)O_2$
	a (Å)	wt%	a (Å)	wt%	a (Å)	wt%	wt%
Following in-situ NPD experiment (equivalent annealing time: 3 – 10 hours, 900°C)							
$Ti_{0.5}Zr_{0.5}NiSn$	5.9754(2)	23.6(1)	6.0268(2)	47.4(1)	6.1011(2)	29.0(1)	
$Ti_{0.5}Hf_{0.5}NiSn$	5.9508(1)	27.1(1)	6.0221(1)	56.3(1)	6.0656(1)	14.1(1)	2.5(1)
$Zr_{0.5}Hf_{0.5}NiSn$	6.09523(4)	100.0					
After long annealing (2 weeks, 900°C); before hot-pressing							
$Ti_{0.5}Zr_{0.5}NiSn$	6.0171(1)	94.6(1)	6.1007(1)	5.4(1)			
$Ti_{0.5}Hf_{0.5}NiSn$	5.9965(1)	57.2(1)	6.0182(1)	38.9(1)			3.9(2)
$Zr_{0.5}Hf_{0.5}NiSn$♦	6.0932(1)	96.6(2)					2.1(2)
After hot-pressing							
$Ti_{0.5}Zr_{0.5}NiSn$*	6.0199(1)	94.8(1)	6.0988(2)	4.7(1)			
$Ti_{0.5}Hf_{0.5}NiSn$*	6.0009(1)	64.1(1)	6.0213(1)	32.8(1)			2.9(2)
$Zr_{0.5}Hf_{0.5}NiSn$♦	6.0927(1)	96.8(1)					1.5(1)

*contains Sn, ♦contains Ni_3Sn_2

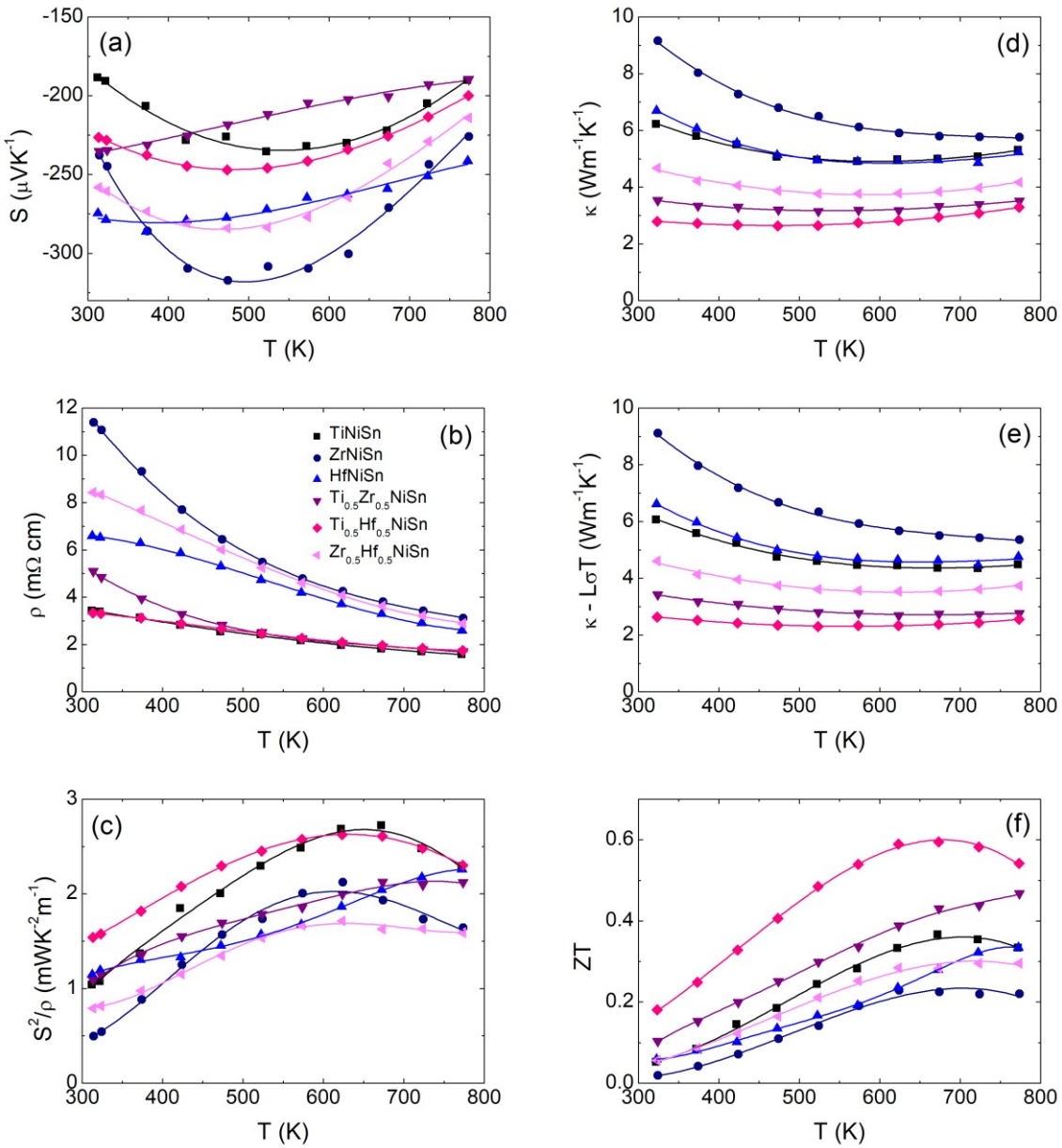

Figure D6. *MNiSn and $M_{0.5}M'_{0.5}$NiSn*: Temperature dependence of **(a)** the absolute Seebeck coefficient (S), **(b)** the resistivity (ρ), **(c)** the thermoelectric power factor (S^2/ρ), **(d)** the total thermal conductivity (κ), **(e)** the lattice thermal conductivity (κ-$L\sigma T$) and **(f)** figure of merit (ZT) for MNiSn and $M_{0.5}M'_{0.5}$NiSn (M = Ti, Zr, Hf).

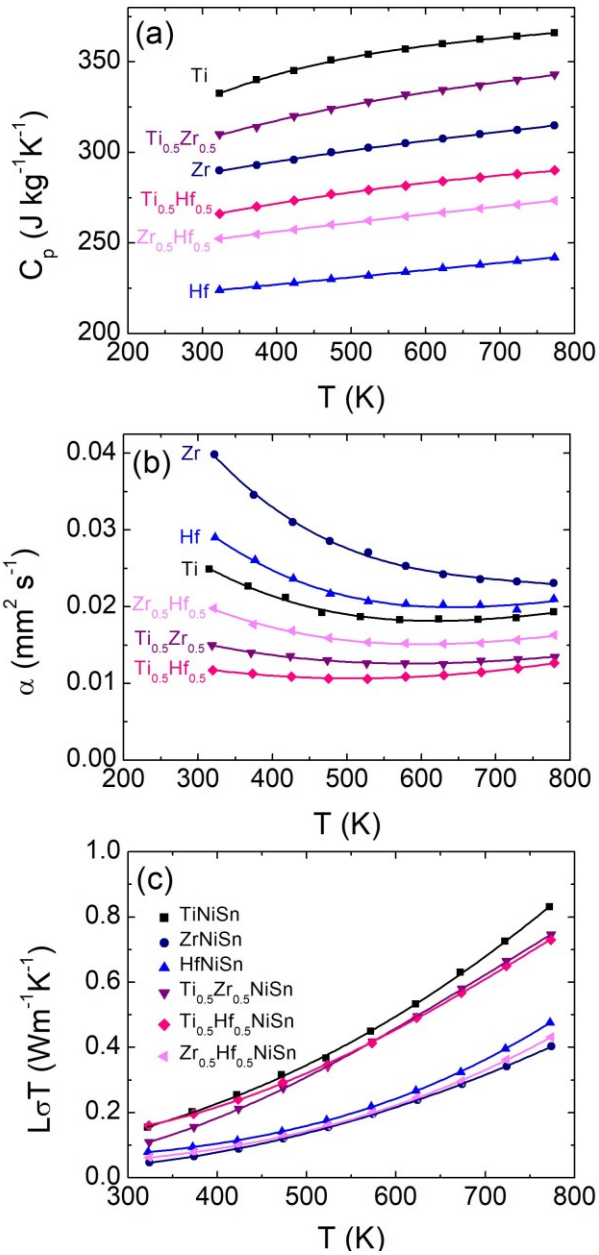

Figure D7. *MNiSn and $M_{0.5}M'_{0.5}$NiSn*: Temperature dependence of **(a)** heat capacity (C_p), **(b)** the thermal diffusivity (α) and **(c)** the electronic thermal conductivity ($L\sigma T$) for MNiSn and $M_{0.5}M'_{0.5}$NiSn (M = Ti, Zr, Hf).